Investigating the dynamics of a population of spiking neurons across spatial scales

A thesis submitted

for the degree of

Doctor of Philosophy

in Physics

by

Sanduni Chavinka Malluwawadu

THE UNIVERSITY OF
WAIKATO
Te Whare Wānanga o Waikato

2021

The University of Waikato

Abstract

Mean-field models describe bulk neural activity in terms of population-average action potential (spike) rates, but do not attempt to address the variations in the firing activity of individual neurons and the interactions among them. In 2016, Waikato Cortical Modelling group published a purely theoretical model [Steyn-Ross et al, *Phys. Rev. E* 93.2 (2016): 022402] that provides a more accurate mapping of spiking dynamics, scaling from single neuron to the macroscopic level by regridding the system using a spatial blocking: a bottom-up neural regridding referred to as True-field. A 2D continuum of identical neurons is constructed from a lattice of spiking neurons that are coupled both synaptically (via chemical synapses) and diffusively (via electrical synapses). The spiking behaviour at the single-neuron level is modelled using the Wilson point neuron equations, steered by incoming electrical impulses from adjacent neurons. These equations are then reblocked to form a coarser-spatial resolution by eliminating the high-frequency spatial modes. The existence of diffusive terms in voltage and recovery equations is crucial for this spatial coarse-graining procedure.

The purpose of this thesis is to conduct a preliminary analysis of the True-field model, which has never been tested in simulations before. The coarse-graining procedure employed in this framework results in a set of nonlinear corrections in the model equations. My first challenge is to recover those corrections and conduct numerical investigations to identify the most significant ones. My next challenge is to tune parameters of the True-field model via a comprehensive series of simulations, looking for "realistic" cortical behaviours. Two approaches are used: point simulations of the homogeneous two-neuron cortex, and full 2D grid simulations of a sheet of cortical tissue. Point simulations are straightforward and time efficient but do not provide any information about spatial variations in firing activity; grid simulations allow examination of spatial patterns, but can be challenging to set up, and are computationally expensive in terms of run times and memory requirements. I demonstrate that True-field can reproduce spiking behaviour of a normal brain across multiple levels using a range of blocking ratios: intracellular spiking for low blocking; agglomerated population events (EEG patterns) when blocking is increased. I also show that the model can produce the seizure-like events (SLE) seen in a slice of mouse brain sustained in a bath of artificial cerebro-spinal fluid (aCSF). My grid simulations confirm the generation and propagation of firing activity across the reblocked cortical grid. In conclusion, this new paradigm provides insights about the spiking dynamics of neurons from microscopic to macroscopic levels in a way that neither single-neuron nor mean-field approaches can do.

Preface

Contents Overview

This thesis conducts a comprehensive preliminary analysis of the True-field model. The thesis proceeds as follows.

Chapter 1 furnishes the basic knowledge about the dynamics of the human brain. I discuss primary neurophysiological facts and various techniques used to measure electrical activity of the brain at multiple scales: electroencephalogram (EEG), electrocorticogram (ECoG), local field potential (LFP), and intracellular recordings. The chapter is concluded by presenting a discussion about various neural modelling approaches and their relevance to the brain dynamics at different scales.

Chapter 2 provides an overview of the concept of modelling individual neurons. I discuss various single neuron models and explain the reason for selecting Wilson's spiking neuron approach to model spiking behaviour of individual neurons in the Waikato True-field model. I then present a detailed survey of Wilson's type-I (human cortical) neuron model. The previous work on the stability analysis of the Wilson neuron is extended by demonstrating the birth and death of spiking.

Chapter 3 surveys the concept of modelling neuronal assemblies. I discuss the downside of single-unit based models and discuss the effectiveness of top-down mean-field approach over single neuron models. I then provide an overview of some well-established mean-field models. The chapter is concluded by explaining the motivation of going beyond mean-field theory to develop Waikato True-field model.

Chapter 4 provides the foundation for True-field model by evaluating the blocking corrections that was resulted by the adiabatic elimination employed in the model. These corrections rely on 16 associated wavenumber integrals which are calculated numerically. I discuss how the strength of these blocking correction coefficients depend on the parameters: voltage and recovery diffusivities; voltage and recovery noises; and the blocking ratio. I wind up the chapter by demonstrating the variation of each correction coefficient with blocking.

In **Chapter 5**, I explore a primary version of the True-field model by turning off the chemical synapses: the reblocked Wilson neuron in the spatially homogeneous limit. The simplified model is then analysed for both negligible noise and first order noise. I then discuss how voltage and recovery noise intensities affect the spiking dynamics of the neuron. Finally, I compare the magnitudes of reblocking corrections and identify the most significant ones.

Chapter 6 shows that True-field is capable of reproducing different realistic cortical behaviours. Using homogeneous-cortex point simulations I tune True-field parameters to generate

normal brain behaviours across multiple scales using a range of blocking ratios: intracellular spiking behaviour for low blocking, and agglomerated population events for higher blocking. Grid simulations are finally used to demonstrate the propagation of slow-wave delta oscillation through the grid.

In **Chapter 7**, I demonstrate that True-field can also reproduce Seizure-like events (SLEs) seen in mouse brain slice. The simulated SLEs are compared with the biological SLEs seen in Dr Logan Voss's mouse brain slice recordings. I then discuss how the parameters can be adjusted to alter the structure and duration of simulated SLEs. Finally, a grid simulation is presented to show the propagation of SLE across the grid.

Chapter 8 concludes the thesis with a brief summary of my work and suggestions for future work.

In **Appendices**, I present MATLAB codes to evaluate wavenumber integrals $\overline{c}_{16}$ and $\overline{c}_3$, and Butterworth Deconvolution Theory.

Original Contributions

The numerical calculations, theoretical analysis, MATLAB codes and most of the graphic presentations are my own work, except:

- MATLAB codes for Butterworth Deconvolution written by my supervisor A/Prof D. A. Steyn-Ross
- Local field potential recordings in mouse brain slice experiment of Section 7.2 provided by Dr. Logan J. Voss

Conference Presentations

- S. C. Malluwawadu, D. A. Steyn-Ross, Moira L. Steyn-Ross and M. T. Wilson. Investigating action potential initiation and death in human cortex using a novel modelling approach, *New Zealand Institute of Physics Conference,* Christchurch, New Zealand, April 2019
- S. C. Malluwawadu, D. A. Steyn-Ross, Moira L. Steyn-Ross and M. T. Wilson. Modelling the spiking behaviour of neurons in human cortex, *Australasian Winter Conference on Brain Research,* Queenstown, New Zealand, August 2018
- S. C. Malluwawadu, D. A. Steyn-Ross, Moira L. Steyn-Ross and M. T. Wilson. Exploring population spiking behaviour of neurons in human cortex, *New Zealand Institute of Physics Conference,* Dunedin, New Zealand, July 2017

Acknowledgements

First and foremost, I would like to express my gratitude to my chief supervisor, Associate Professor Alistair Steyn-Ross for the continuous support for my research, for his patience and motivation. His continuous guidance helped me in every step of this hard journey. I would also like to thank Professor Moira Steyn-Ross for her guidance in understanding the theoretical background of the True-field model. My sincere thanks go to Associate Professor M. T. Wilson for his valuable comments and advices throughout this study. Moreover, I would like to thank Dr. Logan Voss for providing me mouse brain slice recordings and information about electrophysiology experiments. The thesis has also benefited from insightful comments and suggestions made by Professor Jamie Sleigh. All of you have been there to support me to overcome difficult aspects of my research.

I gratefully acknowledge Fisher and Paykel Healthcare, for providing a study award towards my PhD study.

I would also like to express my heartfelt gratitude to my parents for all the support and sacrifices they made for me. Finally a big thank you to my beloved husband who has been by my side throughout this tough journey, giving endless support and encouragement.

Dedication

I dedicate this thesis—

To my husband Sampath Rajakaruna
To my parents Mr. M. W. Chandrawansa and Ms. G. D. Sriyani Samarasekare
To everyone I've encountered with in my research journey

Thanks for the patience and making this journey beautiful...

Contents

List of Figures

List of Tables

Acronyms and Abbreviations

1D, 2D	one-dimensional, two-dimensional
aCSF	artificial cerebro-spinal fluid
ECoG	electrocorticogram (brain activity recorded via electrodes attached directly to the cerebral cortex; cf. EEG)
EEG	electroencephalogram (brain activity recorded via scalp electrodes; cf. ECoG)
EPSP	excitatory postsynaptic potential
GABA	γ-aminobutyric acid (an inhibitory neurotransmitter)
IPSP	inhibitory postsynaptic potential
LFP	local field potential
NMDA	*N*-methyl-D-aspartate (an excitatory neurotransmitter found in most synapses of the central nervous system)
PSP	postsynaptic potential
SLE	seizure-like event
rms	root-mean square

Chapter 1

Background

This chapter lays the foundation for this thesis by providing the necessary prerequisite knowledge about the dynamics of the human brain. After introducing basic neurophysiological facts about cortical neurons, I explain various techniques used to measure brain's electrical activity at different scales: electroencephalogram (EEG) when recorded from the scalp; electrocorticogram (ECoG) when recorded by subdural grid electrodes on the cortical surface; local field potential (LFP) when recorded from the extracellular field; and intracellular recordings when recorded by placing a microelectrode inside a cell. The procedure of recording LFPs in a mouse brain slice is discussed in detail. I conclude the chapter by discussing different neural modelling approaches and their relevance to the brain dynamics at different scales.

1.1 Basic Neurophysiology

1.1.1 What is a Neuron?

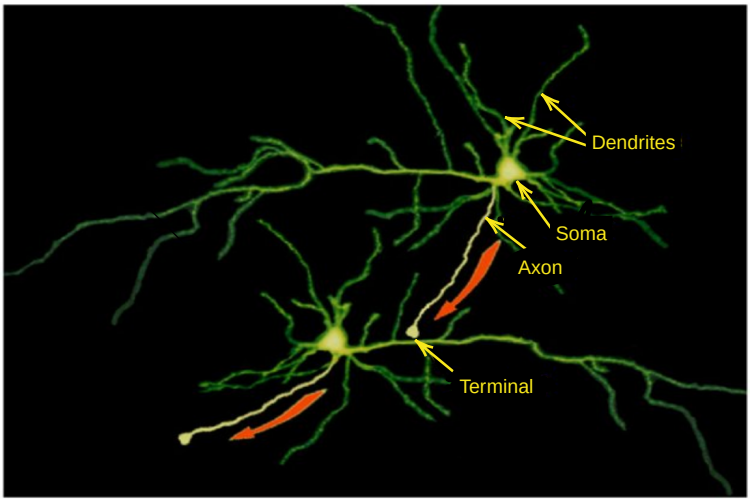

Figure 1.1: Image of pyramidal neurons in human brain. Neurons have been visualised using fluorescent dye and viewed through a microscope. Red arrows show the direction of an electrical impulse. Average diametre of a pyramidal cell body (soma) is about 20 μm. Source: O'Connor *et al* (2012) [59].

The neuron is the fundamental working unit of the brain and nervous system. Sensations, movements, thoughts and memories are all results of signals that pass through neurons. A healthy human brain contains about 85 billion neurons [32, 85]. A neuron has three main parts: cell body (soma), an axon, and dendrites (Fig. 1.1). The cell body contains the nucleus that directs all neuron activity; the axon is a long extension of the neuron that transmits electrical

impulses away from the cell body to other neurons; dendrites are the branching extensions from the cell body that receive messages from other nerve cells.

1.1.2 Reversal Potential

Neurons are encapsulated within a thin plasma membrane (see Fig. 1.2) that acts as both an insulator and a diffusion barrier to the movement of ions (mainly Na^+, K^+, and Cl^-). The membrane potential at which there is no net flow of a particular ion from one side of the membrane to the other is called the *reversal potential*, also known as the *Nernst potential* as it can be calculated using the Nernst equation,

$$E_X = \frac{RT}{zF} \ln \frac{[X]_{in}}{[X]_{out}} \tag{1.1}$$

where E_X is the reversal potential for a single ion type X, $R = 8.314\,J\,K^{-1}mol^{-1}$ is the universal gas constant, T is absolute temperature in kelvin ($K = °C + 273.15$), z is the valence of X (e.g., $z = +1$ for K^+), $F = 9.6485 \times 10^4\,C\,mol^{-1}$ is the Faraday constant, and $[X]_{in}$ and $[X]_{out}$ are the concentration of ion X inside and outside the cell membrane.

Table 1.1 shows the concentrations of the four main ion types and their Nernst potentials for a resting mammalian neuron at 37°C.

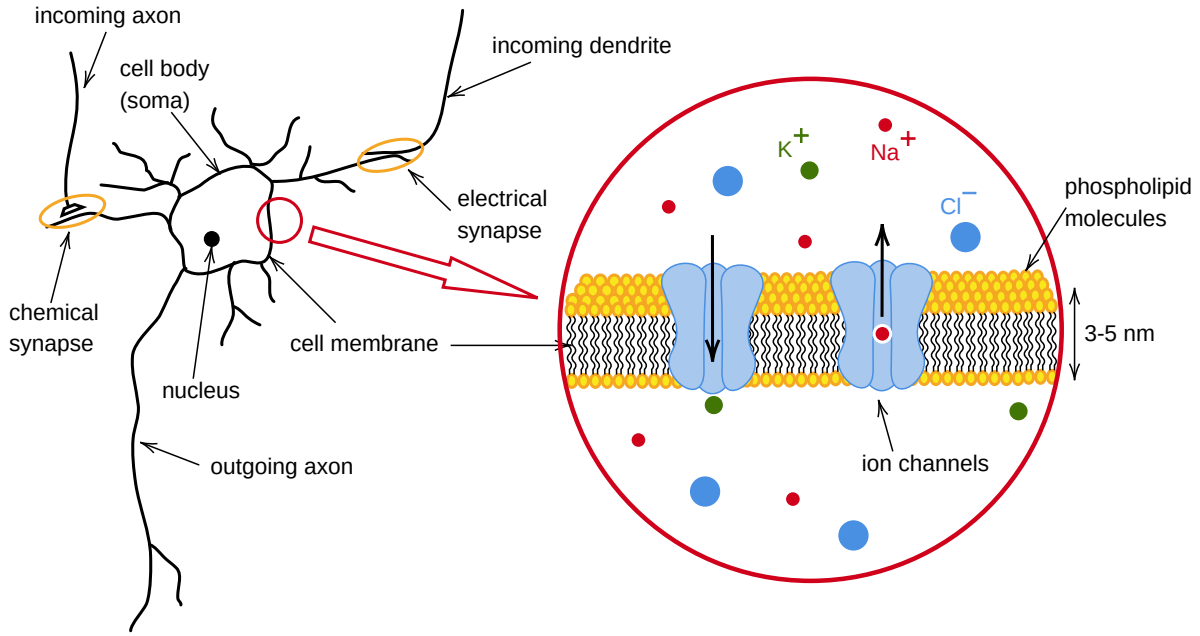

Figure 1.2: Schematic overview of a neuron (left) and cell membrane detail (right). The left diagram includes chemical and electrical synapses which we discuss in Section 1.1.8.

Table 1.1: Ion concentrations and Nernst equilibrium potentials for mammalian neuron at 37°C [41]. Ion concentrations are expressed in millimolar units, mM (10^{-3} mol/L).

Ion	Inside (mM)	Outside (mM)	Nernst Potential
K^+	140	5	−90 mV
Na^+	5 to 15	145	91 to 61 mV
Cl^-	4	110	−89 mV
Ca^{2+}	10^{-4}	2.5 to 5	136 to 145 mV

1.1.3 Resting Membrane Potential

Neurons maintain different concentrations of certain ions (Ca^{2+}, Na^+, K^+, Cl^-) across the cell membrane. This concentration gradient creates an electrical potential difference between inside and outside of the neuron called the *membrane potential* of the neuron,

$$V_m = V_{\text{in}} - V_{\text{out}}$$

A resting neuron maintains a voltage difference with the inside of the cell being more negative than the outside of the cell. This was demonstrated by the experiments carried out by Hodgkin and Huxley in 1939 [45, 47]. The voltage difference of a quiescent cell is called the *resting membrane potential*. In a typical neuron, the resting potential is around −70 mV.

In living cells, the resting membrane potential is not maintained by a single ion type such as K^+, Na^+ or Cl^-. If this were the case, the membrane potential could be easily calculated by the Nernst equation. Instead one needs to consider the combined effect of several ion types. When more than one ion channel is active (open) in the membrane, the equilibrium voltage of the cell depends on the relative permeability of the ions and can be calculated by using the *Goldman-Hodgkin-Katz* equation, which is a genaralization of the Nernst equilibrium discussed above,

$$V = \frac{RT}{F} \ln \left[\frac{P_{\text{K}}[\text{K}]_{\text{o}} + P_{\text{Na}}[\text{Na}]_{\text{o}} + P_{\text{Cl}}[\text{Cl}]_{\text{i}}}{P_{\text{K}}[\text{K}]_{\text{i}} + P_{\text{Na}}[\text{Na}]_{\text{i}} + P_{\text{Cl}}[\text{Cl}]_{\text{o}}} \right] \tag{1.2}$$

where the P_j's are the permeabilities of each of the three ion types.

1.1.4 Membrane Capacitance

The neuronal membrane is composed of a double layer of phospholipid molecules as shown in Fig. 1.2. The polar heads of these molecules face the intracellular cytoplasm and the extracellular space, separating the internal and external solutions. Since this thin insulating layer keeps charges apart, it acts like a *capacitance*. The membrane potential V_m permits the capacitance to build up a charge Q on both sides of the membrane as,

$$Q = CV_m$$

In biophysics, we usually specify capacitance in terms of specific membrane capacitance (capacitance per unit area), in units of Fm^{-2} or μFcm^{-2}. For biological cells, C is of the order of 1 $\mu\text{Fcm}^{-2} = 0.01$ Fm^{-2}. We use this value in Wilson neuron analysis in Section 2.8.

1.1.5 Membrane Resistance

Each ion channel in the neuronal membrane controls the flow of a specific ion type by acting as a gate, in response to chemical or mechanical signals, thus acting as a resistor in an electrical circuit. The inverse of the resistance is *conductance*. We generally use specific conductance i.e., conductance per unit area, measured in units of Scm^{-2} (S $\equiv$ siemen). Typical values of maximal Na^+ and K^+ ion-channel conductances are, 0.12 and 0.036 Scm^{-2} respectively.

As more ion channels open, total conductance increases.

1.1.6 A Simple RC Circuit to Represent Neuronal Membrane

Using the concepts of capacitance and conductance discussed above, we can represent the resting membrane using an electrical equivalent circuit: the plasma membrane using a capacitor; ion channels using conductance; and the concentration gradients across the ion channels using batteries (see Fig. 1.3).

We can describe the dynamics of this circuit by applying Kirchhoff's current law: the sum of the capacitive and ionic currents must add to zero,

$$C\frac{dV}{dt} + I_{\mathrm{Na}} + I_{\mathrm{K}} + I_{\mathrm{Cl}} = 0 \tag{1.3}$$

Here, the membrane potential V_m is represented by V. Using Ohm's law we can then write each ionic current as the product of conductance g_{X} with $(V - E_{\mathrm{X}})$, the displacement of the membrane potential V from ionic reversal value E_{X},

$$\begin{aligned} I_{\mathrm{Na}} &= g_{\mathrm{Na}}(V - E_{\mathrm{Na}}) \\ I_{\mathrm{K}} &= g_{\mathrm{K}}(V - E_{\mathrm{K}}) \\ I_{\mathrm{Cl}} &= g_{\mathrm{Cl}}(V - E_{\mathrm{Cl}}) \end{aligned}$$

Note that, g_{Na} and g_{K} conductances are voltage dependent; this fact is of crucial importance for the formation of action potential spikes, as discussed in the next section.

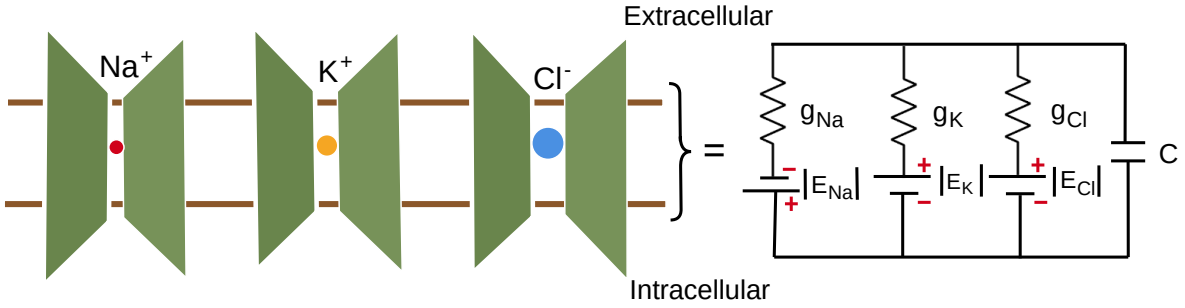

Figure 1.3: Representation of each ion channel as a battery in series with a conductance

1.1.7 Action Potential (Spike)

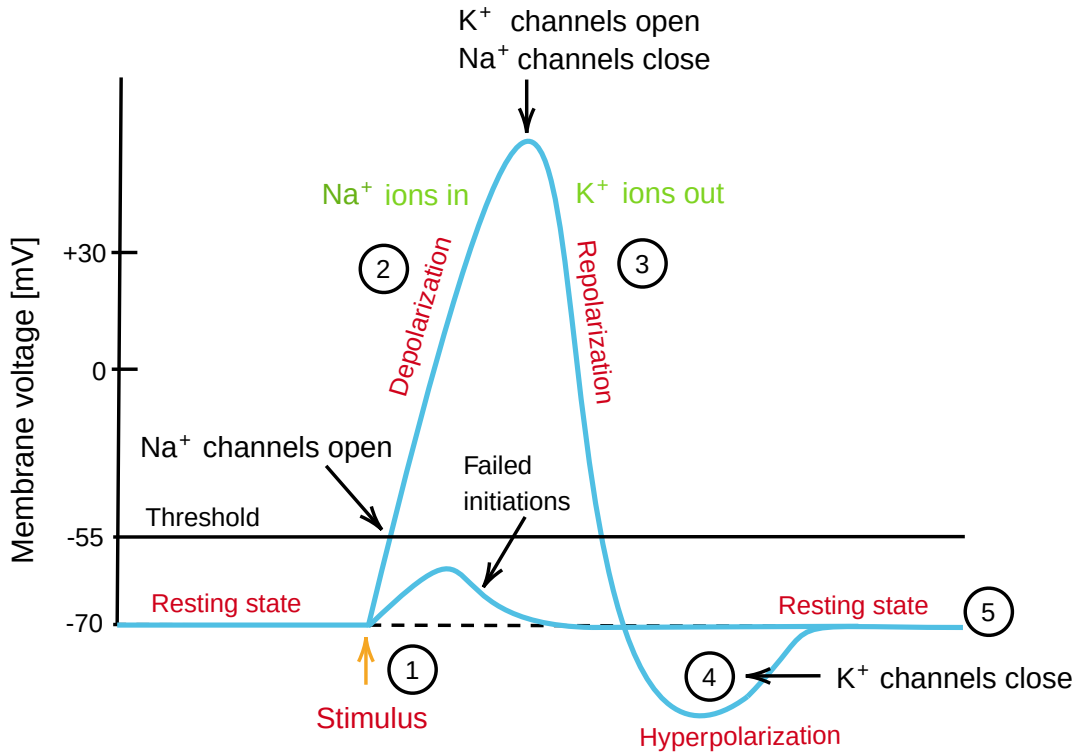

Figure 1.4: Stages of an action potential: (1) Occurrence of a stimulus which is sufficient to raise the voltage above threshold; (2) depolarization via an influx of Na^+ ions; (3) repolarization results from rapid sodium channel inactivation as well as a large outflow of K^+; (4) hyperpolarization (negative overshoot of membrane potential) as outflow of K^+ continues; (5) membrane potential returns to its resting value. A full action potential has a time-course lasting about 2–3 ms.

An action potential is a momentary abrupt shift of neuronal membrane potential caused by sudden ion flows in and out of the plasma membrane. If a large enough depolarization event occurs such that the cell voltage crosses threshold, the voltage-sensitive Na^+ channels open, allowing an influx of Na^+ ions. As a result, the cell become more depolarized with the membrane potential rapidly increasing to about +30 mV, forming the upstroke of an action potential or "spike". Voltage-gated K^+ channels then open and allow K^+ ions to leave the cell. At the same time, Na^+ channels close, stopping the inflow of Na^+ ions and allowing the membrane potential to return to its resting value. Figure 1.4 shows the stages of an action potential.

1.1.8 Chemical and Electrical Synapses

Neurons communicate with each other via chemical and electrical synapses. At a chemical synapse, an electrical signal is translated into a chemical message by means of the neurotransmitters. This process is initiated when an action potential arrives at the terminal of the presynaptic neuron, activating voltage-gated calcium channels in the cell membrane to allow an influx of Ca^{2+} ions. This triggers synaptic vesicles to release neurotransmitters. These molecules diffuse across the synaptic cleft and bind to receptors on the postsynaptic cell, either exciting or

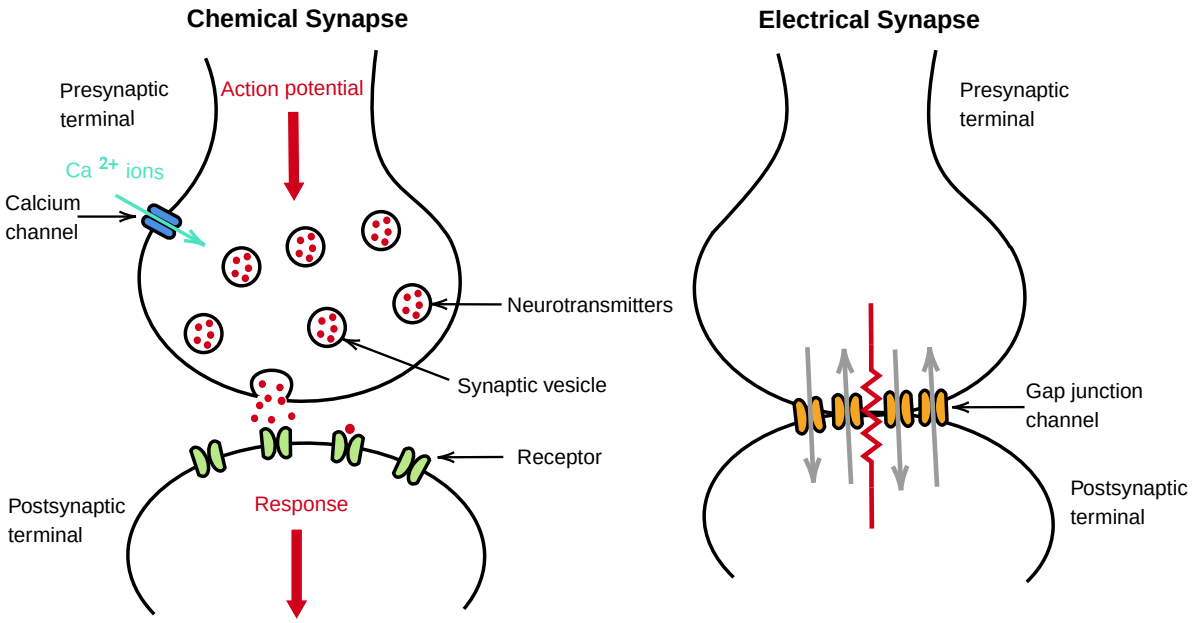

Figure 1.5: Basic structure of chemical (left) and electrical (right) synapses. In chemical synapses communication is done via neurotransmitters, whereas in electrical synapses it is done via direct electrical transmission. Red resistive element indicates that an electrical synapse can be modelled as a simple Ohmic connection.

inhibiting the receiving neuron, depending on the type of neurotransmitter. Excitatory neurotransmitters such as glutamate cause an increase in membrane potential of the receiving cell and increase its likelihood of producing an action potential. This brief positive-going voltage pulse is called an *excitatory postsynaptic potential* (EPSP). In contrast, inhibitory neurotransmitters such as GABA (γ–aminobutyric acid) decrease the firing probability of the target cell by evoking a negative voltage pulse, called an *inhibitory post-synaptic potential* (IPSP).

A spike event at the presynaptic neuron generates a broadened dendritic response Φ at the postsynaptic neuron, that we model as biexponential with rise-rate β and decay-rate α. This response can be described by the second-order differential equation (DE),

$$\left(\frac{d}{dt}+\alpha\right)\left(\frac{d}{dt}+\beta\right)\Phi = \alpha\beta\,\delta(t) \tag{1.4}$$

driven by a delta-function, $\delta(t)$ (unit area spike at time zero). The solution of this DE is,

$$\Phi(t) = \frac{\alpha\beta}{\beta-\alpha}\left(e^{-\alpha t}-e^{-\beta t}\right), \quad t \geq 0 \tag{1.5}$$

Note that the area under the curve represents the quantum of charge transferred during the spike event. When $\alpha = \beta$, the biexponential (Eq. (1.4)) is replaced with the so-called "alpha"-function form with a single rate constant γ,

$$\left(\frac{d}{dt}+\gamma\right)^2\Phi = \gamma^2\,\delta(t) \tag{1.6}$$

with solution,

$$\Phi(t) = \gamma^2 t\, e^{-\gamma t}, \quad t \geq 0 \tag{1.7}$$

In Fig. 1.6, we show the impulse responses generated by Eq. (1.7) for different values of γ.

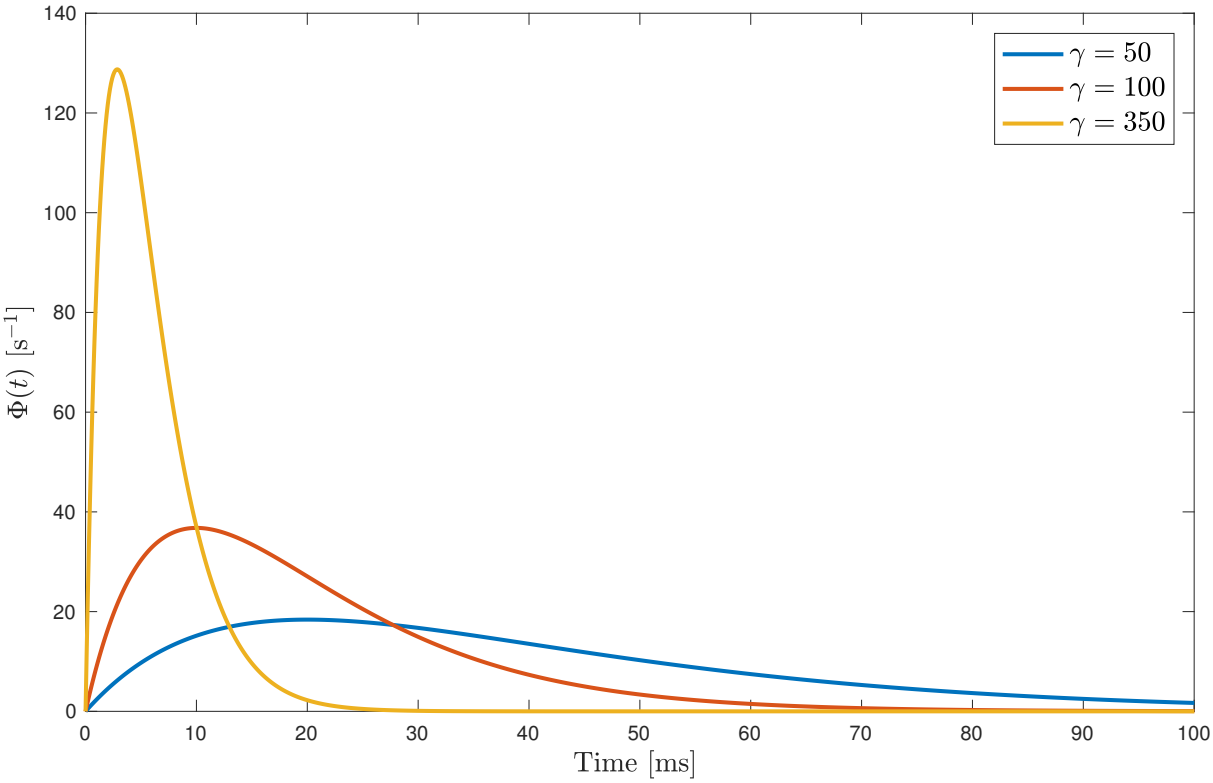

Figure 1.6: The impulse responses given by Eq. (1.7) for $\gamma = 50, 100,$ and 350 s^{-1}. Time-to-peak is given by $1/\gamma$, and each curve has unit area.

When we consider an assembly of neurons, the spiking activity in the presynaptic terminal axons generate sequences of EPSPs and IPSPs depending on the type (excitatory or inhibitory) of upstream neuron. These sequences are called *postsynaptic fluxes*. In Fig. 1.7, we present such sequences of EPSP and IPSP events generated using the True-field model equations of Section 3.3.6.

Unlike chemical synapses, at electrical synapses (gap junctions) there is a direct physical connection between the presynaptic and postsynaptic neurons allowing ions to flow directly from one cell into the other. These direct points of contact between the two membranes can be modelled as resistive connections (see Fig. 1.5 (right)). Due to these direct physical links, gap junctions can support very rapid communication and synchronization of electrical discharges compared to chemical transmissions [12, 80].

It has been shown that including gap junction connections in cortical models can have a major effect on cortical dynamics [76]. Gap junction connections are represented as spatial diffusion terms in the Waikato mean-field and True-field models (see Sections 3.1.8 and 3.3.2). According to physiological experiments, gap junction connections between neurons are common between inhibitory neurons ($I \Longleftrightarrow I$), never occur between excitatory and inhibitory neurons ($E \Longleftrightarrow I$); and very rare between excitatory neurons ($E \Longleftrightarrow E$). Thus, it is reasonable to assume that

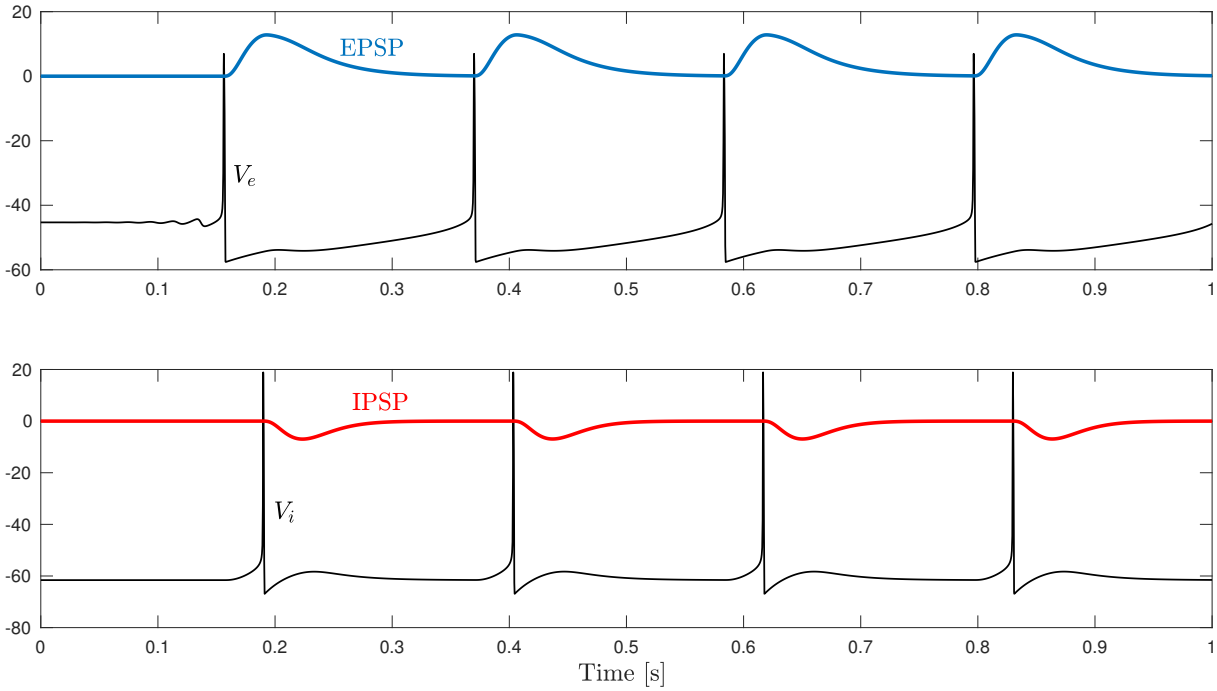

Figure 1.7: Sequences of EPSPs and IPSPs. Impulse responses generated by spike events in excitatory (top) and inhibitory (bottom) neurons: positive-going (blue) voltage impulses are EPSP events and negative-going (red) impulses are IPSP respectively. The voltage traces are generated using True-field model equations (Section 3.3.6) for $\gamma = 100\ \mathrm{s}^{-1}$.

$I \Longleftrightarrow I$ inhibitory diffusion in the cortex is much stronger than $E \Longleftrightarrow E$ excitatory diffusion. It is known that coupling via inhibitory electrical synapses can generate spatially organized patterns of brain activity known as Turing patterns [77].

1.2 Measuring electrical activity of brain

Neuroscientists use various techniques to understand brain's electrical activity at different spatial scales. The most popular and accessible technique is electroencephalogram (EEG) that records electrical signals detected on the surface of scalp using macro-electrodes. EEG has a number

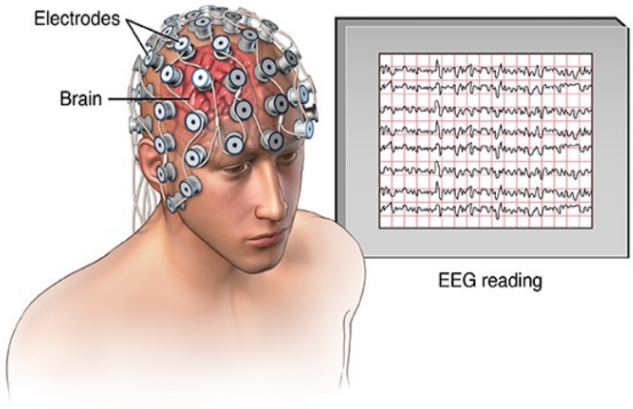

Figure 1.8: Head electrode array and signals measured during an EEG. Source: Examining bioelectric activity using EEG (https://tinyurl.com/ybvtxzrc).

of advantages including low risk, low cost, and high temporal resolution. However, it has poor spatial resolution because the electrical signal is filtered and attenuated by the skull and scalp. On the other hand, electrocorticogram (ECoG) records directly from the subdural surface of the cortex so has good temporal and spatial resolution. Electrodes can also be inserted into the brain to investigate electrical events at deeper locations. The measurement is called a local field potential (LFP) if the electrode is recording from the extracellular field, and an intracellular recording if the electrode is placed inside a cell. An EEG recording is primarily generated by the coordinated and synchronised activity of large populations of cortical pyramidal (excitatory) neurons that are arranged perpendicular to the brain surfaces. The inhibitory neurons do not contribute directly to EEG, because the inhibitory cells are rare in the brain's surface and do not have a preferred orientation.

1.2.1 Intracellular recordings

Intracellular recordings are used to detect the electrical activity of individual neurons by measuring voltage across the cell membrane. This requires the construction of microelectrodes that are small enough to penetrate the cell without damaging it. The diameter of an electrode tip is typically $< 1\,\mu$m, about ten times smaller than the diameter of the cell. Microelectrodes are usually made of thin glass vessels which have been heated and stretched to form very fine (sharp) tips and then filled with a salty solution that has a similar ionic composition to the intracellular fluid of the cell. A DC-amplifier with a large input resistance ($\sim$100 GΩ) is required to measure the cell voltage. These measurements require absolute mechanical stability of probe placement, and continuous monitoring under magnification. Due to these technical challenges, intracellular recordings cannot be used on behaving animals.

1.2.2 Local Field Potentials

Local field potentials (LFP) are extracellular signals assumed to be generated by summed electrical activity of neurons close to the electrode. Either glass or metal-wire microelectrodes can

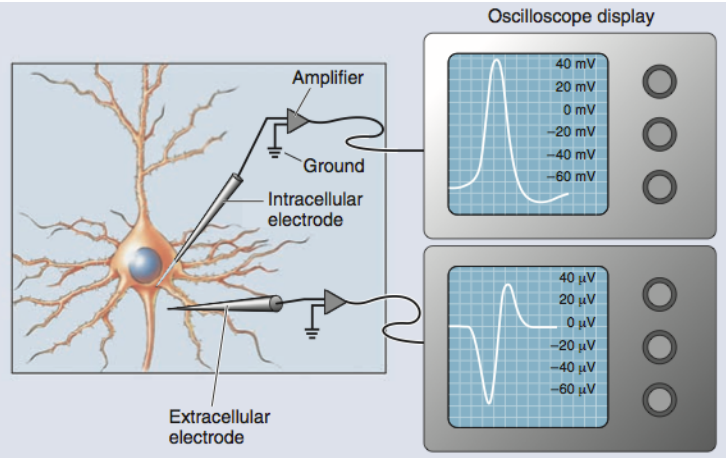

Figure 1.9: Microelectrode placement during intracellular and extracellular recordings. Source: Measuring brain signals (https://tinyurl.com/ybo674zq).

be used to record LFPs (Fig. 1.9 shows glass electrodes). Commonly used metal electrodes include tungsten, silver/silver-chloride, stainless steel, and platinum. These electrodes are usually insulated by a thin layer of teflon or other polymer to supply electrical and moisture insulation (electrode tip is not covered). The diameter of the electrode is usually less than 100 μm. LFP signals from electrodes separated by as little as 1 mm can be very different, because LFPs sample relatively localized populations of neurons [16].

Currently, there is much interest in LFP signals due to ease of recording and the richness of the signal. However, it is notably difficult to interpret and model LFPs because of the contribution of various sources such as synaptic inputs, ion channels, spikes, and glial cells. Therefore, interpreting LFPs as summed electrical activity of neurons close to the electrode is only a first-order approximation [18].

1.2.3 Electroencephalogram

Electroencephalogram (EEG) is a non-invasive technique that records macroscopic brain activity using an array of scalp electrodes (see Fig. 1.8), and is widely used in both research laboratories and clinical practice. EEG signals are typically characterised by frequency range. The most commonly studied rhythms include: delta ($0.5-3$ Hz), theta ($4-8$ Hz), alpha ($8-13$ Hz), beta ($14-30$ Hz), and gamma (>30 Hz) [79] (see Fig. 1.10).

- Delta: High amplitude slow waves seen in deep sleep and anaesthetized human brain; prominently observed in central and frontal areas of the cerebral cortex
- Theta: Slow activity commonly seen in drowsiness and deep meditation
- Alpha: Induced by closing the eyes and relaxing. It is present in the normal background rhythm of adult EEG recordings
- Beta: Normal state of wakefulness in both adults and children. It is mostly observed in central and frontal areas of the cerebral cortex
- Gamma: Generated by synchronized neuronal firing of separated populations of neurons; related to high-level information processing

It is possible to reproduce slow EEG rhythms (delta and theta) using both Waikato mean-field and True-field models. However these models cannot produce higher frequency EEG activity due to lack of explicit connectivity between the cerebral cortex and the other regions of brain such as the thalamus. In contrast, the Robinson thalamo-cortical model [64] is able to generate alpha-rhythm (and its harmonics) by including delayed feedback between thalamus and cortex.

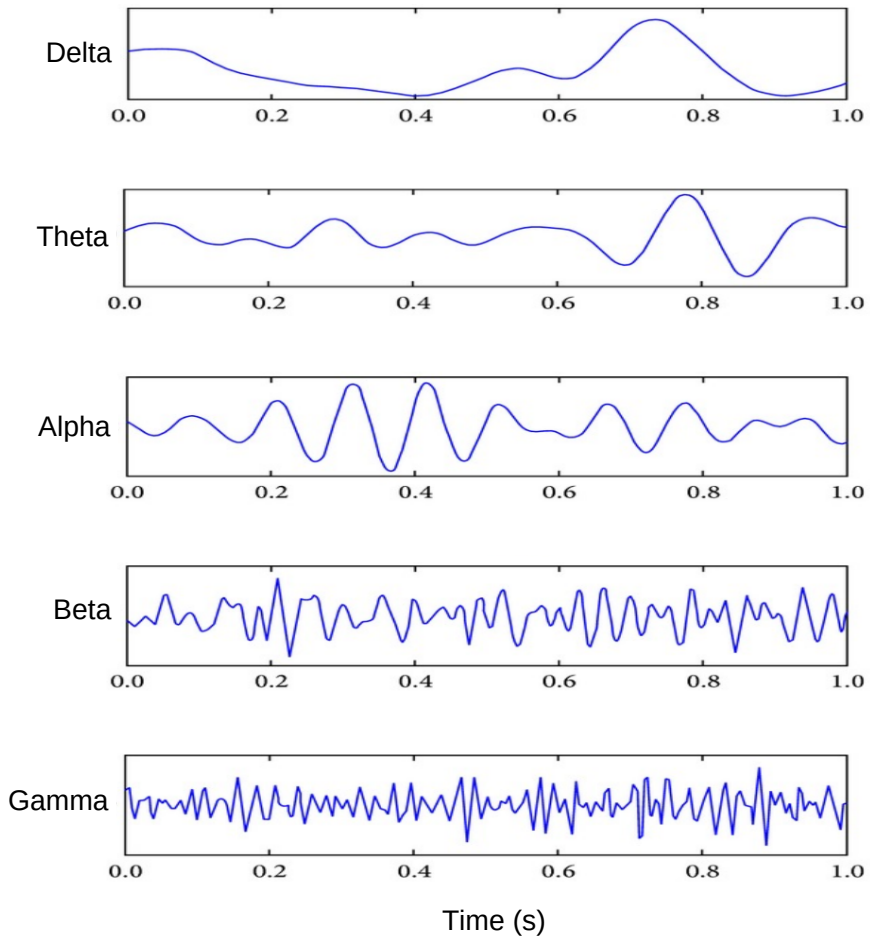

Figure 1.10: EEG brain rhythms: delta ($0.5 - 3$ Hz), slow-wave sleep; theta ($4 - 8$ Hz), drowsiness; alpha ($8 - 13$ Hz), relaxed with closed eyes; beta ($14 - 30$ Hz), normal wakefulness; and gamma (> 30 Hz), information processing. Modified from Jirayucharoensak *et al* (2014) [40].

1.2.4 Measuring electrical activity of a mouse brain slice

Mouse brain slices are commonly used for electrophysiological investigations of epileptic seizure [81], synaptic function and plasticity [52], and analysis of drug effects. Here we describe the

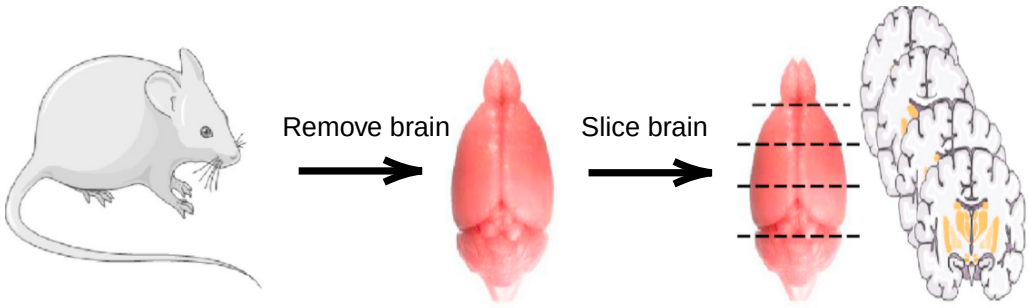

Figure 1.11: Preparation of mouse brain slice. Dashed-lines show the coronal slicing orientation. Modified from Pencheva *et al* (2017) [61].

brain slice experiments performed at the Waikato Electrophysiology Lab by Voss *et al* to study seizure-like events (SLEs) [81, 82].

Slice Preparation

The isolated mouse brain is immersed in ice-cold ($< 4°C$) artificial cerebrospinal fluid (aCSF) to slow metabolic activity. Coronal brain slices of desired thickness ($\sim 400\,\mu$m) are cut in the direction shown in Fig. 1.11, and kept in carbogenated (bubbled with a mixture of 95% oxygen and 5% carbon dioxide) low-magnesium aCSF at room temperature for a minimum of one hour to allow recovery of neural response [82]. The purpose of using a low-magnesium aCSF solution is to induce SLEs in the brain slices: the elimination of extracellular Mg^{2+} unblocks NMDA channels and leads the tissue to produce frequent excitatory currents that result in the generation of SLEs.

Electrical recording

The electrical recording gear includes electrodes, electrode holders, micromanipulator, and a silver/silver-chloride reference electrode. Spontaneous LFP activity is recorded from the brain slice using a single $75\,\mu$m silver/silver-chloride electrode (see Fig. 1.12). The signals picked up by the electrodes are amplified ($1000\times$, A-M Systems, USA) and bandpass filtered (1 and 300 Hz) before being recorded in a computer. These experiments are performed inside a grounded Faraday cage to provide shielding against external electromagnetic fields [81, 82].

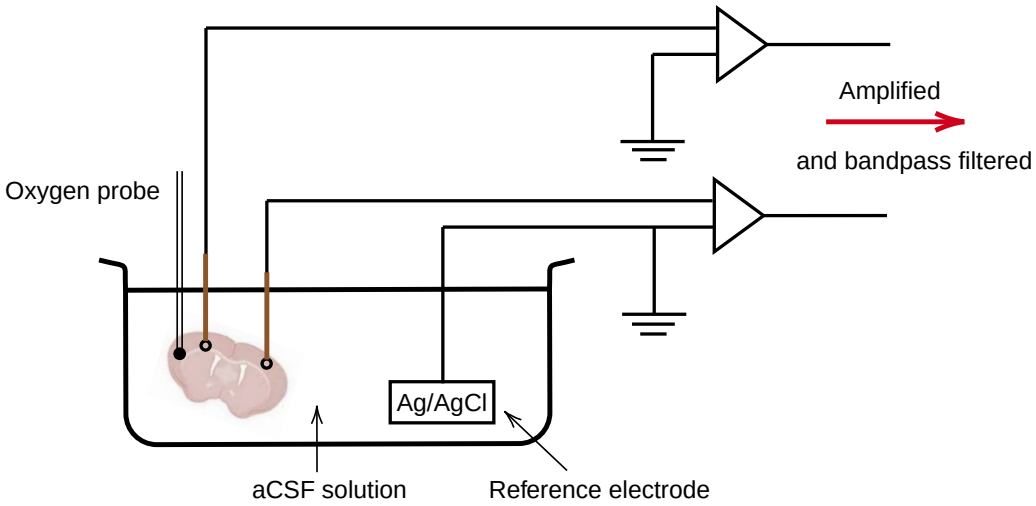

Figure 1.12: Schematic diagram of the LFP recording set-up. Brown coloured probes are Ag/AgCl recording electrodes.

1.3 Neural Modelling

The aim of neural modelling is to develop mathematical forms to mimic the structure and dynamics of human brain at different scales: some models might explain the behaviour of individual neurons (microscopic); others might explore neuronal networks (macroscopic). These models are expressed in terms of coupled differential equations and can be analysed using numerical simulations. Microscopic models can reproduce intracellular single-neuron measurements, whereas

Number of neurons	Spatial scale	Models	Waveform
1	10 μm	**Point neuron** Leaky integrate-and-fire (LIF) Quadratic integrate-and-fire (QIF) Izhikevich Hodgkin-Huxley FitzHugh–Nagumo Wilson True-field ($B \approx 1-2$)	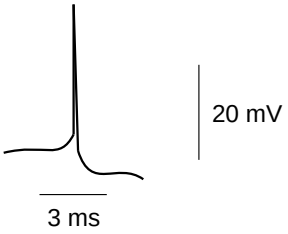
$10^2 - 10^3$	$\sim 50 - 100$ μm	**Local-field** Wilson-Cowan (WC) Wright and Liley Robinson Waikato Mean-field (WMF) True-field ($B \approx 5-10$)	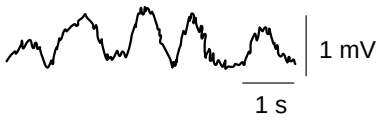
$10^3 - 10^5$	1 mm – 50 cm	**Mean-field** Wilson-Cowan (WC) Nunez Amari Freeman Wright and Liley Robinson Liley Waikato Mean-field (WMF) True-field ($B \approx 100 - 500$)	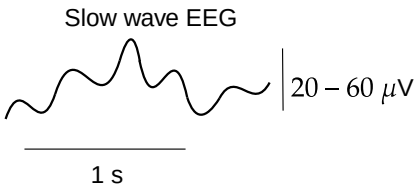

Figure 1.13: Neural models to represent different scales of brain. B is the True-field blocking ratio linking micro and macro scales (see Section 3.3).

macroscopic approaches attempt to describe behaviour of neural populations, interaction of brain parts and also whole brain dynamics, thus can reproduce ECoG or slow EEG rhythms depending on the scale of interest (see Fig. 1.13). There is no single model that can be related to all scales. Some attempt to construct neural networks using huge numbers of single-neuron models (e.g., the Blue Brain project [51]), requiring massive and complex computational facilities. On the other hand, the macroscopic approach adopted by mean-field models can be very effective in explaining the average electrical behaviour at larger scales, but necessarily neglect intracellular dynamics and interactions.

In Chapter 2, we survey a range of common point-neuron models: leaky integrate-and-fire, quadratic integrate-and-fire, Izhikevich, Hodgkin–Huxley, FitzHugh–Nagumo, and Wilson. In Chapter 3, we provide an overview of some well-established mean-field descriptions: Wilson–Cowan, Nunez, Amari, Freeman, Wright and Liley, Robinson, Liley, and the Waikato mean-field model.

Recently, there has been interest in developing hybrid models of single-neuron and rate-based descriptions to understand the human brain at different scales. In 2016, the Waikato Cortical

Modelling Group introduced the so-called "True-field" theoretical prescription that rescales a network of micro-scale spiking neurons to a macro-scale neural population via a bottom-up neural regridding [72] (discussed in Section 3.3). This new paradigm is capable of reproducing electrical behaviour of the brain at multiple scales: intracellular recordings at microscopic level, and slow ECoG/EEG rhythms at macroscopic level.

Chapter 2

Single Spiking Neuron Models

Neurons are the fundamental structural and functional units of the nervous system and also its basic unit for information processing. This chapter, surveys the range of single neuron models to show how computational neuroscientists use mathematical ideas to describe the electrical behaviour of biological neurons. I explain why the two-variable spiking-neuron model of Wilson was selected to represent the spiking behaviour of individual neurons in the Waikato True-field approach. Chapter is concluded with a detailed analysis of Wilson's type-I (human cortical) spiking neuron model. I find the steady-states of the system followed by an eigenvalue analysis to predict the stability of each equilibrium point. I complete the analysis by conducting stochastic simulations for different simulation currents.

2.1 Leaky Integrate-and-Fire Model

Proposed by Louis Lapicque in 1907 [1], the leaky integrate-and-fire model (LIF) is arguably the earliest mathematical model in neuroscience. Although at that time nothing was known about the mechanisms underlying spike generation, Lapicque was able to identify the key idea that integration of subthreshold passive potentials could lead to the formation of spikes.

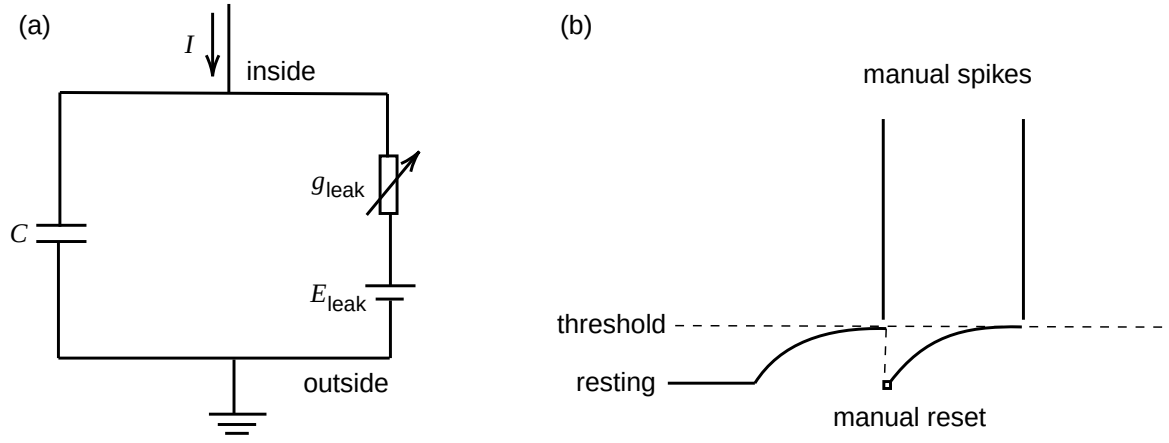

Figure 2.1: (a) Schematic diagram of the LIF model. (b) Manual spike and reset in LIF model (Reproduced from Izhikevich (2007) [39])

The LIF model can be represented as a capacitor in parallel with a resistor driven by a current I, which can be split into resistive and capacitive components I_R and I_C ($I = I_R + I_C$) (see

Fig. 2.1(a)). Using Ohm's law $I_R = V/R$, and by definition of the capacitance, $I_C = CdV/dt$,

$$I = \frac{V}{R} + C\frac{dV}{dt} \tag{2.1}$$

which can be rearranged as,

$$C\frac{dV}{dt} = I - g_{\text{leak}}(V - E_{\text{leak}}) \tag{2.2}$$

where V is the membrane potential, C is the membrane capacitance, g_{leak} is the membrane conductance (inverse resistance), E_{leak} is the equilibrium potential and I is the external current. When the membrane potential crosses a threshold value, it is assumed that the voltage-sensitive currents become active, leading to the firing of an action potential. V is then immediately reset to the K^+ equilibrium potential, E_{K}. Reduced to its simplest non-dimensional form, the LIF model can be written [39],

$$\frac{dv}{dt} = b - v, \quad \text{if} \quad v = 1, \ \text{then} \ v \leftarrow 0 \tag{2.3}$$

where $v = b$ is the resting state, $v = 1$ is the threshold value, and $v = 0$ is the after-spike reset voltage. Thus, the neuron is excitable when $b < 1$ and generates periodic spikes when $b > 1$.

Even though this model has a well defined threshold, it does not have any spike generation mechanism so the spike event must be manually "pasted in" as shown in Fig. 2.1(b). Therefore, the model suffers from discontinuous flow. Despite these limitations, the LIF model demonstrates a number of neurophysiological properties such as the concept of a refractory period, clear distinction between excitation and inhibition, and all-or-none spikes. Since spikes are manually pasted in, they are assumed to be identical in size and duration.

In summary, the integrate-and-fire model can be implemented very easily and efficiently and is useful for proving theorems and deriving analytical expressions, but because it cannot generate spikes autonomously, it cannot be used to study the phase transition from subthreshold stochastics to nonlinear spiking dynamics, nor it is a good model for simulating large-scale neural networks [39, 53].

2.2 Quadratic Integrate-and-Fire Model

Izhikevich designed the simplest spiking neuron description, the quadratic integrate-and-fire model (QIF), by replacing the decay term $-v$ with a $+v^2$ quadratic growth in Eq. (2.3). This replacement ensures hyperbolic growth of voltage to infinity in finite time, thus generating a mathematical "spike". (Note that if the $-v$ term is replaced by $+v$ instead, the resulting exponential growth requires infinite time to reach infinity (see Fig. 2.2)). The non-dimensional form for QIF is,

$$\frac{dv}{dt} = b + v^2, \quad \text{if} \quad v = v_{\text{peak}}, \ \text{then} \ v \leftarrow v_{\text{rest}} \tag{2.4}$$

where v_{peak} is the cutoff value for the generated spikes. For analytical studies, setting $v_{\text{peak}} = +\infty$ is useful but, as it has no physical meaning, we use a sufficiently large value for v_{peak} (e.g., 20 mV) in simulations. When $v(t)$ reaches v_{peak} we say that a spike has been generated and immediately reset $v(t)$ to v_{rest} (see Fig. 2.3) [39].

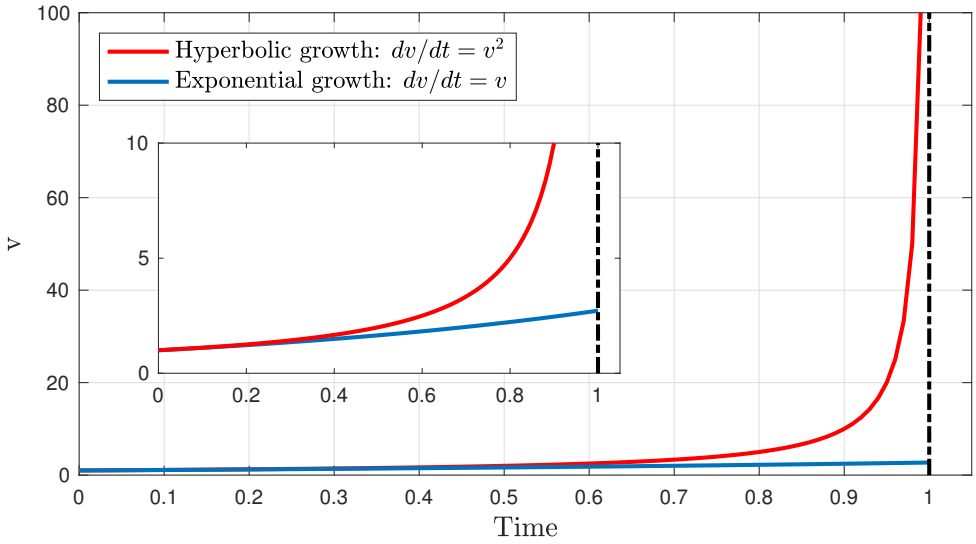

Figure 2.2: Comparing hyperbolic and exponential voltage growth curves. The blue line shows the solution to $dv/dt = v$ (exponential) and the red line shows the solution to $dv/dt = v^2$ (hyperbolic). The red curve diverges to infinity in finite time, thus generating a mathematical spike.

Although the QIF model is a true spiking model, it has the drawback of requiring a manual reset after each firing so, like the LIF model, has flow discontinuities.

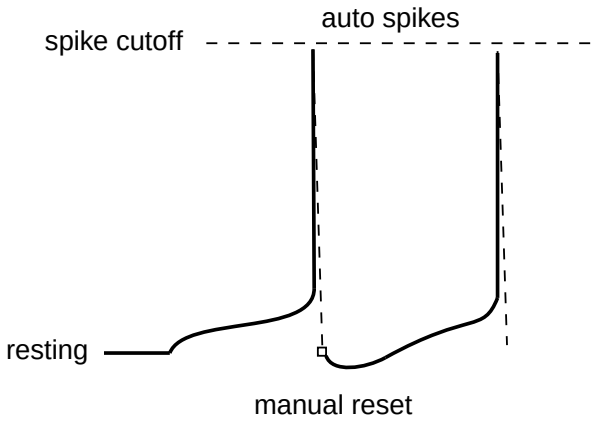

Figure 2.3: Autonomous spike generation and manual reset in QIF model. Reproduced from Izhikevich (2007) [39].

2.3 Izhikevich Neuron Model

Izhikevich proposed this form as a generalization of the quadratic integrate-and-fire model,

$$C\frac{dv}{dt} = k(v - v_r)(v - v_t) - u + I, \quad \text{if} \;\; v \geq v_{\text{peak}}, \;\; \text{then} \;\; v \leftarrow v_{\text{rest}} \tag{2.5a}$$

$$\frac{du}{dt} = a\{b(v - v_r) - u\} \qquad\qquad v \leftarrow c, \;\; u \leftarrow u + d \tag{2.5b}$$

where v is membrane potential, u is recovery current, C is membrane capacitance, v_r is resting membrane potential, v_t is threshold potential and I is the external current input to the cell. The four parameters a, b, c and d control the spiking and bursting behaviour: a is the recovery rate constant, b determines the sensitivity of the recovery variable (u), c is the reset value, d determines the total outward minus inward currents activated during the spike and it affects the post-spike behaviour. Here, k is a constant that determines the sensitivity of the membrane potential. If one knows both the rheobase (i.e., the minimal amplitude of stimulus current required to fire a neuron) and the input resistance of the neuron, parameters b and k can be determined.

By changing these parameter values, the Izhikevich model can be used to generate a wide range of spiking patterns for cortical neurons. For example, the following MATLAB code from [39] simulates a regular spiking (RS) pyramidal neuron.

```
% parameters used for RS
C = 100; vr = -60; vt = -40; k = 0.7;
% neocortical pyramidal neurons
a = 0.03;  b = -2; c = -50; d = 100;
vpeak = 35; % spike cutoff

% time span and step (ms)
T = 1000; tau = 1;
% number of simulation steps
n = round(T/tau);
v = vr*ones(1,n);  u = 0*v; % initial values
% pulse of input DC current
I = [zeros(1, 0.1*n), 70*ones(1, 0.9*n)];

% forward Euler method
for i=1:n-1
    v(i+1) = v(i) + tau*(k*(v(i) - vr)*(v(i) - vt) - u(i) + I(i))/C;
    u(i+1) = u(i) + tau*a*(b*(v(i) - vr) - u(i));
    % a spike is fired!
    if v(i+1) >= vpeak
       v(i) = vpeak;   % padding the spike amplitude
       v(i+1) = c;     % membrane voltage reset
       % recovery variable update
       u(i+1) = u(i+1) + d;
    end;
end;
```

```
% plot the result
plot(tau*(1:n), v);
```

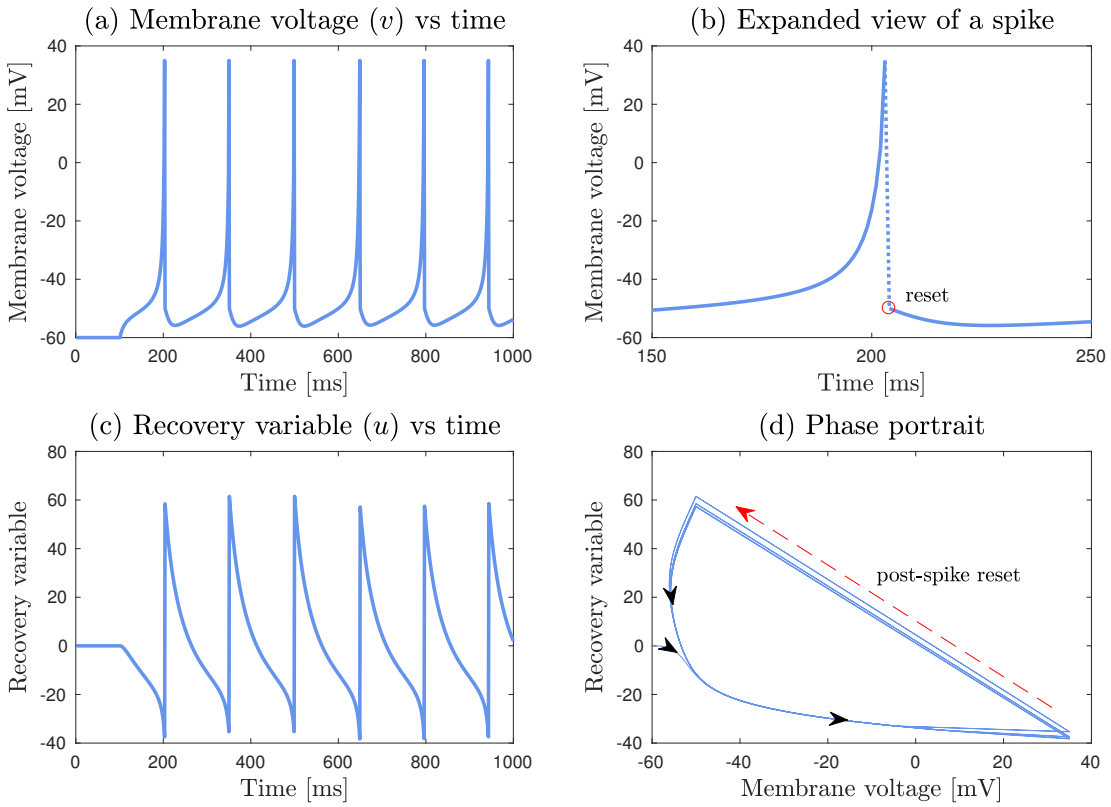

Figure 2.4: Simulation results of Izhikevich model of a regular spiking (RS) pyramidal neuron when a dc stimulus current step of $I = 70$ pA is applied. The integration algorithm used is Euler with time step $\Delta t = 1$ ms. The figure is modelled from Izhikevich (2007) [39].

Even though the spiking patterns generated by this model are remarkably realistic and biologically reasonable, there is no regenerative "downstroke" return to baseline, so requires manual programmed intervention as is the case for the LIF and QIF models.

2.4 Hodgkin–Huxley Model

In 1952 Alan Hodgkin and Andrew Huxley developed a mathematical model for the squid giant axon to describe how action potentials in neurons are initiated and propagated in the nervous system [34–38].

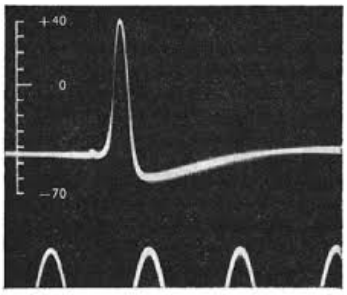

Figure 2.5: The first direct recording of an action potential by Hodgkin and Huxley in 1939 [47]. (The bottom semi-sinusoid wave is a timing mark)

Their ground-breaking research was recognized with a Nobel prize in physiology in 1961. Hodgkin and Huxley chose to work with the squid "giant" axon because of its conveniently large diameter ∼0.5 mm, larger than most other axons [13]. Due to this unusual largeness of the squid axon, they could easily insert a thin electrode along the length of the axon and record its electrical activity (see Fig. 2.5).

In a series of voltage-clamped experiments, they found that the squid axon membrane contains three types of ion channel: sodium, potassium and "leakage" (protein channels that are permeable to Na^+, K^+, and Cl^-), that regulate three different currents: sodium (I_{Na}), potassium (I_K), and leakage (I_L). The equivalent circuit is shown in Fig. 2.6.

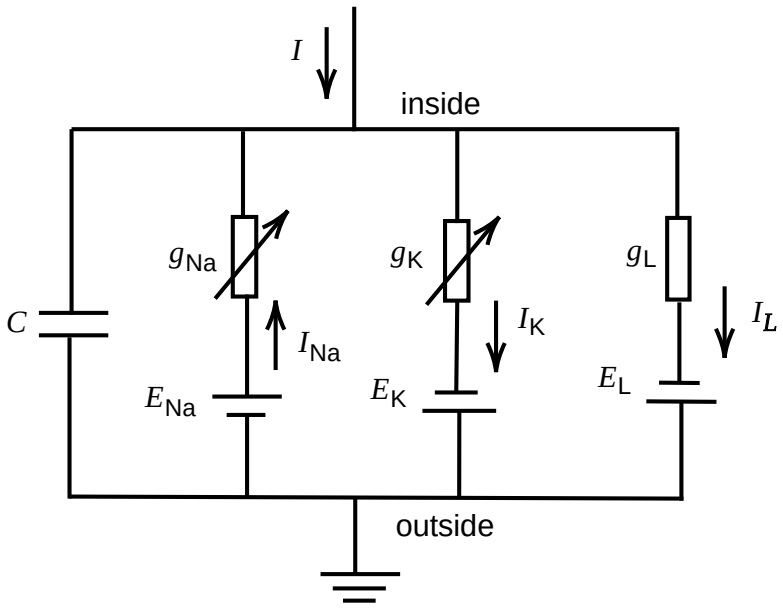

Figure 2.6: Schematic diagram of the Hodgkin–Huxley model. Modified from Gerstner *et al* (2002) [28].

The complete set of Hodgkin–Huxley model equations is listed below. It is assumed that each ionic current (see Eq. (2.6a)) obeys Ohm's law independently. The equations form a fourth-order system of nonlinear differential equations with four state variables: membrane potential V, the rates of Na^+ channel activation m, inactivation h, and K^+ channel activation n [34]. The three state variables m, h and n are called *gating variables*.

$$C\frac{dV}{dt} = -\overbrace{g_{\mathrm{Na}}^{\max} m^3 h(V - E_{\mathrm{Na}})}^{I_{\mathrm{Na}}} - \overbrace{g_{\mathrm{K}}^{\max} n^4 (V - E_{\mathrm{K}})}^{I_{\mathrm{K}}} - \overbrace{g_L(V - E_L)}^{I_{\mathrm{L}}} + I_{\mathrm{in}} \tag{2.6a}$$

$$\frac{dm}{dt} = \frac{1}{\tau_m(V)}(-m + M(V)) \tag{2.6b}$$

$$\frac{dh}{dt} = \frac{1}{\tau_h(V)}(-h + H(V)) \tag{2.6c}$$

$$\frac{dn}{dt} = \frac{1}{\tau_n(V)}(-n + N(V)) \tag{2.6d}$$

where C is membrane capacitance per unit area ($C = 1\,\mu\text{F/cm}^2$); $\tau_m(V)$, $\tau_h(V)$, $\tau_n(V)$ are voltage-dependent time constants; g_{Na} and g_{K} are Na, K ion-channel conductances; and E_{Na}, E_{K}, E_{L} are the equilibrium potentials at which each of the three currents is balanced by ionic concentration differences across the membrane. $M(V)$, $H(V)$ and $N(V)$ are the steady-state ($t \to \infty$) values of the m, h and n gating variables; they are functions of the membrane potential (see Fig. 2.7). Explicit mathematical forms are as follows [2, 39].

$$M(V) = \frac{\alpha_m}{(\alpha_m + \beta_m)} \qquad \tau_m = \frac{1}{(\alpha_m + \beta_m)} \tag{2.7a}$$

$$H(V) = \frac{\alpha_h}{(\alpha_h + \beta_h)} \qquad \tau_h = \frac{1}{(\alpha_h + \beta_h)} \tag{2.7b}$$

$$N(V) = \frac{\alpha_n}{(\alpha_n + \beta_n)} \qquad \tau_n = \frac{1}{(\alpha_n + \beta_n)} \tag{2.7c}$$

$$\alpha_m(V) = \frac{0.1(V+40)}{1 - \exp(-0.1(V+40))} \qquad \beta_m(V) = 4\,\exp(-0.0556(V+65)) \tag{2.8a}$$

$$\alpha_h(V) = 0.07\,\exp(-0.5(V+65)) \qquad \beta_h(V) = \frac{1}{1 + \exp(-0.1(V+35))} \tag{2.8b}$$

$$\alpha_n(V) = \frac{0.01(V+55)}{1 - \exp(-0.1(V+55))} \qquad \beta_n(V) = 0.125\,\exp(-0.0125(V+65)) \tag{2.8c}$$

The equilibrium potentials and conductances in Table 2.1 are empirical parameters. E_{Na}, E_{K} and E_{L} are set assuming that V_{rest} is set to -65 mV. Note that Eqs (2.8) take different forms depending on the assumed V_{rest} value. Using these parameter settings with a constant input current, the Hodgkin–Huxley model is capable of generating spiking behaviour, see Fig. 2.8. The Hodgkin–Huxley model is successful in both explaining voltage-clamped experimental data and simulating action potential responses, so has a close connection to biological reality. However, Hodgkin–Huxley is difficult to analyse because it has four state variables which are complex functions of membrane voltage, V. This motivates the quest for reduced neuron models requiring only two state variables.

Table 2.1: Definitions and parameter settings for Hodgkin–Huxley model [2]

Parameter	Na	K	L	Unit
Ion-channel conductance (g)	120	36	0.3	mS/cm^2
Equilibrium potential (E)	50	-77	-54.4	mV

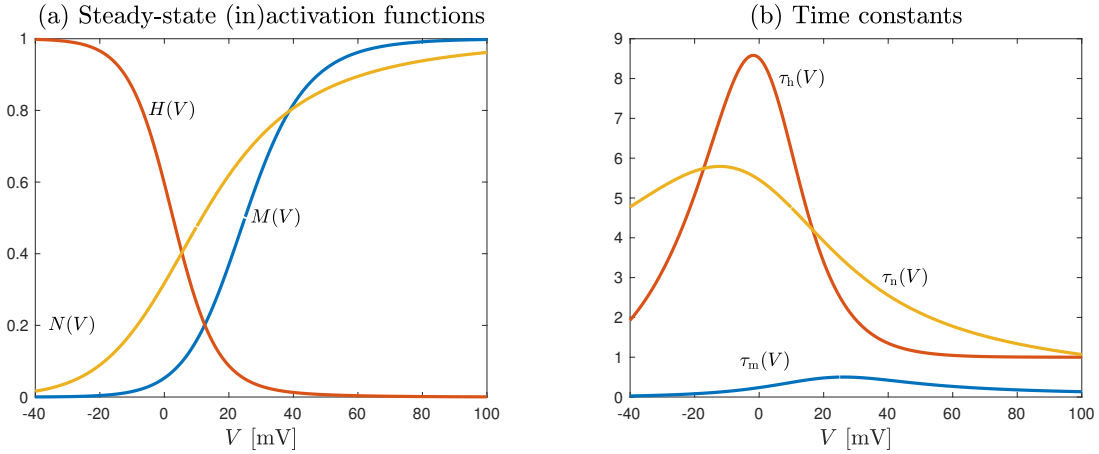

Figure 2.7: Steady-state (in)activation functions and voltage dependent time constants for the three variables m, n and h in the Hodgkin–Huxley model. Modified from Izhikevich (2007) [39].

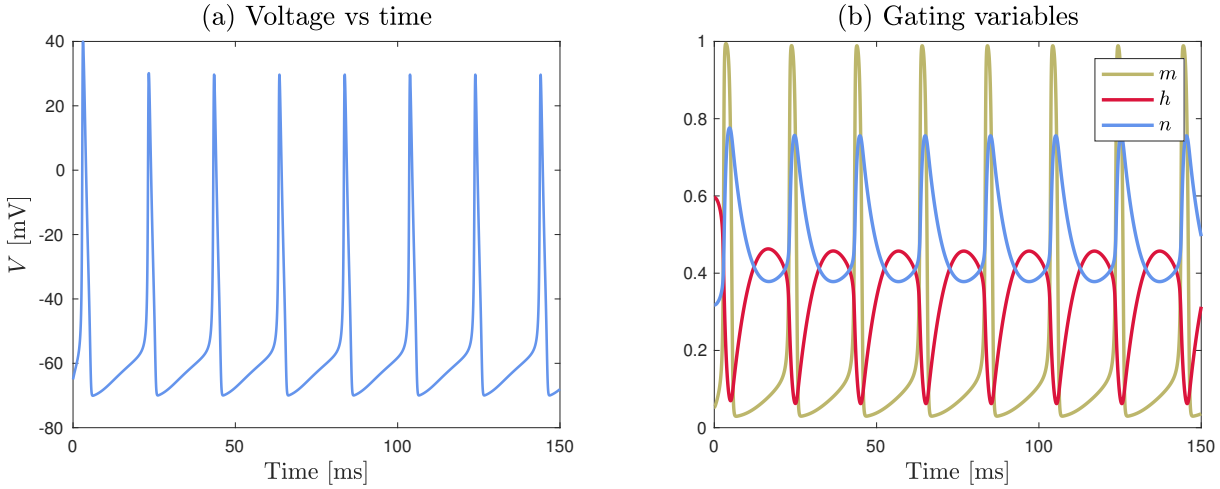

Figure 2.8: (a) Simulations for Hodgkin–Huxley model for constant input current $I_{\text{in}} = 3\,\mu\text{A/cm}^2$. (b) Gating variables vs time. (The resting potential, V_{rest} is set to -65 mV.)

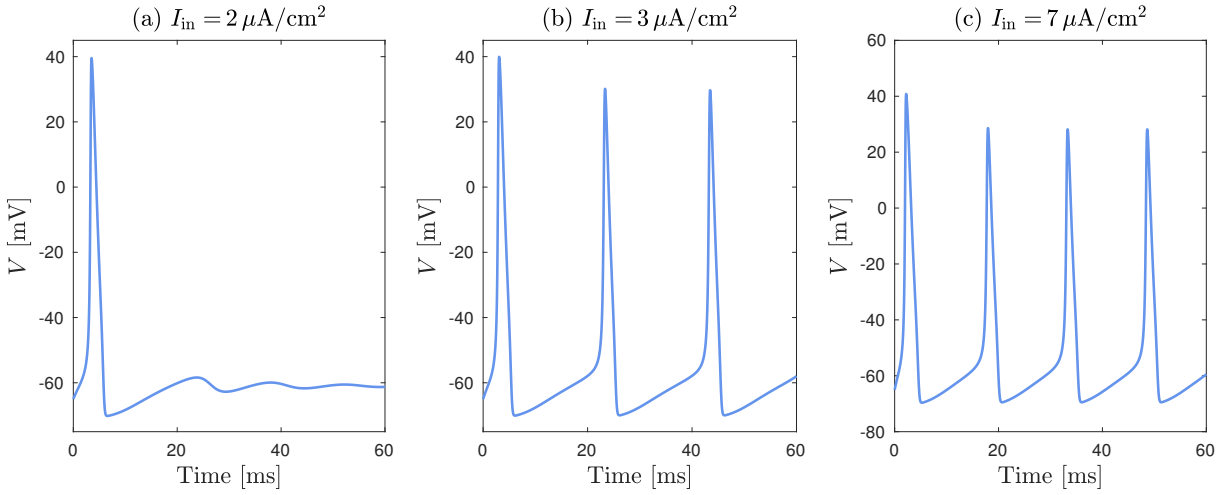

Figure 2.9: Action potentials generated by different input currents $I_{\text{in}} = 2, 3$ and $7\,\mu\text{A/cm}^2$. We observe that higher stimulus currents lead to increase in firing rate and decrease in spike amplitude.

2.5 FitzHugh–Nagumo Model

In 1955, FitzHugh suggested a new description of neuronal excitability as a simplification of the Hodgkin–Huxley model [21]. Subsequently, in 1961, FitzHugh and Nagumo independently developed a two-dimensional model which describes the formation of action potentials in terms of membrane potential V and recovery variable, R [22],

$$\frac{dV}{dt} = 10\,(V - \frac{V^3}{3} - R + I_{\text{input}}) \tag{2.9a}$$

$$\frac{dR}{dt} = 0.8\,(-R + 1.25V + 1.5) \tag{2.9b}$$

The action potentials generated by the FitzHugh–Nagumo model are shown in Fig. 2.10. Even though the FitzHugh–Nagumo equations are mathematically tractable, they neglect some fundamental biophysical elements such as conductance and ionic reversal potentials, and do not produce realistic action potential spikes.

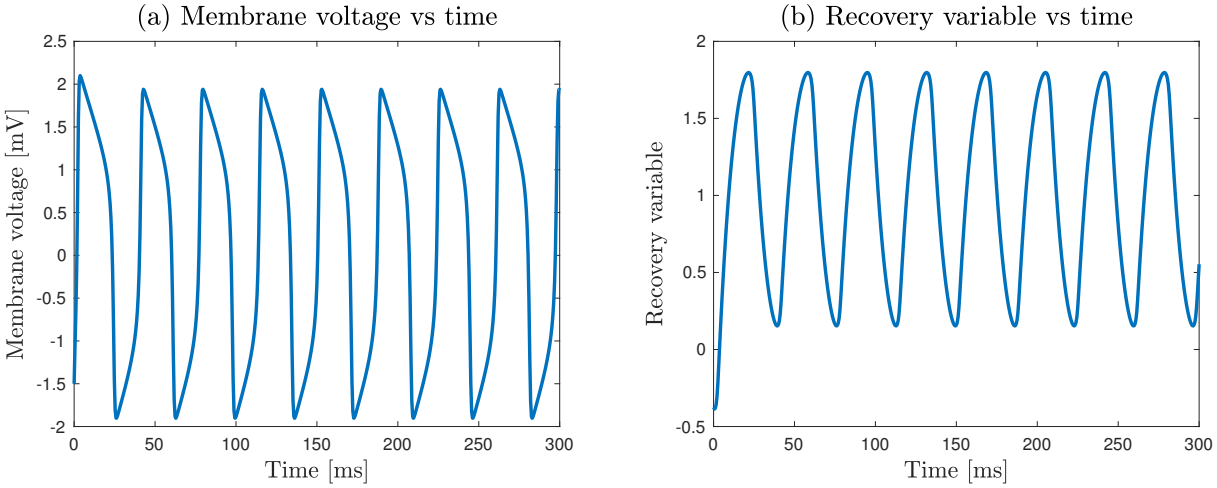

Figure 2.10: Simulation results of FitzHugh–Nagumo model for $I_{\text{dc}} = 1$. The integration algorithm used is Euler with time step $\Delta t = 1$ ms.

2.6 Wilson Spiking-neuron Model

By combining the biophysical significance of the Hodgkin–Huxley model with the mathematical simplicity of FitzHugh–Nagumo model, Wilson developed equations to describe the formation of action potentials in terms of a pair of first-order coupled differential equations [86,87]. As in the Hodgkin–Huxley model, it is assumed that each ionic current obeys Ohm's law independently.

$$C\frac{dV}{dt} = \overbrace{-g_{\text{Na}}(V)(V - E_{\text{Na}})}^{I_{\text{Na}}} \overbrace{-g_{\text{K}}R(V - E_{\text{K}})}^{I_{\text{K}}} + I_{\text{dc}} \tag{2.10a}$$

$$\frac{dR}{dt} = \frac{1}{\tau_R}(-R + R_\infty(V)) \tag{2.10b}$$

where V is the membrane potential, C is membrane capacitance per unit area, R is a (dimensionless) recovery variable, $g_{\text{Na}}(V)$ is the Na^+ activation, g_{K} is the K ion-channel conductance,

Table 2.2: Definitions and parameter settings for Wilson neuron [70]

Symbol	Type-I	Type-II	Unit
C	1	0.8	μF / cm^2
τ	5.6	1.9	ms
E_{Na}	+0.48	+0.55	10^2mV
E_{K}	−0.95	−0.92	10^2mV
$g_{\mathrm{Na}}(V)$	$g_1(V)$	$g_2(V)$	mS / cm^2
g_K	26	26	mS / cm^2
$R_\infty(V)$	$R_1(V)$	$R_2(V)$	

$$g_1(V) = 33.8V^2 + 47.58V + 17.81$$
$$g_2(V) = 32.63V^2 + 47.71V + 17.81$$
$$R_1(V) = 3.30V^2 + 3.798V + 1.26652$$
$$R_2(V) = 1.35V + 1.03$$

$E_{\mathrm{Na}}, E_{\mathrm{K}}$ are the Na^+, K^+ equilibrium potentials, $R_\infty(V)$ is the recovery steady state, and τ_R is recovery time constant.

By changing the parameter settings and the form of the recovery steady-state $R_\infty(V)$, Wilson's spiking neuron model is capable of simulating the spiking behaviour of both human neuron (integrator, type-I) and squid axon (resonator, type-II). Neurons are categorised into two classes based on the two possible routes to periodic spiking: a saddle-node on a limit cycle or a Hopf bifurcation. These two bifurcations result in different subthreshold behaviour of the voltage variable after a short pulse of current is applied. Neurons with damped subthreshold oscillations are referred as *resonators* and those that do not have this feature are called *integrators* [39].

In Wilson's original formulation, the membrane potential V is scaled to units of mV / 100 to keep the constants in Table 2.2 within a reasonable range [86]. Thus, all voltage values and current values should be multiplied by 100 to retrieve their physical values in mV and μA / cm^2. (Hereafter, I use standard SI conventions as presented in Section 2.8.)

To bring stochasticity to the noise-free Wilson model, I add white-noise perturbations to the current and to the recovery. The noise-perturbed Wilson equations are presented in Section 2.8 (see Equation (2.11)).

Fig. 2.11 shows stochastic simulation runs for both human neuron and squid axon at five different stimulation current settings. When the simulation current is low, human neurons can fire at very low spike rates (1 spike/s), but squid axon cannot fire at rates below about 175 spikes/s. This is because the squid axon has only one Na^+ and one K^+ current, while the majority of mammalian neurons have a rapid, transient K^+ current which allows the cell to fire at very low spike rates [87]. In 1989, Rose and Hindmarsh demonstrated that the effect of transient K^+ current can be approximated by making the recovery steady-state $R_\infty(V)$ a quadratic function of voltage (see Table 2.2).

A detailed analysis of the human neuron model is presented at the end of this chapter.

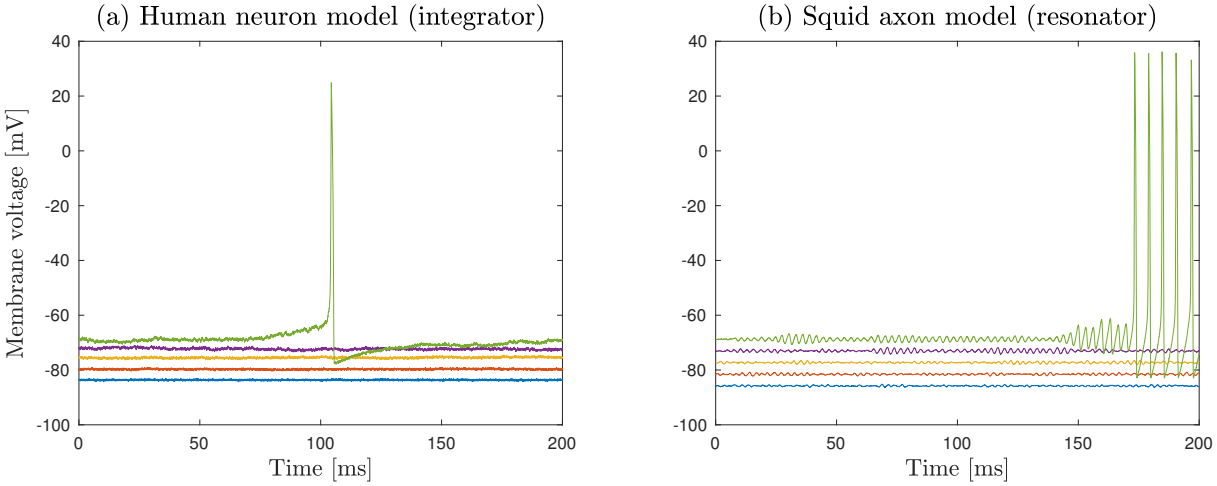

Figure 2.11: Stochastic simulations for the Wilson neuron models for (a) human cortical neuron and (b) squid axon. Five simulations are run for each model for different simulation currents (numbered from bottom to top). (a) For human neuron the simulation currents are $I_{\text{dc}} = -100, -40, 0, 16$, and 21.4752 μA/cm^2. (b) For squid axon the simulation currents are $I_{\text{dc}} = 0, 2, 4, 6$, and 7.7 μA/cm^2. The figure is modelled from Steyn-Ross *et al* (2006) [70].

2.7 Choice of Spiking Neuron Model

As shown previously, the spiking behaviour of individual neurons can be modelled in a variety of ways. The choice of spiking neuron model to build a neural network depends on how much neurophysiological realism we require. For example, the NEURON software [33] recognizes that individual neurons have a spatial structure with a soma, dendrites and an axon. NEURON can be used to construct a detailed single neuron, or a small assembly of such neurons. The example below from Wikipedia [84] creates a simple neuron consisting of a single-compartment soma and a 10-compartment axon (NEURON computes solutions such as membrane potential and ionic concentrations at the centre of each compartment). The dynamics of the cell membrane is simulated for 50 ms using Hodgkin–Huxley squid axon equations.

```
//create two sections, the body of the neuron and a very long axon
//create soma, axon
soma {
        //length is set to 100 micrometers
        L = 100
        //diameter is set to 100 micrometers
        diam = 100
        //insert a mechanism simulating the standard squid Hodgkin-Huxley channels
        insert hh
        //insert a mechanism simulating the passive membrane properties
        insert pas}
axon {
   L = 5000
   diam = 10
   insert hh
   insert pas
   //the axon shall be simulated using 10 compartments.
   //By default a single compartment is used
   nseg = 10}
//connect the proximal end of the axon to the distal end of the soma
```

```
connect axon(0), soma(1)

//declare and insert a current clamp into the middle of the soma
objref stim
soma stim = new IClamp(0.5)

//define some parameters of the stimulus: delay, duration (both in ms) and
//amplitude (in nA)
stim.del = 10
stim.dur = 5
stim.amp = 10

//load a default NEURON library file that defines the run routine
load_file("stdrun.hoc")
tstop = 50 //set the simulation to run for 50 ms

//run the simulation
run()
```

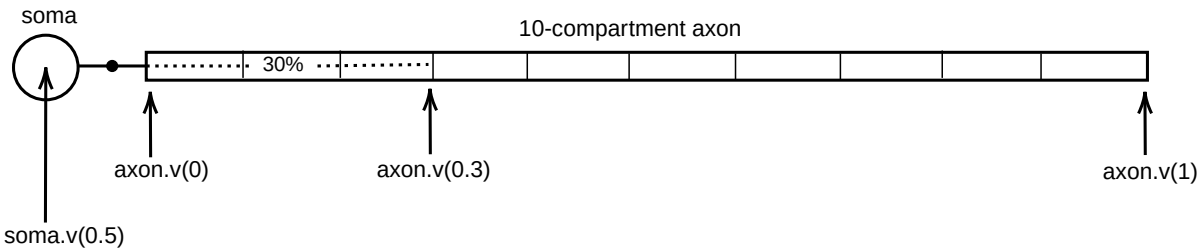

Figure 2.12: Cartoon of a neuron with a soma and a multi-compartment axon. The diameter of the spherical soma is 100 μm. The unmyelinated cylindrical axon is 5000 μm long and has a diameter of 10 μm. A point process (current clamp object) is created in the middle of the soma. Location is specified with a number between 0 and 1 representing the fractional distance along the section to the place of the point process.

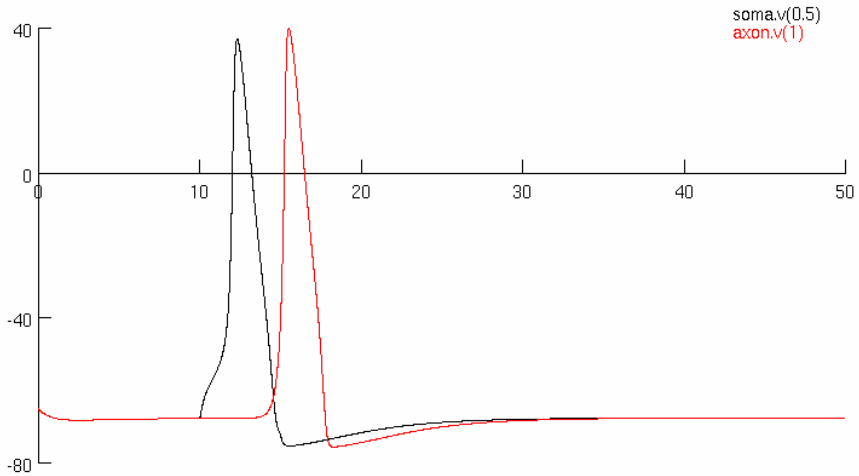

Figure 2.13: Membrane voltage (mV) vs time (ms) at the soma and distal end of the axon. From Wikipedia: NEURON software [84].

If we want to consider the population-averaged behaviours of thousands of neurons, the fine structural details (soma, dendrite, axon) of individual neurons can probably be ignored. Thus, it is convenient to collapse the neuron to zero spatial dimensions to form a "point" neuron. In this simplification, the spatially-extended dendrites and axonal compartments of a real biological neuron are ignored and the neuron is collapsed to an isopotential point. Although the Hodgkin–Huxley model is considered to be the "gold standard" for point neurons, their equations are still too complex for our population level work.

This motivates us to consider mathematically simpler one- and two-variable neuron models. We discard the leaky integrate-and-fire model since it cannot generate action potentials. Even though the quadratic integrate-and-fire neuron (QIF and Izhikevich) models can generate spikes autonomously, those models require a manual reset after each firing event. Therefore, those model equations are non-analytic and cannot be used for our population approach.

Thus, Wilson's two-variable spiking neuron is selected to model individual neurons in the Waikato True-field approach. The Wilson neuron is completely autonomous, it encapsulates the biophysical aspects such as Na^+ and K^+ reversal potentials, and produces action potentials that are very similar to the gold standard Hodgkin–Huxley solutions.

2.8 Analysis of Wilson Human-neuron Model

In this section I present a comprehensive analysis of Wilson's human neuron model. Wilson's 1999 equations presented in Section 2.6 use non-SI units. To reduce calculation errors, I reformulate his parameters to conform with standard SI conventions and I divide the voltage equation by specific capacitance C as in [72].

The updated equations are as follows. Each term in the voltage equation (2.11a) now carries units of volts per second,

$$\frac{dV}{dt} = -g(V)(V - E_{\mathrm{Na}}) - g_R R\,(V - E_{\mathrm{K}}) + \frac{I_{\mathrm{dc}}}{C} + \sigma_I \xi_1(t) \tag{2.11a}$$

$$\frac{dR}{dt} = \frac{1}{\tau_R}(-R + R_\infty(V)) + \sigma_R \xi_2(t) \tag{2.11b}$$

Here, $g(V) = g_{\mathrm{Na}}(V)/C, g_R = g_{\mathrm{K}}/C$ are the scaled conductances carrying units of inverse seconds. Low-level white noises $\xi_1(t)$, $\xi_2(t)$ have been added into the voltage and recovery equation to represent the noisiness in real biological neurons. These white noises have zero mean, infinite variance and are delta-correlated in time.

Table 2.3 shows the updated parameter settings for the human cortical neuron. (Note that, in Section 2.6 I presented the original parameter values as used by Wilson in his 1999 book [87].)

2.8.1 Steady States of the Wilson Neuron

In order to understand the expected behaviour of the Wilson's coupled differential equations, I locate the steady-states or rest points of the system by setting the derivatives of the deterministic form of Eqs (2.11) to zero. At each equilibrium point, the vector of state variables does not change. If the system is close to the equilibrium, the state vector may converge towards, or

diverge away from it. This convergence or divergence depends on the stability of the steady-state which is discussed in the next section.

I evaluate the steady-state coordinate (V^0, R^0) for membrane voltage and recovery, for a given value of dc stimulus current I_{dc}, by solving,

$$F_1 \equiv \frac{dV}{dt} = -g(V)(V - E_{\mathrm{Na}}) - g_R R\,(V - E_{\mathrm{K}}) + \frac{I_{\mathrm{dc}}}{C} = 0 \tag{2.12a}$$

$$F_2 \equiv \frac{dR}{dt} = \frac{1}{\tau_R}(-R + R_\infty(V)) = 0 \tag{2.12b}$$

numerically. When I say dc stimulus current (I_{dc}), I actually mean current *density*; an SI current density of 1 Am^{-2} represents one ampere of electric current flowing through a material with a cross-sectional area of one square metre; this corresponds to 100 $\mu\mathrm{Acm}^{-2}$.

2.8.2 Linear Stability Analysis

In order to study the stability of the steady-states of this system of nonlinear differential equations, I linearize about a given steady-state. This is done by computing the 2×2 Jacobian matrix of partial derivatives, $\mathbf{J}$,

$$\mathbf{J} = \begin{bmatrix} \dfrac{\partial F_1}{\partial V} & \dfrac{\partial F_1}{\partial R} \\ \dfrac{\partial F_2}{\partial V} & \dfrac{\partial F_2}{\partial R} \end{bmatrix}_{|(V^0, R^0)} \tag{2.13}$$

Since the Wilson neuron is a two-variable system, each steady state owns two eigenvalues. The sign of these eigenvalues predict growth or decay of small perturbations about the steady-state. If the dominant eigenvalue $\lambda = \alpha \pm i\omega$ has a negative real part ($\alpha < 0$), the steady-state is stable and the perturbation will decay; if the dominant eigenvalue has a positive real part ($\alpha > 0$), the steady-state is unstable and the perturbation will grow. The magnitude of the dominant eigenvalue determines how fast the system returns to the steady-state after the perturbation [14].

Table 2.3: Definitions and parameter settings for Wilson's human neuron

Symbol	Description	Type-I	Unit
C	Capacitance	0.010	Fm^{-2}
τ	Time constant	5.6×10^{-3}	s
$E_{\mathrm{Na}}, E_{\mathrm{K}}$	Reversal potentials	$(+48, -95) \times 10^{-3}$	V
g_R	Scaled conductance	26×10^3	s^{-1}
$g(V)$	Scaled conductance	$g_1(V)$	s^{-1}
$R_\infty(V)$	Recovery steady-state	$R_1(V)$	

$$g_1(V) = 3.38 \times 10^6 V^2 + 475.8 \times 10^3 V + 17.81 \times 10^3$$
$$R_1(V) = 330V^2 + 37.98V + 1.26652$$

2.8.3 Steady State Distribution and Bifurcation Points

I locate steady-states for the Wilson human neuron for a range of finely-spaced stimulus currents from -0.5 to $+0.5$ Am^{-2}. Fig. 2.14(a) shows the distribution of steady-states and their stability; panel (b) shows that the dominant eigenvalue changes sign from negative to positive at a critical current $I_{\mathrm{dc}}^{\mathrm{crit},1} \approx 0.21475\,\mathrm{Am}^{-2}$, indicating that the membrane becomes unstable for stimulus currents higher than $I_{\mathrm{dc}}^{\mathrm{crit},1}$. For $I_{\mathrm{dc}} < I_{\mathrm{dc}}^{\mathrm{crit},1}$, only the bottom branch of steady-states is stable. Along this branch, fluctuations are predicted to decay to resting state over two different time scales: T_{slow} and T_{fast}. These time scales are determined by the dominant and second eigenvalues: $T_{\mathrm{slow}} = -1/\lambda_1$, $T_{\mathrm{fast}} = -1/\lambda_2$. For the middle branch steady-states, $\lambda_1 > 0$ and $\lambda_2 < 0$ indicating that $I_{\mathrm{dc}}^{\mathrm{crit},1}$ marks a saddle-node on an *invariant circle* (SNIC) bifurcation [39], for which frequency of periodic solutions goes to zero as I_{dc} approaches $I_{\mathrm{dc}}^{\mathrm{crit},1}$ from the right. For the top branch steady-states, both eigenvalues are positive.

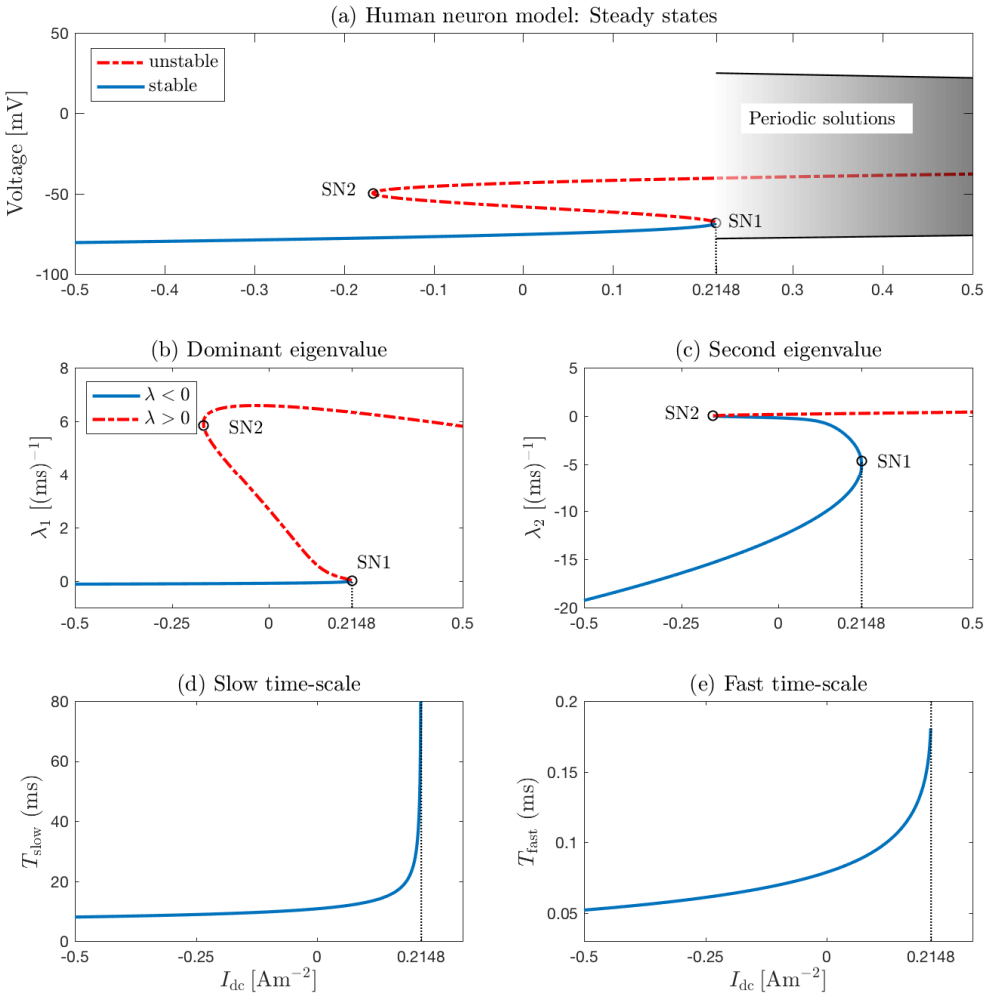

Figure 2.14: Stability analysis for Wilson type-I cortical neuron. (a) Steady-state distribution of membrane voltages as a function of dc stimulus current. The bottom branch is stable for small perturbations and the middle and top branches are unstable. Shaded region shows periodic solutions with a grey-scale gradient that is proportional to the spiking frequency: dark-grey ∼50 spikes/s; white ∼0 spikes/s. (b) and (c) Both eigenvalues are are real and negative until the stimulus current approaches the threshold value. (d) and (e) The slow and fast time scales for relaxation back to steady-state. (Modelled from Steyn-Ross *et al* (2006) [70].)

If we extend the steady-state distribution in Fig. 2.14 by increasing the range of I_{dc} from -5 to $+5$ Am^{-2} we see that the system becomes stable again when $I_{\mathrm{dc}} > I_{\mathrm{dc}}^{\mathrm{crit},2} \approx 3.9955\,\mathrm{Am}^{-2}$. At this point the eigenvalues are purely imaginary (see Fig. 2.15), indicating a Hopf bifurcation of frequency ∼420 Hz.

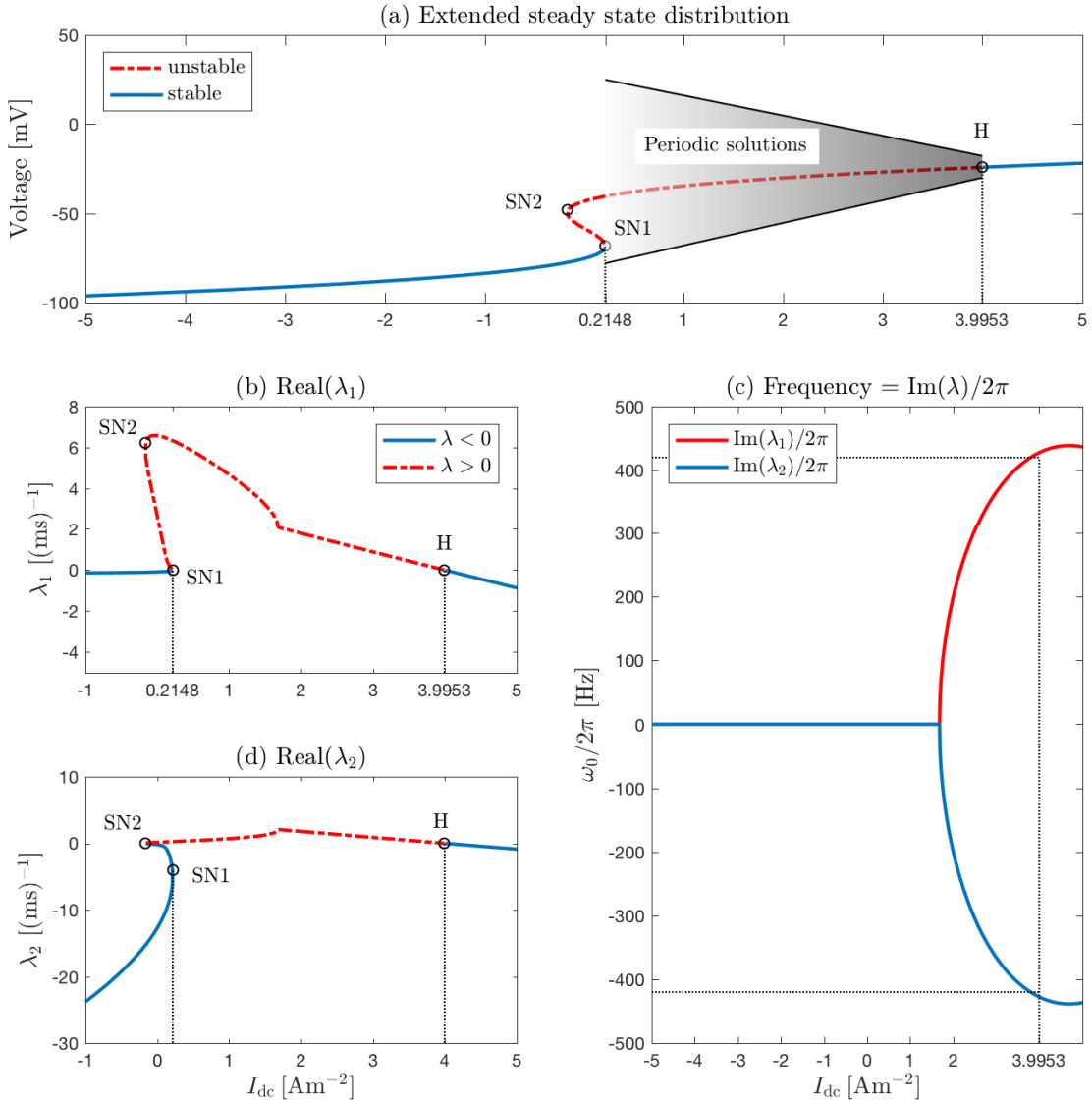

Figure 2.15: Extended stability analysis for Wilson type-I cortical neuron. (a) Extended steady-state distribution. The top branch becomes stable when the stimulus current exceeds a second threshold value. Periodic solutions exist when $I_{\mathrm{dc}}^{\mathrm{crit},1} < I_{\mathrm{dc}} < I_{\mathrm{dc}}^{\mathrm{crit},2}$. Colour gradient is proportional to the spiking frequency with dark-grey represents oscillations of ∼400 Hz. The real and imaginary parts of (b) and (c) the dominant eigenvalue, (d) and (e) the second eigenvalue. At the upper current threshold, both eigenvalues become purely imaginary.

2.8.4 Numerical Simulations

To validate the stability analyses I performed stochastic simulations for several values of dc stimulus current. When the current is lower than the first critical value, $I_{\mathrm{dc}}^{\mathrm{crit},1}$ the neuron is stable (see Fig. 2.16(a), note that the small voltage fluctuations are due to the $\xi_{1,2}(t)$ white

noises, representing the noisy biological background). When the stimulus current just exceeds the first critical value, $I_{\mathrm{dc}}^{\mathrm{crit},1}$ the neuron starts spiking at a low rate (see Fig. 2.16(b)). This marks the birth of spiking. As the stimulus current increases, the spike rate increases and the amplitude of spikes decreases (see Fig. 2.17). When the stimulus current approaches the second critical value, $I_{\mathrm{dc}}^{\mathrm{crit},2}$ the spikes disappear and the neuron becomes stable again. We clearly see that the simulation results agree with the eigenvalue predictions showing that the birth and death of spiking occur when $I_{\mathrm{dc}}^{\mathrm{crit}} \approx 0.21475\,\mathrm{Am}^{-2}$ and $3.9955\,\mathrm{Am}^{-2}$ respectively (see Fig. 2.16).

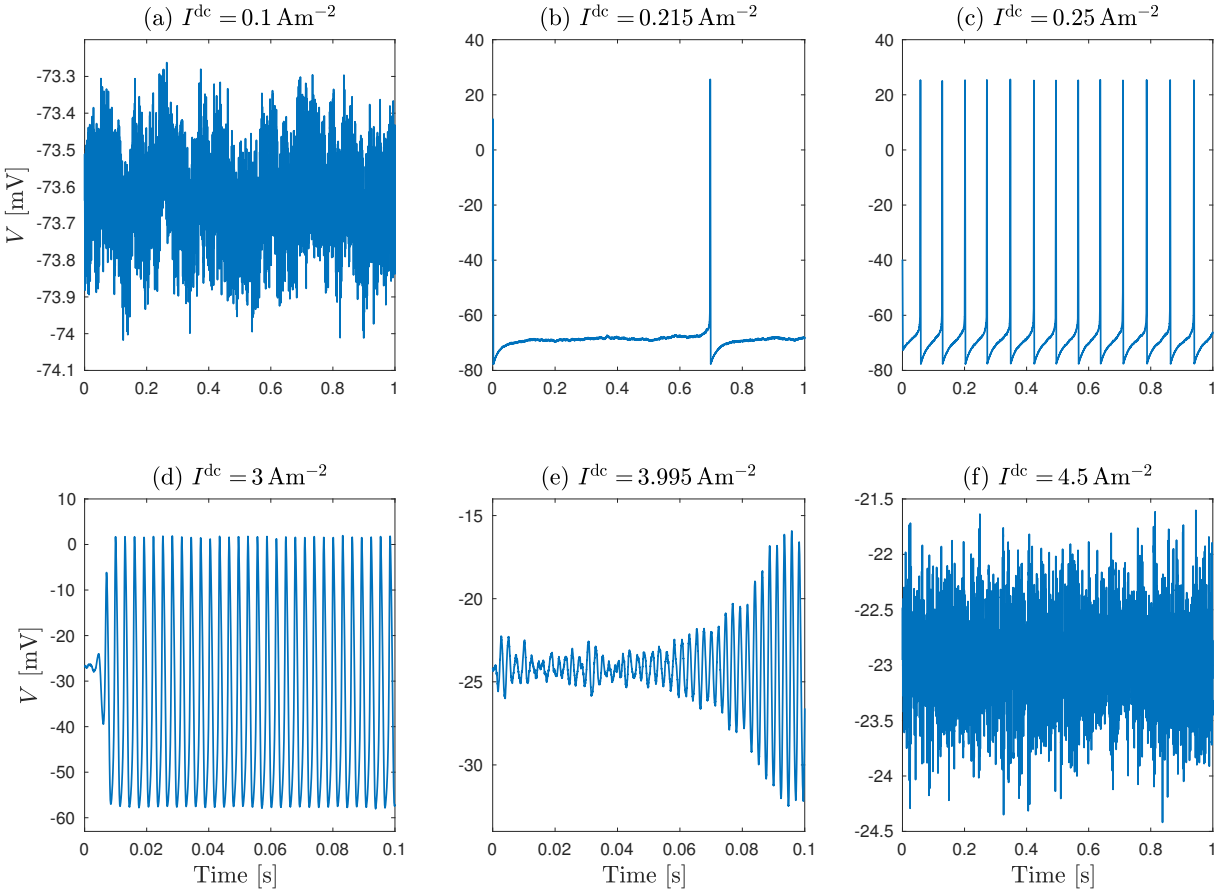

Figure 2.16: Stochastic simulations to demonstrate birth (top panels) and death (bottom panels) of action potentials in Wilson type-I cortical neuron when the dc stimulus current exceeds first and second threshold values, $I_{\mathrm{dc}}^{\mathrm{crit},1}$ and $I_{\mathrm{dc}}^{\mathrm{crit},2}$. The simulation currents are $I_{\mathrm{dc}} =$ 0.1, 0.21475, 0.25, 0.3, 3.995, and $4.5\,\mathrm{Am}^{-2}$. Note that the spike rate increases with the stimulus current. The integration algorithm used is Euler–Maruyama with time step $\Delta t = 0.01$ ms. To improve the visibility of the fluctuation patterns, simulations are plotted only for 0.1 s in panels (d) and (e).

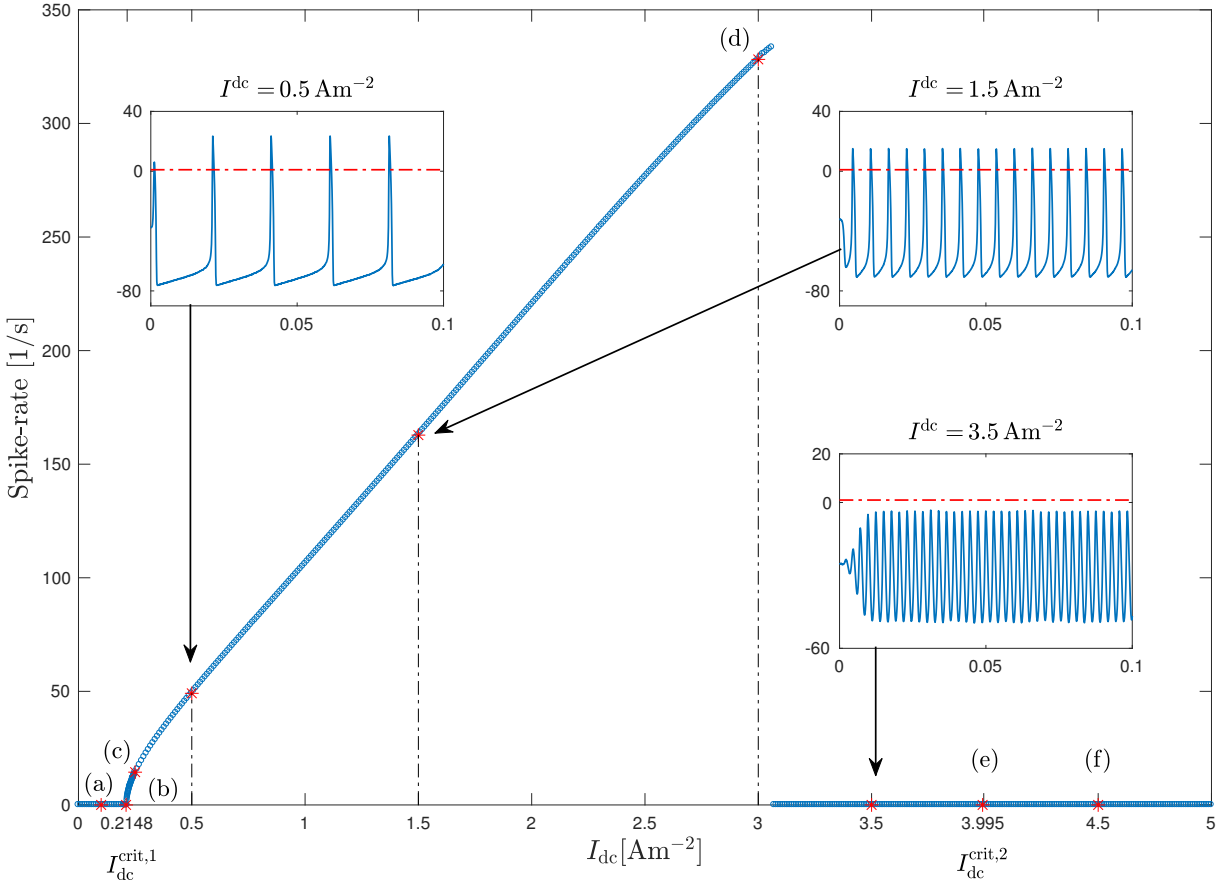

Figure 2.17: Spike-rate as a function of input current for Wilson type-I cortical neuron. The spike-rate curve increases smoothly from zero at $I_{\rm dc}^{\rm crit,1}$ to a maximum value ($\sim$330 s^{-1}), then collapses to zero when spike amplitude fails to reach our pre-defined 0 mV threshold (dashed red line). Small amplitude oscillations are observed until $I_{\rm dc}$ exceeds $I_{\rm dc}^{\rm crit,2}$.

2.9 Chapter Summary

This chapter surveyed several important point neuron models. I discussed the reason for selecting Wilson's two-variable spiking-neuron model to represent the spiking behaviour of individual neurons in the Waikato True-field approach. The chapter was concluded by presenting a detailed analysis of Wilson's type-I (human cortical) spiking neuron model.

In the next chapter, the concept of modelling neuronal assemblies will be discussed.

Chapter 3

Models of Neuronal Assemblies

It is well known that neurons work together to process information. A grouping of neurons that are coupled via synaptic connections to form a neural network is called a neuronal assembly. Within each such group, thousands of spikes are emitted each millisecond. Thus, it is very challenging to model such networks on a single-unit basis. The Blue Brain project is attempting to develop such massive networks but requires supercomputing facilities [42, 51]. The grand ambition of the Blue Brain project is to create an artificial brain that can "think", respond, and form memories in the same way that a real brain does. The simulations are run on the IBM Blue Gene supercomputer using NEURON software.

A common and efficient way to avoid the limitations of spike-based aggregates is to describe the *mean* activity of the neuronal population, rather than tracking the spiking of individual neurons. This approach is called *mean-field* modelling. The population activity in a mean-field context is given by [28],

$$A(t) = \lim_{\Delta t \to 0} \frac{1}{\Delta t} \frac{n}{N} \tag{3.1}$$

where N is the size of neuron population, n is the number of spikes in a small time interval Δt. This gives the population-average spike rate.

In this chapter, I discuss the top-down mean-field approach to describe the behaviour of population-averaged neuronal assemblies. I show how this concept has evolved over time by examining several different mean-field prescriptions. I discuss the limitations of mean-field averaging, motivating the development of the Waikato "true-field" equations that are expected to provide a more accurate mapping from single neuron dynamics to population level cooperative behaviours. I discuss the construction of the True-field equations and the coarse-graining philosophy that allows spatial rescaling from the micro (single neuron) to the macro (neural aggrgates) level.

3.1 Mean-field Models

Mean-field models usually employ a nonlinear transfer function such as a sigmoid to map membrane potential (mV) to spike rates (spikes/s) [65, 67, 74, 75], and assumes that each neuron experiences the "mean-field" bulk activity of all other neurons in the population. As shown in Fig. 3.1, the sigmoid rises steeply around a mean threshold, then saturates at the maximum spike rate.

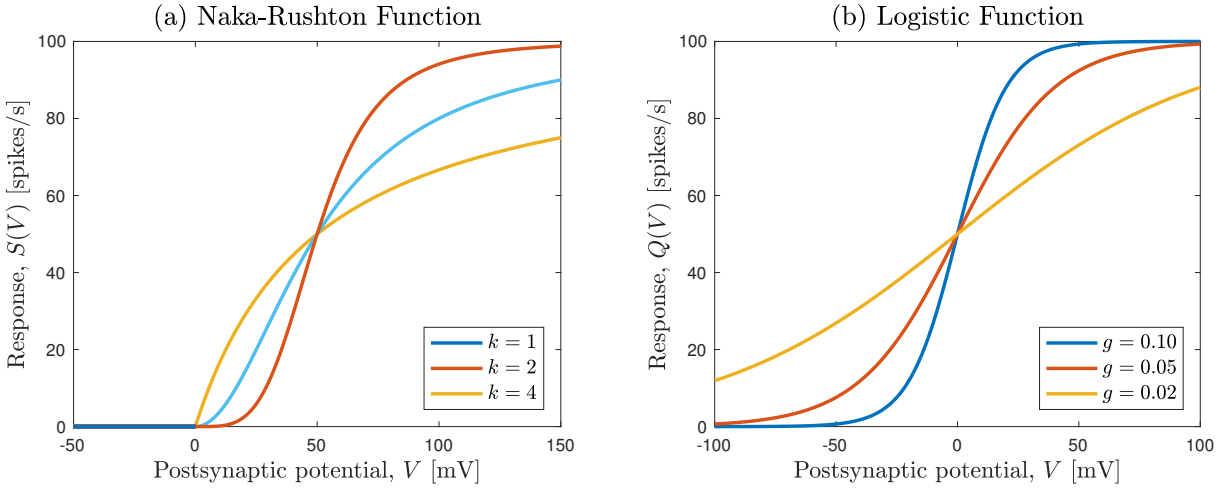

Figure 3.1: Two sigmoid functions in common use: (a) Naka-Rushton function, $S(V) = MV^k/(\sigma^k + V^k)$ and (b) Logistic function, $Q(V) = M/(1 + \exp(-gV))$. Graphs set $M = 100$ and $\sigma = 50$, for three values of N and g. The figure is modified from Wilson (1999) [87].

The mean-field paradigm is well-suited for exploring large-scale phenomena such as electrical activity in the cerebral cortex recorded via electrodes on the scalp. These signals, known as EEGs (electroencephalograms), have been used to interpret the dynamics of phase transitions between wake and sleep, recovery from drug-induced anaesthesia, and onset of seizures [92]. Beurle [8] introduced the concept of mean-field modelling in 1956. His equations described a population of excitatory neurons interconnected by fibres with connection densities assumed to drop off exponentially with neuron separation. He defined the number of neurons per unit volume that become active per unit time as 'activity'. He assumed that the membrane potential of a neuron would be its resting value plus the sum of incoming postsynaptic potentials. He also assumed that after a firing event, a neuron has a refractory period during which it cannot fire again. While this refractory period prevents uncontrolled runaway firing, it is insufficient to provide the stability of a real cortex. Griffith in 1963 [30] solved this issue by introducing inhibitory synapses which act to hyperpolarise the postsynaptic neuron and make it less likely to fire.

3.1.1 Wilson-Cowan Model

In 1972, Wilson and Cowan introduced a mean-field description of the dynamics of interactions between populations of excitatory and inhibitory neurons [88, 89]. They assumed equal numbers of uniformly distributed excitatory and inhibitory neurons in the cortex (see Fig. 3.2), and quantified their behaviour in terms of their average firing-rates. The dynamics of spatially localized excitatory and inhibitory neuron populations was expressed as a pair of coupled nonlinear differential equations,

$$\tau_E \frac{\partial}{\partial t} E(x,t) = -E(x,t) + S_E\big[w_{EE}(x) \otimes E(x,t) - w_{IE}(x) \otimes I(x,t) + P\big] \tag{3.2a}$$

$$\tau_I \frac{\partial}{\partial t} I(x,t) = -I(x,t) + S_I\big[w_{EI}(x) \otimes E(x,t) - w_{II}(x) \otimes I(x,t) + Q\big] \tag{3.2b}$$

where $E(x,t)$ and $I(x,t)$ are the average firing rates of excitatory and inhibitory populations at position x; τ_E, τ_I are the time constants for each population; $w_{jk}(j,k \in E,I)$ are the density

of the synaptic couplings between and within populations; S_E, S_I are the sigmoidal response functions mapping voltage to firing rate; P, Q are external voltage inputs to each population; and $\otimes$ indicates the spatial convolution between synaptic coupling density and firing rate. For functions $f(x)$ and $g(x)$ of a continuous variable x, the spatial convolution is defined as:

$$f(x) \otimes g(x) = \int f(x')\, g(x - x')\, dx'$$

Using this model, Wilson and Cowan were able to demonstrate multiple stable states, limit cycle activity, hysteresis, and pattern formation. Elements of this model form the basis for most mean-field approaches used today.

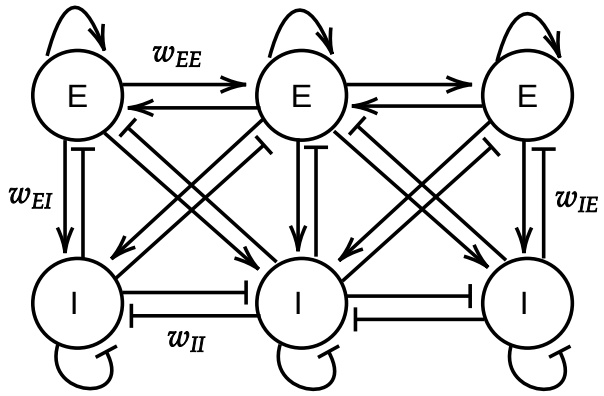

Figure 3.2: Spatial interactions of excitatory and inhibitory neurons in Wilson-Cowan model. (Modified from Wilson *et al* (1973) [89].)

3.1.2 Nunez Model

In 1974, Nunez developed a mean-field theory [57, 58] to model communication between brain regions. He introduced the concept of "neural mass" to represent the average properties of a large number of neurons. He derived an integral wave equation with axonal delays to describe the spatial and temporal variation of cortical potential. His equations supported electrical oscillations that are dependent on the proportion of excitatory and inhibitory connections between neural masses and the physiological state of the brain. For spherical boundary conditions he predicted global oscillatory modes with frequencies that matched the major cerebral rhythms.

3.1.3 Amari Model

Amari in 1975 [3,4], presented a field-theoretic approach to model pattern formation in a continuum description of neuronal activity. His model described interacting excitatory and inhibitory neuron populations coupled via Mexican-hat kernels. The equation for cortical activity is,

$$\frac{\partial}{\partial t} u(x,t) = -u(x,t) + \int_B w(x,y) f(u(y,t)) dy, \quad x \in B,\ t \geq 0 \tag{3.3a}$$

where initial conditions $u(x,0) = u_0(x), \quad x \in B$ are given. B is some domain where the neuronal activity occurs, f is the sigmoidal firing rate function and w is a Mexican-hat connectivity function.

Generally, the kernel w is chosen to be homogeneous (i.e. $w(x,y) = w(x-y)$). In this case, the integral becomes a convolution integral, so that the Eq. (3.3a) can be written in the form,

$$\frac{\partial}{\partial t}u(x,t) = -u + w \otimes f(u) \tag{3.3b}$$

3.1.4 Freeman model

In 1975, Freeman modelled the EEG activity at the surface of the olfactory bulb of animals during the perception of odours [7, 23]. This cortical model was implemented based on the concept that populations of neurons influence one another in a measurable and quantifiable manner. He introduced an interacting hierarchy of neural sets (referred to as K0, KI, KII) with different interconnection properties. As in the previous mean-field modelling approaches, Freeman also used a sigmoid nonlinearity to represent the transformation of analogue input, in the form of EPSPs or IPSPs to spiking output at the population level. Furthermore, he included synaptic and dendritic delays in his model and observed that inclusion of these delays in feedback loops can lead to oscillatory behaviour in populations of excitatory and inhibitory neurons.

3.1.5 Wright and Liley Model

Wright and Liley implemented a spatially discretized model [93–95], by treating the cortex as 2D and dividing it into patches. Each of these patches is described by the mean densities of excitatory and inhibitory neurons, their firing rates and the average number of interconnections (synapses). They used a Green function formulation to describe the interconnections between patches as a function of the neuron type and their separation using anatomical data, a sigmoid function to map between membrane voltage and firing rates, triangular functions to represent PSPs, and axonal and dendritic delays. However, the inclusion of the Green function makes simulations very slow and limited to very small systems (or very coarse resolution in larger systems).

3.1.6 Robinson Model

In 1997, Robinson, Rennie and Wright introduced a mean-field model based on the neurophysics of Wright and Liley model [67]. Their main focus was to develop a model of cortical electrical activity, including the essential dynamics, nonlinearities, axonal and dendritic time lags, variable geometries and boundary conditions in 2D. They used nonlinear equations to model the behaviour of waves of cortical electrical activity that generate the signals observed in EEGs. Their model is similar to that of Wright and Liley, but with the Green function being replaced with a more realistic damped wave equation to improve the runtime of numerical simulations and increase spatial resolution. In contrast to discretized Wright and Liley equation, Robinson used a continuum form and was able to study wave properties and their stability analytically.

The relationship between the mean firing rate of an excitatory/ inhibitory neuron averaged over many neurons, $Q_{e,i}$ and the mean dendritic potential, $V_{e,i}$ is represented by a sigmoid,

$$Q_{e,i} = \frac{1}{1 + e^{-C(V_{e,i} - V_0)}} \tag{3.4a}$$

where voltage units are standard deviations (SD) of the threshold distribution, with a mean threshold of V_0. Here, C is a positive constant. The values used for C and V_0 are 1.82 and 3 respectively.

Within a certain neuron, relationship between the rate of arrival of incoming pulses, Q_{ae} or Q_{ai}, and the corresponding potential, V_e or V_i is given by a biexponential response function,

$$V_{e,i}(\mathbf{r}, t) = g \, \frac{\alpha\beta}{\beta - \alpha} \left[U_{e,i}(\mathbf{r}, t) - W_{e,i}(\mathbf{r}, t) \right] \tag{3.4b}$$

where β, α are the rise-rate and the decay-rate respectively; g is a positive constant; $U_{e,i}$ and $W_{e,i}$ are auxiliary potentials given by,

$$\frac{dU_{e,i}(\mathbf{r}, t)}{dt} = Q_{ae,ai}(\mathbf{r}, t) - \alpha U_{e,i}(\mathbf{r}, t) \tag{3.4c}$$

$$\frac{dW_{e,i}(\mathbf{r}, t)}{dt} = Q_{ae,ai}(\mathbf{r}, t) - \beta W_{e,i}(\mathbf{r}, t) \tag{3.4d}$$

The outward propagation of spike density is approximated as a wave $\phi_{e,i}$ generated by the source $Q_{e,i}$,

$$\left(\frac{\partial^2}{\partial t^2} + 2\,\gamma_{e,i} \frac{\partial}{\partial t} + \gamma_{e,i}^2 - v^2 \nabla^2 \right) \phi_{e,i}(\mathbf{r}, t) = \gamma_{e,i}^2 \; Q_{e,i}(\mathbf{r}, t) \tag{3.4e}$$

where v is the characteristic axonal propagation velocity, $\gamma_{e,i} = v / r_{e,i}$ and $r_{e,i}$ is the characteristic range of the axons.

The incoming potentials Q_{ae} and Q_{ai} at a certain location consists of contributions from the wave potentials $\phi_{e,i}$ and inputs external to the cortex.

$$Q_{ae}(\mathbf{r}, t) = M_e Q_s(\mathbf{r}, t) + \mu_e Q_{ns} + a_{ee}\phi_e(\mathbf{r}, t) - a_{ei}\phi_i(\mathbf{r}, t) \tag{3.4f}$$

$$Q_{ai}(\mathbf{r}, t) = M_i Q_s(\mathbf{r}, t) + \mu_i Q_{ns} + a_{ie}\phi_e(\mathbf{r}, t) - a_{ii}\phi_i(\mathbf{r}, t) \tag{3.4g}$$

The external inputs consists of *nonspecific* and *specific* excitations, Q_{ns} and Q_s respectively. Q_{ns} is not involved in a particular stimulus under study and is a result of inputs from noncortical structures in the brain. Q_s is due to stimuli that include both noisy and coherent components which may or may not be spatially localized. In the model, Q_{ns} is defined to be constant in time and space and Q_s is defined to have zero spatial and temporal means. The constants M_e and M_i determine the coupling strength of specific inputs to excitatory and inhibitory neurons respectively; μ_e and μ_i are the densities of synapses associated with nonspecific stimuli; a_{ee}, a_{ei}, a_{ie} and a_{ii} are the synaptic densities associated with excitatory and inhibitory inputs to excitatory and inhibitory neurons. The parameter settings (for human) in these equations are

given in the following table.

Table 3.1: Parameter settings for human defined for Robinson model [67]

Parameter	a_{ee}	a_{ii}	a_{ie}	a_{ei}	μ_e	μ_i	r_e (m)	r_i (m)	g
Value	0.853	0.002	0.126	0.011	0.007	0.001	0.08	10^{-4}	36

3.1.7 Liley Model

The Liley model [48–50] is a mean-field approach that attempts to reproduce the electrocortical dynamics of a cortical *macrocolumn* (a group of 40,000 to 100,000 excitatory (85%) and inhibitory (15%) neurons acting cooperatively within a small cylindrical volume of cerebral cortex) [74]. Liley represented the cortex as a 1D continuum of macrocolumn mass.

The model consists of a system of eight coupled differential equations that describe mean membrane potential averaged over the neurons within a macrocolumn. The equations of motion for the population-averaged excitatory and inhibitory soma voltages, h_e and h_i, are given by,

$$\tau_e \frac{d}{dt} = (h_e^{\text{rest}} - h_e) + \psi_{ee}(h_e) I_{ee}(h_e) + \psi_{ie}(h_e) I_{ie}(h_i) \tag{3.5a}$$

$$\tau_i \frac{d}{dt} = (h_i^{\text{rest}} - h_i) + \psi_{ei}(h_i) I_{ei}(h_e) + \psi_{ii}(h_i) I_{ii}(h_i) \tag{3.5b}$$

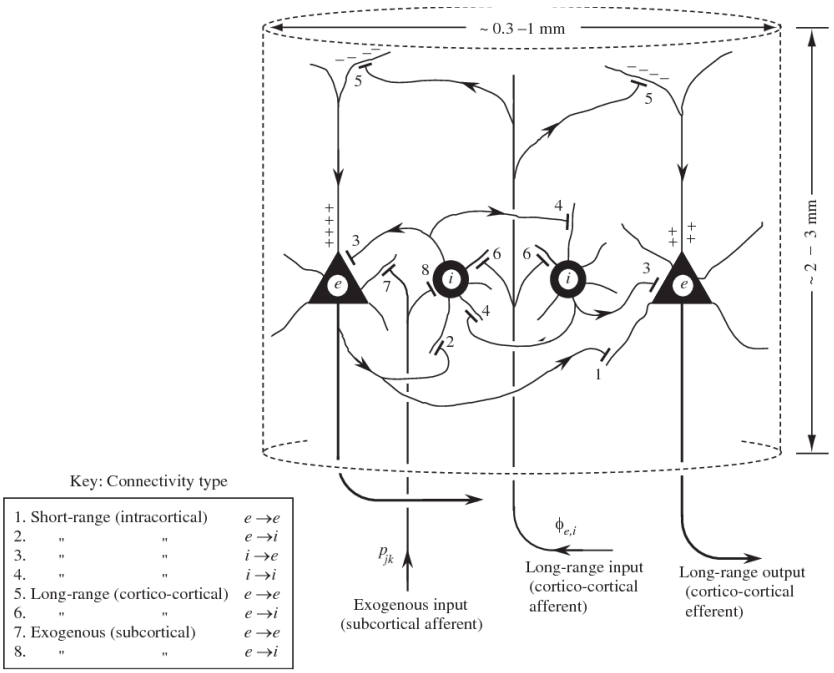

Figure 3.3: Schematic representation of the neuronal connections within a cortical macrocolumn (occupying a cylindrical volume of diameter $\sim 0.3 - 1$ mm and length $\sim 2 - 3$ mm). Triangles are excitatory cells and circles are inhibitory cells. Source: Steyn-Ross *et al* (1999) [74].

where $\tau_{e,i}$ are the excitatory and inhibitory membrane time constants, I_{ek} and I_{ik} (where $k = e, i$) are excitatory and inhibitory PSPs and $\psi_{j,k}$ ($j, k \in \{e, i\}$) are dimensionless weighting factors,

$$\psi_{jk}(h_k) = \frac{h_j^{\text{rev}} - h_k}{|h_j^{\text{rev}} - h_k^{\text{rest}}|} \tag{3.5c}$$

The PSPs are modelled as alpha function impulses of the form $\gamma t \exp(-\gamma t)$ where γ is a rate constant and $1/\gamma$ is the time to peak. Thus, excitatory and inhibitory PSPs, I_{ek} and I_{ik} (where $k = e, i$) are given by the following second-order differential equations.

$$\left(\frac{d}{dt} + \gamma_e\right)^2 I_{ee}(h_e) = \left[N_{ee}^{\beta}\mathcal{S}_e(h_e) + \phi_{ee}(h_e) + p_{ee}\right] G_e\gamma_e e \tag{3.5d}$$

$$\left(\frac{d}{dt} + \gamma_e\right)^2 I_{ei}(h_e) = \left[N_{ei}^{\beta}\mathcal{S}_e(h_e) + \phi_{ei}(h_e) + p_{ei}\right] G_e\gamma_e e \tag{3.5e}$$

$$\left(\frac{d}{dt} + \gamma_i\right)^2 I_{ie}(h_i) = \left[N_{ie}^{\beta}\mathcal{S}_i(h_i) + p_{ie}\right] G_i\gamma_i e \tag{3.5f}$$

$$\left(\frac{d}{dt} + \gamma_i\right)^2 I_{ii}(h_i) = \left[N_{ii}^{\beta}\mathcal{S}_i(h_i) + p_{ii}\right] G_i\gamma_i e \tag{3.5g}$$

where N_{jk}^{β} are the numbers of $j \to k$ local connections, p_{jk} are spike-rate inputs (units: s^{-1}) entering the macrocolumn from subcortical sources, $\phi_{ee,ei}$ are long range (cortico-cortical) excitatory spike inputs from distant macrocolumns elsewhere in the cortex, $G_{e,i}$ are the peak amplitudes (in mV) for the EPSP and IPSP response functions respectively, and $\mathcal{S}_j$ are sigmoidal transfer functions that map membrane voltage to firing rate,

$$\mathcal{S}_e(h_e) = \frac{\mathcal{S}_e^{\max}}{1 + \exp[-g_e(h_e - \theta_e)]} \tag{3.5h}$$

$$\mathcal{S}_i(h_i) = \frac{\mathcal{S}_i^{\max}}{1 + \exp[-g_i(h_i - \theta_i)]} \tag{3.5i}$$

where $\theta_{e,i}$ is the inflexion point voltage, and $g_{e,i}$ is the slope of the sigmoid function at inflexion.

The long-range contributions from distant macrocolumns to the population EPSPs and IPSPs are modelled using 1D wave equations,

$$\left[\left(\frac{d}{dt} + \bar{v}\Lambda_{ee}\right)^2 - \bar{v}^2\frac{\partial^2}{\partial^2 x}\right]\phi_{ee} = \bar{v}\Lambda_{ee}N_{ee}^{\alpha}\left(\frac{d}{dt} + \bar{v}\Lambda_{ee}\right)\mathcal{S}_e(h_e) \tag{3.5j}$$

$$\left[\left(\frac{d}{dt} + \bar{v}\Lambda_{ei}\right)^2 - \bar{v}^2\frac{\partial^2}{\partial^2 x}\right]\phi_{ei} = \bar{v}\Lambda_{ei}N_{ei}^{\alpha}\left(\frac{d}{dt} + \bar{v}\Lambda_{ei}\right)\mathcal{S}_e(h_e) \tag{3.5k}$$

where $\bar{v}$ is the mean axonal conduction speed, Λ_{ek} is the characteristic inverse-length scale for cortico-cortical connections and N_{ek}^{α} are the numbers of long-range connections of type $e \to k$.

3.1.8 The Waikato Mean-field Model

The Waikato cortical modelling group of Steyn-Ross and colleagues modified the Liley model to incorporate the effect of general anaesthetic [73, 74]. They assumed that the effectiveness of *inhibitory* synaptic events increases as the anaesthetic concentration increases. Therefore, the

anaesthetic effect was modelled by lengthening the duration of the IPSP via a reduction in the neurotransmitter rate constant,

$$\gamma_i \to \gamma_i/\lambda_{\mathrm{GABA}}$$

where λ_{GABA} is a dimensionless factor assumed to be proportional to anaesthetic concentration: $\lambda_{\mathrm{GABA}} = 1$ implies no anaesthetic effect and an increase in λ_{GABA} implies increase in anaesthetic concentration.

The second significant change was to introduce white noise fluctuations into the four p_{jk} spike-rate inputs in Eq. (3.5d)–(3.5g). Thus, each p_{jk} term is replaced by the sum of a mean value plus a stochastic variation about the mean,

$$p_{jk} \to \langle p_{jk} \rangle = \alpha \sqrt{\langle p_{jk} \rangle}\, \xi_n(t), \quad n = 1, ..., 4 \tag{3.6}$$

where α is a dimensionless scale-factor to ensure that the stochastic fluctuations always remain small. Each $\xi_n(t)$ is an independent, Gaussian-distributed white noise source of zero mean and delta-function covariance (units: $\mathrm{s}^{-1/2}$),

$$\big\langle \xi_n(t) \big\rangle = 0, \quad \big\langle \xi_n(t) \xi_m(t') \big\rangle = \delta_{mn} \delta(t - t') \tag{3.7}$$

This inclusion of white noise allowed the development of a theoretical fluctuation spectrum for the effect of anaesthetic, successfully predicting the "biphasic" response in which patient EEG activity initially surges, then collapses into unconsciousness, as anaesthetic concentration is steadily increased.

The Waikato mean-field model has been in continuous development since 1999 [69,73–75]. In 2007, the Waikato group employed a mean-field argument to derive an expression for *electrical* synaptic connections (gap junctions) to supplement the *chemical* synaptic connections [76, 77]. Earlier mean-field models had all assumed that communication between neurons is via chemical synapses only.

Gap junctions are the direct connections between the cytoplasm of two cells that exchange electric charge, mostly K^+. Following Fukuda [24], Steyn-Ross *et al* [77] assumed that all gap junctions along the dendrite contribute equally and that the maximum radial extent of gap-junction sensitivity is $\sim 200\,\mu$m. According to previous studies [24, 25, 29], it is known that the gap-junction connections obey Ohms law, $I_{\mathrm{gap}} = g\Delta V$, where g is the gap-junction conductance (inverse resistance) and ΔV is the voltage difference between the joined cells. The total diffusive current per unit area entering the neuron at the centre, node (x, y) is written as (see Fig. 3.4),

$$I_{\mathrm{gap}} = I_{\mathrm{E}} + I_{\mathrm{W}} + I_{\mathrm{N}} + I_{\mathrm{S}} \tag{3.8a}$$

$$I_{\mathrm{E}} = g[V(x + \Delta x, y) - V(x, y)] \tag{3.8b}$$

$$I_{\mathrm{W}} = g[V(x - \Delta x, y) - V(x, y)] \tag{3.8c}$$

where $g = 1/R$; thus

$$I_{\mathrm{E}} + I_{\mathrm{W}} = \frac{\Delta x^2}{R} \left[\frac{V(x + \Delta x, y) - 2V(x, y) + V(x - \Delta x, y)}{\Delta x^2} \right] \approx \frac{\Delta x^2}{R} \frac{\partial^2 V}{\partial x^2} \tag{3.8d}$$

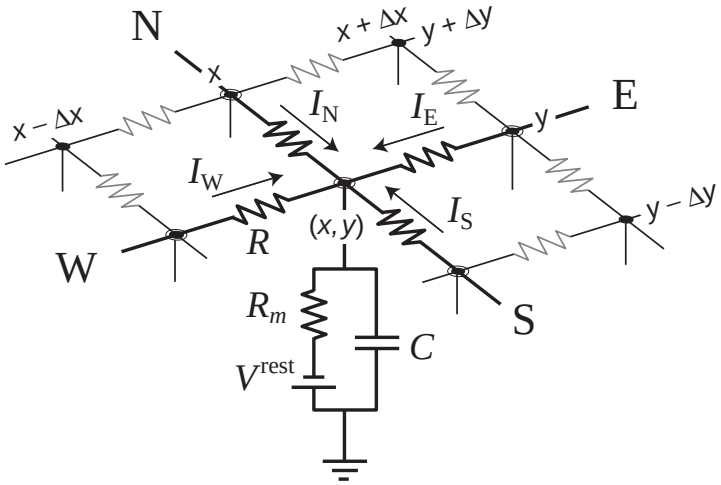

Figure 3.4: Schematic representation of the cortex modelled as a 2D square lattice of cells, each cell connected to its four nearest neighbours via gap-junctions. The total diffusive current per unit area entering the neuron at the centre node (x, y) is given by summing the diffusive currents from neighbours, N, S, W, E. Source: Steyn-Ross *et al* (2007) [77].

Similarly,

$$I_{\rm N} + I_{\rm S} = \frac{\Delta y^2}{R}\left[\frac{V(x, y+\Delta y) - 2V(x,y) + V(x, y-\Delta y)}{\Delta y^2}\right] \approx \frac{\Delta y^2}{R}\frac{\partial^2 V}{\partial y^2} \tag{3.8e}$$

Addition of the two equations above gives,

$$I_{\rm gap} = \frac{a}{R}\left[\frac{\partial^2 V}{\partial x^2} + \frac{\partial^2 V}{\partial y^2}\right] = \frac{a}{R}\nabla^2 V \tag{3.8f}$$

where $\Delta x^2 = \Delta y^2 = a$, is the area of the Fukuda diffusion cell (zone of diffusive sensitivity) and R is the effective Fukuda resistance.

Multiplying both sides of Equation (3.8f) by membrane resistance $R_m = \tau/C$, and substituting the effective Fukuda resistance R gives,

$$V^{\rm diff} = D_2 \nabla^2 V \tag{3.8g}$$

where $D_2 = aR_m/R$ is the diffusive coupling strength for inhibitory neurons. The diffusive coupling strength for excitatory neurons (D_1) is assumed to be much weaker than D_2 because gap junction connections between pairs of excitatory neurons are both rare and sparse [77].

Thus, the most recent version of the Waikato model is a 2D mean-field description of a cortical tissue that contains excitatory and inhibitory neural assemblies that are connected locally via both neurotransmitter-mediated chemical synapses and gap junctions, and over distance via

long-range myelinated axons. The differential equations for membrane voltage are,

$$\tau_e \frac{\partial V_e}{\partial t} = V_e^{\text{rest}} - V_e + [\rho_e \psi_{ee} \Phi_{ee} + \rho_i \psi_{ie} \Phi_{ie}] + D_1 \nabla^2 V_e \tag{3.9a}$$

$$\tau_i \frac{\partial V_i}{\partial t} = V_i^{\text{rest}} - V_i + \underbrace{[\rho_e \psi_{ei} \Phi_{ei} + \rho_i \psi_{ii} \Phi_{ii}]}_{\text{Chemical}} + \underbrace{D_2 \nabla^2 V_i}_{\text{Electrical}} \tag{3.9b}$$

where $\rho_{e,i}$ are the synaptic coupling strengths of the chemical synapses given by the area under EPSP and IPSP functions ($\rho_e > 0$ indicates excitation and $\rho_i < 0$ indicates inhibition), $D_{1,2}$ are excitatory and inhibitory diffusive coupling strengths, $\psi_{j,k}$ are normalized reversal-potential functions,

$$\psi_{jk} = \frac{V_j^{\text{rev}} - V_k}{|V_j^{\text{rev}} - V_k^{\text{rest}}|}, \qquad j,k \in \{e,i\} \tag{3.9c}$$

where V_j^{rev} is the synaptic reversal potential for neurons of type j and V_k is the resting voltage for neurons of type k.

Φ_{ee}, Φ_{ie} are the excitatory and inhibitory flux inputs (units: spikes/s) entering the excitatory population, obeying second-order differential equations,

$$\left(\frac{d}{dt} + \gamma_{ee}\right)^2 \Phi_{ee} = \gamma_{ee}^2 \left[N_{ee}^{\alpha} \phi_{ee} + N_{ee}^{\beta} Q_e + \phi_{ee}^{\text{sc}}\right] \tag{3.9d}$$

$$\left(\frac{d}{dt} + \gamma_{ie}\right)^2 \Phi_{ie} = \gamma_{ie}^2 N_{ie}^{\beta} Q_i \tag{3.9e}$$

Φ_{ei}, Φ_{ii} are the excitatory and inhibitory flux inputs entering the inhibitory population,

$$\left(\frac{d}{dt} + \gamma_{ei}\right)^2 \Phi_{ei} = \gamma_{ei}^2 \left[N_{ei}^{\alpha} \phi_{ei} + N_{ei}^{\beta} Q_e + \phi_{ei}^{\text{sc}}\right] \tag{3.9f}$$

$$\left(\frac{d}{dt} + \gamma_{ii}\right)^2 \Phi_{ii} = \gamma_{ii}^2 N_{ii}^{\beta} Q_i \tag{3.9g}$$

The long-range excitatory fluxes ϕ_{ee} and ϕ_{ei} are modelled using the Robinson damped wave equation [67],

$$\left[\left(\frac{d}{dt} + v\Lambda_{ek}\right)^2 - v^2 \nabla^2\right] = v^2 \Lambda_{ek}^2 Q_e, \quad k = e,i \tag{3.9h}$$

where v is the mean axonal conduction speed, Λ_{ek} is the inverse-length scale for long-range $e \to k$ connections.

Q_e and Q_i are sigmoidal transfer functions that map membrane voltage $V_{e,i}$ to firing rate,

$$Q_k = \frac{Q_k^{\max}}{1 + \exp[-C(V_k - \theta_k)/\sigma_k]}, \quad k = e,i \tag{3.9i}$$

where $C = \pi/\sqrt{3}$, θ_k is the population-average threshold voltage for firing, σ_k is its standard deviation and $Q_k^{\max}$ is the maximum firing rate for the $k = e,i$ neural population.

The stochastic fluctuations entering via subcortical sources ϕ^{sc}_{ee}, ϕ^{sc}_{ei} is modelled as Gaussian-distributed white-noise perturbations,

$$\phi^{\text{sc}}_{ek} = \left\langle \phi^{\text{sc}}_{ek} \right\rangle + s\sqrt{\left\langle \phi^{\text{sc}}_{ek} \right\rangle}\,\xi_m(\vec{r},t), \quad m = 1,2; \;\; k = e,i \tag{3.9j}$$

where $\left\langle \phi^{\text{sc}}_{ek} \right\rangle$ is the mean level of incoming subcortical activity, s is a dimensionless scale factor that changes the level of stochasticity, and the two $\xi_m(\vec{r},t)$ are independent, zero-mean, white-noise sources that are delta-correlated in time and space:

$$\left\langle \xi_m(\vec{r},t) \right\rangle = 0, \quad \left\langle \xi_m(\vec{r},t)\xi_n(\vec{r'},t') \right\rangle = \delta_{mn}\delta(t-t')\delta(\vec{r}-\vec{r'}) \tag{3.9k}$$

3.2 Moving beyond Mean-field Theory

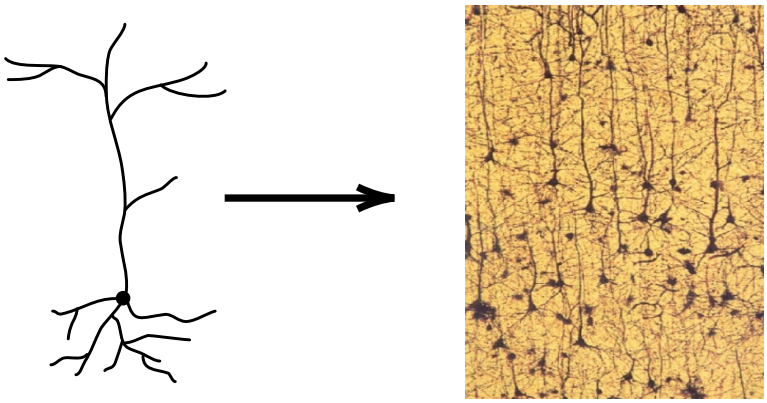

Figure 3.5: Single neuron and a population of neurons. Source: Network of cortical neurons (https://tinyurl.com/w3xw4rc)

The mean-field modelling concept of the cortex has been widely used to investigate brain activity on a coarse spatial scale. However, because mean-field describes population-average properties, it necessarily neglects the characteristics of single neurons and cannot track the percolation of spiking behaviour and noise from single neuron to population. The relationship between aggregate properties of neural populations versus microscale properties of single neurons is not well understood. To date, there is much interest in understanding the dynamics of human brain across multiple scales [6,9–11,15,19,91]. One such new approach is to develop a hybrid of spiking-based and rate-based models [66] in which the behaviour of a chain of spiking neurons is compared with a spiking-rate approximation of the population. Another approach is to develop mesoscopic models that describe the neural dynamics at the level of minicolumns (vertical column-like cortical organisations of $\sim$80$-$120 neurons aligned perpendicular to the pial surface within a diameter of $\sim$30$-$60 μm) rather than the full cortical population [15,68]. Some of these modellers adopt a master equation formulation to map single spiking neurons to neural networks [9, 11, 19]. The master equation is used to describe jump processes that are connected with chemical reactions and other birth-death processes [26]. Unlike mean-field descriptions, these models include the correlations between firing activity at different cortical locations.

However, it is unclear how these new approaches can be adapted to model the percolation of spiking behaviour and noise contributions from ion channel and synaptic sources from microscopic (single neuron) level all the way up to the macroscopic (population) level.

To address these issues, the Waikato Cortical Modelling group introduced a rigorous formalism which systematically regrids and rescales a network of spiking neurons from the micro-level of individual units to increasingly coarser spatial scales [72]. This bottom-up neural regridding is named "True-field". This is not a mean-field calculation, and does not make the ad hoc assumptions of mean-field modelling. It is based on regridding cortical tissue using a spatial blocking (coarse-graining) technique similar to K.Wilson's renormalisation group theory for critical phenomena [90]. This rescaling should allow determination of population spike rates which incorporate the dynamics of a single spiking neuron.

3.3 Bottom-up Neural Regridding: True-field

The motivation for True-field is to provide a better way of representing the summed activation of many thousands of neurons in the human cortex by more accurately aggregating from single neuron activity to neural population dynamics without suppressing local fluctuations and correlations between connected neurons.

3.3.1 An Overview of the Model

We consider a 2D patch of cortical tissue which is partitioned into a network of $(2n+1)^2$ unit cells (see Fig. 3.6(b)). Each of these cells occupies an area of ℓ^2 ($\ell \approx 10\mu$m) and contains a pair of excitatory (e) and inhibitory (i) neurons. We assume that these neurons are coupled via

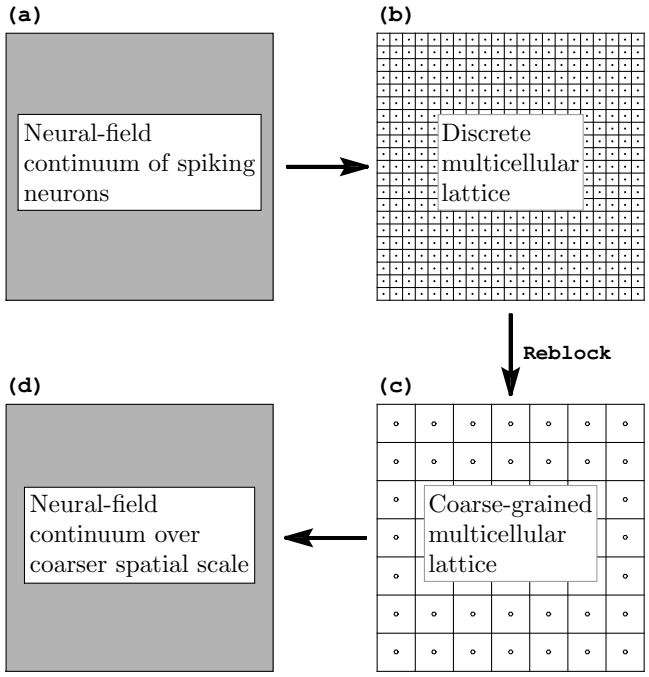

Figure 3.6: Mapping a cortical patch to a coarser spatial scale. (a) Continuum field equations for a square patch of cortical tissue are discretized to a fine-grained microscale lattice of spiking neurons (b), then reblocked onto a coarser spatial grid (c) and inverted back to continuum form. Source: Steyn-Ross and Steyn-Ross (2016) [72].

both chemical and electrical (i–i and e–e gap-junction) synapses that are perturbed by synaptic and ion-channel white noises. We choose to model these individual neurons using the Wilson two-variable spiking neuron because it is both physiologically meaningful and mathematically tractable.

We then map the 2D patch of cortex to a coarser-grained network of $(2N+1)^2$ compartments of side-length $L = B\ell$ with $L \approx 1$mm, and where B is defined as the blocking ratio, $B = (2n+1)/(2N+1) \gg 1$ (see Fig. 3.6(c)). Thus, the Wilson spiking neuron equations are mapped to the areal extent of a macrocolumn. These rescaled equations now describe the stochastic variables that have been spatially averaged over the coarser grid.

3.3.2 Model Equations

The following differential equations [72] describe a spiking neuron embedded within its neural field of diffusive and synaptic input fluxes. The labels $\{a, b\} \in \{e, i\}$ identify excitatory (e) or inhibitory (i) populations of neurons. The rate of change in membrane potential V_b is given by,

$$\frac{\partial V_b}{\partial t} = \underbrace{-g(V_b)(V_b - E_{\mathrm{Na}}) - g_{R,b}R_b \cdot (V_b - E_{\mathrm{K}})}_{\text{Wilson neuron (voltage)}} + \underbrace{D_b \nabla^2 V_b}_{\text{Diffusive input}} + \underbrace{\sum_a \rho_{ab}\, \Phi_{ab}}_{\text{Synaptic input}} + I_b^{\mathrm{dc}}/C \quad (3.10a)$$

where $g(V_b) = a_0 + a_1 V + a_2 V^2$ and $g_{R,b}$ are the Wilson neuron conductances of Table 2.3 divided by membrane capacitance, E_{Na} and E_{K} are the equilibrium potentials for Na^+ and K^+ respectively, C is the membrane capacitance, I_b^{dc} is the external stimulus current density, and D_b and D_R are the voltage and recovery diffusion coefficients respectively. The chemical synaptic input fluxes are given by,

$$\sum_a \rho_{ab}\, \Phi_{ab} \;=\; \rho_{eb}\, \Phi_{eb}(\vec{r}, t) + \rho_{ib}\, \Phi_{ib}(\vec{r}, t), \;\; b \in \{e, i\}$$

where ρ_{eb}, ρ_{ib} are the synaptic gains with $\rho_{eb} > 0$ (excitation) and $\rho_{ib} < 0$ (inhibition).

Table 3.2: Wilson neuron model constants adapted for True-field model

Symbol	Value	Unit
C	0.010	$\mathrm{F\,m^{-2}}$
$\tau_{e,i}$	$(11.2, 5.6) \times 10^{-3}$	s
$g_{R,b}$	26×10^3	$\mathrm{s^{-1}}$
E_{Na}	48×10^{-3}	V
E_{K}	-95×10^{-3}	V
a_0	17.81×10^3	$\mathrm{s^{-1}}$
a_1	475.8×10^3	$\mathrm{s^{-1}V^{-1}}$
a_2	3.380×10^6	$\mathrm{s^{-1}V^{-2}}$
a_3	$a_1 - a_2 E_{\mathrm{Na}}$	$\mathrm{s^{-1}V^{-1}}$
b_0	1.26652	–
b_1	37.98	$\mathrm{V^{-1}}$
b_2	330	$\mathrm{V^{-2}}$

Note: All other True-field model constants are listed in Table 6.1.

The rate-change of recovery R_b depends on its voltage-dependent steady-state $R_\infty(V_b)$ and time constant τ_b,

$$\frac{\partial R_b}{\partial t} = \underbrace{-\frac{1}{\tau_b}[R_b - R_\infty(V_b)]}_{\text{Wilson neuron (recovery)}} + \underbrace{\frac{D_R \nabla^4 V_b}{\tau_b}}_{\text{Diffusive input}} \tag{3.10b}$$

$$\text{where} \quad R_\infty(V) \;=\; b_0 + b_1 V + b_2 V^2$$

See Table 3.2 for a list of model constants.

The postsynaptic dendritic response Φ_{ab} arising from an incoming flux ϕ_{ab} of presynaptic spiking events is modelled in [72] as a biexponential with rise-rate β and decay-rate α,

$$\Big(\frac{d}{dt} + \alpha_{ab}\Big)\Big(\frac{d}{dt} + \beta_{ab}\Big)\Phi_{ab} = \alpha_{ab}\,\beta_{ab}\,\psi_{ab}(\overline{V}_b)\,N_{ab}\,\phi_{ab}$$

But for the present work we choose to use an alpha-function simplification given by,

$$\Big(\frac{d}{dt} + \gamma_{ab}\Big)^2 \Phi_{ab} = \gamma_{ab}^2\,\psi_{ab}(\overline{V}_b)\,N_{ab}\,\phi_{ab} \tag{3.10c}$$

with a single rate constant γ_{ab}. N_{ab} is the mean number of synaptic connections from neurons of population a onto each neuron of population b, and ψ_{ab} is the synaptic reversal potential function operating on $\overline{V}_b$, the temporally-smoothed membrane voltage from Eq. (3.10e).

$$\psi_{ab}(\overline{V}_b) \;\equiv\; \frac{V_a^{\text{rev}} - \overline{V}_b(t)}{V_a^{\text{rev}} - V_b^{\text{rest}}} \tag{3.10d}$$

where V_a^{rev} is the synaptic reversal potential for neurons of type a and V_b^{rest} is the resting voltage for neurons of type b. The bar represents an exponential moving average over a characteristic time-scale T that is long compared to the duration of a single spike event,

$$\frac{d\overline{V}_b(t)}{dt} = -\frac{1}{T}\big[\,\overline{V}_b(t) - V_b(t)\big] \tag{3.10e}$$

The axonal propagation of spiking activity ϕ_{ab} across a 2D cortical continuum of gray-matter is modelled using the Robinson [67] damped wave equation,

$$\Big[\Big(\frac{\partial}{\partial t} + v\Lambda_{ab}\Big)^2 - (v\nabla)^2\Big]\phi_{ab} = (v\Lambda_{ab})^2\,S_a \cdot (V_a - V_a^{\text{rest}}) \tag{3.10f}$$

where S_a is the spike area-normalization defined by the following equation,

$$S_a^{-1} \;=\; \int_{\text{spike}} (V_a(t) - V_a^{\text{rest}})\,dt \tag{3.10g}$$

Low level spatiotemporal white noises $\sqrt{\Gamma}\,\xi(\vec{r},t)$ are introduced into the model equations to represent the biological reality of noisiness in membrane voltage, ion channel conductance and synaptic response. These white noises have zero-mean, are delta-correlated in both time and

space,

$$\begin{aligned}\langle \xi(\vec{r},t)\rangle &= 0,\\ \langle \xi(\vec{r},t)\,\xi(\vec{r}',t')\rangle &= \delta(\vec{r}-\vec{r}')\,\delta(t-t')\end{aligned}$$

and have intensity Γ.

Thus, the stochastic versions of the above model equations are as follows. Note that the second-order post- and presynaptic flux equations Eqs (3.10c) and (3.10f) are written as pairs of first-order differential equations using their ancillaries Z_{ab} and Π_{ab}.

Soma voltage:

$$\frac{\partial V_b}{\partial t} = \text{RHS}(3.10\text{a}) + \sqrt{\Gamma_b}\,\xi_b(\vec{r},t) \tag{3.11a}$$

Recovery:

$$\frac{\partial R_b}{\partial t} = \text{RHS}(3.10\text{b}) + \sqrt{\Gamma_{Rb}}\,\xi_{Rb}(\vec{r},t) \tag{3.11b}$$

Synaptic flux:

$$\frac{d\Phi_{ab}}{dt} = Z_{ab} \tag{3.11c}$$

$$\frac{dZ_{ab}}{dt} = -(2\gamma_{ab})Z_{ab} - \gamma_{ab}^2\Phi_{ab} + \gamma_{ab}^2 N_{ab}\psi_{ab}(\overline{V}_b)\,\phi_{ab} + \sqrt{\Gamma_{Z_{ab}}}\,\xi_{Z_{ab}}(\vec{r},t) \tag{3.11d}$$

Average soma voltage:

$$\frac{d\overline{V}_b}{dt} = \text{RHS}(3.10\text{e}) \tag{3.11e}$$

Axonal propagation of spiking activity:

$$\frac{d\phi_{ab}}{dt} = \Pi_{ab} \tag{3.11f}$$

$$\frac{\partial \Pi_{ab}}{\partial t} = -2v\Lambda_{ab}\Pi_{ab} - [(v\Lambda_{ab})^2 - (v\nabla)^2]\,\phi_{ab} + (v\Lambda_{ab})^2 S_a(V_a - V_a^{\text{rest}}) + \sqrt{\Gamma_{\Pi_{ab}}}\,\xi_{\Pi_{ab}}(\vec{r},t) \tag{3.11g}$$

To obtain a full picture of the nature of above multi-variable system (Eqs (3.11a) to (3.11g)), a single equivalent Fokker–Planck equation is used. This formation describes the time evolution of all state variables. The Fokker–Planck equation for the probability density $P(\chi,t)$ of the state

variable χ is given by,

$$P \equiv P(\chi, t), \quad \chi \in \Big\{ V_{b,\vec{j}},\, R_{b,\vec{j}},\, \Phi_{ab,\vec{j}},\, Z_{ab,\vec{j}},\, \phi_{ab,\vec{j}},\, \Pi_{ab,\vec{j}} \Big\}$$

with equation of motion,

$$\begin{aligned}
\frac{\partial P}{\partial t} =& \Bigg[\sum_b \Bigg\{ - \sum_{\vec{j},\vec{k}} \frac{\partial}{\partial V_{b,\vec{j}}} D_b^{\vec{j}\vec{k}}\, V_{b,\vec{k}} + \sum_{\vec{j}} \frac{\partial}{\partial V_{b,\vec{j}}} \big[g(V_{b,\vec{j}})\,(V_{b,\vec{j}} - E_{\mathrm{Na}}) - I_b^{\mathrm{dc}}/C \\
& + R_{b,\vec{j}}\, g_{R,b}\,(V_{b,\vec{j}} - E_{\mathrm{K}}) - \sum_a \rho_a \Phi_{ab,\vec{j}} \big] + \frac{\Gamma_b}{2\ell^2} \sum_{\vec{j}} \frac{\partial^2}{\partial V_{b,\vec{j}}^2} \Bigg\} \\
& + \sum_b \sum_{\vec{j}} \Bigg\{ \frac{1}{\tau_b} \frac{\partial}{\partial R_{b,\vec{j}}} \big[R_{b,\vec{j}} - R_\infty(V_{b,\vec{j}}) \big] - \sum_{\vec{k}} \frac{\partial}{\partial R_{b,\vec{j}}} D_R^{\vec{j}\vec{k}}\, V_{b,\vec{k}} + \frac{\Gamma_R}{2\ell^2} \frac{\partial^2}{\partial R_{b,\vec{j}}^2} \Bigg\} \\
& + \sum_{a,b} \sum_{\vec{j}} \Bigg\{ - \frac{\partial}{\partial \Phi_{ab,\vec{j}}} Z_{ab,\vec{j}} + \frac{\partial}{\partial Z_{ab,\vec{j}}} \big[(2\gamma_{ab}) Z_{ab,\vec{j}} \\
& + \gamma_{ab}^2\, \Phi_{ab,\vec{j}} - \gamma_{ab}^2 N_{ab}\, \psi_{ab,\vec{j}}\, \phi_{ab,\vec{j}} \big] + \frac{\Gamma_{Z_{ab}}}{2\ell^2} \frac{\partial^2}{\partial Z_{ab,\vec{j}}^2} \Bigg\} \\
& + \sum_{a,b} \sum_{\vec{j}} \Bigg\{ - \frac{\partial}{\partial \phi_{ab,\vec{j}}} \Pi_{ab,\vec{j}} + \frac{\partial}{\partial \Pi_{ab,\vec{j}}} \big[2v\Lambda_{ab}\, \Pi_{ab,\vec{j}} \\
& + (v\Lambda_{ab})^2\, \phi_{ab,\vec{j}} - (v\Lambda_{ab})^2 S_a \cdot (V_{a,\vec{j}} - V_a^{\mathrm{rest}}) \big] \\
& - \sum_{\vec{k}} \frac{\partial}{\partial \Pi_{ab,\vec{j}}} D_{\phi_b}^{\vec{j}\vec{k}}\, \phi_{ab,\vec{k}} + \frac{\Gamma_{\Pi_{ab}}}{2\ell^2} \frac{\partial^2}{\partial \Pi_{ab,\vec{j}}^2} \Bigg\} \Bigg] P
\end{aligned} \tag{3.12}$$

where subscripts of state variables $\{a, b\}$ label neural populations $\{e, i\}$. The discretized Laplacian operator is given by,

$$D_r^{\vec{j}\vec{k}} = \frac{D_r}{\ell^2} \Big\{ \big[\delta_{j_x,k_x+1} + \delta_{j_x,k_x-1} - 2\delta_{j_x,k_x} \big] \delta_{j_y,k_y} + \big[\delta_{j_y,k_y+1} + \delta_{j_y,k_y-1} - 2\delta_{j_y,k_y} \big] \delta_{j_x,k_x} \Big\} \tag{3.13a}$$

and discretized biharmonic operator is given by,

$$D_R^{\vec{j}\vec{k}} = \frac{D_R}{\ell^4 \tau_b} \big[D_{R,x^4}^{\vec{j}\vec{k}} + D_{R,x^2y^2}^{\vec{j}\vec{k}} + D_{R,y^4}^{\vec{j}\vec{k}} \big] \tag{3.13b}$$

where,

$$\begin{aligned}
D_{R,x^4}^{\vec{j}\vec{k}} &= \big[\delta_{j_x,k_x+2} + \delta_{j_x,k_x-2} - 4\big(\delta_{j_x,k_x+1} + \delta_{j_x,k_x-1} \big) + 6\, \delta_{j_x,k_x} \big] \delta_{j_y,k_y} \\
D_{R,x^2y^2}^{\vec{j}\vec{k}} &= 2 \big[\delta_{j_x,k_x+1} + \delta_{j_x,k_x-1} - 2\, \delta_{j_x,k_x} \big] \times \big[\delta_{j_y,k_y+1} + \delta_{j_y,k_y-1} - 2\, \delta_{j_y,k_y} \big] \\
D_{R,y^4}^{\vec{j}\vec{k}} &= \big[\delta_{j_y,k_y+2} + \delta_{j_y,k_y-2} - 4\big(\delta_{j_x,k_y+1} + \delta_{j_y,k_y-1} \big) + 6\, \delta_{j_y,k_y} \big] \delta_{j_x,k_x}
\end{aligned}$$

with recovery subscript R indexing over both the excitatory and inhibitory neural populations, $R \in \{R_e, R_i\}$. The 2D Laplacian and biharmonic stencils are shown in Fig. 3.7.

3.3.3 Coarse-graining Procedure

The coarse-graining in the model is done by eliminating the high wavenumber ($\vec{q}$) modes by utilising a projection operator as set out in Gardiner [27], and Steyn-Ross and Gardiner [71]. Equation (3.12) is Fourier transformed to momentum space by defining the eigenfunctions and eigenvalues of the discretized Laplacian and biharmonic operators. The momentum scales are then separated into two modes: low-frequency (long-wavelength) $\vec{Q}$-modes and high-frequency (small-wavelength) $\vec{q}$-modes,

$$\sum_{\vec{q}} \chi(\vec{q}) \longrightarrow \sum_{\vec{Q}\in\mathscr{R}(N)} \chi(\vec{Q}) + \sum_{\vec{q}\notin\mathscr{R}(N)} \chi(\vec{q}) \tag{3.14}$$

where

$$Q \in \mathscr{R}(N) = \frac{2\pi}{(2n+1)\ell}\,[-N, -N+1, \ldots, N].$$

The blocking procedure regrids the $L_0 \times L_0$ cortical patch into $(2N+1)^2$ macrocells, each of area L^2 where, $L = B\ell$ with $L \approx 1$mm, and B is the blocking ratio defined in Section 3.3.1 (see Fig. 3.8). The $\vec{q}$-space Fokker–Planck equation is given by,

$$\frac{\partial P}{\partial t} = (L_1 + L_2 + L_3)P \tag{3.15}$$

where the three L_j terms are chosen to achieve the elimination procedure:

- L_1 depends on high $\vec{q}$-modes only: defines the projection operator
- L_2 depends on $(\vec{q}, \vec{Q})$

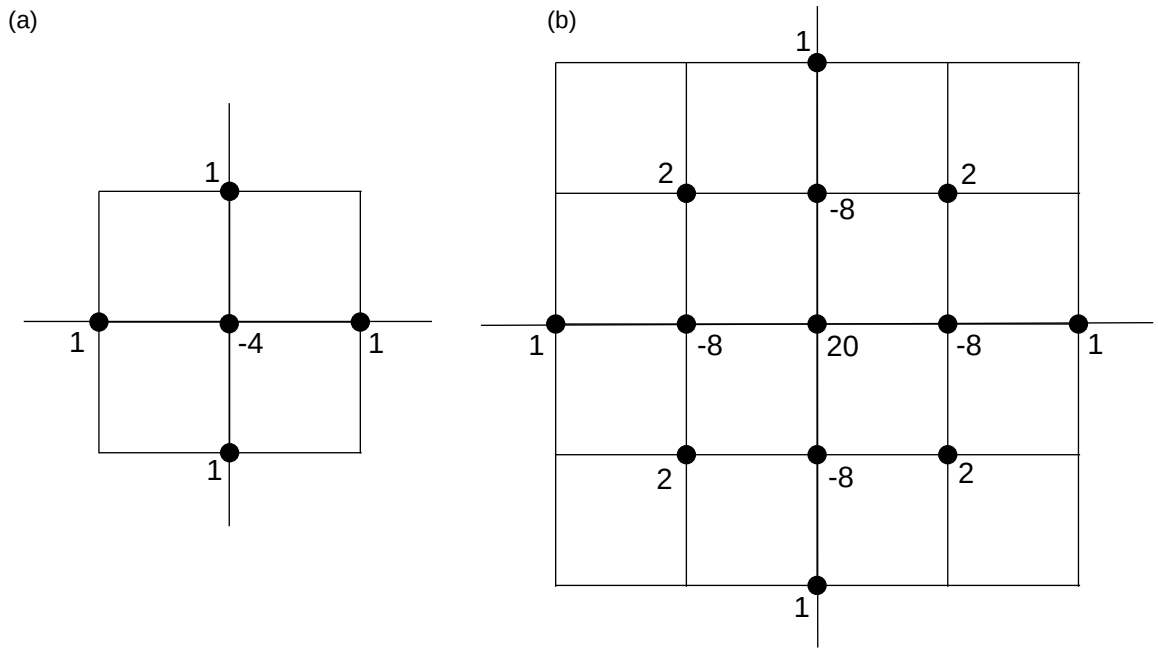

Figure 3.7: 2D (a) Laplacian and (b) biharmonic stencils

- L_3 is expressed as the sum of a mixed-mode operator $\mathscr{L}_3(\vec{q},\vec{Q})$ plus a slow-mode operator $L_3(\vec{Q})$.

The adiabatic elimination of high $\vec{q}$-modes is done by following the projection-operator elimination method described in [27,71]. This results in a loss of spatial resolution which is similar to a coarse-graining in space, defined as the "blocking" in the True-field model. This scale change generates a set of correction terms, so the coarse-grained Fokker–Planck equation reads,

$$\frac{\partial \widehat{P}}{\partial t} = \frac{\partial \widehat{P}}{\partial t}\Big|_{(1)} - \frac{\partial \widehat{P}}{\partial t}\Big|_{(2:\text{Drift})} - \frac{\partial \widehat{P}}{\partial t}\Big|_{(2:\text{Diffusion})} \tag{3.16}$$

where $\widehat{P}$ is the probability distribution function for $\widetilde{\chi}$, the macroscopic state variables and $\frac{\partial \widehat{P}}{\partial t}\big|_{(1)}$ is the spatially rescaled version of Eq. (3.12). The drift and diffusion terms represent corrections. The terms in the RHS of Eq. (3.16) are as follows:

$$\begin{aligned}
\frac{\partial \widehat{P}}{\partial t}\Big|_{(1)} = \Bigg[& \sum_b \Bigg\{ -\sum_{\vec{J},\vec{K}} \frac{\partial}{\partial \widetilde{V}_{b,\vec{J}}} D_b^{\vec{J}\vec{K}}\, \widetilde{V}_{b,\vec{K}} + \sum_{\vec{J}} \frac{\partial}{\partial \widetilde{V}_{b,\vec{J}}} \big[g(\widetilde{V}_{b,\vec{J}})\,(\widetilde{V}_{b,\vec{J}} - E_{\mathrm{Na}}) - I_b^{\mathrm{dc}}/C \\
& + \widetilde{R}_{b,\vec{J}}\, g_{R,b}\,(\widetilde{V}_{b,\vec{J}} - E_{\mathrm{K}}) - \sum_a \rho_a \widetilde{\Phi}_{ab,\vec{J}} \big] + \frac{\Gamma_b}{2(B\ell)^2} \sum_{\vec{J}} \frac{\partial^2}{\partial \widetilde{V}_{b,\vec{J}}^2} \Bigg\} \\
& + \sum_b \sum_{\vec{J}} \Bigg\{ \frac{1}{\tau_b} \frac{\partial}{\partial \widetilde{R}_{b,\vec{J}}} \big[\widetilde{R}_{b,\vec{J}} - R_\infty(\widetilde{V}_{b,\vec{J}}) \big] - \sum_{\vec{K}} \frac{\partial}{\partial \widetilde{R}_{b,\vec{J}}} D_R^{\vec{J}\vec{K}}\, \widetilde{V}_{b,\vec{K}} + \frac{\Gamma_R}{2(B\ell)^2} \frac{\partial^2}{\partial \widetilde{R}_{b,\vec{J}}^2} \Bigg\} \\
& + \sum_{a,b} \sum_{\vec{J}} \Bigg\{ -\frac{\partial}{\partial \widetilde{\Phi}_{ab,\vec{J}}} \widetilde{Z}_{ab,\vec{J}} + \frac{\partial}{\partial \widetilde{Z}_{ab,\vec{J}}} \big[(2\gamma_{ab}) \widetilde{Z}_{ab,\vec{J}} \\
& + \gamma_{ab}^2\, \widetilde{\Phi}_{ab,\vec{J}} - \gamma_{ab}^2 N_{ab}\, \widetilde{\psi}_{ab,\vec{J}}\, \widetilde{\phi}_{ab,\vec{J}} \big] + \frac{\Gamma_{Z_{ab}}}{2(B\ell)^2} \frac{\partial^2}{\partial \widetilde{Z}_{ab,\vec{J}}^2} \Bigg\}
\end{aligned}$$

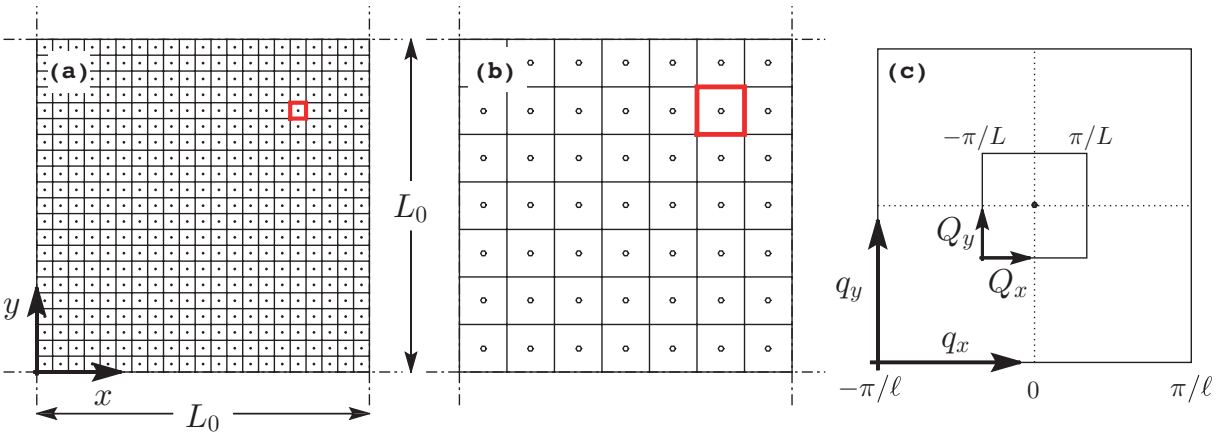

Figure 3.8: Mapping of a cortical patch to a coarser spatial scale. (a) A 2D patch of cortical tissue is divided into $(2n+1)^2$ identical square microcells, each of side-length ℓ such that $L_0 = (2n+1)\ell$. (b) The microcell lattice is mapped into a $(2N+1)^2$ macrocells, each of side-length $L = B\ell$ so that $L_0 = (2N+1)L$, with $B = (2n+1)/(2N+1) \gg 1$. (c) In Fourier space, these griddings correspond to wavenumber domains $|q_x|$, $|q_y| \leq \pi/\ell$ for micro-grid, and $|Q_x|$, $|Q_y| \leq \pi/L$ for the macro-grid. For descriptive purposes, B is set to 3. Source: Steyn-Ross and Steyn-Ross (2016) [72].

$$
\begin{aligned}
&+\sum_{a,b}\sum_{\vec{J}}\Bigg\{-\frac{\partial}{\partial\widetilde{\phi}_{ab,\vec{J}}}\,\widetilde{\Pi}_{ab,\vec{J}}+\frac{\partial}{\partial\widetilde{\Pi}_{ab,\vec{J}}}\big[2v\Lambda_{ab}\,\widetilde{\Pi}_{ab,\vec{J}}\\
&+(v\Lambda_{ab})^2\,\widetilde{\phi}_{ab,\vec{J}}-(v\Lambda_{ab})^2 S_a\cdot(\widetilde{V}_{a,\vec{J}}-V_a^{\rm rest})\big]\\
&-\sum_{\vec{K}}\frac{\partial}{\partial\widetilde{\Pi}_{ab,\vec{J}}}\,D_{\phi_b}^{\vec{J}\vec{K}}\,\widetilde{\phi}_{ab,\vec{K}}+\frac{\Gamma_{\Pi_{ab}}}{2(B\ell)^2}\,\frac{\partial^2}{\partial\widetilde{\Pi}^2_{ab,\vec{J}}}\Bigg\}\Bigg]\,\widehat{P}
\end{aligned}
\tag{3.17}
$$

where the tilde-variables represent the spatially rescaled system variables of Eq. (3.12), i.e.,

$$[V,R,Z,\Phi,\Pi,\phi]\;\longrightarrow\;[\widetilde{V},\widetilde{R},\widetilde{Z},\widetilde{\Phi},\widetilde{\Pi},\widetilde{\phi}]$$

When comparing Eqs (3.12) and (3.17), it is notable that the coarse-graining (blocking) has led to a reduction in the constant-intensity noise contributions,

$$\Gamma_{[b,R,Z,\Pi]}/\ell^2\;\longrightarrow\;\Gamma_{[b,R,Z,\Pi]}/(B\ell)^2.$$

The nonlinear drift corrections in Eq. (3.16) are given by,

$$
\begin{aligned}
\left.\frac{\partial\widehat{P}}{\partial t}\right|_{\text{(2:Drift)}}&=\sum_{b,\vec{J}}\Bigg\{\frac{\partial}{\partial\widetilde{V}_{b,\vec{J}}}\Big[d_0+d_1\widetilde{V}_{b,\vec{J}}+d_2\widetilde{V}^2_{b,\vec{J}}+d_3\widetilde{V}^3_{b,\vec{J}}\\
&\quad+d_4\widetilde{V}^4_{b,\vec{J}}+d_5\widetilde{V}_{b,\vec{J}}\widetilde{R}_{b,\vec{J}}+d_6\widetilde{V}^2_{b,\vec{J}}\widetilde{R}_{b,\vec{J}}+d_7\widetilde{R}_{b,\vec{J}}\Big]\\
&\quad+\frac{\partial}{\partial\widetilde{R}_{b,\vec{J}}}\Big[d_8+d_9\widetilde{R}_{b,\vec{J}}+d_{10}\widetilde{V}_{b,\vec{J}}+d_{11}\widetilde{V}^2_{b,\vec{J}}+d_{12}\widetilde{V}^3_{b,\vec{J}}\Big]\Bigg\}\widehat{P}\\
&\equiv\sum_{b,\vec{J}}\left\{\frac{\partial}{\partial\widetilde{V}_{b,\vec{J}}}\,G_1\;+\;\frac{\partial}{\partial\widetilde{R}_{b,\vec{J}}}\,G_2\right\}\widehat{P}
\end{aligned}
\tag{3.18}
$$

The nonlinear diffusion corrections in (3.16) are defined by,

$$
\begin{aligned}
\left.\frac{\partial\widehat{P}}{\partial t}\right|_{\text{(2:Diffusion)}}&=\sum_{b,\vec{J}}\Bigg\{\frac{\partial^2}{\partial\widetilde{V}^2_{b,\vec{J}}}\Big[g_0+g_1\widetilde{V}_{b,\vec{J}}+g_2\widetilde{V}^2_{b,\vec{J}}+g_3\widetilde{V}^3_{b,\vec{J}}+g_4\widetilde{V}_{b,\vec{J}}\widetilde{R}_{b,\vec{J}}\Big]\\
&\quad+\frac{\partial^2}{\partial\widetilde{R}^2_{b,\vec{J}}}g_5+\frac{\partial^2}{\partial\widetilde{V}_{b,\vec{J}}\partial\widetilde{R}_{b,\vec{J}}}\Big[g_6+g_7\,\widetilde{V}_{b,\vec{J}}\Big]\Bigg\}\widehat{P}\\
&\equiv\sum_{b,\vec{J}}\left\{\frac{\partial^2}{\partial\widetilde{V}^2_{b,\vec{J}}}\,G_3\;+\;\frac{\partial^2}{\partial\widetilde{R}^2_{b,\vec{J}}}\,g_5\;+\;\frac{\partial^2}{\partial\widetilde{V}_{b,\vec{J}}\partial\widetilde{R}_{b,\vec{J}}}\,G_4\right\}\widehat{P}
\end{aligned}
\tag{3.19}
$$

All drift and diffusion coefficients are listed in next section and calculated in the next chapter. These correction coefficients depend on one or more of the following:

- voltage and recovery noise, Γ_b, Γ_R
- voltage and recovery diffusivities, D_b, D_R
- side-length blocking ratio, B
- side-length of microcell, ℓ

Therefore, one parameter change requires recalculation of all corrections (see Fig. 3.9).

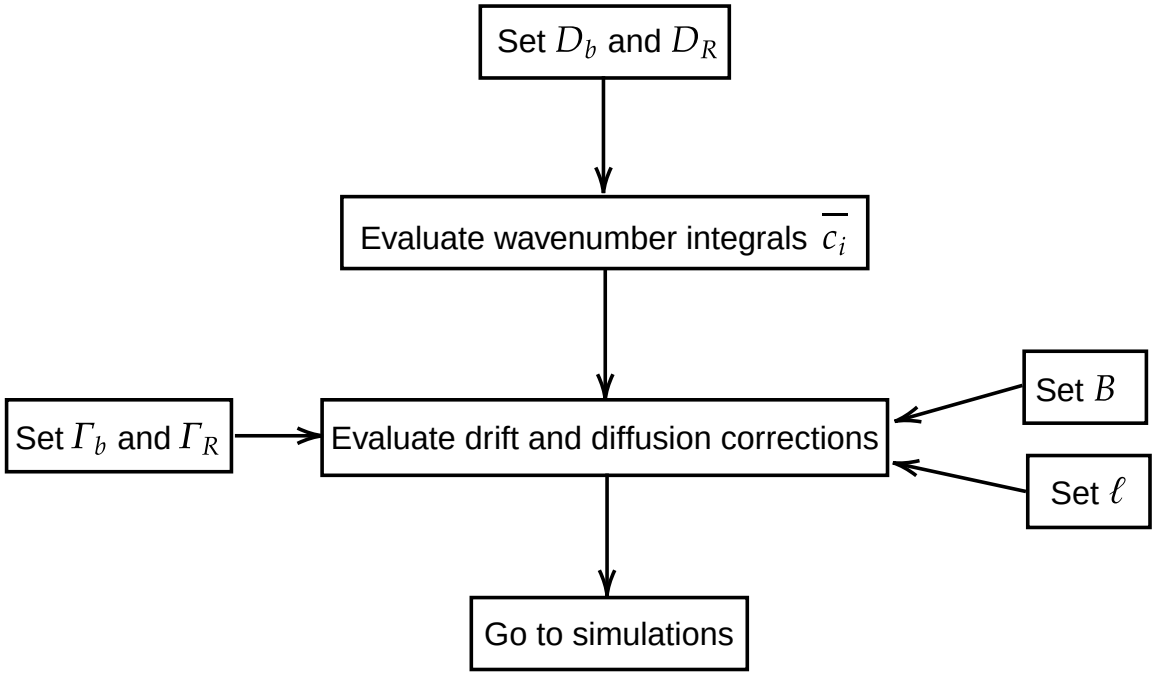

Figure 3.9: Flowchart showing the parameter dependence on corrections

3.3.4 Drift and Diffusion Coefficients

The drift and diffusion coefficients in Eqs (3.18) and (3.19) (along with their SI units) are listed below. We have detected some typographical errors (noted in red) in the [72] paper relating to two of the drift coefficients (d_2, d_4) and three of the diffusion coefficients (g_0, g_3, g_4). Note that all the drift corrections other than d_3, d_4, d_6, and d_{12} are noise dependent.

Drift coefficients:

$$d_0 = \frac{\Gamma_b}{2(2\pi)^2}\Bigg[- a_{3,b}\,\overline{c}_0 + a_{1,b}\,a_{3,b}\,\overline{c}_1 E_{\mathrm{Na}} - a_{2,b}\,a_{3,b}\,\Gamma_b\left(\frac{\overline{c}_2}{[(2n+1)\ell]^2} + \frac{\overline{c}_3}{2(2\pi)^2}\right) + \frac{a_{2,b}\,\Gamma_b}{2(2\pi)^2}\left(-\sqrt{\frac{g_{R,b}}{|E_{\mathrm{K}}|}}\;\overline{c}_{6a} + \frac{b_{2,b}\,\overline{c}_{6b}\sqrt{g_{R,b}|E_{\mathrm{K}}|}}{\tau_b}\right) - \frac{a_{3,b}\,\overline{c}_7}{\tau_b} + \frac{a_{3,b}\,\overline{c}_8\,g_{R,b}\,|E_{\mathrm{K}}|\,\Gamma_R}{\Gamma_b} - \sqrt{\frac{g_{R,b}}{|E_{\mathrm{K}}|}}\;\frac{\overline{c}_9}{\tau_b} + \frac{\sqrt{g_{R,b}^3\,|E_{\mathrm{K}}|}\,\overline{c}_{10}\,\Gamma_R}{\Gamma_b} - \frac{3\,a_{2,b}\,a_{3,b}\,\overline{c}_{11}\,\Gamma_b}{2(B\ell)^2}\Bigg] \quad \left[\tfrac{\mathrm{V}}{\mathrm{s}}\right]$$

$$d_1 = \frac{\Gamma_b}{2(2\pi)^2}\Bigg[- 3a_{2,b}\,\overline{c}_0 - (2a_{3,b}^2 - 3a_{1,b}\,a_{2,b}\,E_{\mathrm{Na}})\,\overline{c}_1 - 3\,a_{2,b}^2\,\Gamma_b\left(\frac{\overline{c}_2}{[(2n+1)\ell]^2} + \frac{\overline{c}_3}{2(2\pi)^2}\right) - \frac{3\,a_{2,b}\,\overline{c}_7}{\tau_b} + \frac{3\,a_{2,b}\,\overline{c}_8\,g_{R,b}\,|E_{\mathrm{K}}|\,\Gamma_R}{\Gamma_b} - \frac{9\,a_{2,b}^2\,\overline{c}_{11}\,\Gamma_b}{2(B\ell)^2}\Bigg] + \frac{S_1^2\,\Gamma_b}{2(B\ell)^2\,|E_{\mathrm{K}}|^2} \quad \left[\mathrm{s}^{-1}\right]$$

$$d_2 = \frac{3\,a_{2,b}\,\Gamma_b}{2(2\pi)^2}\left[- 3\,a_{3,b}\,\overline{c}_1 - \frac{\overline{c}_{16}\,S_1\,(B\ell)^4}{(2\pi)^4\,|E_{\mathrm{K}}|}\right] \quad \left[\tfrac{1}{\mathrm{Vs}}\right]$$

$$d_3 = \frac{a_{3,b}\,S_1^2}{|E_{\mathrm{K}}|} - \frac{9\,a_{2,b}^2\,\overline{c}_1\,\Gamma_b}{2(2\pi)^2} + \left[2\,a_{3,b}\,\overline{c}_4 - \frac{\overline{c}_5}{|E_{\mathrm{K}}|}\right]\frac{b_{2,b}\,S_1\,(B\ell)^4}{(2\pi)^4\,\tau_b} \quad \left[\tfrac{1}{\mathrm{V^2s}}\right]$$

$$d_4 = a_{2,b}\,S_1\left[\frac{S_2}{|E_{\mathrm{K}}|} + \frac{3\,b_{2,b}\,\overline{c}_4\,(B\ell)^4}{(2\pi)^4\,\tau_b}\right] \quad \left[\tfrac{1}{\mathrm{V^3s}}\right]$$

$$d_5 = \frac{-3\, a_{2,b}\, \bar{c}_1\, g_{R,b}\, \Gamma_b}{2(2\pi)^2} \qquad [\mathrm{s}^{-1}]$$

$$d_6 = g_{R,b}\, S_1 \left[\frac{S_1}{|E_\mathrm{K}|} + \frac{b_{2,b}\, \bar{c}_4\, (B\ell)^4}{(2\pi)^4\, \tau_b} \right] \qquad \left[\frac{1}{\mathrm{Vs}}\right]$$

$$d_7 = \frac{g_{R,b}\, \Gamma_b}{2(2\pi)^2} \left[-a_{3,b}\, \bar{c}_1 + \frac{\bar{c}_{15}\, S_1\, (B\ell)^2}{(2\pi)^2 |E_\mathrm{K}|} \right] \qquad \left[\frac{\mathrm{V}}{\mathrm{s}}\right]$$

$$d_8 = \frac{b_{2,b}\, \Gamma_b}{2(2\pi)^2\, \tau_b} \left[\bar{c}_0 - a_{1,b}\, \bar{c}_1\, E_\mathrm{Na} + \frac{a_{2,b}\, \bar{c}_2\, \Gamma_b}{[(2n+1)\ell]^2} + \frac{\bar{c}_7}{\tau_b} - \frac{\bar{c}_8\, g_{R,b}\, |E_\mathrm{K}|\, \Gamma_R}{\Gamma_b} \right] \qquad [\mathrm{s}^{-1}]$$

$$d_9 = \frac{b_{2,b}\, \bar{c}_1\, g_{R,b}\, \Gamma_b}{2(2\pi)^2\, \tau_b} \qquad [\mathrm{s}^{-1}]$$

$$d_{10} = \frac{b_{2,b}\, \Gamma_b}{(2\pi)^2\, \tau_b} \left[a_{3,b}\, \bar{c}_1 + \frac{\bar{c}_{15}\, S_1 (B\ell)^2}{(2\pi)^2\, |E_\mathrm{K}|} \right] \qquad \left[\frac{1}{\mathrm{Vs}}\right]$$

$$d_{11} = \frac{3\, a_{2,b}\, b_{2,b}\, \bar{c}_1\, \Gamma_b}{2(2\pi)^2\, \tau_b} \qquad \left[\frac{1}{\mathrm{V}^2\mathrm{s}}\right]$$

$$d_{12} = \frac{-2\, b_{2,b}^2\, \bar{c}_4\, S_1 (B\ell)^4}{(2\pi)^4\, \tau_b^2} \qquad \left[\frac{1}{\mathrm{V}^3\mathrm{s}}\right]$$

Diffusion coefficients:

$$g_0 = \frac{\Gamma_b^2}{4(2\pi)^2 (B\ell)^2} \left[a_{3,b}^2\, \bar{c}_{11} + \frac{a_{2,b}^2\, \bar{c}_{12}\, \Gamma_b}{2(2\pi)^2} \right] \qquad [\mathrm{V}^2\mathrm{s}^{-1}]$$

$$g_1 = \frac{3\, a_{2,b}\, a_{3,b}\, \bar{c}_{11} \Gamma_b^2}{4(2\pi)^2 (B\ell)^2} \qquad [\mathrm{Vs}^{-1}]$$

$$g_2 = \frac{\Gamma_b}{2(B\ell)^2} \left[\frac{9\, a_{2,b}^2\, \bar{c}_{11} \Gamma_b}{2(2\pi)^2} - \frac{S_1^2}{|E_\mathrm{K}|^2} \right] \qquad [\mathrm{s}^{-1}]$$

$$g_3 = 0 \qquad [\mathrm{V}^{-1}\mathrm{s}^{-1}]$$

$$g_4 = 0 \qquad [\mathrm{Vs}^{-1}]$$

$$g_5 = \frac{b_{2,b}^2\, \bar{c}_{11}\, \Gamma_b^2}{4(2\pi)^2\, (B\ell)^2\, \tau_b^2} \qquad [\mathrm{s}^{-1}]$$

$$g_6 = \frac{-\, a_{3,b}\, b_{2,b}\, \bar{c}_{11}\, \Gamma_b^2}{2(2\pi)^2\, (B\ell)^2\, \tau_b} \qquad [\mathrm{Vs}^{-1}]$$

$$g_7 = \frac{-\, 3\, a_{2,b}\, b_{2,b}\, \bar{c}_{11}\, \Gamma_b^2}{2(2\pi)^2\, (B\ell)^2\, \tau_b}. \qquad [\mathrm{s}^{-1}]$$

These drift and diffusion coefficients rely on 14 associated wavenumber integrals $\bar{c}_j$ listed in the next section. The other constants are listed in Table 3.2 (Note that there is no ambiguity between the a_js and b_js in table and $a_{j,b}$s and $b_{j,b}$s in drift and diffusion coefficients.)

3.3.5 Wavenumber Integrals

The $\overline{c}_j$ wavenumber integrals defined in the d_j drift and g_j diffusion coefficients (along with their SI units) are listed below [72].

$$\overline{c}_0 = \int \frac{d\vec{q}}{\Lambda_b(\vec{q})} \qquad [\mathrm{m}^{-2}\mathrm{s}]$$

$$\overline{c}_1 = -\int \frac{d\vec{q}}{2[\Lambda_b(\vec{q})]^2} \qquad [\mathrm{m}^{-2}\mathrm{s}^2]$$

$$\overline{c}_2 = -\int \frac{d\vec{q}}{2[\Lambda_b(\vec{q})]^3} \qquad [\mathrm{m}^{-2}\mathrm{s}^3]$$

$$\overline{c}_3 = \iint \frac{g(\vec{q}_1,\vec{q}_2)\, d\vec{q}_1 d\vec{q}_2}{\Lambda_b(\vec{q}_1)\,\Lambda_b(\vec{q}_2)} \ \boxed{\mathrm{R0}} \qquad [\mathrm{m}^{-4}\mathrm{s}^3]$$

$$\overline{c}_4 = \iint \frac{d\vec{Q}_1 d\vec{Q}_2}{\Lambda_R(\vec{Q}_1+\vec{Q}_2)} \ \boxed{\mathrm{R1}} \qquad [\mathrm{m}^{-4}\mathrm{Vs}]$$

$$\overline{c}_5 = \iint \frac{\Lambda_b(\vec{Q}_1+\vec{Q}_2)\, d\vec{Q}_1 d\vec{Q}_2}{\Lambda_R(\vec{Q}_1+\vec{Q}_2)} \ \boxed{\mathrm{R1}} \qquad [\mathrm{m}^{-4}\mathrm{V}]$$

$$\overline{c}_{6a} = \iint \frac{h(\vec{q}_1,\vec{q}_2)\sqrt{\Lambda_R(\vec{q}_1+\vec{q}_2)}\, d\vec{q}_1 d\vec{q}_2}{\Lambda_b(\vec{q}_1)\,\Lambda_b(\vec{q}_1+\vec{q}_2)} \ \boxed{\mathrm{R0}} \qquad \left[\frac{\mathrm{s}^{5/2}}{\mathrm{m}^4\mathrm{V}^{1/2}}\right]$$

$$\overline{c}_{6b} = \iint \frac{h(\vec{q}_1,\vec{q}_2)\, d\vec{q}_1 d\vec{q}_2}{\Lambda_b(\vec{q}_1)\,\Lambda_b(\vec{q}_2)\sqrt{\Lambda_R(\vec{q}_1+\vec{q}_2)}} \ \boxed{\mathrm{R0}} \qquad \left[\frac{\mathrm{V}^{1/2}\mathrm{s}^{7/2}}{\mathrm{m}^4}\right]$$

$$\overline{c}_7 = \overline{c}_1 \qquad [\mathrm{m}^{-2}\mathrm{s}^2]$$

$$\overline{c}_8 = -\int \frac{d\vec{q}}{2\Lambda_b(\vec{q})\,\Lambda_R(\vec{q})} \qquad [\mathrm{m}^{-2}\mathrm{Vs}^2]$$

$$\overline{c}_9 = \frac{\overline{c}_0}{\sqrt{g_{0,R}}} \qquad [\mathrm{m}^{-2}\mathrm{V}^{-1/2}\mathrm{s}^{3/2}]$$

$$\overline{c}_{10} = \frac{1}{\sqrt{g_{0,R}}}\int \frac{d\vec{q}}{\Lambda_R(\vec{q})} \qquad [\mathrm{m}^{-2}\mathrm{V}^{1/2}\mathrm{s}^{3/2}]$$

$$\overline{c}_{11} = \overline{c}_2 \qquad [\mathrm{m}^{-2}\mathrm{s}^3]$$

$$\overline{c}_{12} = \iint \frac{g(\vec{q}_1,\vec{q}_2)\, d\vec{q}_1 d\vec{q}_2}{\Lambda_b(\vec{q}_1)\,\Lambda_b(\vec{q}_2)\,\Lambda_b(\vec{q}_1+\vec{q}_2)} \ \boxed{\mathrm{R0}} \qquad [\mathrm{m}^{-4}\mathrm{s}^4]$$

$$\overline{c}_{15} = \iint \frac{d\vec{Q}_1 d\vec{Q}_2}{\Lambda_b(\vec{Q}_1+\vec{Q}_2)} \ \boxed{\mathrm{R1}} \qquad [\mathrm{m}^{-4}\mathrm{s}]$$

$$\overline{c}_{16} = \iiint \frac{d\vec{Q}_1 d\vec{Q}_2 d\vec{Q}_3}{\Lambda_b(\vec{Q}_1+\vec{Q}_2+\vec{Q}_3)} \ \boxed{\mathrm{R2}} \qquad [\mathrm{m}^{-6}\mathrm{s}]$$

where the wavenumber restrictions are stipulated as,

$$\begin{aligned} &\mathrm{R0}: \quad \vec{q}_1+\vec{q}_2=\vec{q} && (\overline{c}_3, \overline{c}_{6a}, \overline{c}_{6b}, \overline{c}_{12}) \\ &\mathrm{R1}: \quad \vec{Q}_1+\vec{Q}_2=\vec{q} && (\overline{c}_4, \overline{c}_5, \overline{c}_{15}) \end{aligned}$$

$$\text{R2:} \quad \vec{Q}_1 + \vec{Q}_2 + \vec{Q}_3 = \vec{q} \qquad (\bar{c}_{16})$$

and the required Λ_b and Λ_R definitions are,

$$\Lambda_b(\vec{q}) = \lambda_b(\vec{q}) + a_0, \quad \Lambda_R(\vec{q}) = \lambda_R(\vec{q}) + b_1/\tau_b \tag{3.20}$$

with eigenvalues $\lambda_b(\vec{q})$, $\lambda_R(\vec{q})$ defined as,

$$\lambda_b(\vec{q}) \;=\; \frac{4D_b}{\ell^2}\big[\sin^2(q_x\ell/2) + \sin^2(q_y\ell/2)\big] \tag{3.21a}$$

$$\lambda_R(\vec{q}) \;=\; \frac{16D_R}{\ell^4\,\tau_b}\big[\sin^2(q_x\ell/2) + \sin^2(q_y\ell/2)\big]^2 \tag{3.21b}$$

The two-argument functions $g(\cdot)$ (appearing in the $\bar{c}_3$ and $\bar{c}_{12}$ integrals) and $h(\cdot)$ (in $\bar{c}_{6a}$ and $\bar{c}_{6b}$) are defined as follows,

$$\begin{aligned} g(\vec{q}_1, \vec{q}_2, \vec{q}_3) =& \Delta_1^2 \times \bigg\{ - \frac{L_{11}L_{12}L_{13}}{L_{11}+L_{12}+L_{13}} + \frac{L_{11}L_{12}L_{23}}{L_{11}+L_{12}+L_{23}} + \frac{L_{11}L_{22}L_{13}}{L_{11}+L_{22}+L_{13}} - \frac{L_{11}L_{22}L_{23}}{L_{11}+L_{22}+L_{23}} \\ &+ \frac{L_{21}L_{12}L_{13}}{L_{21}+L_{12}+L_{13}} - \frac{L_{21}L_{12}L_{23}}{L_{21}+L_{12}+L_{23}} - \frac{L_{21}L_{22}L_{13}}{L_{21}+L_{22}+L_{13}} + \frac{L_{21}L_{22}L_{23}}{L_{21}+L_{22}+L_{23}} \bigg\} \end{aligned}$$

and

$$\begin{aligned} h(\vec{q}_1, \vec{q}_2, \vec{q}_3) = \Delta_1^2 \sqrt{L_{11}L_{21}} \times \\ \bigg\{ &- \frac{L_{12}L_{13}}{L_{11}+L_{12}+L_{13}} + \frac{L_{12}L_{23}}{L_{11}+L_{12}+L_{23}} \\ &+ \frac{L_{22}L_{13}}{L_{11}+L_{22}+L_{13}} - \frac{L_{22}L_{23}}{L_{11}+L_{22}+L_{23}} \\ &+ \frac{L_{12}L_{13}}{L_{21}+L_{12}+L_{13}} - \frac{L_{12}L_{23}}{L_{21}+L_{12}+L_{23}} \\ &- \frac{L_{22}L_{13}}{L_{21}+L_{22}+L_{13}} + \frac{L_{22}L_{23}}{L_{21}+L_{22}+L_{23}} \bigg\} \end{aligned}$$

where the L_{mn} represent

$$L_{mn} = \lambda_m(\vec{q}_n)$$

with $\lambda_m \in \{\lambda_1, \lambda_2\}$ and $\vec{q}_n \in \{\vec{q}_1, \vec{q}_2, \vec{q}_3\}$, and where

$$\Delta_1^2 = \frac{1}{\delta(\vec{q}_1)\,\delta(\vec{q}_2)\,\delta(\vec{q}_3)}$$

$\lambda_m(\vec{q})$ and $\delta(\vec{q})$ are defined as,

$$\lambda_{\substack{1\\2}}(\vec{q}) = \big(\Lambda_b(\vec{q}) \pm \delta(\vec{q})\big)/2 \tag{3.22a}$$

$$\delta(\vec{q}) = \big(\Lambda_b^2(\vec{q}) - 4\omega_0^2(\vec{q})\big)^{\frac{1}{2}} \tag{3.22b}$$

$$\omega_0^2(\vec{q}) = g_{0,R}\,\Lambda_R(\vec{q}) \tag{3.22c}$$

$$g_{0,R} = g_{R,b}\,|E_{\mathrm{K}}| \tag{3.22d}$$

3.3.6 Rescaled Model Equations

The coarse-grained stochastic DEs are then extracted from Eq. (3.17). The spatially rescaled system variables are defined by the 20-element column vector below:

$$\widetilde{\vec{\chi}} = [\widetilde{V}_e, \widetilde{V}_i, \widetilde{R}_e, \widetilde{R}_i, \widetilde{\Phi}_{ee}, \widetilde{Z}_{ee}, \widetilde{\Phi}_{ei}, \widetilde{Z}_{ei}, \widetilde{\Phi}_{ie}, \widetilde{Z}_{ie}, \widetilde{\Phi}_{ii}, \widetilde{Z}_{ii}, \widetilde{\phi}_{ee}, \widetilde{\Pi}_{ee}, \widetilde{\phi}_{ei}, \widetilde{\Pi}_{ei}, \widetilde{\phi}_{ie}, \widetilde{\Pi}_{ie}, \widetilde{\phi}_{ii}, \widetilde{\Pi}_{ii}]^{\mathrm{T}}$$

The reblocked stochastic DEs are written as,

$$\frac{\partial \widetilde{\chi}_1}{\partial t} \equiv \frac{\partial \widetilde{V}_e}{\partial t} = \widetilde{\mathrm{RHS}}(3.10\mathrm{a})_e + G_{1,e} + \sum_{k=1}^{20} C_{1k}\,\xi_k \tag{3.23a}$$

$$\frac{\partial \widetilde{\chi}_2}{\partial t} \equiv \frac{\partial \widetilde{V}_i}{\partial t} = \widetilde{\mathrm{RHS}}(3.10\mathrm{a})_i + G_{1,i} + \sum_{k} C_{2k}\,\xi_k \tag{3.23b}$$

$$\frac{\partial \widetilde{\chi}_3}{\partial t} \equiv \frac{\partial \widetilde{R}_e}{\partial t} = \widetilde{\mathrm{RHS}}(3.10\mathrm{b})_e + G_{2,e} + \sum_{k} C_{3k}\,\xi_k \tag{3.23c}$$

$$\frac{\partial \widetilde{\chi}_4}{\partial t} \equiv \frac{\partial \widetilde{R}_i}{\partial t} = \widetilde{\mathrm{RHS}}(3.10\mathrm{b})_i + G_{2,i} + \sum_{k} C_{4k}\,\xi_k \tag{3.23d}$$

$$\frac{\partial}{\partial t}\widetilde{\chi}_j \equiv \frac{d\widetilde{\Phi}_{ab}}{dt} = \widetilde{Z}_{ab}, \tag{3.23e}$$

$$\begin{aligned}\frac{\partial}{\partial t}\widetilde{\chi}_{j+1} &\equiv \frac{d\widetilde{Z}_{ab}}{dt} \\ &= -(2\gamma_{ab})\widetilde{Z}_{ab} - \gamma_{ab}^2\widetilde{\Phi}_{ab} + \gamma_{ab}^2 N_{ab}\psi_{ab}(\overline{\widetilde{V}}_b)\,\widetilde{\phi}_{ab} + \sum_k C_{j+1,k}\,\xi_k\end{aligned} \tag{3.23f}$$

$$\frac{\partial}{\partial t}\widetilde{\chi}_{j+8} \equiv \frac{d\widetilde{\phi}_{ab}}{dt} = \widetilde{\Pi}_{ab} \tag{3.23g}$$

$$\begin{aligned}\frac{\partial}{\partial t}\widetilde{\chi}_{j+9} &\equiv \frac{\partial\widetilde{\Pi}_{ab}}{\partial t} \\ &= -2v\Lambda_{ab}\widetilde{\Pi}_{ab} - \left[(v\Lambda_{ab})^2 - (v\nabla)^2\right]\widetilde{\phi}_{ab} + (v\Lambda_{ab})^2 S_a(\widetilde{V}_a - V_a^{\mathrm{rest}}) + \sum_k C_{j+9,k}\,\xi_k\end{aligned} \tag{3.23h}$$

$$\frac{d\overline{V}_b(t)}{dt} = -\frac{1}{T}\left[\overline{V}_b(t) - V_b(t)\right] \tag{3.23i}$$

where label ab cycles through $\{ee, ei, ie, ii\}$ as index j steps through $\{5, 7, 9, 11\}$ in Eqs (3.23e)–(3.23h). C_{jk} denotes the $(j,k)^{\mathrm{th}}$ element of a 20×20 noise-amplitude matrix $\mathbf{C}$ obeying $\mathbf{C}\mathbf{C}^{\mathrm{T}} = \mathbf{B}$ where $\mathbf{B}$ is the noise intensity matrix. The ξ_k (with $k =$ 1:4, 6:2:20) are 12 independent white-noise sources that are delta-correlated in time and 2D space.

The nonzero elements of $\mathbf{B}$ are listed as follows.

$$\begin{aligned} B_{11} &= -2(B\ell)^2 G_{3,e} + \Gamma_e, & B_{22} &= -2(B\ell)^2 G_{3,i} + \Gamma_i \\ B_{33} &= -2(B\ell)^2 g_{5,e} + \Gamma_{R_e}, & B_{44} &= -2(B\ell)^2 g_{5,i} + \Gamma_{R_i} \\ B_{13} &= B_{31} = -(B\ell)^2 G_{4,e}\,, & B_{24} &= B_{42} = -(B\ell)^2 G_{4,i} \\ B_{66} &= \Gamma_{Z_{ee}}, & B_{88} &= \Gamma_{Z_{ei}} \end{aligned}$$

$$B_{10,10} = \Gamma_{Z_{ie}}, \qquad B_{12,12} = \Gamma_{Z_{ii}}$$
$$B_{14,14} = \Gamma_{\Pi_{ee}}, \qquad B_{16,16} = \Gamma_{\Pi_{ei}}$$
$$B_{18,18} = \Gamma_{\Pi_{ie}}, \qquad B_{20,20} = \Gamma_{\Pi_{ii}}$$

where B is the blocking ratio, ℓ and L are the lengths of a microcell and a macrocell respectively.

3.4 Chapter Summary

In this chapter, I discussed the practical limitations of the single-unit based neural networks. Several important mean-field approaches are reviewed and the common drawback of neglecting the characteristics of single neurons is discussed. As a better a proposition, I surveyed True-field model of the Waikato Cortical Modelling group that systematically rescales networks of spiking neurons from microscopic level to coarser spatial scales. I presented the model equations and discussed how spatial rescaling is achieved via reblocking corrections.

These corrections will be evaluated and studied in the next chapter by carefully setting values for the diffusivities (D_b, D_R), noise (Γ_b, Γ_R), blocking ratio (B), and side-length of microcell (ℓ).

Chapter 4

Analysis of Blocking Corrections

As shown in the previous chapter, the adiabatic elimination employed in the True-field model results in model equations defined at a larger spatial scale, with equivalent differential equations and blocking corrections: 13 drift corrections d_i, eight diffusion corrections g_i. The strength of these corrections depends on voltage and recovery noises (Γ_b and Γ_R), voltage and recovery diffusivities (D_b and D_R), side-length blocking ratio (B), and side-length of microcell (ℓ) as shown in Fig. 3.9. For my initial calculations I choose fixed values for blocking ratio ($B=100$) and side-length of microcell ($\ell=10\,\mu$m), then later I investigate the effect of blocking on corrections. I begin this chapter by explaining how I set the voltage and recovery diffusivities, D_b and D_R. The drift and diffusion corrections depend on the wavenumber integrals $\bar{c}_j$, which in turn depend

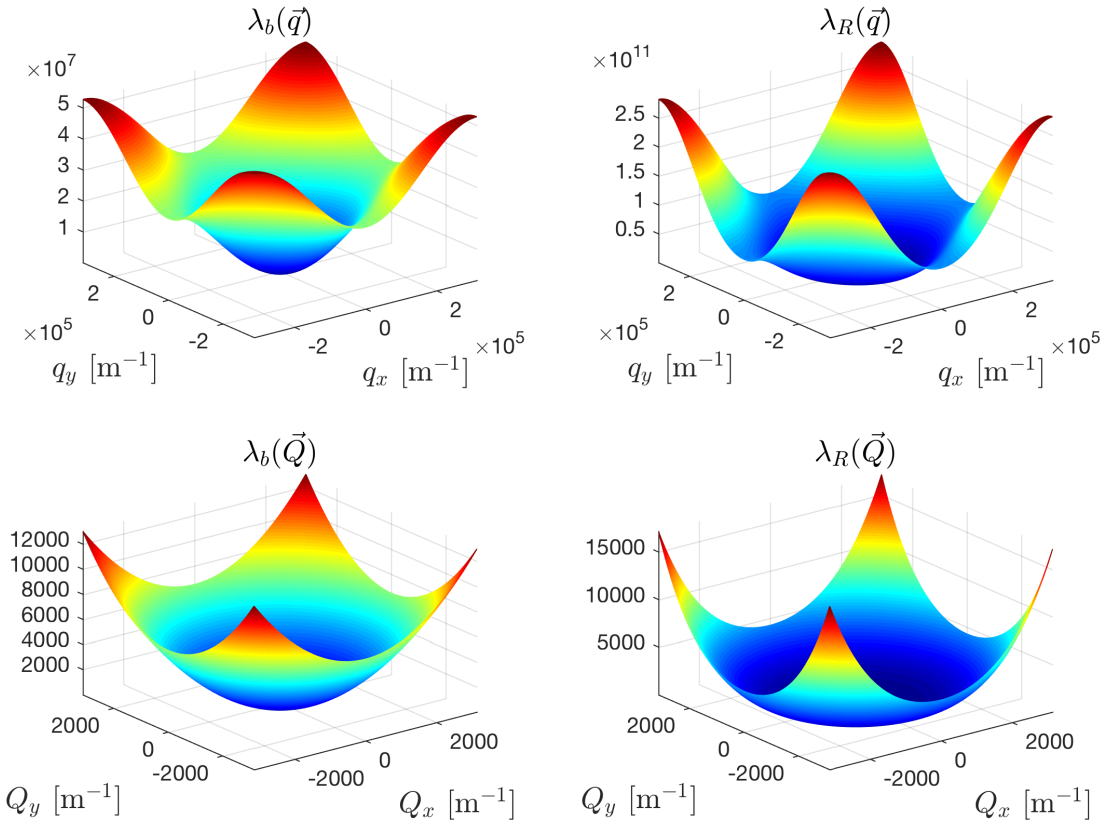

Figure 4.1: Graphical representation of eigenvalues evaluated with high-frequency $\vec{q}$-modes (top panels) and low-frequency $\vec{Q}$-modes (bottom panels). Here, $D_b = 6.6 \times 10^{-4}$ m^2/s, $D_R = 2.47 \times 10^{-13}$ m^4/V, $\tau = 5.6$ ms, $\ell = 10\,\mu$m, and $B = 100$.

on the Λ_b and Λ_R definitions presented previously in Eq. (3.20),

$$\Lambda_b(\vec{q}) = \lambda_b(\vec{q}) + a_0, \quad \Lambda_R(\vec{q}) = \lambda_R(\vec{q}) + b_1/\tau_b \tag{4.1}$$

with the $\lambda(\vec{q})$ being eigenvalues of the discretized Laplacian (Eq. (3.13a)) and biharmonic (Eq. (3.13b)) operators,

$$\lambda_b(\vec{q}) = \frac{4D_b}{\ell^2}\left[\sin^2(q_x\ell/2) + \sin^2(q_y\ell/2)\right] \qquad \left[\mathrm{s}^{-1}\right] \tag{4.2a}$$

$$\lambda_R(\vec{q}) = \frac{16D_R}{\ell^4\,\tau_b}\left[\sin^2(q_x\ell/2) + \sin^2(q_y\ell/2)\right]^2 \qquad \left[\mathrm{V}^{-1}\mathrm{s}^{-1}\right] \tag{4.2b}$$

I present these two eigenvalues graphically in Fig. 4.1: top and bottom panels show the eigenvalues evaluated with high-frequency $\vec{q}$-modes and low-frequency $\vec{Q}$-modes respectively. Note that the low-frequency $\vec{Q}$-modes are a subset of the high-frequency $\vec{q}$-modes: $(Q_x^{\max}, Q_y^{\max}) = (q_x^{\max}, q_y^{\max})/B$. This is clearly shown in the contour plots in Fig. 4.2.

Since the eigenvalues depend on D_b and D_R respectively, the wavenumber integrals rely on either one or both of these diffusivities (see Fig. 4.3). Note that there are specific wavenumber restrictions (red labels) that to be considered when evaluating these integrals. I discuss the various numerical methods used to compute and validate these integrals.

It is important to ensure that the noise intensities are large enough to make an impact on the system, but not so high as to make the corrections dominate the system. For my primary calculations, I set the noise intensities at reasonably small values ($\Gamma_b = 10^{-10}$ m^{2}V^{2}s^{-1}, $\Gamma_R = 10^{-10}$ m^{2}s^{-1}). After calculating the wavenumber integrals and setting the noise intensities, I estimate the drift and diffusion corrections.

I conclude this chapter with an investigation of how the drift and diffusion correction coefficients vary with blocking ratio.

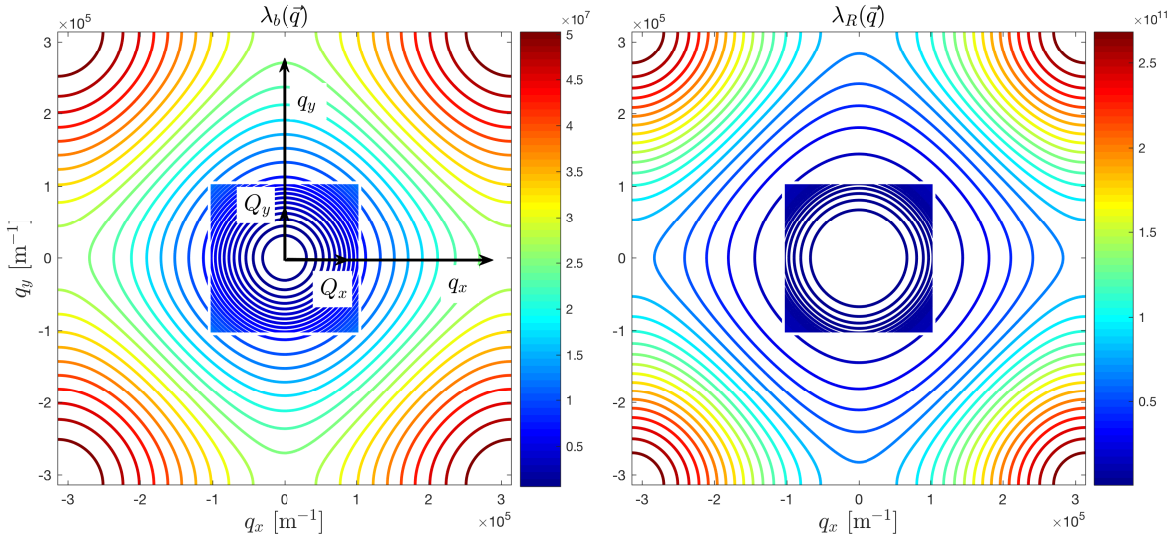

Figure 4.2: Contour plots for eigenvalues evaluated with high-frequency $\vec{q}$-modes and low-frequency $\vec{Q}$-modes (inside the square). Here, $D_b = 6.6 \times 10^{-4}$ m^2/s, $D_R = 2.47 \times 10^{-13}$ m^4/V, $\tau = 5.6$ ms, and $\ell = 10\,\mu$m. To aid visibility, the blocking ratio is set at a very low value: $B = 3$.

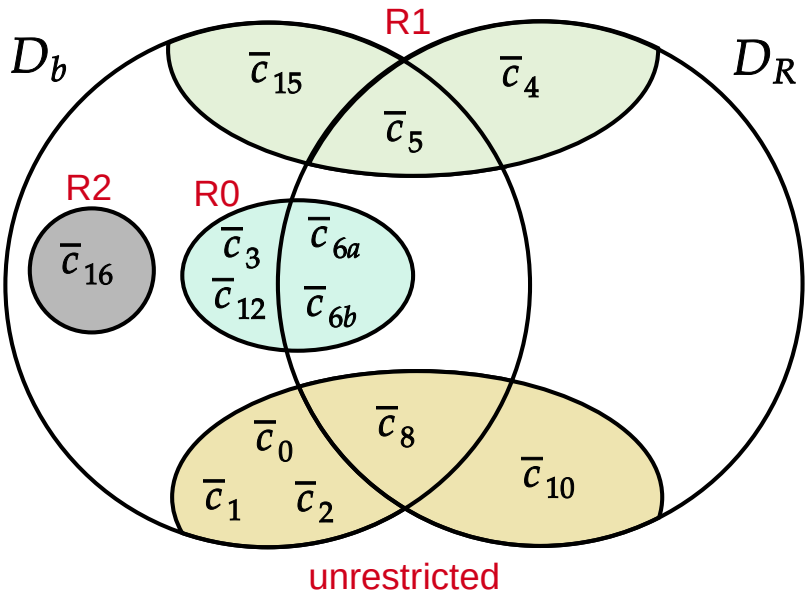

Figure 4.3: Dependencies of wavenumber integrals on diffusivities and wavenumber restrictions. For example, $\bar{c}_4$ depends on recovery diffusivity D_R and is subject to restriction R1, whereas $\bar{c}_8$ depends on both D_b and D_R and is unrestricted. The red labels show wavenumber restrictions that are (defined in Section 3.3.5) required when calculating the integrals.

4.1 Estimating D_b and D_R diffusivities

The excitatory and inhibitory voltage diffusion coefficients are labelled D_e, D_i, and the corresponding recovery diffusion coefficients are $D_{R,e}$, $D_{R,i}$. The voltage diffusion coefficients can be estimated by linking the present spiking model with the Waikato mean-field cortical model for gap-junction connectivity [77]. However, the values of the biharmonic diffusion coefficients $D_{R,b}$ are much more uncertain.

In [77], the inhibitory diffusive constant D_2 is defined as the areal region of influence of a "Fukuda cell", giving bounds,

$$0.1 \leq D_2 \leq 0.6 \text{ cm}^2$$

The ratio D_2/T, where $T = 40\,\text{ms}$ (soma time constant), can be interpreted as a mean-field voltage diffusion coefficient,

$$2.5 \times 10^{-4} \leq D_2/T \leq 15 \times 10^{-4} \text{ m}^2/\text{s}$$

In [72], Steyn-Ross *et al* set $D_2/T = 6.6 \times 10^{-4}\,\text{m}^2/\text{s}$ (towards the bottom end of the range), so in this thesis I set

$$D_i \equiv D_2/T = 6.6 \times 10^{-4} \text{ m}^2/\text{s}$$

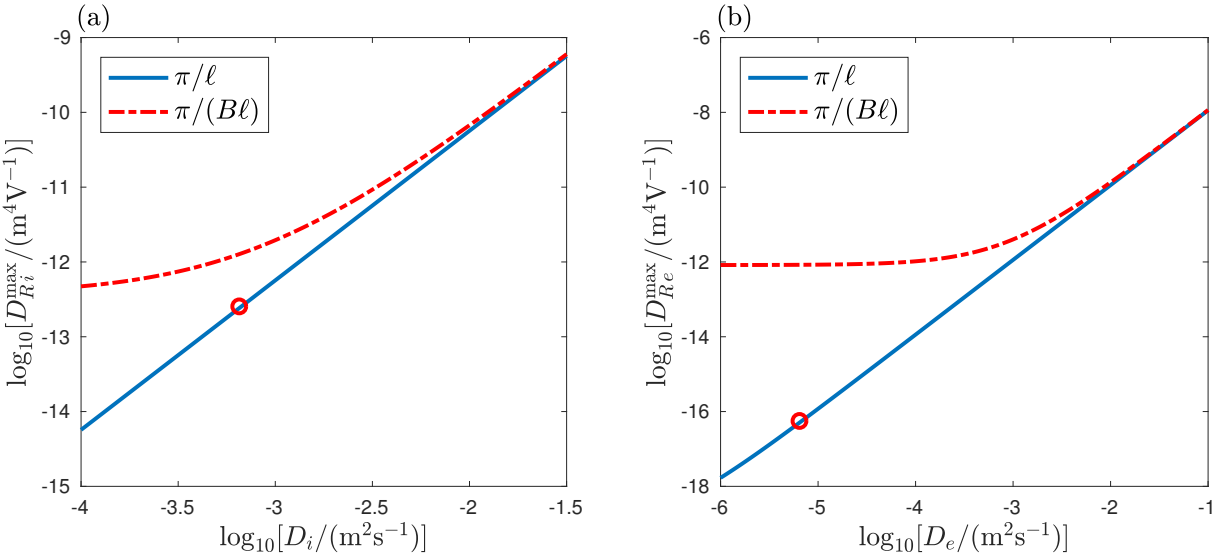

Figure 4.4: Upper bounds for recovery diffusivity $D_{R,b}$ as a function of voltage diffusion coefficient D_b with (a) $b=i$ and (b) $b=e$. Dashed curves represent the small wavenumber limit $q=Q^{\max}=\pi/L$; solid lines represent $q=q^{\max}=\pi/\ell$. Selected points are circled: (a) $D_i=6.6\times10^{-4}$ m^2/s, $D_{R,i}=2.47\times10^{-13}$ m^4/V; (b) $D_e=D_i/100$, $D_{R,e}=5.2761\times10^{-17}$ m^4/V. Panel (a) is modified from Steyn-Ross and Steyn-Ross (2016) [72].

Even though the strategy for setting a value for $D_{R,b}$ is unsure, we can establish a *mathematical* upper bound on D_R by considering the inequality,

$$\begin{aligned} &\Lambda_b^2(\vec{q}) \geq 4\omega_0^2(\vec{q}) \\ \text{i.e.,}\quad &\Lambda_b^2(\vec{q}) \geq 4g_{R,b}\,|E_{\mathrm{K}}|\,\Lambda_R(\vec{q}) \end{aligned} \tag{4.3}$$

in order for $\delta(\vec{q}) = \left(\Lambda_b^2(\vec{q}) - 4\omega_0^2(\vec{q})\right)^{\frac{1}{2}}$ in Eq. (3.22b) to be real [72]. This condition ensures that all wavenumber integrals remain purely real. Using Eq. (4.3) we can write,

$$\Lambda_b^2(\vec{q}) \geq 4g_{R,b}\,|E_{\mathrm{K}}|\left[\frac{16D_{R,b}}{\ell^4\,\tau_b}\left[\sin^2(q_x\ell/2)+\sin^2(q_y\ell/2)\right]^2 + b_1/\tau_b\right]$$

By rearranging, we get an upper bound for $D_{R,b}$ as,

$$D_{R,b} \leq \frac{\ell^4\tau_b}{64\sin^4(q\ell/2)}\left[\frac{\left[(8D_b/\ell^2)\sin^2(q\ell/2)+a_0\right]^2}{4g_R|E_{\mathrm{K}}|} - b_1/\tau_b\right] \tag{4.4}$$

I define $D_R^{\max}$ to be the upper bound of inequality (4.4) and plot $D_R^{\max}$ as a function of D_b (see Fig. 4.4(a)). When plotting $D_R^{\max}$ need to consider two alternative curves (dashed and solid) suggested by the inner (small wavenumber) and outer (large wavenumber) Fourier limits in Fig. 3.6(c): the inner boundary at $q = Q^{\max} = \pi/L = \pi/B\ell$, and the outer boundary at $q = q^{\max} = \pi/\ell$. The latter sets the more conservative boundary for $D_R^{\max}$. Therefore, I use the estimated value for D_b, and set $D_R^{\max}$ at its maximum value as shown in Fig. 4.4(a) [72].

As mentioned in Section 3.1.8 it is believed that, in cortical tissue, inhibitory diffusion strongly dominates excitatory diffusion, i.e, $D_i \gg D_e$ [77]. In [20], Ermentrout shows theoretically that the strong gap junction coupling between excitatory neurons causes the death of neural activity. Thus, the excitatory voltage diffusion coefficient D_e is considered to be a small, but

nonzero, fraction of the inhibitory diffusion. As was done in [77], I set $D_e = D_i/100$ and follow the same procedure explained above to choose a value for excitatory recovery diffusion, $D_{R,e}$ (see Fig. 4.4(b)).

4.2 Calculation of Wavenumber Integrals

The d_j drift and g_j diffusion dependencies on wavenumber integrals are shown in Figs. 4.5 and 4.6. Thus, in order to calculate these corrections, we must evaluate the wavenumber integrals, and this is done numerically. Several of these have wavenumber restrictions: R0, R1, and R2, that need to be applied during the integration. (The definition for each wavenumber integral was listed in Section 3.3.5 along with its wavenumber restrictions.)

Since our wavenumber integrals are defined in an m-dimensional space with $m = 2$ ($\bar{c}_0$, $\bar{c}_1$, $\bar{c}_2$, $\bar{c}_7$, $\bar{c}_8$, $\bar{c}_9$, $\bar{c}_{10}$, $\bar{c}_{11}$), $m = 4$ ($\bar{c}_3$, $\bar{c}_4$, $\bar{c}_5$, $\bar{c}_{6a}$, $\bar{c}_{6b}$, $\bar{c}_{12}$, $\bar{c}_{15}$,), and $m = 6$ ($\bar{c}_{16}$), standard numerical integration methods, such as trapezoidal integration and Gaussian quadrature, can sometimes fail due to excessively slow convergence [62]. For this reason, I elect to use Monte Carlo integration to evaluate these integrals. Fortunately, some integrals can be computed using other methods in MATLAB such as discrete summation, `quad2d`, and `integralN`, thus providing a validation cross-check on the Monte Carlo result.

Monte Carlo integration uses random sampling to evaluate integrals with a convergence rate that is independent of the dimensionality of the integrand. Because of this randomness, the final

	$\bar{c}_0$	$\bar{c}_1$	$\bar{c}_2$	$\bar{c}_3$	$\bar{c}_4$	$\bar{c}_5$	$\bar{c}_{6a}$	$\bar{c}_{6b}$	$\bar{c}_8$	$\bar{c}_{10}$	$\bar{c}_{12}$	$\bar{c}_{15}$	$\bar{c}_{16}$	
d_0	●	●	●	●			●	●	●	●				const.
d_1	●	●	●	●					●					V
d_2		●											●	V^2
d_3		●			●	●								V^3
d_4					●									V^4
d_5		●												VR
d_6					●									V^2R
d_7		●										●		R
d_8	●	●	●						●					const.
d_9		●												R
d_{10}		●										●		V
d_{11}		●												V^2
d_{12}					●									V^3

Figure 4.5: Drift (d_i) dependencies on wavenumber integrals. For example, d_0 depends on the wavenumber integrals $\bar{c}_0$, $\bar{c}_1$, $\bar{c}_2$, $\bar{c}_3$, $\bar{c}_{6a}$, $\bar{c}_{6b}$, $\bar{c}_8$, and $\bar{c}_{10}$. Note that $\bar{c}_7$, $\bar{c}_9$, $\bar{c}_{11}$ are redundant because $\bar{c}_7 = \bar{c}_1$, $\bar{c}_9 = \bar{c}_0/\sqrt{g_{0,R}}$, and $\bar{c}_{11} = \bar{c}_2$, so are not listed in the column headers. The isolated column on the right presents the corresponding terms of the drift coefficients. Thus the drift corrections read, d_0 (constant), $d_1 V$, $d_2 V^2$, $d_3 V^3$, and so forth.

	$\overline{c}_0$	$\overline{c}_1$	$\overline{c}_2$	$\overline{c}_3$	$\overline{c}_4$	$\overline{c}_5$	$\overline{c}_{6a}$	$\overline{c}_{6b}$	$\overline{c}_8$	$\overline{c}_{10}$	$\overline{c}_{12}$	$\overline{c}_{15}$	$\overline{c}_{16}$
g_0			●								●		
g_1			●						●				
g_2			●										
g_3													
g_4													
g_5			●										
g_6			●										
g_7			●										

Figure 4.6: Diffusion (g_i) dependencies on wavenumber integrals. Note that after the typographical errors in [72] (see Section 3.3.4) are corrected, g_3 and g_4 become zero and therefore do not depend on any wavenumber integral.

result of Monte Carlo integration is an approximation of the correct value, with an associated uncertainty bound.

Consider an m-dimensional integral over $\vec{x} = [x_1, x_2, ..., x_n]$,

$$I = \int_\Omega f(\vec{x})\, d\vec{x}$$

We can approximate this integral by averaging samples of the function f at uniformly distributed random points within the interval as,

$$\begin{aligned} I &= \int_\Omega f(\vec{x}) d\vec{x} \\ I &\simeq \overline{f(\vec{x})} \int_\Omega d\vec{x} \\ &\simeq \frac{1}{N} \sum_{i=1}^{N} f(\vec{x}) \underbrace{\int_\Omega d\vec{x}}_{V} \\ &= V \frac{1}{N} \sum_{i=1}^{N} f(\vec{x}) \end{aligned}$$

where $f(\vec{x})$ is the value of integrand at a given sample point, N is the number of trials, and Ω is a subset of $\mathbb{R}^m$, with a volume V. Note that when N approaches infinity, Monte Carlo approximation converges to the exact value of the integral.

The standard error for I is given by,

$$\delta = V \frac{\sigma_N}{\sqrt{N}} \tag{4.5}$$

where σ_N is the sample standard deviation [83].

I present the procedure for calculating each wavenumber integral, starting with the simplest first. Note that each wavenumber integral has two distinct values: $\bar{c}_{j,e}$ and $\bar{c}_{j,i}$ that relate to the excitatory and inhibitory populations respectively.

4.2.1 Evaluation of Unrestricted Wavenumber Integrals

The wavenumber integrals $\bar{c}_0$, $\bar{c}_1$, $\bar{c}_2$, $\bar{c}_7$, $\bar{c}_8$, $\bar{c}_9$, $\bar{c}_{10}$, $\bar{c}_{11}$ do not have any wavenumber restriction to apply during the integration. However, we have to consider the limits of the domain when calculating the integrals. Since these wavenumber integrals are 2D integrals over the large spatial frequency $\vec{q} = (q_x, q_y)$ domain,

$$\int_{\vec{q}\,\text{domain}} d\vec{q} = \int\int_{-\pi/\ell}^{\pi/\ell} dq_x\, dq_y \tag{4.6}$$

we have to ensure that we exclude the contributions from the small spatial frequency $\vec{Q} = (Q_x, Q_y)$ domain (the inner square in Fig. 4.7(a)).

Thus, the first wavenumber integral,

$$\bar{c}_0 = \int \frac{d\vec{q}}{\Lambda_b(\vec{q})}$$

can be approximated by Monte Carlo integration as,

$$\bar{c}_0 = V \frac{1}{n} \sum_{i=1}^{n} \frac{1}{\Lambda_b(\vec{q})} \tag{4.7}$$

where V is the volume of the shaded region in Fig. 4.7(a),

$$V = \left[\frac{2\pi}{\ell}\right]^2 - \left[\frac{2\pi}{L}\right]^2 = \left[\frac{2\pi}{\ell}\right]^2 \left[1 - \frac{1}{B}\right]^2 \quad \because L = B\ell$$

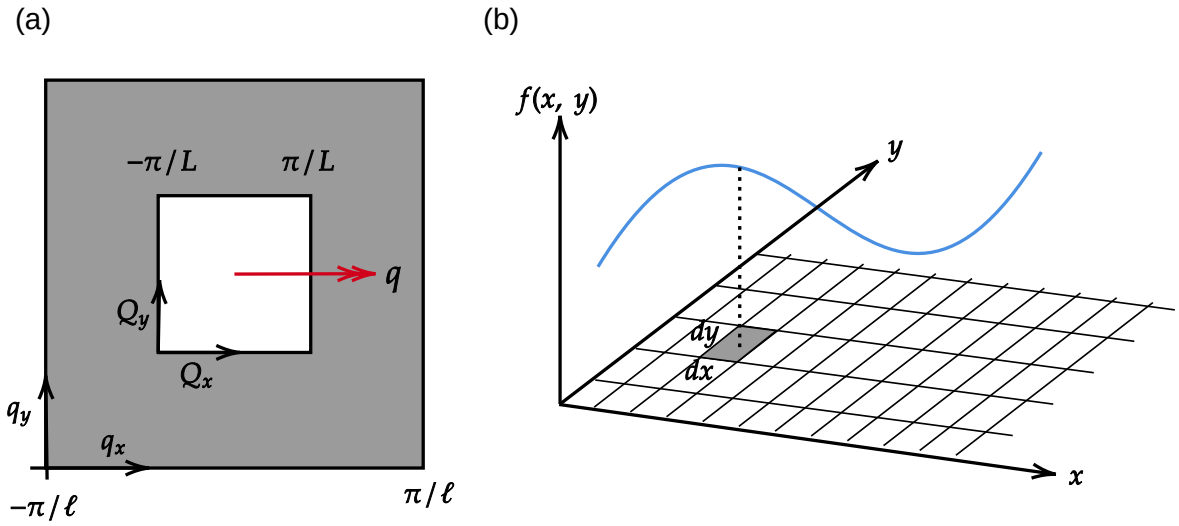

Figure 4.7: (a) Spatial representation of unrestricted wavenumber integral bounds. (b) Representation of numerical integration using tiled method.

Since the integration is done over the square annulus, n is the number of points landing in the annulus.

To calculate the integral, I generate a random vector in the $\vec{q}$ domain using MATLAB `rand` and I find the points that fall inside the annulus. I then calculate the mean value of the integrand over this accepted random vector and multiply it by the volume of the domain V to get the values for $\overline{c}_{0,e}$ and $\overline{c}_{0,i}$.

I evaluate the other unrestricted wavenumber integrals using the same procedure. The Monte Carlo approximation for each integral is given in Table 4.1 and the integral values are presented in Table 4.2.

Table 4.1: Monte Carlo approximations for unrestricted wavenumber integrals. Here, n is the number of trials (points landing in the annulus); volume of the domain is $V = \left[\frac{2\pi}{\ell}\right]^2 - \left[\frac{2\pi}{L}\right]^2$.

Integral	Monte Carlo approximation
$\overline{c}_0 = \int \frac{d\vec{q}}{\Lambda_b(\vec{q})}$	$V \frac{1}{n} \sum_{i=1}^{n} \frac{1}{\Lambda_b(\vec{q})}$
$\overline{c}_1 = \overline{c}_7 = -\int \frac{d\vec{q}}{2[\Lambda_b(\vec{q})]^2}$	$-0.5\, V \frac{1}{n} \sum_{i=1}^{n} \frac{1}{(\Lambda_b(\vec{q}))^2}$
$\overline{c}_2 = \overline{c}_{11} = -\int \frac{d\vec{q}}{2[\Lambda_b(\vec{q})]^3}$	$-0.5\, V \frac{1}{n} \sum_{i=1}^{n} \frac{1}{(\Lambda_b(\vec{q}))^3}$
$\overline{c}_8 = -\int \frac{d\vec{q}}{2\Lambda_b(\vec{q})\,\Lambda_R(\vec{q})}$	$-0.5\, V \frac{1}{n} \sum_{i=1}^{n} \frac{1}{(\Lambda_b(\vec{q}))(\Lambda_R(\vec{q}))}$
$\overline{c}_9 = \frac{\overline{c}_0}{\sqrt{g_{0,R}}}$	$\frac{1}{\sqrt{g_{0,R}}}\, V \frac{1}{n} \sum_{i=1}^{n} \frac{1}{\Lambda_b(\vec{q})}$
$\overline{c}_{10} = \frac{1}{\sqrt{g_{0,R}}} \int \frac{d\vec{q}}{\Lambda_R(\vec{q})}$	$\frac{1}{\sqrt{g_{0,R}}}\, V \frac{1}{n} \sum_{i=1}^{n} \frac{1}{\Lambda_R(\vec{q})}$

Table 4.2: Values for unrestricted wavenumber integrals using Monte Carlo approximation and other numerical integration techniques. Blocking ratio $B = 100$.

	Integral	Monte Carlo approximation (number of samples $\approx 9.99 \times 10^6$)	`integralN` (Abs tol $= 10^{-10}$) `quad2d` (Abs tol $= 10^{-8}$)	Unit
	$\overline{c}_{0,e}$	$(2.2119 \pm 0.001) \times 10^6$	2.2126×10^6	$\mathrm{m}^{-2}\mathrm{s}$
	$\overline{c}_{0,i}$	$(4.2863 \pm 0.008) \times 10^4$	4.2830×10^4	$\mathrm{m}^{-2}\mathrm{s}$
	$\overline{c}_{1,e} = \overline{c}_{7,e}$	$-(1.4440 \pm 0.002) \times 10^1$	-1.4450×10^1	$\mathrm{m}^{-2}\mathrm{s}^2$
$\rightarrow$	$\overline{c}_{1,i} = \overline{c}_{7,i}$	$-(9.2492 \pm 0.095) \times 10^{-2}$	-9.1917×10^{-2}	$\mathrm{m}^{-2}\mathrm{s}^2$
	$\overline{c}_{2,e} = \overline{c}_{11,e}$	$-(3.8572 \pm 0.007) \times 10^{-4}$	-3.8603×10^{-4}	$\mathrm{m}^{-2}\mathrm{s}^3$
$\rightarrow$	$\overline{c}_{2,i} = \overline{c}_{11,i}$	$-(1.7796 \pm 0.029) \times 10^{-6}$	-1.7708×10^{-6}	$\mathrm{m}^{-2}\mathrm{s}^3$
	$\overline{c}_{8,e}$	$-(2.4277 \pm 0.006) \times 10^1$	-2.4293×10^1	$\mathrm{m}^{-2}\mathrm{Vs}^2$
$\rightarrow$	$\overline{c}_{8,i}$	$-(5.5825 \pm 0.117) \times 10^{-2}$	-5.5948×10^{-2}	$\mathrm{m}^{-2}\mathrm{Vs}^2$
	$\overline{c}_{9,e}$	$(4.4506 \pm 0.002) \times 10^4$	4.4519×10^4	$\mathrm{m}^{-2}\mathrm{V}^{-1/2}\mathrm{s}^{3/2}$
	$\overline{c}_{9,i}$	$(8.6244 \pm 0.017) \times 10^2$	8.6179×10^2	$\mathrm{m}^{-2}\mathrm{V}^{-1/2}\mathrm{s}^{3/2}$
	$\overline{c}_{10,e}$	$(2.5412 \pm 0.005) \times 10^4$	2.5433×10^4	$\mathrm{m}^{-2}\mathrm{V}^{1/2}\mathrm{s}^{3/2}$
$\rightarrow$	$\overline{c}_{10,i}$	$(9.1739 \pm 0.141) \times 10^1$	9.1454×10^1	$\mathrm{m}^{-2}\mathrm{V}^{1/2}\mathrm{s}^{3/2}$

$D_{i,e} = 6.6 \times 10^{-4}$, $D_i/100$ m^2/s
$D_{R,i,e} = 2.47 \times 10^{-13}, 5.2761 \times 10^{-17}$ m^4/V
Monte Carlo, `integralN`, and `quad2d` calculations take $\sim$7 s, 0.1 s, and 0.4 s respectively in Boyle (part of a local Linux cluster - CPU Intel w-2123 running at 3.6 GHz, physical memory 160 GB, OS: Ubuntu 16.04.6 LTS).
$\rightarrow$ The arrowed entries have a large relative uncertainty compared to the other entries. Worst case uncertainty is seen in $\overline{c}_{8,i}$ with a relative error of $\sim$2%.

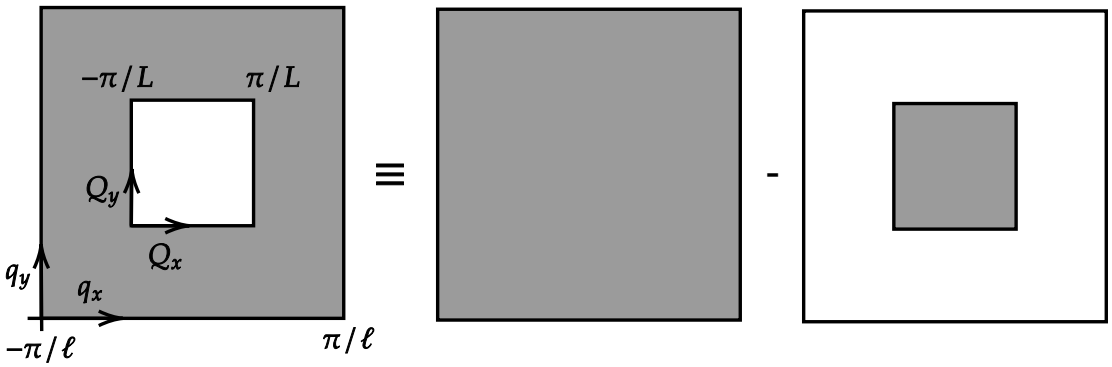

Figure 4.8: The technique used to evaluate unrestricted wavenumber integrals via `integral2` and `quad2d`: $\int_{-\pi/\ell}^{\pi/\ell}\left[\text{unrestricted}\right]\,d\vec{q} = \int_{-\pi/\ell}^{\pi/\ell} d\vec{q} - \int_{-\pi/L}^{\pi/L} d\vec{q}$

I confirm these integral values using two other numerical integration methods in MATLAB: `integral2` and `quad2d`. Both approximate the double integral of the function over a planar region using the tiled method (see Fig. 4.7(b)). The double integral is approximated by summation of small volume strips,

$$I \approx \sum_{y_i}\sum_{x_i} f(x_i, y_i)\,\Delta x\,\Delta y. \tag{4.8}$$

Since it is not possible to do the unrestricted integral calculation directly using either of these methods, we have to perform integration twice: once over the large square, and once over the small square, then subtract the small-square value from the large one as shown in Fig. 4.8. The default absolute error tolerances for `integral2` and `quad2d` are 10^{-10} and 10^{-5} respectively. I use the default tolerance for `integral2`. However, to get an agreement with the `integral2` results, I use much smaller error tolerance for `quad2d` (10^{-8}). Pleasingly, we see that in all cases, the solutions given by `integral2` or `quad2d` lie within the standard error bounds suggested by the Monte Carlo integration (see Table 4.2).

```
% Matlab code to evaluate c0 using Monte Carlo integration
clear; clc;

% parameter values
a0 = 17.81e3;       % per s
% Voltage diffusivity coefficients in m^2/s
Di = 6.60e-4;
De = Di/100;
% Recovery diffusivity coefficients
DRi = 2.47e-13;     % m^4/V
DRe = 5.276e-17;
n_throws = 1e7;     % number of throws
l = 10e-6;          % side length of microcell in m
B = 100;            % blocking ratio
L = B*l;            % side length of macrocell in m

% define inner and outer bounds
vL = 2*pi/(L);
vl = 2*pi/(l);
```

```
% define integrand
lambda_b = @(qx, qy, Db) (4*Db/(l^2))*((sin(qx*l/2)).^2 + (sin(qy*l/2)).^2);
Lambda_b = @(qx, qy, Db) lambda_b(qx, qy, Db) + a0;

% generate random number matrix
R = (2*rand(2, n_throws) - 1).*pi/l;
% define a vector in q domain
q1 = R(1, :) + 1i*R(2, :);
% find indices of points that fall inside annulus
index = find(abs(real(q1)) > pi/L | abs(imag(q1)) > pi/L);
% accepted q vector
q = q1(index);
n = length(q); % points landing inside annulus
qx = real(q); qy = imag(q);

% mean value of the integrand
fc0_e = Lambda_b(qx, qy, De).^-1;
fc0_e_mean = (1/n)*sum(fc0_e);
fc0_i = Lambda_b(qx, qy, Di).^-1;
fc0_i_mean = (1/n)*sum(fc0_i);

% volume of the domain
V = vl^2 - vL^2;

% Monte carlo integration approximation
c0_e = V*fc0_e_mean
c0_i = V*fc0_i_mean

% standard error
dc0_e = V*std(fc0_e)/sqrt(n);
dc0_i = V*std(fc0_i)/sqrt(n);
```

4.2.2 Evaluation of R1-restricted Wavenumber Integrals

The wavenumber integrals $\overline{c}_4$, $\overline{c}_5$, $\overline{c}_{15}$ are 4D integrals over the full bounds of small spatial frequency $\vec{Q} = (Q_x, Q_y)$ domain,

$$\iint_{\vec{Q}\text{ domain}} d\vec{Q}_1\, d\vec{Q}_2 = \int\int\int\int_{-\pi/L}^{\pi/L} dQ_{1x}\, dQ_{1y}\, dQ_{2x}\, dQ_{2y} \tag{4.9}$$

with a wavenumber restriction R1: $\vec{Q}_1 + \vec{Q}_2 = \vec{q}$. Therefore, the integration is done only over the inner square in Fig. 4.9(a) and we have to ensure that the integrand always complies with the wavenumber restriction.

Thus, the first wavenumber integral of the set,

$$\overline{c}_4 = \iint \frac{d\vec{Q}_1\vec{Q}_2}{\Lambda_R(\vec{Q}_1 + \vec{Q}_2)}$$

can be approximated by Monte Carlo integration as,

$$\overline{c}_4 = V_1 \frac{1}{N} \sum_{i=1}^{N} \frac{1}{\Lambda_R(\vec{Q}_1 + \vec{Q}_2)} \tag{4.10}$$

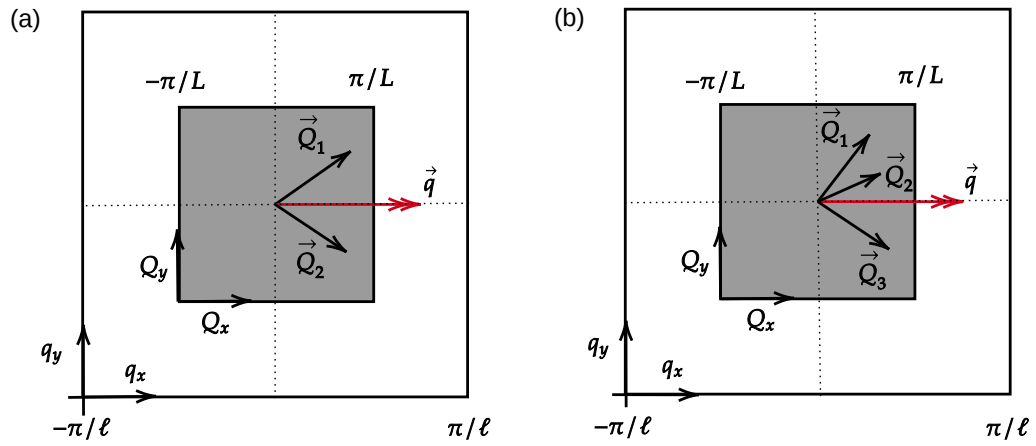

Figure 4.9: Spatial representation of wavenumber restrictions (a) R1 and (b) R2.

where V_1 is the volume of the shaded square in Fig. 4.9(a),

$$V_1 = \left[\frac{2\pi}{L}\right]^4$$

As the integration is done over the inner square, N is the number of trials.

To evaluate the integral, I generate two random vectors $\vec{Q}_1$ and $\vec{Q}_2$ in the $\vec{Q}$ domain by considering the wavenumber restriction R1: $\vec{Q}_1 + \vec{Q}_2 = \vec{q}$. The mean value of the integrand over N number of $\vec{Q}_1 + \vec{Q}_2$ random vectors is then multiplied by the volume of the domain V_1 to obtain the approximation for $\overline{c}_{4,e}$ and $\overline{c}_{4,i}$.

I estimate other wavenumber integrals of the set using the same procedure. The Monte Carlo approximation for each wavenumber integral is given in Table 4.3 and the results are given in Table 4.4. I confirm these values using MATLAB's `integralN` function that utilizes `integral2` and `integral3` to perform integrals of order 4, 5, and 6. The `integralN` function is expected to be slow on fourth-order integrals, very slow on fifth-order and extremely slow on sixth-order. Therefore, to get a result in a reasonable time frame, I loosen the tolerance (Abs tol = 10^{-5}) considerably. Because of this, some of the `integralN` values do not lie in between the error bounds suggested by Monte Carlo integration (see Table 4.4).

Table 4.3: Monte Carlo approximations for R1-restricted wavenumber integrals. Here, N is the number of trials; volume of the domain is $V_1 = \left[\frac{2\pi}{L}\right]^4$.

Integral	Monte Carlo approximation
$\overline{c}_4 = \iint \frac{d\vec{Q}_1 d\vec{Q}_2}{\Lambda_R(\vec{Q}_1+\vec{Q}_2)}$	$V_1 \frac{1}{N} \sum_{i=1}^{N} \frac{1}{\Lambda_R(\vec{Q}_1+\vec{Q}_2)}$
$\overline{c}_5 = \iint \frac{\Lambda_b(\vec{Q}_1+\vec{Q}_2)\, d\vec{Q}_1 d\vec{Q}_2}{\Lambda_R(\vec{Q}_1+\vec{Q}_2)}$	$V_1 \frac{1}{N} \sum_{i=1}^{N} \frac{\Lambda_b(\vec{Q}_1+\vec{Q}_2)}{\Lambda_R(\vec{Q}_1+\vec{Q}_2)}$
$\overline{c}_{15} = \iint \frac{d\vec{Q}_1 d\vec{Q}_2}{\Lambda_b(\vec{Q}_1+\vec{Q}_2)}$	$V_1 \frac{1}{N} \sum_{i=1}^{N} \frac{1}{\Lambda_b(\vec{Q}_1+\vec{Q}_2)}$

Table 4.4: Values for R1-restricted wavenumber integrals using Monte Carlo approximation and MATLAB's `integralN`. Blocking ratio $B = 100$.

	Integral	Monte Carlo approximation (number of samples $= 10^7$)	Uncertainty in Monte Carlo approximation	`integralN` (Abs tol $= 10^{-5}$)	Unit
	$\overline{c}_{4,e}$	2.0085×10^{11}	1.0558×10^{5}	2.0091×10^{11}	$\mathrm{m}^{-4}\mathrm{Vs}$
$\rightarrow$	$\overline{c}_{4,i}$	2.7719×10^{10}	1.0069×10^{7}	2.7738×10^{10}	$\mathrm{m}^{-4}\mathrm{Vs}$
	$\overline{c}_{5,e}$	3.6077×10^{15}	6.9622×10^{9}	3.6087×10^{15}	$\mathrm{m}^{-4}\mathrm{V}$
$\rightarrow$	$\overline{c}_{5,i}$	8.3801×10^{14}	2.1961×10^{11}	8.3851×10^{14}	$\mathrm{m}^{-4}\mathrm{V}$
	$\overline{c}_{15,e}$	3.7951×10^{10}	9.2276×10^{4}	3.7962×10^{10}	$\mathrm{m}^{-4}\mathrm{s}$
	$\overline{c}_{15,i}$	2.1281×10^{10}	2.5489×10^{6}	2.1291×10^{10}	$\mathrm{m}^{-4}\mathrm{s}$

$D_{i,e} = 6.6 \times 10^{-4}$, $D_i/100$ m^2/s
$D_{R,i,e} = 2.47 \times 10^{-13}, 5.2761 \times 10^{-17}$ m^4/V
$\rightarrow$ In [72] $\overline{c}_{4,i}$ and $\overline{c}_{5,i}$ are calculated by considering N as the number of points landing inside the annulus. But N should be the number of points landing in the inner square i.e., the number of throws.
Note that the `integralN` calculations take ∼12 h to complete in both Boyle and NeSI (New Zealand eScience Infrastructure - New Zealand's super computer cluster). If we decrease the absolute error tolerance we obtain more decimal places of precision, but the calculations become significantly slower. In comparison, Monte Carlo calculations take only ∼5 s.

```
% Evaluate c4 using Monte Carlo integration
clear; clc;

% parameter values
b1 = 37.98;          % per V
% Voltage diffusivity coefficients
Di = 6.60e-4;        % m^2/s
De = Di/100;
% Recovery diffusivity coefficients
DRi = 2.47e-13;      % m^4/V
DRe = 5.276e-17;
% recovery time constants
tau_e = 2*5.6e-3;
tau_i = 5.6e-3;
n_throws = 1e7;      % number of throws
l = 10e-6;           % side length of microcell in m
B = 100;             % blocking ratio
L = B*l;             % side length of macrocell in m

% define inner and outer bounds
vL = 2*pi/(L);

% define integrand
lambda_R = @(qx, qy, DR, taub) (16*DR/(l^4*taub))*((sin(qx*l/2)).^2 ...
           + (sin(qy*l/2)).^2).^2;
Lambda_R = @(qx, qy, DR, taub) lambda_R(qx, qy, DR, taub) + (b1/taub);

% generate random number matrix
R = (2*rand(4, n_throws) - 1).*pi/L;
% define vectors in Q domain
```

```
Q1 = R(1,:) + 1i*R(2,:);
Q2 = R(3,:) + 1i*R(4,:);
Q = Q1 + Q2;
% find indices of points that fall inside annulus
index = find(abs(real(Q)) > pi/L | abs(imag(Q)) > pi/L);
% accepted q vector that satisfies the condition R1
q = Q(index);
n = length(q);
qx = real(q); qy = imag(q);

% mean value of the integrand
fc4_e = Lambda_R(qx, qy, DRe, tau_e).^-1;
fc4_e_mean = (1/n_throws)*sum(fc4_e);
fc4_i = Lambda_R(qx, qy, DRi, tau_i).^-1;
fc4_i_mean = (1/n_throws)*sum(fc4_i);

% volume of the domain
V_1 = vL^4;

% Monte carlo integration approximation
c4_e = V_1*fc4_e_mean;
c4_i = V_1*fc4_i_mean;

% standard error
d_c4_e = V_1*std(fc4_e)/sqrt(n_throws);
d_c4_i = V_1*std(fc4_i)/sqrt(n_throws);
```

4.2.3 Evaluation of R2-restricted Wavenumber Integrals

The wavenumber integral $\bar{c}_{16}$ is a 6D integral over the full bounds of the small spatial frequency $\vec{Q} = (Q_x, Q_y)$ domain,

$$\iiint_{\vec{Q}\text{ domain}} d\vec{Q}_1\, d\vec{Q}_2\, d\vec{Q}_3 = \int_{-\pi/L}^{\pi/L}\int_{-\pi/L}^{\pi/L}\int_{-\pi/L}^{\pi/L}\int_{-\pi/L}^{\pi/L}\int_{-\pi/L}^{\pi/L}\int_{-\pi/L}^{\pi/L} dQ_{1x}\, dQ_{1y}\, dQ_{2x}\, dQ_{2y}\, dQ_{3x}\, dQ_{3y} \tag{4.11}$$

with a wavenumber restriction R1: $\vec{Q}_1 + \vec{Q}_2 + \vec{Q}_3 = \vec{q}$. Since the limits of the domain and the wavenumber restriction are similar to that of the previous case, the calculation procedure is similar to that of R1-restricted wavenumber integrals.

Thus, the wavenumber integral,

$$\bar{c}_{16} = \iiint \frac{d\vec{Q}_1 \vec{Q}_2 \vec{Q}_3}{\Lambda_b(\vec{Q}_1 + \vec{Q}_2 + \vec{Q}_3)}$$

is approximated by Monte Carlo integration as,

$$\bar{c}_{16} = V_2 \frac{1}{N} \sum_{i=1}^{N} \frac{1}{\Lambda_R(\vec{Q}_1 + \vec{Q}_2 + \vec{Q}_3)} \tag{4.12}$$

Table 4.5: Values for R2-restricted wavenumber integrals using Monte Carlo approximation. Blocking ratio $B = 100$.

Integral	Monte Carlo approximation (number of samples $= 10^7$)	Uncertainty in Monte Carlo approximation	Unit
$\bar{c}_{16,e}$	1.8971×10^{18}	6.4904×10^{12}	$\mathrm{m}^{-6}\mathrm{s}$
$\bar{c}_{16,i}$	9.5923×10^{17}	1.3152×10^{14}	$\mathrm{m}^{-6}\mathrm{s}$

$D_{i,e} = 6.6 \times 10^{-4}$, $D_i/100$ m^2/s
$D_{R,i,e} = 2.47 \times 10^{-13}, 5.2761 \times 10^{-17}$ m^4/V
The Monte Carlo integration takes ∼6 s in Boyle.

where V_2 is the volume of the shaded square in Fig. 4.9(b),

$$V_2 = \left[\frac{2\pi}{L}\right]^6$$

and N is the number of trials. The spatial representation of R2 wavenumber restriction is shown in Fig. 4.9(b) and the MATLAB code is presented in Appendix A. Due to the higher order dimension of this integral, it is hard to evaluate $\bar{c}_{16}$ using `integralN` within a sensible time frame. Therefore, I present the values for $\bar{c}_{16,e}$ and $\bar{c}_{16,i}$ by using Monte Carlo method only (see Table 4.5).

4.2.4 Evaluation of R0-restricted Wavenumber Integrals

R0-restricted wavenumber integrals $\bar{c}_3$, $\bar{c}_{6a}$, $\bar{c}_{6b}$, $\bar{c}_{12}$ are the hardest ones to calculate due to their complicated integrands. Note that there is a possibility of getting complex values (meaningless) for these integrals if D_R is set without considering Eq. (4.4).

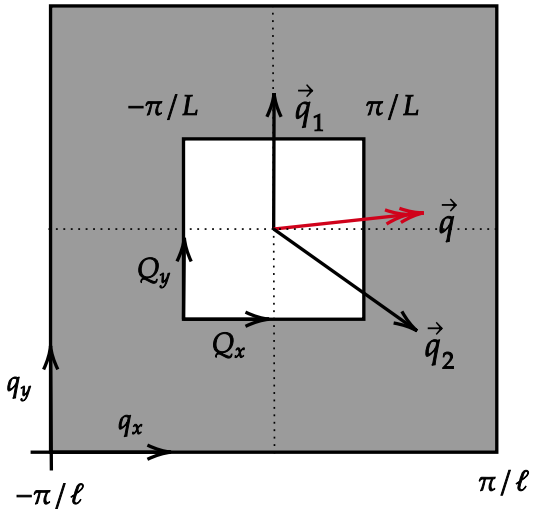

Figure 4.10: Spatial representation of wavenumber restriction R0.

Table 4.6: Monte Carlo approximations for R0-restricted wavenumber integrals. Here, n is the number of trials (points landing in the annulus); volume of the domain is $V = \left[\frac{2\pi}{\ell}\right]^4 - \left[\frac{2\pi}{L}\right]^4$.

Integral	Monte Carlo approximation
$\overline{c}_3 = \iint \frac{g(\vec{q}_1,\vec{q}_2)d\vec{q}_1 d\vec{q}_2}{\Lambda_b(\vec{q}_1)\Lambda_b(\vec{q}_2)}$	$V\frac{1}{n}\sum_{i=1}^{n}\frac{g(\vec{q}_1,\vec{q}_2)}{\Lambda_b(\vec{q}_1)\Lambda_b(\vec{q}_2)}$
$\overline{c}_{6a} = \iint \frac{h(\vec{q}_1,\vec{q}_2)\sqrt{\Lambda_R(\vec{q}_1+\vec{q}_2)}\,d\vec{q}_1 d\vec{q}_2}{\Lambda_b(\vec{q}_1)\,\Lambda_b(\vec{q}_1+\vec{q}_2)}$	$V\frac{1}{n}\sum_{i=1}^{n}\frac{h(\vec{q}_1,\vec{q}_2)\sqrt{\Lambda_R(\vec{q}_1+\vec{q}_2)}}{\Lambda_b(\vec{q}_1)\,\Lambda_b(\vec{q}_1+\vec{q}_2)}$
$\overline{c}_{6b} = \iint \frac{h(\vec{q}_1,\vec{q}_2)\,d\vec{q}_1 d\vec{q}_2}{\Lambda_b(\vec{q}_1)\,\Lambda_b(\vec{q}_2)\sqrt{\Lambda_R(\vec{q}_1+\vec{q}_2)}}$	$V\frac{1}{n}\sum_{i=1}^{n}\frac{h(\vec{q}_1,\vec{q}_2)}{\Lambda_b(\vec{q}_1)\,\Lambda_b(\vec{q}_2)\sqrt{\Lambda_R(\vec{q}_1+\vec{q}_2)}}$
$\overline{c}_{12} = \iint \frac{g(\vec{q}_1,\vec{q}_2)\,d\vec{q}_1 d\vec{q}_2}{\Lambda_b(\vec{q}_1)\,\Lambda_b(\vec{q}_2)\,\Lambda_b(\vec{q}_1+\vec{q}_2)}$	$V\frac{1}{n}\sum_{i=1}^{n}\frac{g(\vec{q}_1,\vec{q}_2)}{\Lambda_b(\vec{q}_1)\,\Lambda_b(\vec{q}_2)\,\Lambda_b(\vec{q}_1+\vec{q}_2)}$

The R0-restricted wavenumber integrals are 4D integrals over the large spatial frequency $\vec{q} = (q_x, q_y)$ domain,

$$\iint_{\vec{q}\,\text{domain}} d\vec{q_1}\, d\vec{q_2} = \int\int\int\int_{-\pi/\ell}^{\pi/\ell} dq_{1x}\, dq_{1y}\, dq_{2x}\, dq_{2y} \tag{4.13}$$

with a wavenumber restriction R0: $\vec{q}_1 + \vec{q}_2 = \vec{q}$. When calculating these integrals we have to exclude the contributions from the small spatial frequency $\vec{Q} = (Q_x, Q_y)$ domain as done in evaluating the unrestricted wavenumber integrals.

The first integral of the set,

$$\overline{c}_3 = \iint \frac{g(\vec{q}_1,\vec{q}_2)\,d\vec{q}_1 d\vec{q}_2}{\Lambda_b(\vec{q}_1)\,\Lambda_b(\vec{q}_2)}$$

is approximated by Monte Carlo integration as,

$$\overline{c}_3 = V_0\,\frac{1}{n}\sum_{i=1}^{n}\frac{g(\vec{q}_1,\vec{q}_2)}{\Lambda_b(\vec{q}_1)\,\Lambda_b(\vec{q}_2)} \tag{4.14}$$

where V_0 is the volume of the shaded square annulus in Fig. 4.10,

$$V_0 = \left[\frac{2\pi}{\ell}\right]^4 - \left[\frac{2\pi}{L}\right]^4 = \left[\frac{2\pi}{\ell}\right]^4\left[1 - \frac{1}{B}\right]^4 \quad \because L = B\ell$$

and since we integrate over the square annulus, n is the number of points landing in the annulus.

As the domain limits of these integrals are similar to those of the unrestricted wavenumber integrals, the calculation is done in a similar manner. The Monte Carlo approximation for the R0-restricted integrals are given in Table 4.6 and the MATLAB code is presented in Appendix A. The integral values are given in Table 4.7. Note that the uncertainty for some of these integrals is very large, but it is not sensible to calculate these integrals using any other integration method due to their complicated integrands and higher order dimension. Fortunately, it is possible to safely ignore the contribution from these wavenumber integrals in our True-field analysis; this exclusion is explained in Section 4.3.

Table 4.7: Values for R0-restricted wavenumber integrals using Monte Carlo approximation. Blocking ratio $B = 100$.

	Integral	Monte Carlo approximation (number of samples $\approx 1.56 \times 10^7$)	Uncertainty in Monte Carlo approximation	Unit
	$\bar{c}_{3,e}$	-3.0114×10^7	5.5419×10^3	$\mathrm{m^{-4}s^3}$
$\rightarrow$	$\bar{c}_{3,i}$	-1.3636×10^4	1.5653×10^2	$\mathrm{m^{-4}s^3}$
	$\bar{c}_{6a,e}$	1.7110×10^9	8.7448×10^4	$\mathrm{m^{-4}V^{-1/2}s^{5/2}}$
	$\bar{c}_{6a,i}$	2.7155×10^5	3.0415×10^1	$\mathrm{m^{-4}V^{-1/2}s^{5/2}}$
	$\bar{c}_{6b,e}$	1.0552×10^3	2.8225×10^{-1}	$\mathrm{m^{-4}V^{1/2}s^{7/2}}$
$\rightarrow$	$\bar{c}_{6b,i}$	3.7435×10^{-3}	4.2180×10^{-5}	$\mathrm{m^{-4}V^{1/2}s^{7/2}}$
	$\bar{c}_{12,e}$	-3.0211×10^2	1.8093×10^{-1}	$\mathrm{m^{-4}s^4}$
$\rightarrow$	$\bar{c}_{12,i}$	-6.5166×10^{-2}	1.4478×10^{-3}	$\mathrm{m^{-4}s^4}$

$D_{i,e} = 6.6 \times 10^{-4}$, $D_i/100$ $\mathrm{m^2/s}$
$D_{R,i,e} = 2.47 \times 10^{-13}, 5.2761 \times 10^{-17}$ $\mathrm{m^4/V}$
It takes $\sim$4 min to complete Monte Carlo integrations in Boyle.
$\rightarrow$ The arrowed entries have a large relative uncertainty compared to the other entries.

4.3 Reblocking Corrections

By using the wavenumber integrals evaluated in previous sections and setting the diffusivities and noise intensities to reasonable values, I calculate the drift and diffusion correction coefficients (definitions are listed in Section 3.3.4). Before presenting the calculated correction coefficients, I present a possible simplification for correction coefficients by setting the squared-noise terms to zero (i.e. $\Gamma_b^2 = 0$) in the drift and diffusion coefficient equations in Section 3.3.4. This is justified because Γ_b is small, so Γ_b^2 terms will be negligible; this claim is validated in Figs. 4.11

Table 4.8: Values for first-order drift correction coefficients. Blocking ratio $B = 100$.

Drift coefficient	Excitatory	Inhibitory	Unit
d_0	-9.9326×10^{-1}	-1.7869×10^{-2}	$\mathrm{Vs^{-1}}$
d_1	-2.9785×10^1	-5.5520×10^{-1}	$\mathrm{s^{-1}}$
d_2	1.7418×10^2	1.0917	$\mathrm{V^{-1}s^{-1}}$
d_3	1.3615×10^6	7.7346×10^5	$\mathrm{V^{-2}s^{-1}}$
d_4	2.5495×10^7	1.3298×10^7	$\mathrm{V^{-3}s^{-1}}$
d_5	4.8163	3.1180×10^{-2}	$\mathrm{s^{-1}}$
d_6	9.5586×10^4	6.4311×10^4	$\mathrm{V^{-1}s^{-1}}$
d_7	1.4908×10^{-1}	1.0459×10^{-3}	$\mathrm{Vs^{-1}}$
d_8	9.6989×10^{-2}	3.3678×10^{-3}	$\mathrm{s^{-1}}$
d_9	-1.3995×10^{-2}	-1.8120×10^{-4}	$\mathrm{s^{-1}}$
d_{10}	-3.3723×10^{-1}	-3.9999×10^{-3}	$\mathrm{V^{-1}s^{-1}}$
d_{11}	-5.4580	-7.0669×10^{-2}	$\mathrm{V^{-2}s^{-1}}$
d_{12}	-9.7914×10^4	-5.4062×10^4	$\mathrm{V^{-3}s^{-1}}$

$D_{i,e} = 6.6 \times 10^{-4}$, $D_i/100$ $\mathrm{m^2/s}$
$D_{R,i,e} = 2.47 \times 10^{-13}, 5.2761 \times 10^{-17}$ $\mathrm{m^4/V}$
$\Gamma_b = 10^{-10}$ $\mathrm{m^2V^2s^{-1}}$, $\Gamma_R = 10^{-10}$ $\mathrm{m^2s^{-1}}$
Monte Carlo integration is used to compute wavenumber integrals.
Note that the uncertainties are ignored here as they are very small (e.g., the uncertainty of d_0 is 1.2×10^{-9}).

and 4.12. Thus, it is clear that there is no effect of this simplification on our analysis.

The three drift coefficients (d_0, d_1, d_8) that depend on Γ_b^2 can be simplified as,

$$d_0 = \frac{\Gamma_b}{2(2\pi)^2}\Bigg[- a_{3,b}\,\overline{c}_0 + a_{1,b}\,a_{3,b}\,\overline{c}_1 E_{\mathrm{Na}} - \frac{a_{3,b}\,\overline{c}_7}{\tau_b} + \frac{a_{3,b}\,\overline{c}_8\,g_{R,b}\,|E_{\mathrm{K}}|\,\Gamma_R}{\Gamma_b} - \sqrt{\frac{g_{R,b}}{|E_{\mathrm{K}}|}}\,\frac{\overline{c}_9}{\tau_b} + \frac{\sqrt{g_{R,b}^3\,|E_{\mathrm{K}}|}\,\overline{c}_{10}\,\Gamma_R}{\Gamma_b}\Bigg]$$

$$d_1 = \frac{\Gamma_b}{2(2\pi)^2}\Bigg[- 3a_{2,b}\,\overline{c}_0 - (2a_{3,b}^2 - 3a_{1,b}\,a_{2,b}\,E_{\mathrm{Na}})\,\overline{c}_1 - \frac{3\,a_{2,b}\,\overline{c}_7}{\tau_b} + \frac{3\,a_{2,b}\,\overline{c}_8\,g_{R,b}\,|E_{\mathrm{K}}|\,\Gamma_R}{\Gamma_b}\Bigg] + \frac{S_1^2\,\Gamma_b}{2(B\ell)^2\,|E_{\mathrm{K}}|^2}$$

$$d_8 = \frac{b_{2,b}\,\Gamma_b}{2(2\pi)^2\,\tau_b}\left[\overline{c}_0 - a_{1,b}\,\overline{c}_1\,E_{\mathrm{Na}} + \frac{\overline{c}_7}{\tau_b} - \frac{\overline{c}_8\,g_{R,b}\,|E_{\mathrm{K}}|\,\Gamma_R}{\Gamma_b}\right]$$

Since all of the diffusion coefficient corrections (g_i) depend on Γ_b^2, the only non-zero first-order diffusion coefficient is,

$$g_2 = \frac{\Gamma_b}{2(B\ell)^2}\left[- \frac{S_1^2}{|E_{\mathrm{K}}|^2}\right]$$

(The full form of these correction coefficients was listed in Section 3.3.4).

Hereafter I use the simplified versions for both drift and diffusion coefficients which I refer to as first-order correction coefficients.

In Table 4.8, I list the values for the first-order drift coefficients. The only non-zero first-order diffusion coefficient is evaluated as,

$$g_2 = g_{2,e} = g_{2,i} = -1.0604 \times 10^{-3}\ \mathrm{s}^{-1}$$

4.4 The Effect of Blocking on Correction Coefficients

In this section I investigate how each correction coefficient varies with blocking ratio, B, across the range $1 \leq B \leq 1000$. In Fig. 4.11, I plot the distributions of the first drift correction coefficients, d_0. In the previous section, I showed that d_0 can be simplified by considering only first-order noise. I present both full and first-order expressions for d_0 in Fig. 4.11 plotted on both linear scales (top panels) and logarithmic scales (bottom panels).

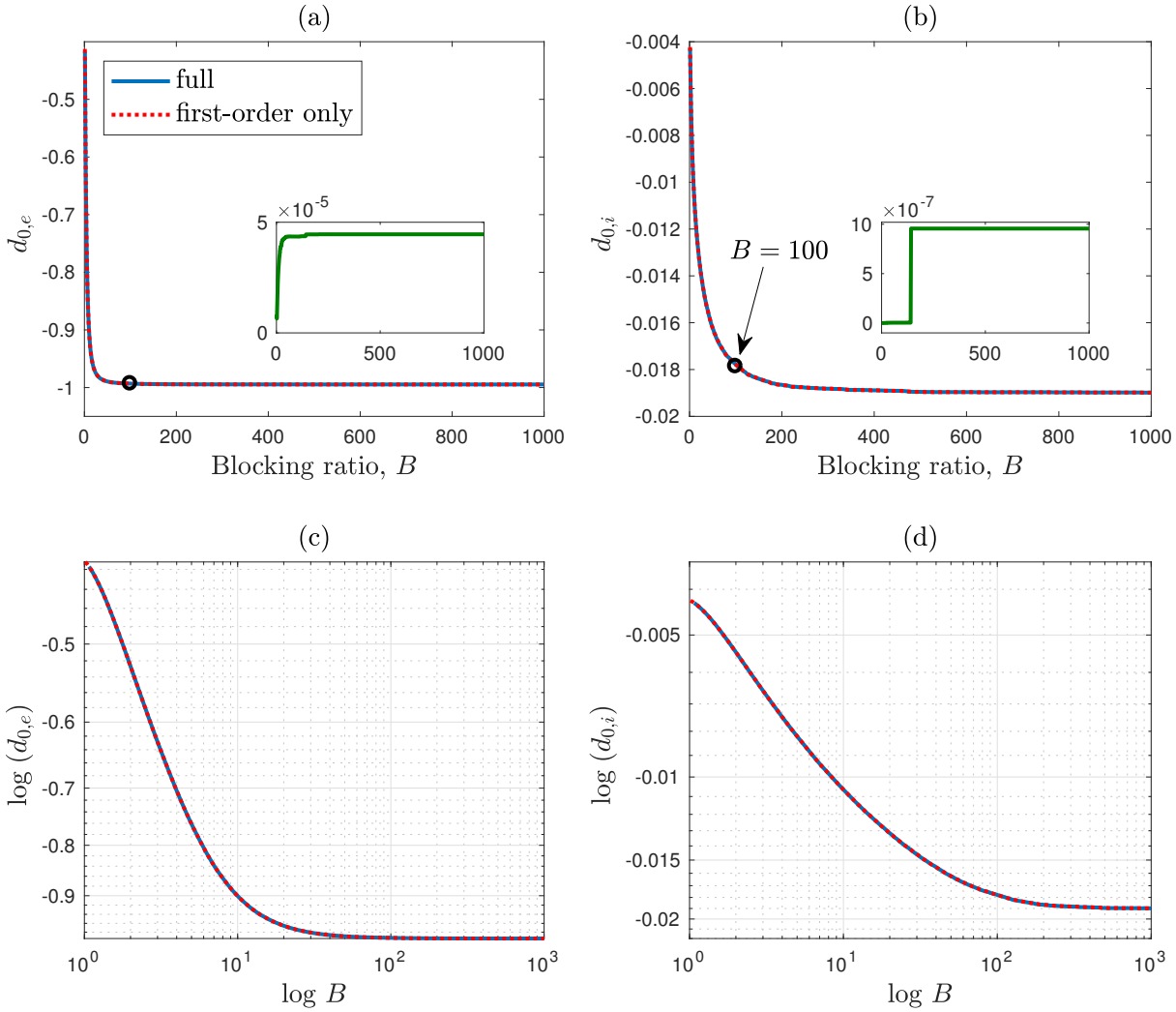

Figure 4.11: Full and first-order drift correction coefficient, d_0 for (a) excitatory and (b) inhibitory neural populations. Here, $D_{i,e} = 6.6 \times 10^{-4}$, $D_i/100$ m^2/s; $D_{R,i,e} = 2.47 \times 10^{-13}, 5.2761 \times 10^{-17}$ m^4/V; noise intensities are $\Gamma_b = 10^{-10}$ m^{2}V^{2}s^{-1} and $\Gamma_R = 10^{-10}$ m^{2}s^{-1}. (c), (d) The bottom panels show log-log plots of $d_{0,e}$ and $d_{0,i}$. Red-solid lines show full corrections; blue-dotted lines show first-order corrections. (Green lines in the inset graphs show the discrepancy between full and first-order corrections.)

The other three simplifiable correction coefficients (d_1, d_8, and g_2) are presented in Fig. 4.12. Since the discrepancy between the full and first-order drift correction coefficient is very small (the worst case discrepancy is less than 0.01%) in all four correction coefficients, this neglect of second-order noise terms is reasonable.

Interestingly, we observe that we can fit power series models to the excitatory correction coefficients ($d_{1,e}$, $d_{8,e}$, and $g_{2,e}$) in Fig. 4.12 when we consider the range $10 \leq B \leq 1000$ (see Fig. 4.13).

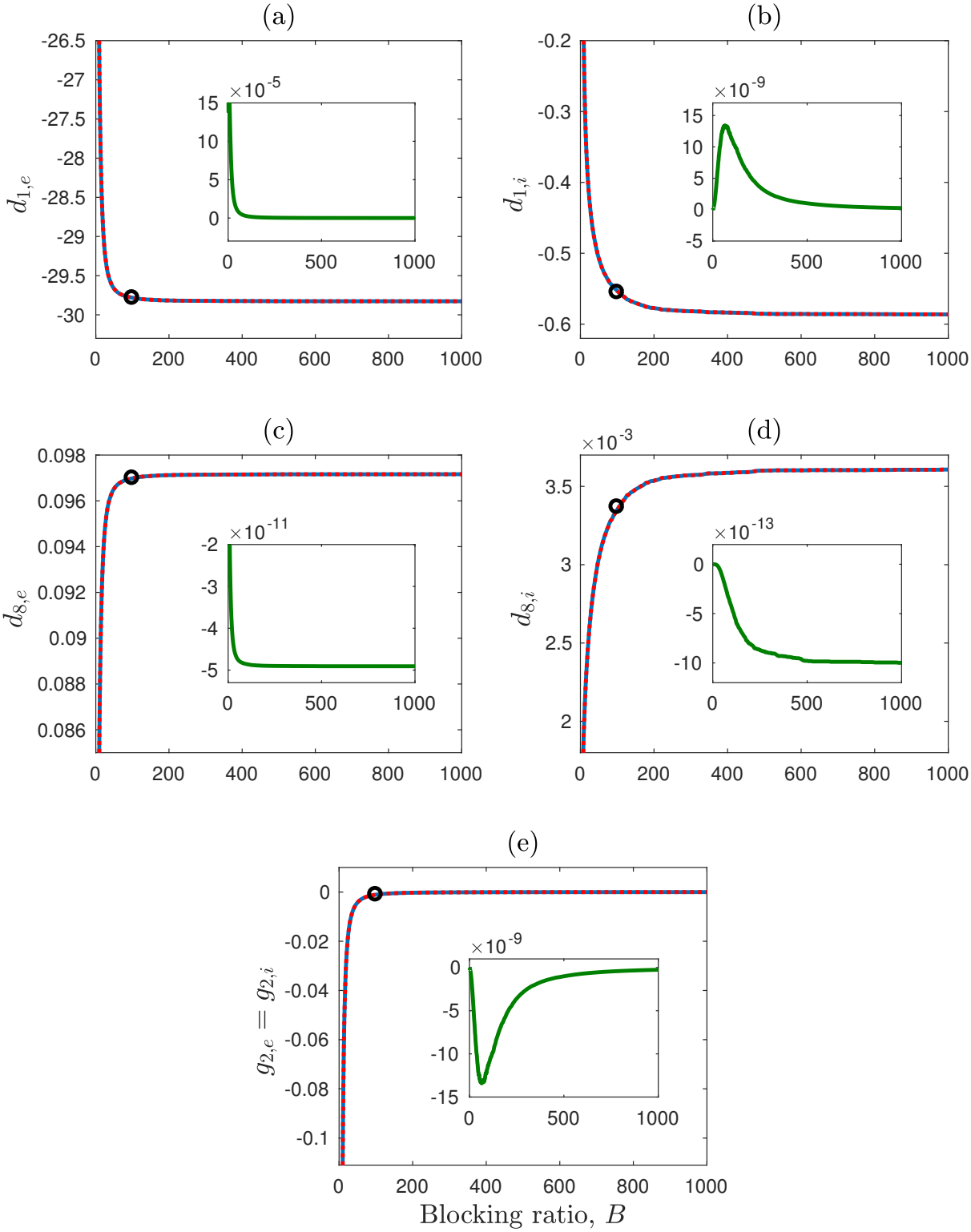

Figure 4.12: Full and first-order d_1, d_8, and g_2 correction coefficients for excitatory (left-hand panels) and inhibitory (right-hand panels) neural populations. Here, $D_{i,e} = 6.6 \times 10^{-4}$, $D_i/100$ m^2/s; $D_{R,i,e} = 2.47 \times 10^{-13}, 5.2761 \times 10^{-17}$ m^4/V; noise intensities are $\Gamma_b = 10^{-10}$ m^{2}V^{2}s^{-1} and $\Gamma_R = 10^{-10}$ m^{2}s^{-1}. Red lines show the full corrections; blue-dotted lines show first-order corrections. Green lines in the inset graphs show (full) − (first-order) discrepancies.

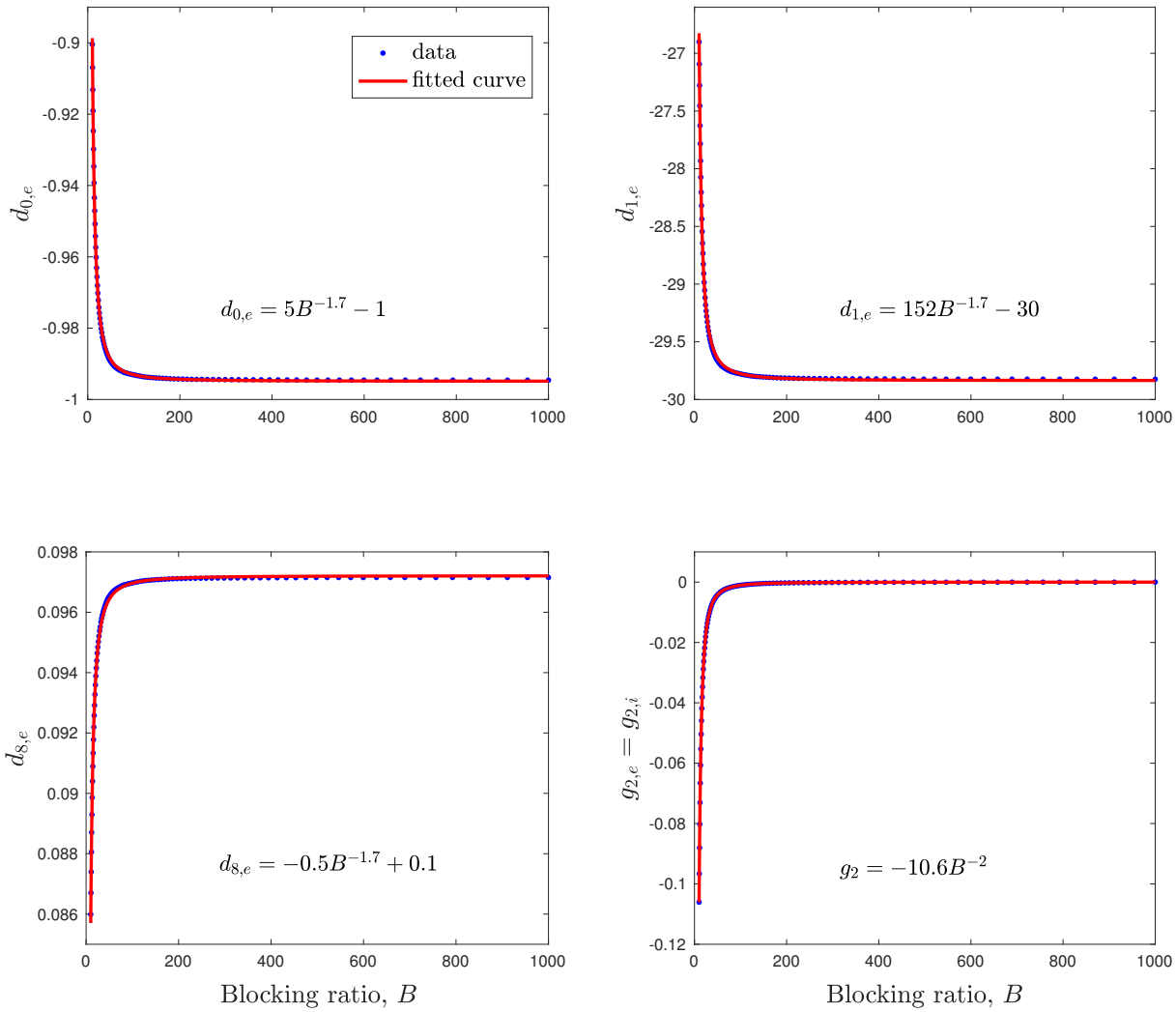

Figure 4.13: The power series fits for $d_{0,e}$, $d_{1,e}$, $d_{8,e}$, and g_2. Curves are fitted using MATLAB's `fit` function in curve fitting tool box. The model type for $d_{0,e}$, $d_{1,e}$, and $d_{8,e}$ is `power2` and for g_2 is `power1`.

I present the remaining first-order correction coefficient distributions in Figs. 4.14 and 4.15. Noticeably, all the blocking correction coefficients have either rapid growth or decay for low blocking ratios ($\sim 10 - 200$) and tend to settle down to some value at higher blocking ($B > 500$). We also see that both excitatory and inhibitory drift correction coefficient distributions have similar trends. However, their onset of growth or decay is different (see Figs. 4.14 and 4.15).

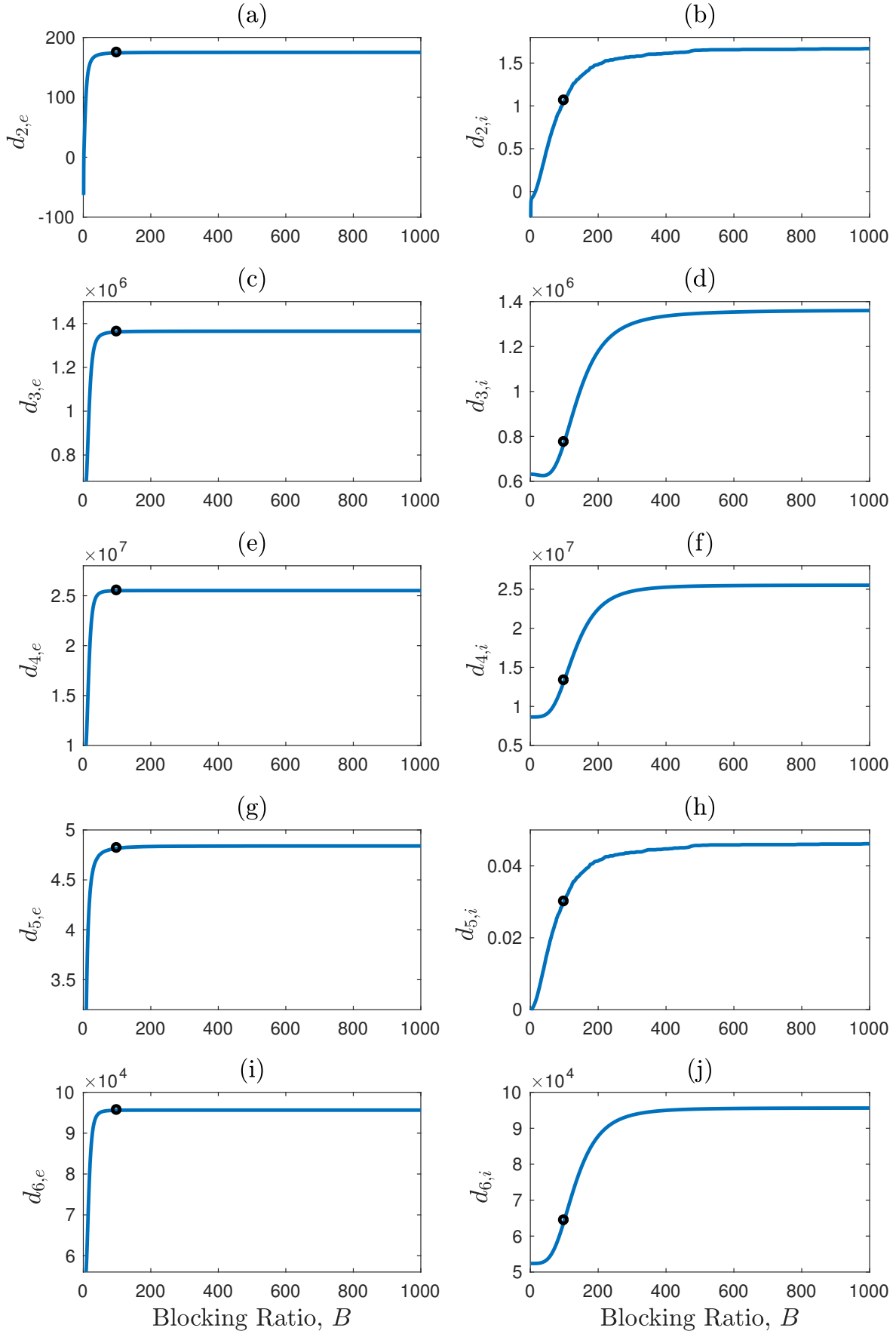

Figure 4.14: The drift correction coefficients (d_2, d_3, d_4, d_5 and d_6) for excitatory (left panel) and inhibitory (right panel) neural populations vs B. Circles represent $B = 100$. Here, $D_{i,e} = 6.6 \times 10^{-4}$, $D_i/100$ m^2/s; $D_{R,i,e} = 2.47 \times 10^{-13}, 5.2761 \times 10^{-17}$ m^4/V; noise intensities, $\Gamma_b = 10^{-10}$ m^{2}V^{2}s^{-1} and $\Gamma_R = 10^{-10}$ m^{2}s^{-1}.

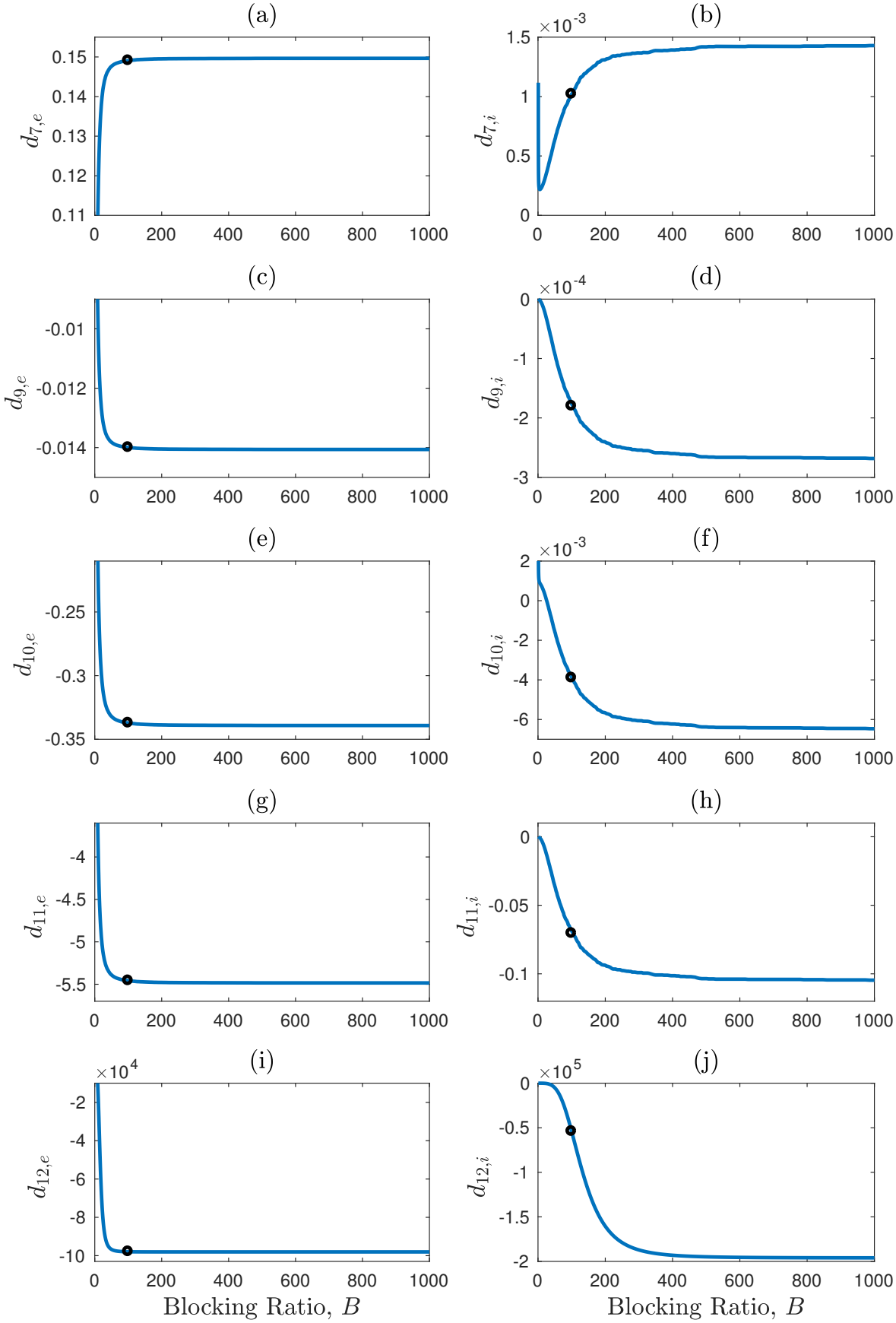

Figure 4.15: The drift correction coefficients (d_7, d_9, d_{10}, d_{11} and d_{12}) for excitatory (left panel) and inhibitory (right panel) neural populations vs B. Here, $D_{i,e} = 6.6 \times 10^{-4}$, $D_i/100$ m^2/s; $D_{R,i,e} = 2.47 \times 10^{-13}, 5.2761 \times 10^{-17}$ m^4/V; noise intensities, $\Gamma_b = 10^{-10}$ m^{2}V^{2}s^{-1} and $\Gamma_R = 10^{-10}$ m^{2}s^{-1}.

4.5 Chapter Summary

This chapter discussed the effect of five parameters on blocking corrections: voltage and recovery noises (Γ_b and Γ_R); voltage and recovery diffusivities (D_b and D_R); and blocking ratio (B). Throughout the chapter I have assumed a fixed side-length of microcell (ℓ) of 10 μm. I explained how I set values for these parameters and using those set values calculated wavenumber integrals via different numerical methods. By pointing out a possible simplification of the correction coefficients, I evaluated the first-order blocking corrections using pre-computed wavenumber integrals. The chapter was concluded by presenting the variation of each drift and diffusion correction coefficient with blocking. I found that at low blocking ratios there is a rapid change in all the correction coefficients whereas for high blocking ratios, all the correction coefficients tend to settle down to some asymptotic value.

In the next chapter these correction coefficients are used to present a primary demonstration of the True-field model. The Wilson neuron is reblocked for the case of no chemical synapses and considered the spatially homogeneous limit.

Chapter 5

Reblocked Wilson Assembly

The main purpose of the True-field approach is to introduce a systematic algorithm for spatial reblocking for a 2D cortical network of excitatory and inhibitory neurons. In this chapter, as a preliminary demonstration, I simplify the 20-dimensional True-field model into a 2-dimensional model by suppressing chemical synapses and consider the reblocked Wilson neuron in the spatially homogeneous limit. I first analyse the reblocked neuron for negligible noise (small-noise limit) by re-doing the analysis done by Steyn-Ross and Steyn-Ross in [72]. I point out some corrections that lead to a change in the mode of bifurcation to spiking: from Hopf to a saddle–node. I present a steady-state analysis and confirm the predicted stability by conducting some stochastic simulations for different simulation currents. I then turn on the noise-dependent terms in the reblocking corrections and compare the dynamical behaviour of the reblocked Wilson neuron with the original Wilson neuron. I discuss how the voltage and recovery noise intensities Γ_b and Γ_R affect spiking dynamics. Finally, by fixing the noise intensities at reasonable values, I compare the magnitudes of individual reblocking correction terms by considering steady-state values just below threshold and dynamic spiking values just above threshold and identify those terms that make the greatest contribution to the reblocking corrections.

5.1 Small-noise Limit

For this simple demonstration, I suppress the synaptic input by setting $\Phi_{ab} = 0$ in Eq. (3.23a) and I assume that the neuron is embedded in a network of identical spiking neurons that are coupled via gap junctions only. Thus, the 20-equation system reduces to a pair of differential equations for V and R, the reblocked voltage and recovery variables within a single population,

$$\frac{\partial V}{\partial t} = -g(V)(V - E_{\rm Na}) - g_R R.(V - E_{\rm K}) \; + \; D_b \nabla^2 V \; + \; \frac{I^{\rm dc}}{C} \; + \; G_1(V,R) \tag{5.1a}$$

$$\frac{\partial R}{\partial t} = -\frac{1}{\tau_b}[R - R_\infty(V)] \; + \; \frac{D_R \nabla^4 V}{\tau_b} \; + \; G_2(V,R) \tag{5.1b}$$

where $G_1(V,R)$, $G_2(V,R)$ are the reblocking drift corrections from Eq. (3.18).

For this analysis I set the microcell dimension at $\ell = 10$ μm and the blocking ratio at $B = 100$. Since we are assuming that the noise is negligible, I set $\Gamma_b = \Gamma_R = 0$, thus the reduced G_1 and G_2 corrections are,

$$G_1(V,R) = d_3 V^3 + d_4 V^4 + d_6 V^2 R$$

$$G_2(V,R) = d_{12}V^3$$

with noise-independent drift coefficients,

$$d_3 = \frac{a_3\,S_1^2}{|E_{\rm K}|} + \left[2\,a_3\,\bar{c}_4 - \frac{\bar{c}_5}{|E_{\rm K}|}\right]\frac{b_2\,S_1(B\ell)^4}{(2\pi)^4\,\tau_b}$$

$$d_4 = a_2\,S_1\left[\frac{S_2}{|E_{\rm K}|} + \frac{3\,b_2\,\bar{c}_4\,(B\ell)^4}{(2\pi)^4\,\tau_b}\right] \qquad (S_1 \text{ and } S_2 \text{ were swapped in [72]})$$

$$d_6 = g_R\,S_1\left[\frac{S_1}{|E_{\rm K}|} + \frac{b_2\,\bar{c}_4\,(B\ell)^4}{(2\pi)^4\,\tau_b}\right]$$

$$d_{12} = \frac{-2\,b_2^2\,\bar{c}_4\,S_1(B\ell)^4}{(2\pi)^4\,\tau_b^2}$$

Having set the diffusivities as $D_b = D_i = 6.6\times10^{-4}$ m^2/s and $D_R = D_{R,i} = 2.47\times10^{-13}$ m^4/V, I extract the values of $\bar{c}_{4,i}$ and $\bar{c}_{5,i}$ approximated by Monte Carlo integration from Table 4.2 as,

$$\bar{c}_4 = \bar{c}_{4,i} = 2.7719\times10^{10}\ \text{Vs/m}^4 \quad [\text{in Ref [72]}\ \ 6.337\times10^{10}]$$
$$\bar{c}_5 = \bar{c}_{5,i} = 8.3801\times10^{14}\ \text{V/m}^4 \quad [\text{in Ref [72]}\ \ 19.16\times10^{14}]$$

Using the above values I compute the four inhibitory diffusion corrections:

$$d_3 = d_{3,i} = 7.7339\times10^{5}\ \text{V}^{-2}\text{s}^{-1}$$
$$d_4 = d_{4,i} = 1.3296\times10^{7}\ \text{V}^{-3}\text{s}^{-1}$$
$$d_6 = d_{6,i} = 6.4306\times10^{4}\ \text{V}^{-1}\text{s}^{-1}$$
$$d_{12} = d_{12,i} = -5.4040\times10^{4}\ \text{V}^{-3}\text{s}^{-1}$$

Note:

1. There is a change in d_4 due to the correction pointed out in Section 3.3.4 and highlighted above.
2. There was a typographical error in the original MATLAB code (in estimating d_3) used to analyse the small-noise limit.
3. $\bar{c}_{4,i}$ and $\bar{c}_{5,i}$ differ from those quoted in [72] because of using an incorrect number of trials in Monte Carlo integration (pointed out in Section 4.2.2).

Because of these corrections the results I present here differ from the original work done in [72].

5.1.1 Linear Stability Analysis

The noiseless homogeneous cortex is explored by setting the derivatives of Eqs (5.1) to zero,

$$F_1 \equiv \frac{dV}{dt} = -g(V)(V-E_{\rm Na}) - g_R R\,(V-E_{\rm K}) + \frac{I_{\rm dc}}{C} + d_3V^3 + d_4V^4 + d_6V^2R = 0 \qquad (5.2a)$$

$$F_2 \equiv \frac{dR}{dt} = \frac{1}{\tau_b}(-R + R_\infty(V)) + d_{12}V^3 = 0 \qquad (5.2b)$$

For a given value of dc stimulus current ($I_{\rm dc}$), I compute equilibrium point (V^0, R^0) by solving Eqs (5.2) numerically: by substituting,

$$R = R_\infty(V) + \tau_b\, d_{12} V^3$$

from Eq. (5.2b) into (5.2a), I obtain a polynomial expression of V, which is then solved using MATLAB's `roots` function. The results are cross checked by solving the two simultaneous equations (Eqs (5.2)) using MATLAB's `vpasolve`. I then evaluate the Jacobian matrix, **J** at each equilibrium point,

$$\mathbf{J} = \begin{bmatrix} \frac{\partial F_1}{\partial V} & \frac{\partial F_1}{\partial R} \\ \frac{\partial F_2}{\partial V} & \frac{\partial F_2}{\partial R} \end{bmatrix}_{|(V^0,R^0)} \tag{5.3}$$

The partial derivatives,

$$\begin{aligned} J_{11} &= \frac{\partial F_1}{\partial V} = -g(V) - (V_e - E_{\rm Na})(a_1 + 2\,a_2 V) - g_R R + 3\,d_3 V^2 + 4\,d_4 V^3 + 2\,d_6 V R \\ J_{12} &= \frac{\partial F_1}{\partial R} = -g_{R,b}(V - E_{\rm K}) + d_6 V^2 \end{aligned}$$

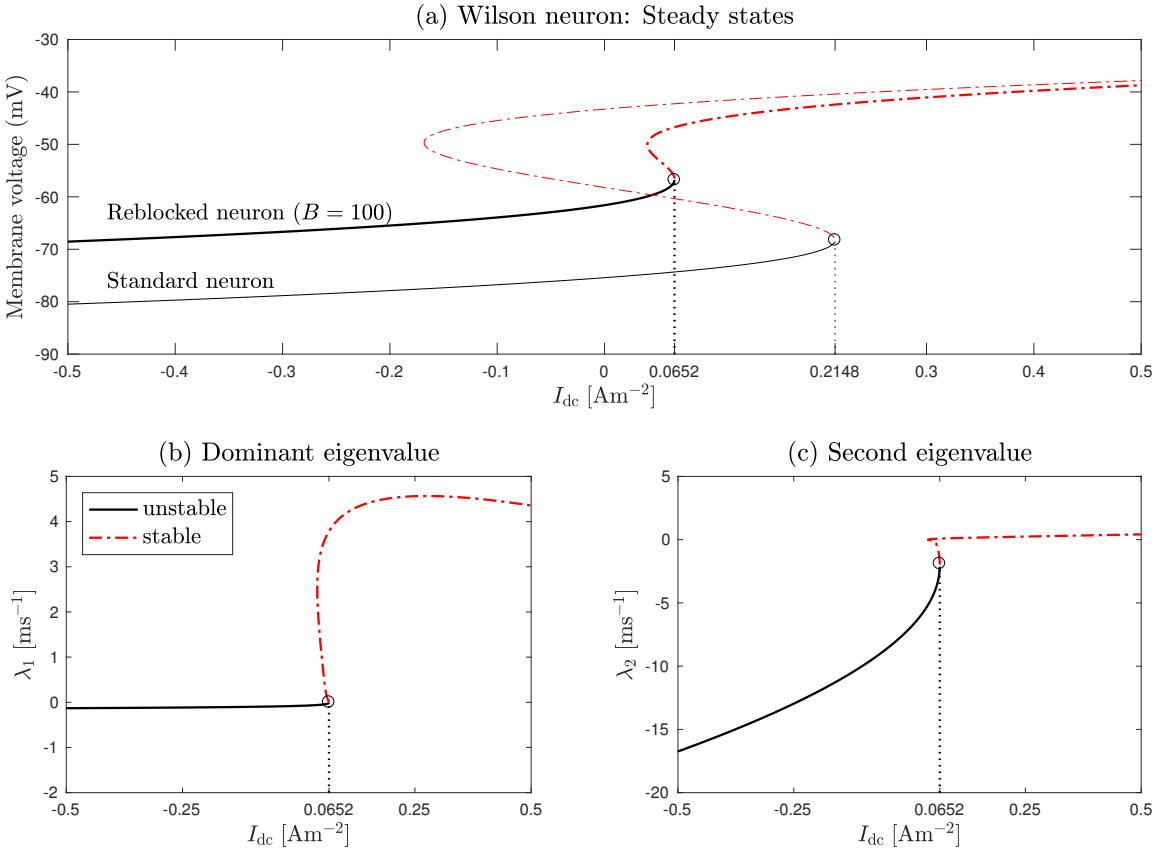

Figure 5.1: Stability analysis of small-noise limit diffusive Wilson neuron. (a) Steady-state distribution of membrane potential as a function of dc stimulus current for standard Wilson neuron and reblocked diffusive Wilson neuron. Periodic solutions exist to the right of saddle-node ($I_{\rm dc}^{\rm crit}$) similar to those shown in Fig. 2.14 but, omitted here for clarity. For diffusive neuron (b) and (c) both eigenvalues are real and negative until the stimulus current reaches a threshold value. Threshold currents are $I_{\rm dc}^{\rm crit}$ ~0.2148, 0.0652 Am^{-2} for standard and reblocked Wilson neurons respectively.

$$J_{21} = \frac{\partial F_2}{\partial V} = \frac{1}{\tau_b}(b_1 + 2\,b_2 V) + 3\,d_{12}V^2$$
$$J_{22} = \frac{\partial F_2}{\partial R} = -\frac{1}{\tau_b}$$

present the elements of Jacobian matrix, **J**. The stability of each steady-state is predicted using the real parts of the eigenvalues of this matrix: if both eigenvalues have negative real parts, steady-state is stable; if either eigenvalue has a positive real part, steady-state is unstable.

The distribution of steady-states with their stability predictions are presented in Fig. 5.1. As a comparison I also plot the steady-states of the standard unblocked Wilson neuron. To confirm the stability predictions of the eigenvalue analysis, I conduct some simulations for different stimulus currents (see Fig. 5.2(b)).

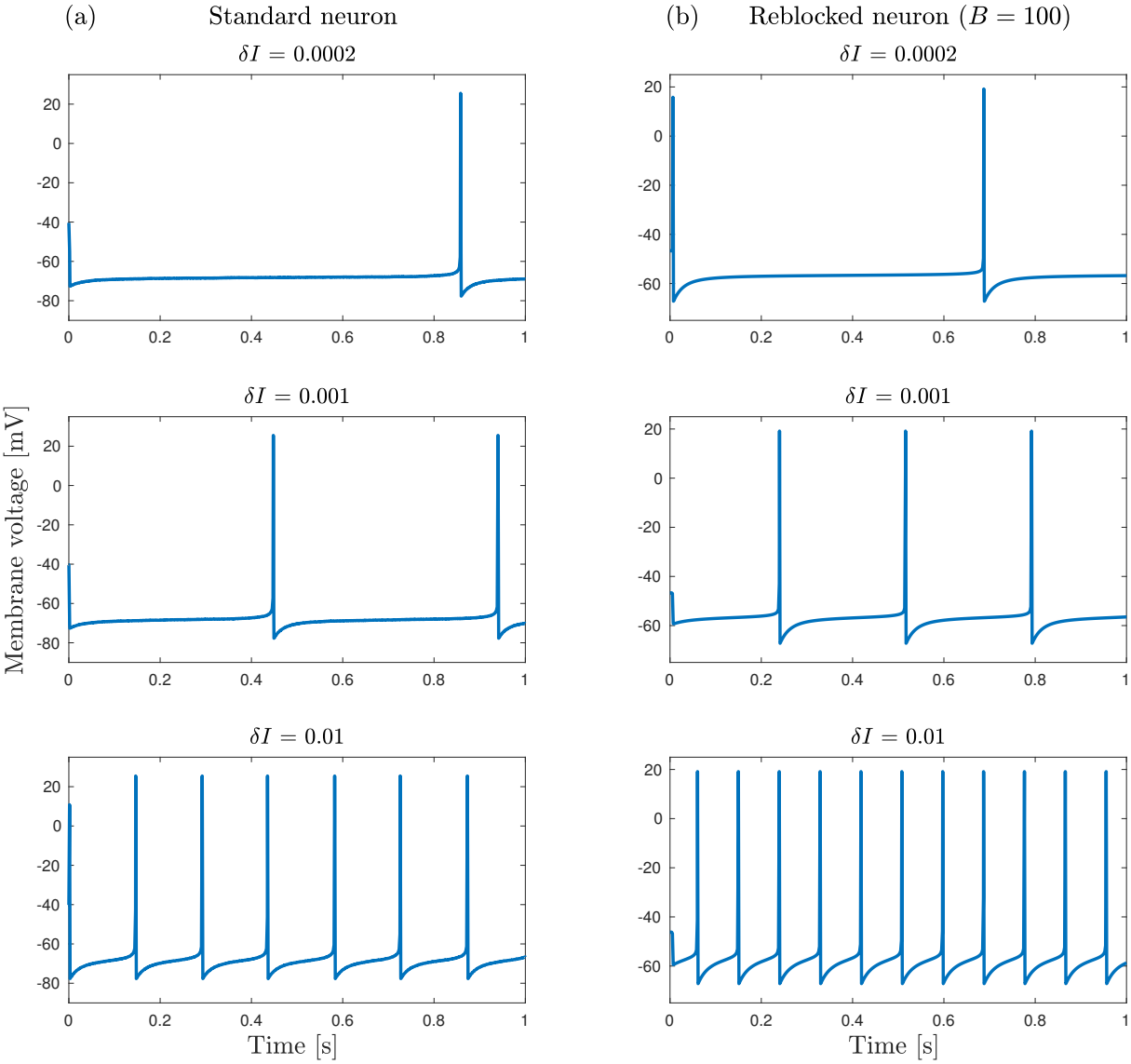

Figure 5.2: Spike generation of (a) standard Wilson neuron (left-hand panels) and (b) diffusive Wilson neuron (right-hand panels) for three settings of $I_{\rm dc}$ drive current just above threshold: $I_{\rm dc} = I_{\rm dc}^{\rm crit} + \delta I$. In the left-hand panels white-noise perturbations of amplitude 10^{-5} are added to both voltage and recovery. In the right-hand panels the noise was set to a very low value of amplitude 10^{-12} (i.e., enough to simulate spiking). The firing patterns are similar in two neurons but firing rate is slightly raised in diffusive neuron.

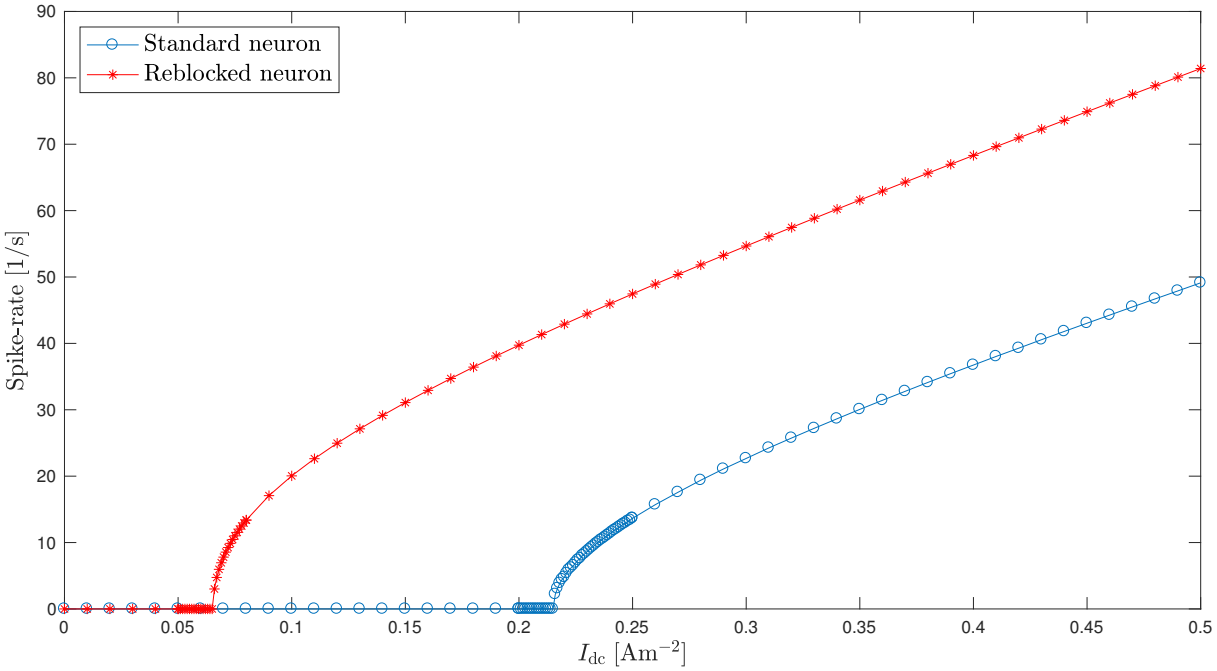

Figure 5.3: Current-to-firing-rate transfer functions for standard Wilson neuron (blue) and reblocked diffusive Wilson neuron (red) in the low-noise limit. Here, $B = 100$ for the reblocking corrections. The noise settings are same as in Fig. 5.2.

The simulations confirm that the system is stable for lower stimulus currents and eventually becomes unstable when I_{dc} reaches $I_{\mathrm{dc}}^{\mathrm{crit}} \approx 0.0652$ Am^{-2}, indicated by the birth of spikes shown in Fig. 5.2(b). The simulations are consistent with the stability predictions of eigenvalue analysis: in Fig. 5.1(b) the dominant eigenvalue crosses zero when I_{dc} approaches the critical value. Since the dominant eigenvalue is purely real, this transition marks a saddle–node bifurcation. This contrasts with the findings of Steyn-Ross and Steyn-Ross [72] who reported that transition to spiking occurred via a Hopf bifurcation. (The reason for this evident change in neuron behaviour was pointed out in page 84).

The comparison between the standard and reblocked transfer functions are shown in Fig. 5.3.

5.2 First-order Noise Limit

In this section, I extend our analysis by turning on the noise-dependent correction terms. Thus the revised drift corrections are,

$$G_1(V,R) = \boxed{d_0} + \boxed{d_1 V} + \boxed{d_2 V^2} + d_3 V^3 + d_4 V^4 + \boxed{d_5 VR} + d_6 V^2 R + \boxed{d_7 R}$$

$$G_2(V,R) = \boxed{d_8} + \boxed{d_9 R} + \boxed{d_{10} V} + \boxed{d_{11} V^2} + d_{12} V^3$$

where the drift coefficients are defined in Section 3.3.4, and the boxed terms are the newly added correction terms.

Here, I use the simplified versions of d_0, d_1, and d_8 (i.e., by ignoring the second-order noise terms) as presented in Section 4.3. I set microcell dimension, blocking ratio and diffusivities at

the same values as used earlier:

$$\ell = 10\ \mu\text{m}, \quad B = 100$$
$$D_b = D_i = 6.6 \times 10^{-4}\ \text{m}^2/\text{s}$$
$$D_R = D_{R,i} = 2.47 \times 10^{-13}\ \text{m}^4/\text{V}$$

I extract the values for the wavenumber integrals $\overline{c}_{j,i}$ that are required to calculate the correction coefficients from the previous chapter (see Table 5.1). In the small-noise analysis of the previous section I assumed negligible noise, but since we are enabling the noise dependent correction terms for present analysis, I now set the noise intensities at $\Gamma_b = 10^{-7}\ \text{m}^2\text{V}^2\text{s}^{-1}$ and $\Gamma_R = 10^{-7}\ \text{m}^2\text{s}^{-1}$. Table 5.2 lists the calculated values for the first-order correction coefficients.

Table 5.1: Values for wavenumber integrals approximated by Monte Carlo integration. Blocking ratio $B = 100$. Entries are extracted from Tables 4.2, 4.4, and 4.5.

Wavenumber integral	Value	Unit
$\overline{c}_{0,i}$	4.2863×10^{4}	m^{-2}s
$\overline{c}_{1,i} = \overline{c}_{7,i}$	-9.2492×10^{-2}	$\text{m}^{-2}\text{s}^{2}$
$\overline{c}_{2,i}$	-1.7796×10^{-6}	$\text{m}^{-2}\text{s}^{3}$
$\overline{c}_{4,i}$	2.7719×10^{10}	m^{-4}Vs
$\overline{c}_{5,i}$	8.3801×10^{14}	m^{-4}V
$\overline{c}_{8,i}$	-5.5825×10^{-2}	$\text{m}^{-2}\text{Vs}^{2}$
$\overline{c}_{9,i}$	8.6244×10^{2}	$\text{m}^{-2}\text{V}^{-1/2}\text{s}^{3/2}$
$\overline{c}_{10,i}$	9.1739×10^{1}	$\text{m}^{-2}\text{V}^{1/2}\text{s}^{3/2}$
$\overline{c}_{15,i}$	2.1281×10^{10}	m^{-4}s
$\overline{c}_{16,i}$	9.5923×10^{17}	m^{-6}s

$D_{i,e} = 6.6 \times 10^{-4}$, $D_i/100\ \text{m}^2/\text{s}$
$D_{R,i,e} = 2.47 \times 10^{-13}, 5.2761 \times 10^{-17}\ \text{m}^4/\text{V}$

Table 5.2: Calculated values for correction coefficients. Blocking ratio $B = 100$. Note that the correction coefficient values are different from Table 4.8, as different noise intensities are used here.

Correction coefficient	Value	Unit
$d_{0,i}$	-1.7861×10^{1}	Vs^{-1}
$d_{1,i}$	-5.5506×10^{2}	s^{-1}
$d_{2,i}$	1.0810×10^{3}	$\text{V}^{-1}\text{s}^{-1}$
$d_{3,i}$	7.8544×10^{5}	$\text{V}^{-2}\text{s}^{-1}$
$d_{4,i}$	1.3296×10^{7}	$\text{V}^{-3}\text{s}^{-1}$
$d_{5,i}$	3.0883	s^{1}
$d_{6,i}$	6.4306×10^{4}	$\text{V}^{-1}\text{s}^{-1}$
$d_{7,i}$	1.0368	Vs^{-1}
$d_{8,i}$	3.3657	s^{-1}
$d_{9,i}$	-1.7948×10^{-1}	s^{-1}
$d_{10,i}$	-3.9585	$\text{V}^{-1}\text{s}^{-1}$
$d_{11,i}$	-6.9997×10^{1}	$\text{V}^{-2}\text{s}^{-1}$
$d_{12,i}$	-5.4040×10^{4}	$\text{V}^{-3}\text{s}^{-1}$

$D_{i,e} = 6.6 \times 10^{-4}$, $D_i/100\ \text{m}^2/\text{s}$
$D_{R,i,e} = 2.47 \times 10^{-13}, 5.2761 \times 10^{-17}\ \text{m}^4/\text{V}$
$\Gamma_b = 10^{-7}\ \text{m}^2\text{V}^2\text{s}^{-1}$, $\Gamma_R = 10^{-7}\ \text{m}^2\text{s}^{-1}$

For a given value of dc stimulus current ($I_{\rm dc}$), I determine the steady-states of the homogeneous cortex by numerically solving the simultaneous equations,

$$F_1' = 0$$
$$F_2' = 0$$

where

$$F_1' \equiv \frac{dV}{dt} = -g(V)(V - E_{\rm Na}) - g_R R\,(V - E_{\rm K}) + \frac{I_{\rm dc}}{C} + d_0 + d_1 V + d_2 V^2 + d_3 V^3 + d_4 V^4 + d_5 V R + d_6 V^2 R + d_7 R \tag{5.4a}$$

$$F_2' \equiv \frac{dR}{dt} = \frac{1}{\tau_R}(-R + R_\infty(V)) + d_8 + d_9 R + d_{10} V + d_{11} V^2 + d_{12} V^3 \tag{5.4b}$$

I then calculate the Jacobian matrix, $\mathbf{J}$ at each equilibrium point,

$$\mathbf{J} = \begin{bmatrix} \frac{\partial F_1'}{\partial V} & \frac{\partial F_1'}{\partial R} \\ \frac{\partial F_2'}{\partial V} & \frac{\partial F_2'}{\partial R} \end{bmatrix}_{|(V^0,R^0)} \tag{5.5}$$

using the partial derivatives,

$$J_{11} = \frac{\partial F_1'}{\partial V} = -g(V) - (V_e - E_{\rm Na})(a_1 + 2\,a_2 V) - g_R R + d_1 + 2\,d_2 V + 3\,d_3 V^2 + 4\,d_4 V^3 + d_5 R + 2\,d_6 V R$$

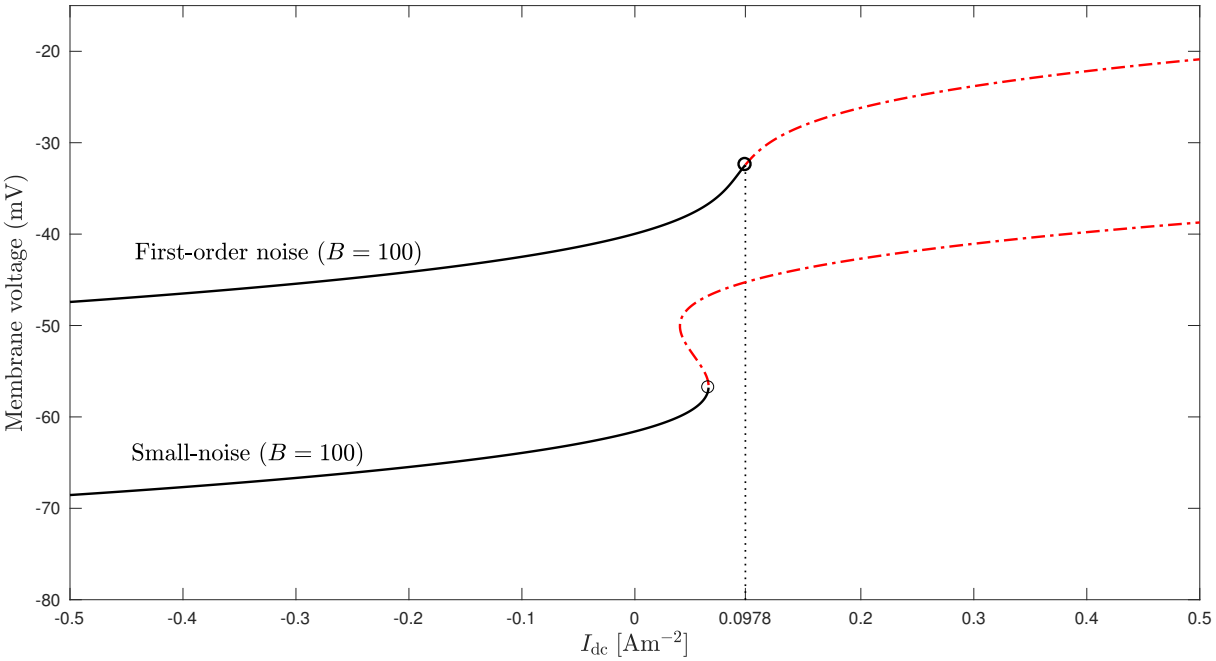

Figure 5.4: Steady-state distribution of membrane potential as a function of dc stimulus current for diffusive Wilson neuron reblocked with first-order noise corrections (upper trace), and compared with small-noise limit (lower trace). To improve visibility, the first-order noise trace has been displaced vertically upwards by 20 mV. The threshold currents for the two cases are $I_{\rm dc}^{\rm crit}$ ~0.0978 and 0.0652 Am^{-2} respectively. Periodic solutions exist to the right of saddle-node ($I_{\rm dc}^{\rm crit}$) similar to those shown in Fig. 2.14 but, omitted here for clarity.

$$
\begin{aligned}
J_{12} &= \frac{\partial F_1'}{\partial R} &&= -\,g_{R,b}(V - E_{\mathrm{K}}) + d_5 V + d_6 V^2 + d_7 \\
J_{21} &= \frac{\partial F_2'}{\partial V} &&= \frac{1}{\tau_b}(b_1 + 2\,b_2 V) + d_{10} + 2\,d_{11} V + 3\,d_{12} V^2 \\
J_{22} &= \frac{\partial F_2'}{\partial R} &&= -\,\frac{1}{\tau_b} + d_9
\end{aligned}
$$

The new steady-states and stability predictions are presented in Fig. 5.4. As a comparison, I illustrate the steady-states of small-noise limit analysis in the same figure. When compared with the small-noise limit (copied from Fig. 5.1(a)), we see that enabling the noise-dependent correction terms raises the threshold current from 0.0652 Am^{-2} to 0.0978 Am^{-2}, making the neuron less sensitive. Evidently, simultaneous increases in voltage and recovery noise intensities Γ_b and Γ_R shift the threshold current to the right. I perform a more detailed analysis of the effect of noise intensities on transition to spiking in the next section. I show that voltage and recovery noise intensities have contrary impacts on neuron sensitivity: raising Γ_b raises the threshold current, while raising Γ_R lowers the threshold, making the neuron more responsive.

The transition to spiking occurs via a saddle–node bifurcation, as was the case for the small-noise neuron. However, with the present noise settings we lose multiple steady-states (see Fig. 5.4).

5.3 The Effect of Voltage and Recovery Noise Intensities

In this section, I analyse the impact of variations in the voltage and recovery noise intensities. I first turn off recovery noise Γ_R to investigate the effect of voltage noise Γ_b on transition to firing,

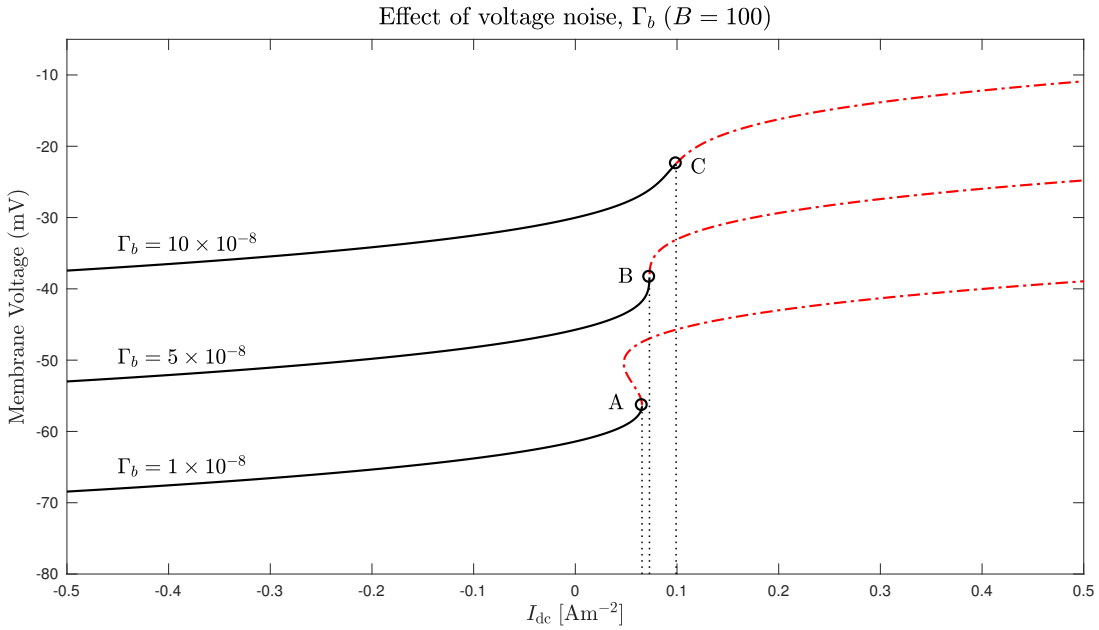

Figure 5.5: Steady state distribution of reblocked diffusive Wilson neuron for three voltage noise intensity settings: 1×10^{-8}, 5×10^{-8}, and 10×10^{-8} $\mathrm{m^2V^2s^{-1}}$. Here, Γ_R is set to zero. Threshold currents marked by A, B, and C are $I_{\mathrm{dc}}^{\mathrm{crit}}$ ∼0.0656, 0.0729, and 0.0991 Am^{-2} respectively. Periodic solutions exist to the right of saddle-node ($I_{\mathrm{dc}}^{\mathrm{crit}}$) similar to those shown in Fig. 2.14 but, omitted here for clarity. (To aid visibility, $\Gamma_b = 5 \times 10^{-8}$ and $\Gamma_b = 1 \times 10^{-7}$ traces are displaced vertically by 15 mV and 30 mV respectively.)

exploring how the transition to firing varies with Γ_b across the range $0 \leq \Gamma_b \leq 10^{-7}$ $\mathrm{m^2V^2s^{-1}}$. Note that I set upper bound as 10^{-7}, because when $\Gamma_b > 10^{-7}$, the threshold current shifts beyond 10 $\mathrm{Am^{-2}}$ (1000 $\mu\mathrm{Acm^{-2}}$), which I assume has no biophysical relevance (According to the literature, current density threshold for exciting the motor cortex area of the brain is ∼2.5 $\mathrm{Am^{-2}}$ [46]).

In Fig. 5.5, I present steady-state distributions of membrane potential as a function of dc stimulus current for three different voltage noise Γ_b settings: $(1, 5, 10) \times 10^{-8}$ $\mathrm{m^2V^2s^{-1}}$. We observe that as Γ_b increases, the critical current shifts to the right making the neuron less sensitive. We also see that as Γ_b is increased the S-bend gradually flattens and at some point we lose multiple steady states.

I then fix Γ_b at 10^{-10} $\mathrm{m^2V^2s^{-1}}$ and study the effect of recovery noise intensity on transition to firing. I set recovery noise intensity Γ_R across the range $0 \leq \Gamma_R \leq 10^{-5}$ $\mathrm{m^2s^{-1}}$. When Γ_R exceeds 10^{-5} the threshold current becomes negative. Figure 5.6 shows steady-state distributions of membrane potential as a function of dc stimulus current for three different voltage noise Γ_R settings: 10^{-7}, 10^{-6}, and 10^{-5} $\mathrm{m^2s^{-1}}$. When I increase recovery noise intensity at fixed voltage noise, threshold current shifts to the left indicating that the neuron becomes more sensitive. However, in all cases the multiple steady-state nature is preserved. In Fig. 5.7, I present a more detailed survey of the change in critical current as the voltage and recovery noise intensities are varied independently.

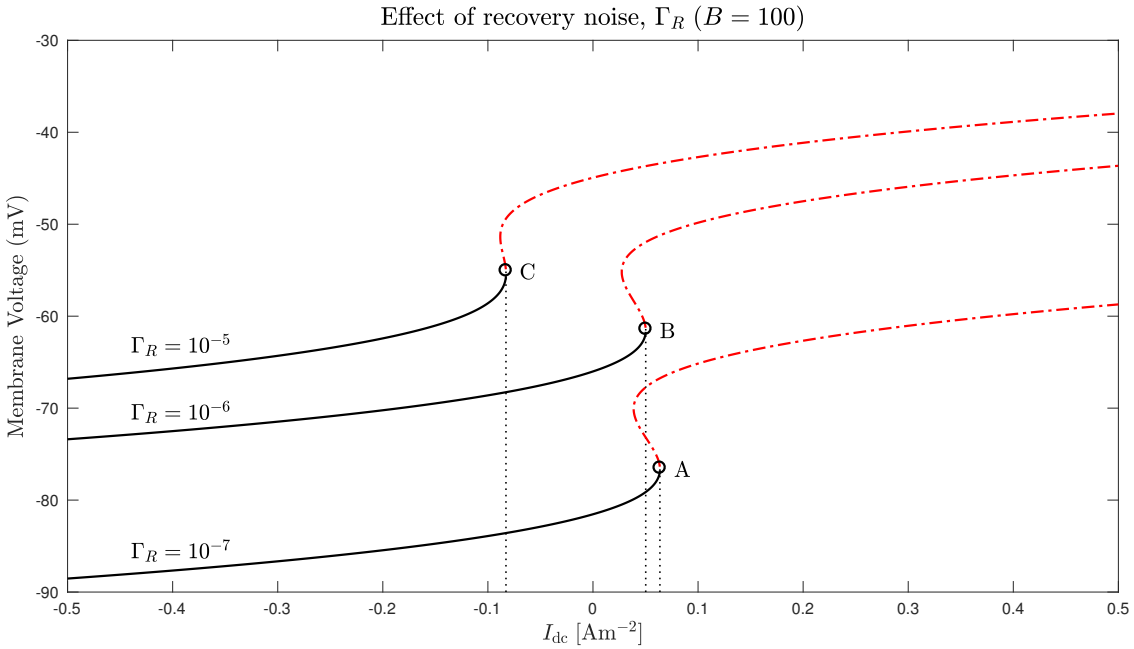

Figure 5.6: Steady state distribution of reblocked diffusive Wilson neuron for three recovery noise intensity settings: 10^{-7}, 10^{-6}, and 10^{-5} $\mathrm{m^2s^{-1}}$. Here, Γ_b is fixed at 10^{-10} $\mathrm{m^2V^2s^{-1}}$. Threshold currents marked by A, B, and C are $I_{\mathrm{dc}}^{\mathrm{crit}}$ ∼0.0637, 0.0502, and −0.0826 $\mathrm{Am^{-2}}$ respectively. Periodic solutions exist to the right of saddle-node ($I_{\mathrm{dc}}^{\mathrm{crit}}$) similar to those shown in Fig. 2.14 but, omitted here for clarity. (To aid visibility, $\Gamma_b = 10^{-6}$ and $\Gamma_b = 10^{-7}$ traces have been displaced vertically by −5 mV and −20 mV respectively.)

I conclude that increasing voltage noise intensity makes the reblocked Wilson neuron less sensitive, while increasing recovery noise makes the neuron more sensitive.

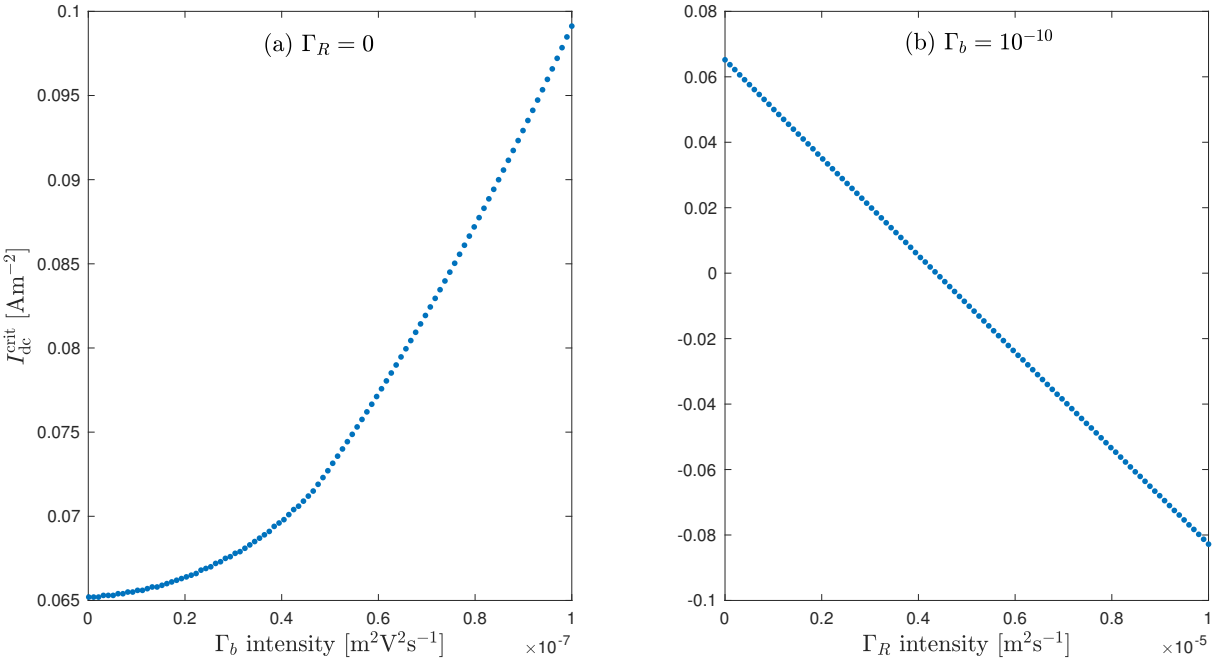

Figure 5.7: Effect of independent variations in (a) voltage noise (with $\Gamma_R = 0$), and (b) recovery noise (with $\Gamma_b = 10^{-10}$ m^{2}V^{2}s^{-1}) ($B = 100$).

5.4 Analysis of Individual Correction Term Contributions

In this section I investigate the impact of each correction term towards the reblocking corrections,

$$G_1(V,R) = d_0 + d_1V + d_2V^2 + d_3V^3 + d_4V^4 + d_5VR + d_6V^2R + d_7R$$

$$G_2(V,R) = d_8 + d_9R + d_{10}V + d_{11}V^2 + d_{12}V^3$$

in the Wilson's equations (Eqs (5.1)). I identify the significance of these correction terms by comparing them with the other terms in the equation. Since we consider a homogeneous cortex I rewrite Eqs (5.1) as,

$$\frac{\partial V}{\partial t} = \underbrace{-g(V)(V-E_{\rm Na})}_{\text{term V1}}\underbrace{-g_R R.(V-E_{\rm K})}_{\text{term V2}} + \frac{I^{\rm dc}}{C} + G_1(V,R) \tag{5.6a}$$

$$\frac{\partial R}{\partial t} = \underbrace{-\frac{R}{\tau_b}}_{\text{term R1}} + \underbrace{\frac{R_\infty(V)}{\tau_b}}_{\text{term R2}} + G_2(V,R) \tag{5.6b}$$

For this analysis I set the three parameters: microcell dimension, noise intensities and diffusivities at,

$$\begin{aligned}
\ell &= 10\ \mu\text{m} \\
D_b &= D_i = 6.6\times 10^{-4}\ \text{m}^2/\text{s} \\
D_R &= D_{R,i} = 2.47\times 10^{-13}\ \text{m}^4/\text{V} \\
\Gamma_b &= 10^{-10}\ \text{m}^2\text{V}^2\text{s}^{-1} \\
\Gamma_R &= 10^{-10}\ \text{m}^2\text{s}^{-1}
\end{aligned}$$

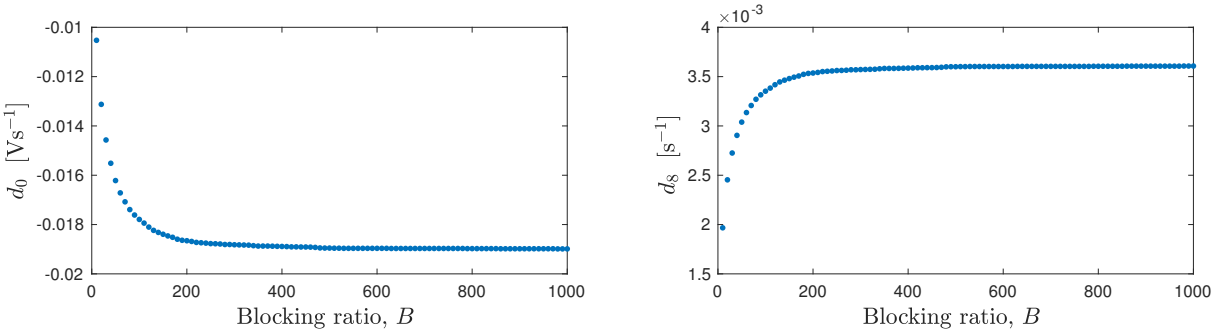

Figure 5.8: Voltage- and recovery-independent correction terms as a function of blocking.

I explore the individual correction terms (d_1V, d_2V^2, d_3V^3, d_4V^4, d_5VR, d_6V^2R, d_7R, d_9R, $d_{10}V$, $d_{11}V^2$, $d_{12}V^3$) in a range of blocking ratios $1 \leq B \leq 1000$ in two regimes: sub-threshold and super-threshold. Note that the first two correction terms of the voltage and recovery equations (d_0 and d_8) have same values in both regimes as they are independent of V and R (see Fig. 5.8).

For each B, I first find the critical current for spiking. For the sub-threshold regime, I use a stimulus just below the threshold ($I_{\mathrm{dc}} = I_{\mathrm{dc}}^{\mathrm{crit}} - 0.01$) and conduct 1 s simulations for each blocking. Due to the static nature of the sub-threshold regime, the voltage and recovery variables stay at their equilibrium values throughout the simulation. (e.g., sub-threshold time series for $B = 100$ are shown in red-dashed lines in Figs 5.9 and 5.10).

However, the analysis in the super-threshold regime is more challenging, because of the fact that the system is now dynamic as demonstrated in the super-threshold time series for $B = 100$ in Figs 5.9 and 5.10. Unlike in the sub-threshold regime, the voltage and recovery variables

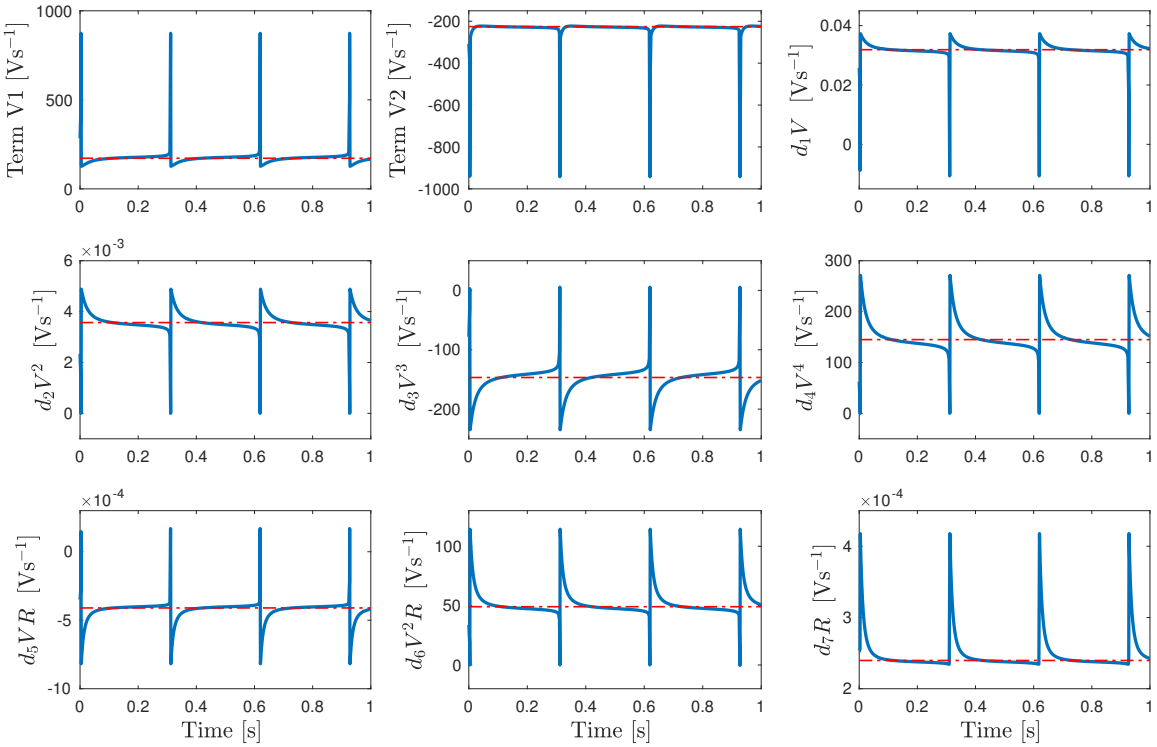

Figure 5.9: Time series of the individual terms of voltage equation (5.6a) for $B = 100$. Blue lines show super-threshold time series; red-dashed lines show sub-threshold equilibrium values.

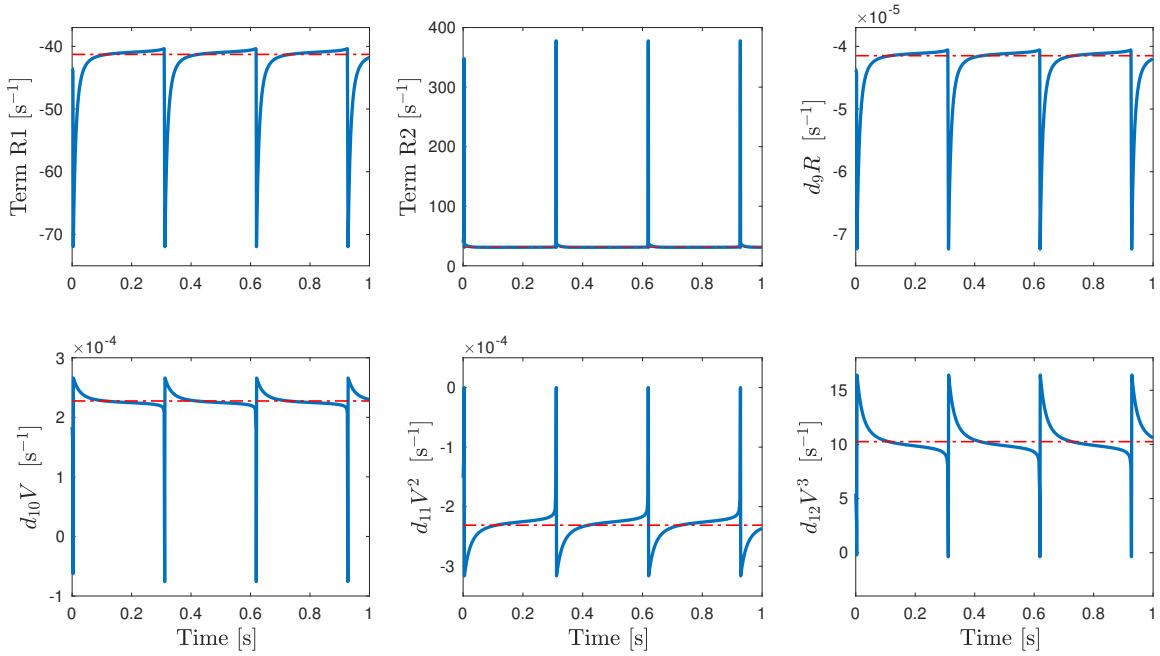

Figure 5.10: Time series of the individual terms of recovery equation (5.6b) for $B = 100$. Blue lines show super-threshold time series; red-dashed lines show sub-threshold equilibrium values.

follow spiking trajectories throughout the simulation. Therefore we need a different measure to compare the impact of each correction term. I elect the method of using root mean square (rms) values.

For each B, I conduct a 20 s simulation using a stimulus just above threshold ($I_{\mathrm{dc}} = I_{\mathrm{dc}}^{\mathrm{crit}} + 0.01$) and calculate the rms value of each term in the voltage and recovery equations using MATLAB `rms`. For a set of n values $\{x_1, x_2, \ldots, x_n\}$, rms is defined as:

$$\mathrm{rms} = \sqrt{\frac{1}{n}\sum_i x_i^2}$$

In Figs 5.11 and 5.12 I compare the blocking dependencies of the super-threshold rms terms (blue) with the sub-threshold variations (red). Thus allows us to identify d_3V^3, d_4V^4, and d_6V^2R as dominant voltage correction terms, and $d_{12}V^3$ as the dominant recovery correction term. Fig. 5.13 highlights these significant correction terms.

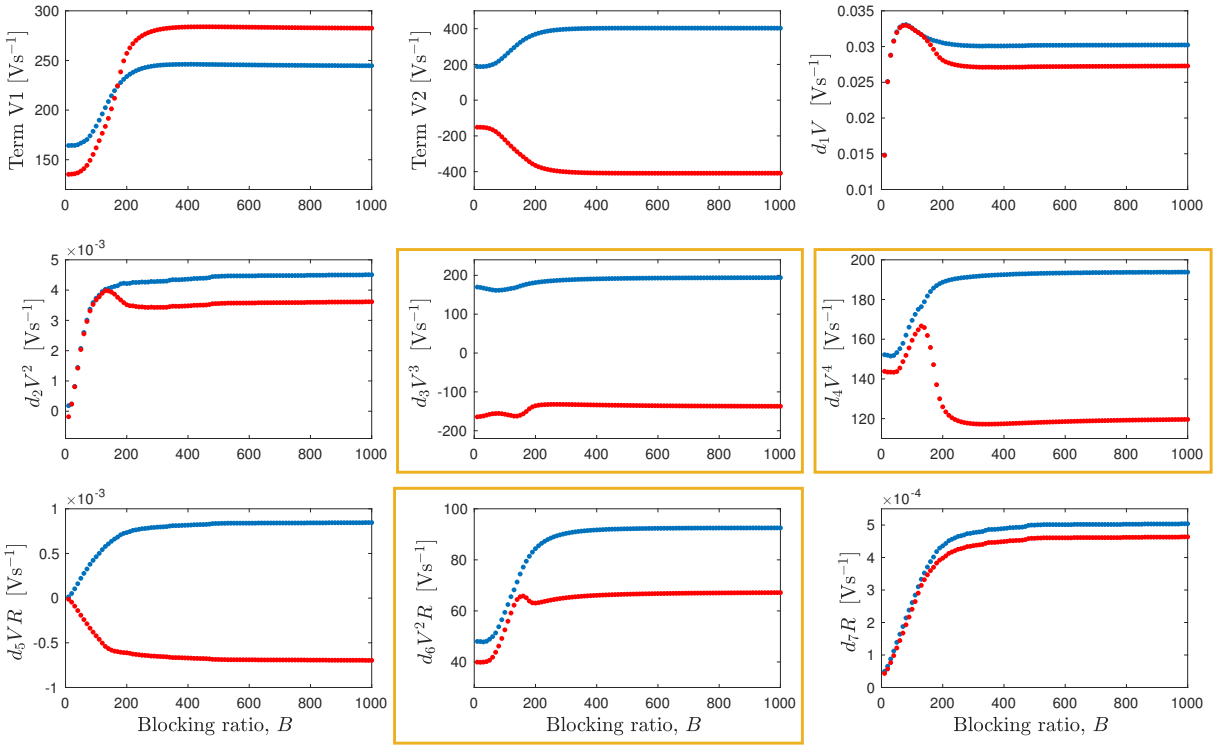

Figure 5.11: Variation of the individual terms of the voltage equation (5.6a) as a function of blocking. Red-dotted trends show the sub-threshold blocking dependencies; blue-dotted trends show the super-threshold rms variations. Boxed subplots show the dominant correction terms.

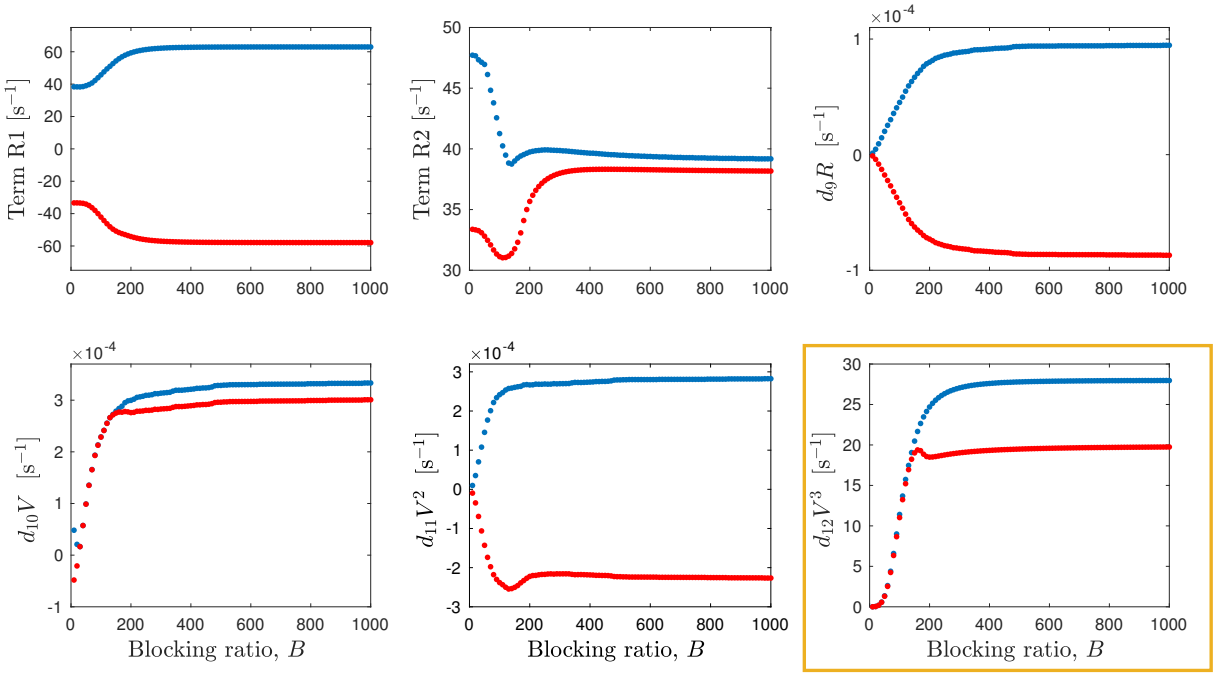

Figure 5.12: Variation of the individual terms of the recovery equation (5.6b) as a function of blocking. Red-dotted trends show the sub-threshold blocking dependencies; blue-dotted trends show the super-threshold rms variations. Single boxed subplot indicates the dominant correction term.

	$\overline{c}_0$	$\overline{c}_1$	$\overline{c}_2$	$\overline{c}_3$	$\overline{c}_4$	$\overline{c}_5$	$\overline{c}_{6a}$	$\overline{c}_{6b}$	$\overline{c}_8$	$\overline{c}_{10}$	$\overline{c}_{12}$	$\overline{c}_{15}$	$\overline{c}_{16}$	
d_0	●	●	●	●			●	●	●	●				const.
d_1	●	●	●	●					●					V
d_2		●											●	V^2
d_3		●			●	●								V^3
d_4					●									V^4
d_5		●												VR
d_6					●									V^2R
d_7		●										●		R
d_8	●	●	●						●					const.
d_9		●												R
d_{10}		●										●		V
d_{11}		●												V^2
d_{12}					●									V^3

	$\overline{c}_0$	$\overline{c}_1$	$\overline{c}_2$	$\overline{c}_3$	$\overline{c}_4$	$\overline{c}_5$	$\overline{c}_{6a}$	$\overline{c}_{6b}$	$\overline{c}_8$	$\overline{c}_{10}$	$\overline{c}_{12}$	$\overline{c}_{15}$	$\overline{c}_{16}$
g_0			●								●		
g_1			●						●				
g_2			●										
g_3													
g_4													
g_5			●										
g_6			●										
g_7			●										

Figure 5.13: Copies of Figs. 4.5 and 4.6 showing the most-significant drift (d_j) and diffusion (g_j) correction terms for the first-order noise limit. In the right-hand figure the R0-restricted wavenumber integrals ($\overline{c}_3$, $\overline{c}_{6a}$, $\overline{c}_{6b}$ and $\overline{c}_{12}$) are excluded when first-order noise limit is considered.

In Fig. 5.14, I compare the magnitudes of dominant corrections in voltage and recovery equations with the size of the other terms in original Wilson equations. I show the discrepancy between the full corrections and the most-significant corrections. Since the discrepancies are much less than 0.02%, we can conclude that the impact of other correction terms (d_1V, d_2V^2, d_5VR, d_7R, d_9R, $d_{10}V$, and $d_{11}V^2$) is not pronounced and we can safely ignore these less-significant correction terms.

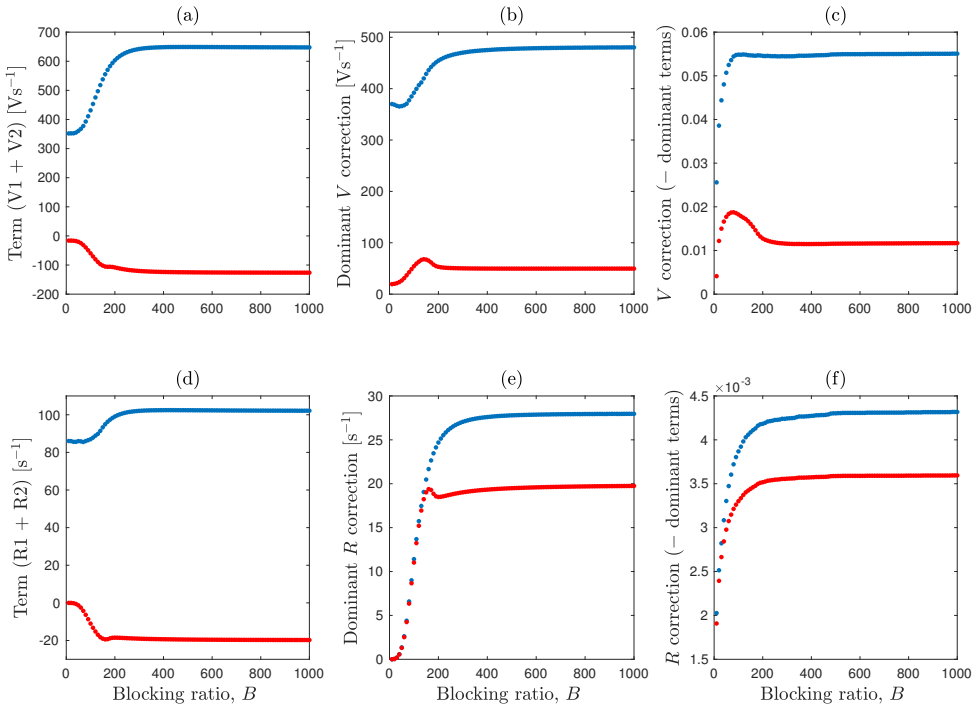

Figure 5.14: Comparison of the full voltage and recovery corrections with the first two terms of the voltage and recovery equations of original Wilson neuron (5.6). Red-dotted trends show the sub-threshold blocking dependencies; blue-dotted lines show the super-threshold rms variations. Here, (a) and (d) are the variations of first two terms in the voltage and recovery equations; (b) and (e) are dominant voltage and recovery corrections; (c) and (f) are discrepancies between the full corrections and the most-significant correction terms in voltage and recovery equations.

5.5 Chapter Summary

In this chapter, I explored a simple demonstration of the True-field model by turning off the chemical synapses. This adaptation converted the 20-dimensional True-field system into a single reblocked Wilson neuron. I considered the spatially homogeneous limit and analysed the reblocked neuron in two cases: first blocked with only noise independent corrections (small-noise limit) and then by enabling the noise-dependent corrections (first-order noise limit). For both cases I found steady states, conducted a stability analysis and compared the behaviour of the reblocked Wilson neuron with the behaviour of original Wilson neuron. I identified some corrections in the previous small-noise limit analysis done by Steyn-Ross and Steyn-Ross (2016) and that caused a change in the mode of bifurcation to spiking from Hopf to a saddle–node.

I then analysed the effect of voltage and recovery noise intensities Γ_b and Γ_R on threshold for spiking. I found that the simultaneous increase in Γ_b and Γ_R makes neuron less sensitive; increase of Γ_b at fixed Γ_R ($\Gamma_R = 0$) makes neuron less sensitive; and increase of Γ_R at fixed Γ_b ($\Gamma_b = 10^{-10}$) makes neuron more sensitive.

Finally by comparing the magnitudes of the correction terms in both sub-threshold and super-threshold regimes, I identified the most significant voltage and recovery correction terms as (d_3V^3, d_4V^4, and d_6V^2R) and $d_{12}V^3$ respectively.

In the next chapter, I use the knowledge about the noise intensities and the dominant correction terms gained in this chapter to tune the parameters in the 20-dimensional True-field model which we can simulate in a 2D grid.

Chapter 6

True-field Cortex

The goal of this chapter is to tune the True-field parameters to enable the model to reproduce different realistic cortical behaviours. I first identify the set of primary parameters which are evaluated, then kept fixed for subsequent analyses. Two approaches are used: point simulations of a homogeneous two-neuron cortex, and full 2D grid simulations of a patch of cortical tissue. The point simulations provide an economical way of tuning the secondary parameters as I seek to demonstrate that True-field can generate normal brain behaviours across multiple scales using a range of blocking ratios: intracellular spiking behaviour for low blocking, and collective population events (EEG patterns) for higher blocking. Once the point-simulation tunings are complete, I run a series of grid simulations to investigate spatial variations and interactions in firing activity across a 2D sheet of cortical tissue.

6.1 True-field Equations

In Section 3.3.6, I presented the spatially rescaled True-field equations with compact labelling convention ab which cycles through $\{ee,\ ei,\ ie,\ ii\}$. In this section I expand the gathered equations (3.23), and use symmetry to identify a small reduction in the equation set.

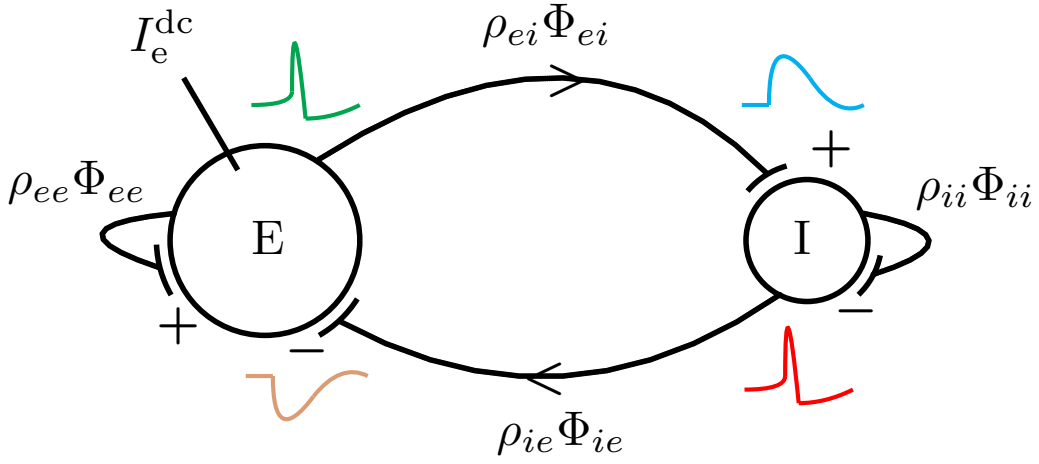

Figure 6.1: Synaptic interactions of excitatory (E) and inhibitory (I) neural populations within the True-field model. $I_{\mathrm{e}}^{\mathrm{dc}}$ is the input current to E. Spiking activity of E (green) and I (red) generate positive (blue) and negative (brown) voltage perturbations ($\rho_{eb}\phi_{eb}$ and $\rho_{ib}\phi_{ib}$) in the receiving neuron respectively. ρ_{eb}, ρ_{ib} are synaptic gains with $\rho_{eb} > 0$ (excitation) and $\rho_{ib} < 0$ (inhibition).

Fig. 6.1 is a cartoon representation of the synaptic interactions within the True-field model for a pair of interacting excitatory (E) and inhibitory (I) populations. Anatomical evidence [54] indicates that the excitatory population in cortex is four times larger than the inhibitory population so we set the number of excitatory synaptic connections at four times the number of inhibitory connections: $N_{eb} = 4N_{ib}$.

Membrane Potential

$$\frac{\partial V_e}{\partial t} = -g(V_e)(V_e - E_{\rm Na}) - g_{R,b}R_e \cdot (V_e - E_{\rm K}) \; + \; D_e \, \nabla^2 V_e \; + \; \rho_{ee} \, \Phi_{ee} \; + \; \rho_{ie} \, \Phi_{ie} \\ + \; I_e^{\rm dc}/C + G_{1,e} + \sum_{k=1}^{16} C_{1k} \, \xi_k \tag{6.1a}$$

$$\frac{\partial V_i}{\partial t} = -g(V_i)(V_i - E_{\rm Na}) - g_{R,b}R_i \cdot (V_i - E_{\rm K}) \; + \; D_i \, \nabla^2 V_i \; + \; \rho_{ei} \, \Phi_{ei} \; + \; \rho_{ii} \, \Phi_{ii} \\ + G_{1,i} + \sum_{k} C_{2k} \, \xi_k \tag{6.1b}$$

The excitatory and inhibitory membrane potentials V_e and V_i are functions of time t and 2D space (x, y): $V_e = V_e(x, y, t)$ and $V_i = V_i(x, y, t)$. The first equation is the stochastic form of the Wilson neuron, modified to include diffusive and synaptic flux, and drift corrections ($G_{1,(e,i)}$). The firing activity of excitatory population generates positive voltage perturbations $\rho_{ee} \, \Phi_{ee}$, $\rho_{ei} \, \Phi_{ei}$ in the excitatory and inhibitory populations respectively. Similarly, the firing activity of inhibitory population generates negative voltage perturbations $\rho_{ie} \, \Phi_{ie}$, $\rho_{ii} \, \Phi_{ii}$ in the excitatory and inhibitory populations respectively (see Fig. 6.1).

Recovery

$$\frac{\partial R_e}{\partial t} = -\frac{1}{\tau_e}[R_e - R_\infty(V_e)] \; + \; \frac{D_{Re} \nabla^4 V_e}{\tau_e} + G_{2,e} + \sum_k C_{3k} \, \xi_k \tag{6.2a}$$

$$\frac{\partial R_i}{\partial t} = -\frac{1}{\tau_i}[R_i - R_\infty(V_i)] \; + \; \frac{D_{Ri} \nabla^4 V_i}{\tau_i} + G_{2,i} + \sum_k C_{4k} \, \xi_k \tag{6.2b}$$

The form of excitatory and inhibitory recovery equations is the stochastic version of the Wilson neuron, modified to include diffusive flux and drift corrections ($G_{2,(e,i)}$).

Synaptic Flux

$$\frac{d\Phi_{ee}}{dt} = Z_{ee} \tag{6.3a}$$

$$\frac{dZ_{ee}}{dt} = -2\gamma_{ee} Z_{ee} - \gamma_{ee}^2 \, \Phi_{ee} + \gamma_{ee}^2 \, N_{eb} \, \psi_{ee}(\overline{V}_e) \, \phi_{eb} + \sum_k C_{6,k} \, \xi_k \tag{6.3b}$$

$$\frac{d\Phi_{ei}}{dt} = Z_{ei} \tag{6.3c}$$

$$\frac{dZ_{ei}}{dt} = -2\gamma_{ei} Z_{ei} - \gamma_{ei}^2 \, \Phi_{ei} + \gamma_{ei}^2 \, N_{eb} \, \psi_{ei}(\overline{V}_i) \, \phi_{eb} + \sum_k C_{8,k} \, \xi_k \tag{6.3d}$$

$$\frac{d\Phi_{ie}}{dt} = Z_{ie} \tag{6.3e}$$

$$\frac{dZ_{ie}}{dt} = -2\gamma_{ie}Z_{ie} - \gamma_{ie}^2\,\Phi_{ie} + \gamma_{ie}^2\,N_{ib}\,\psi_{ie}(\overline{V}_e)\,\phi_{ib} + \sum_k C_{10,k}\,\xi_k \tag{6.3f}$$

$$\frac{d\Phi_{ii}}{dt} = Z_{ii} \tag{6.3g}$$

$$\frac{dZ_{ii}}{dt} = -2\gamma_{ii}Z_{ii} - \gamma_{ii}^2\,\Phi_{ii} + \gamma_{ii}^2\,N_{ib}\,\psi_{ii}(\overline{V}_i)\,\phi_{ib} + \sum_k C_{12,k}\,\xi_k \tag{6.3h}$$

Equations (6.3) are the four dendritic responses (Φ_{ee}, Φ_{ei}, Φ_{ie}, Φ_{ii}) generated by the incoming flux of presynaptic spiking events. The dendritic responses are modelled as alpha-function impulses (see Fig. 1.7) that represent the EPSP (Φ_{eb}) and IPSP (Φ_{ib}) postsynaptic responses.

Axonal Propagation of Spiking Activity

$$\frac{d\phi_{eb}}{dt} = \Pi_{eb} \tag{6.4a}$$

$$\begin{aligned}\frac{\partial\Pi_{eb}}{\partial t} &= -2v\Lambda_{eb}\Pi_{eb} - [(v\Lambda_{eb})^2 - (v\nabla)^2]\,\phi_{eb} + (v\Lambda_{eb})^2 S_e(V_e - V_e^{\text{rest}}).H_e(V_e) \\ &\quad + \sum_k C_{14,k}\,\xi_k\end{aligned} \tag{6.4b}$$

$$\frac{d\phi_{ib}}{dt} = \Pi_{ib} \tag{6.4c}$$

$$\begin{aligned}\frac{\partial\Pi_{ib}}{\partial t} &= -2v\Lambda_{ib}\Pi_{ib} - [(v\Lambda_{ib})^2 - (v\nabla)^2]\,\phi_{ib} + (v\Lambda_{ib})^2 S_i(V_i - V_i^{\text{rest}}).H_i(V_i) \\ &\quad + \sum_k C_{16,k}\,\xi_k\end{aligned} \tag{6.4d}$$

where the $H_{e,i}$ are Heaviside functions used to detect the presence of a spike event,

$$H_e(V_e) = \begin{cases} 1 & \text{if } V_e > V_e^{\text{thresh}} \\ 0 & \text{if } V_e \leq V_e^{\text{thresh}} \end{cases}$$

and

$$H_i(V_i) = \begin{cases} 1 & \text{if } V_i > V_i^{\text{thresh}} \\ 0 & \text{if } V_i \leq V_i^{\text{thresh}} \end{cases}$$

These are stochastic versions of the Robinson damped-wave equation of [67], but modified to include a Boolean mask (highlighted in red) to ensure that synaptic flux is only generated when membrane voltage exceeds a threshold value, $V_{e,i}^{\text{thresh}}$ here taken to be -20 mV. Thus PSP generation in Eqs (6.3) is possible only after a spike event has been detected.

To simplify the set of wave equations, we assume that the incoming flux depends only on the source of activity and not the target, thus $\phi_{ee} = \phi_{ei}$ and $\phi_{ie} = \phi_{ii}$. This reduces the number of first-order differential equations in the True-field model from 22 to 18.

Average Membrane Potential

$$\frac{d\overline{V}_e(t)}{dt} = -\frac{1}{T}\big[\,\overline{V}_e(t) - V_e(t)\big] \tag{6.5a}$$

$$\frac{d\overline{V}_i(t)}{dt} = -\frac{1}{T}\big[\,\overline{V}_i(t) - V_i(t)\big] \tag{6.5b}$$

$\overline{V}_e$ and $\overline{V}_i$ represent the temporally-smoothed excitatory and inhibitory membrane potentials respectively. The characteristic time-scale T is long compared to the duration of a single spike event. In this thesis I have set T at 10 times the duration of a spike. The magnitudes of the dendritic responses in Eqs (6.3) are controlled by the deviation of bar variables ($\overline{V}_{e,i}$) from their respective synaptic reversal potentials.

Noise Sources

In Eqs (6.1) to (6.5), C_{jk} denotes the $(j,k)^{\text{th}}$ element of a 16×16 noise-amplitude matrix $\mathbf{C}$ obeying $\mathbf{C}\mathbf{C}^{\mathrm{T}} = \mathbf{B}$ where $\mathbf{B}$ is the noise intensity matrix. The ξ_k (with k = 1:4, 6:2:16) are 10 independent white-noise sources that are delta-correlated in time and 2D space. Due to the simplification of correction coefficients made in Section 4.3 by setting squared-noise terms $\Gamma_b^2 = 0$, $\mathbf{B}$ becomes a diagonal matrix with the nonzero elements given by,

$$\begin{aligned}
B_{11} &= -2(B\ell)^2 G_{3,e} + \Gamma_e, & B_{22} &= -2(B\ell)^2 G_{3,i} + \Gamma_i \\
B_{33} &= \Gamma_{R_e}, & B_{44} &= \Gamma_{R_i} \\
B_{66} &= \Gamma_{Z_{ee}}, & B_{88} &= \Gamma_{Z_{ei}} \\
B_{10,10} &= \Gamma_{Z_{ie}}, & B_{12,12} &= \Gamma_{Z_{ii}} \\
B_{14,14} &= \Gamma_{\Pi_{eb}}, & B_{16,16} &= \Gamma_{\Pi_{ib}}
\end{aligned}$$

B =

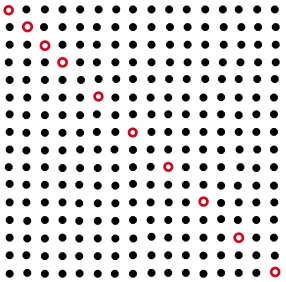

With this diagonal symmetry, the noise amplitudes simplify to $C_{jk} \to Cjj = \sqrt{B_{jj}}$.
$G_{3,e}$ and $G_{3,i}$ are reblocking diffusion corrections from Eq. (3.19).

6.2 Parameter Values of the True-field Model

Tuning the model to ensure biologically plausible cortical behaviour is challenging, requiring careful selection and balancing of parameter values. There are 14 model parameters:

- recovery time constants of excitatory and inhibitory spiking neurons (τ_e, τ_i)
- spike normalisation (inverse spike area) of excitatory and inhibitory action potentials (S_e, S_i)
- mean number of synaptic connections (N_{eb}, N_{ib})
- synaptic gains (ρ_{ee}, ρ_{ie}, ρ_{ei}, ρ_{ii})
- voltage and recovery diffusivities (D_b, D_R)
- voltage and recovery noise intensities (Γ_b, Γ_R)

In this section, I explain how values for the first six parameters (time constants, area of excitatory and inhibitory spikes, number of synaptic connections) were established. These parameters then

remain fixed for all subsequent analyses. In the next section I describe how the other parameters were tuned to reproduce cortical dynamics at multiple scales.

6.2.1 Setting Primary Parameters

In human cortex, inhibitory neurons are fast-spiking (FS) cells while excitatory neurons are regular-spiking (RS). Spike widths at half-amplitude average 0.95 ms for RS cells and 0.60 ms for FS cells [86]. This was achieved by setting $\tau_i = 5.6$ ms for the inhibitory time constant, and $\tau_e = 2\tau_i$ for the excitatory time constant. We observe in Fig. 6.2 that the inhibitory spikes are narrower and slightly reduced in height when compared with the excitatory spikes. The spike normalization, S_a (inverse-area) is then computed numerically via

$$S_a \;=\; \left[\int_{\text{spike}} (V_a(t) - V_a^{\text{rest}})\, dt\right]^{-1}$$

as defined in Eq. (3.10g), giving:

$$\begin{aligned} S_e &= 7.9861 \times 10^3 \text{ V}^{-1}\text{s}^{-1} \\ S_i &= 1.3399 \times 10^4 \text{ V}^{-1}\text{s}^{-1} \end{aligned}$$

As mentioned previously in Section 6.1, by considering the availability of excitatory and inhibitory neurons $(4:1)$ in the cortex we set the mean number of synaptic connections $N_{eb} = 1200$ and $N_{ib} = 300$. All other parameters that are not specified in Section 6.2 are adopted from the Waikato mean-field model. Table 6.1 lists the True-field parameters.

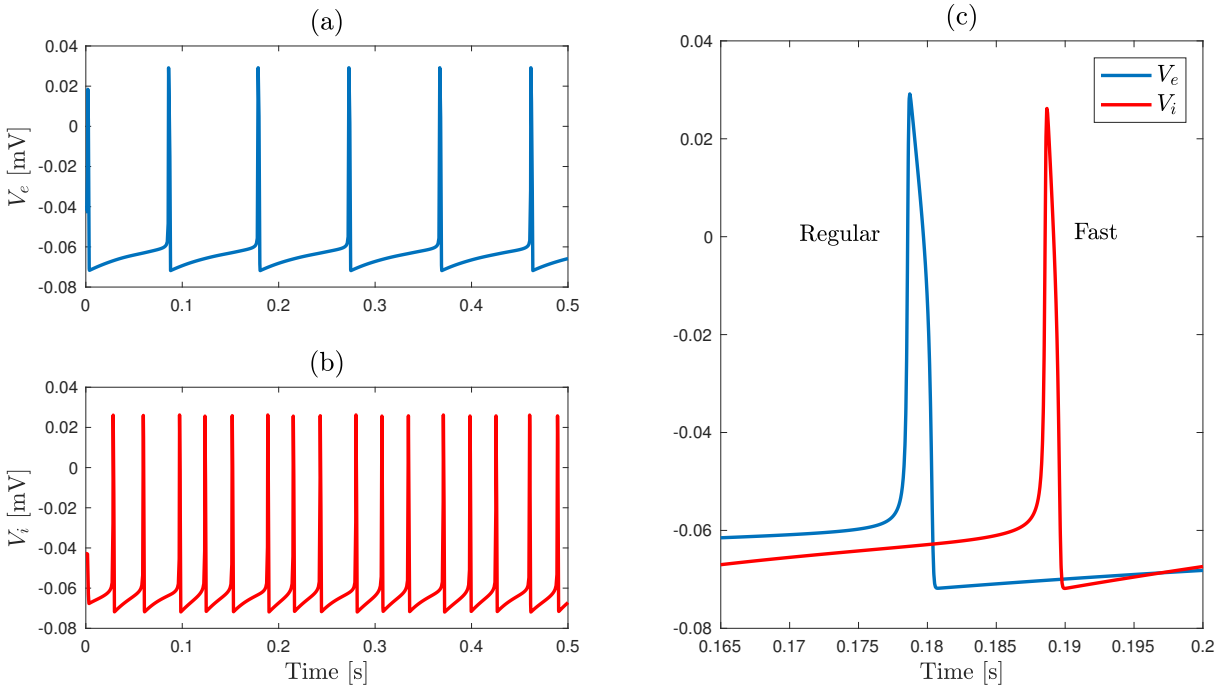

Figure 6.2: Stochastic simulations to show the action potentials generated in the True-field model by (a) excitatory and (b) inhibitory neurons. (c) Comparison between excitatory (RS) and inhibitory (FS) spike shapes. Here, $\tau_i = 5.6$ ms, $\tau_e = 2\tau_i$ and $I^{\text{dc}} = 0.02$ Am^{-2}. Simulation time step is $\Delta t = 10\,\mu$s.

Table 6.1: Symbol definitions and parameter values for True-field model.

Symbol	Description	Value	Unit
$\tau_{e,i}$	recovery time constants	$11.2, 5.6$	ms
$V_{e,i}^{\text{rest}}$	resting potential	$-60, -60$	mV
$V_{e,i}^{\text{rev}}$	reversal potential	$0, -70$	mV
γ_{eb}	excitatory synaptic rate constant	170	s^{-1}
γ_{ib}	inhibitory synaptic rate constant	100	s^{-1}
Λ_{eb}	inverse length scale for excitatory connections	200	m^{-1}
Λ_{ib}	inverse length scale for inhibitory connections	400	m^{-1}
$N_{eb,ib}$	mean number of synaptic connections	$1200, 300$	-
v	mean axonal conduction speed	0.2	ms^{-1}
T	characteristic time scale for average membrane potential (Eq. (6.5))	19	ms

6.3 True-field Simulations

I use two approaches to tune the secondary parameters of the model to establish cortical dynamics at multiple scales.

6.3.1 Point Simulations

Under point simulations we consider a homogeneous two neuron cortex, without attempting to address 2D space (x, y). Thus the diffusion terms in Eqs (6.1), (6.2), and (6.4) are set to zero ($\nabla^2 = 0$ and $\nabla^4 = 0$). Point simulations are simple, efficient, and fast, therefore enable us to run a series of simulations and tune the parameters looking for the desired behaviour at

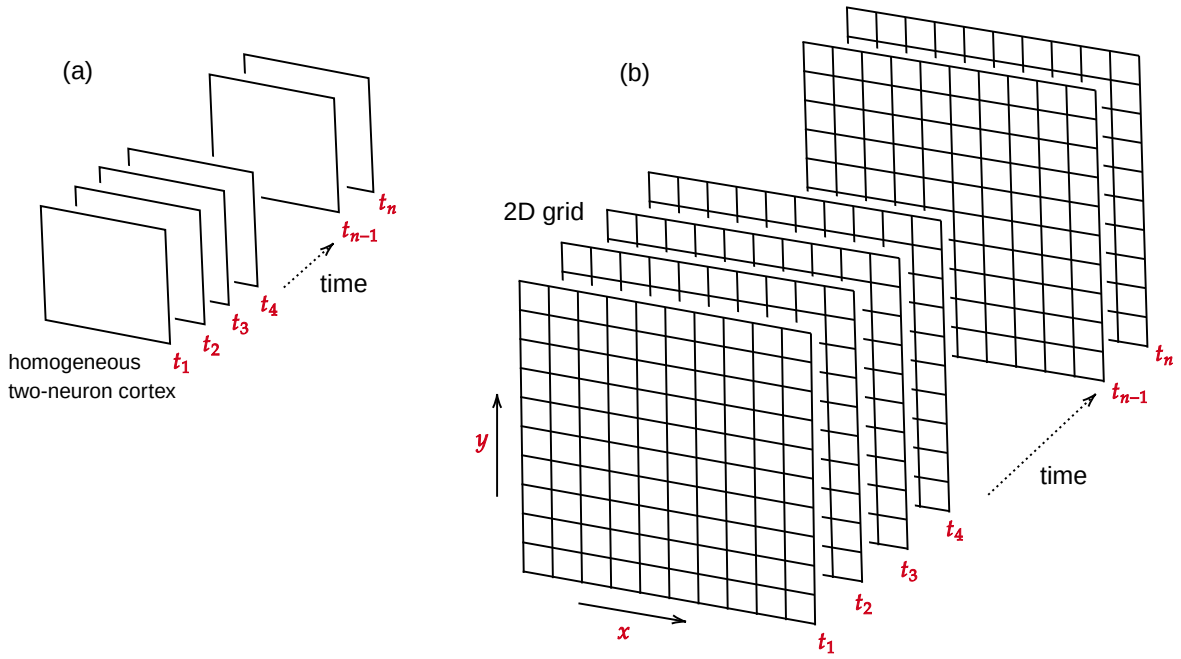

Figure 6.3: Comparison between point and grid simulations. Time-step for point simulations is a small fraction of recovery time constant whereas for grid simulations it is chosen by applying the Courant stability criterion for both wave equation and inhibitory diffusion. In grid simulations, $N_x \times N_y$ number of elements are updated in a single time-step.

micro and macro scales. However, point simulations cannot provide any information about the spatial variations across the cortex. Figure 6.3 illustrates the distinction between point and grid simulations. An Euler–Maruyama integration scheme [44] with time step $\Delta t = 10\,\mu$s is used for all point simulations discussed in the subsequent sections.

6.3.2 2D Grid Simulations

For grid simulations, I consider a 2D patch of cortex partitioned into a network of unit cells (see Fig. 6.3(b)), each cell of area ℓ^2 ($\ell = 10\,\mu$m) and containing a pair of excitatory and inhibitory neurons. Our unblocked ($B = 1$) model cortex is a square sheet with periodic boundary conditions, of side length 1 mm, with grid spacing $\Delta x = \Delta y = (B\ell) = 10\,\mu$m, corresponding to a square grid containing $100^2 = 10\,000$ sample points. At each time step, all 10 000 grid points are updated simultaneously using MATLAB array operators. Laplacians in Eqs (6.1) and (6.4) are approximated by a second-order finite difference approximation using a Taylor expansion. The most commonly used finite difference equation is the five-point equation (see Eq. (3.13a)) which is given by the stencil,

$$\mathbf{L5} = \frac{1}{h^2}\begin{bmatrix} 0 & 1 & 0 \\ 1 & -4 & 1 \\ 0 & 1 & 0 \end{bmatrix} \tag{6.6}$$

where $h = \Delta x = \Delta y$. I also consider nine-point finite difference equation denoted by the stencil,

$$\mathbf{L9} = \frac{1}{6h^2}\begin{bmatrix} 1 & 4 & 1 \\ 4 & -20 & 4 \\ 1 & 4 & 1 \end{bmatrix} \tag{6.7}$$

The numerical performance of both stencils was tested. Following [77], diffusion and wave Laplacians are implemented as a circular convolution of the 3×3 second-difference operator $\mathbf{L}$, acting on V (diffusion) and ϕ (wave equation flux).

The simulation time-step is selected by applying the Courant stability criterion twice: once for the wave equation, and then for inhibitory diffusion (D_i). Courant stability, also known as Courant-Friedrichs-Lewy (CFL) stability, is essential to ensure stable numerics when solving partial differential equations.

Stability Condition for Wave Equation

For the one-dimensional case, the Courant-Friedrichs-Lewy (CFL) condition requires that,

$$\frac{v\Delta t}{\Delta x} \leq 1 \tag{6.8}$$

where Δt is the simulation time-step, Δx is the spatial resolution, and v is the wave speed. The condition stipulates that the time-step be smaller than the time it takes for the wave to travel to an adjacent grid point.

Table 6.2: Relationship between blocking (B) and the simulation time-step (Δt)

Blocking ratio (B)	Spatial resolution ($\Delta x = B\ell$)	Maximum time-step ($\Delta t_{\max}$) predicted by CFL ($\Delta t \leq \Delta t_{\max}$)	Side length of 100×100 cortex
1	$10\,\mu$m	$0.038\,\mu$s	1 mm
10	$100\,\mu$m	$3.8\,\mu$s	10 mm
100	1 mm	0.38 ms	10 cm
1000	10 mm	38 ms	1 m

The CFL condition for wave propagation on a 2D grid can be derived as [63],

$$\Delta t \leq \frac{1}{v}\left[\frac{1}{(\Delta x)^2} + \frac{1}{(\Delta y)^2}\right]^{-\frac{1}{2}} = \frac{\Delta x}{\sqrt{2}v}, \qquad \text{since } \Delta x = \Delta y \tag{6.9}$$

Stability Condition for Voltage Equation

Within a time Δt, a diffusive voltage perturbation is expected to propagate on a 2D sheet through an rms distance $\sqrt{4D_i\Delta t}$ [77]. Requiring this distance to be less than Δx gives the diffusion stability condition,

$$\Delta t \leq \frac{(\Delta x)^2}{4D_i} \tag{6.10}$$

For $\Delta x = 10\,\mu$m, $v = 0.2$ ms^{-1}, $D_i = 6.6 \times 10^{-4}$ m^{2}s^{-1}, and $B = 1$ (i.e., no blocking), the wave and diffusion stability conditions are,

$$\Delta t_{\text{wave}} \leq 35\,\mu\text{s} \quad \text{and} \quad \Delta t_{\text{diffusion}} \leq 0.038\,\mu\text{s}$$

For numerical stability we need to select the tighter of these two criteria, namely $\Delta t \leq 0.038\,\mu$s, which is very small. However, for simulations at higher blocking we can loosen the time-step, because the effective grid spacing increases with blocking. Table 6.2 shows how the time-step can be relaxed as blocking ratio B is increased. Thus, grid simulations with higher blocking ratios can be run faster than simulations with lower blocking.

Previous researchers have suggested that larger Laplacian stencil approximations increase the maximum stable time-step [31, 60, 78]. Figure 6.4 shows simulations of the prototypical diffusion equation,

$$\frac{\partial V(\vec{r},t)}{\partial t} = D\nabla^2 V(\vec{r},t) \tag{6.11}$$

driven by a momentary delta-function impulse $\delta(x,y,t) = \delta(x_0,y_0,0)$ applied at time $t = 0$ to the centre of the grid using both five-point (L5) and nine-point (L9) stencils. On a 2D grid, the delta-function is numerically implemented as an impulse of unit volume. Thus at $t = 0$,

$$\text{grid}(N_x/2, N_y/2) = \frac{1}{(\Delta x)(\Delta y)}$$

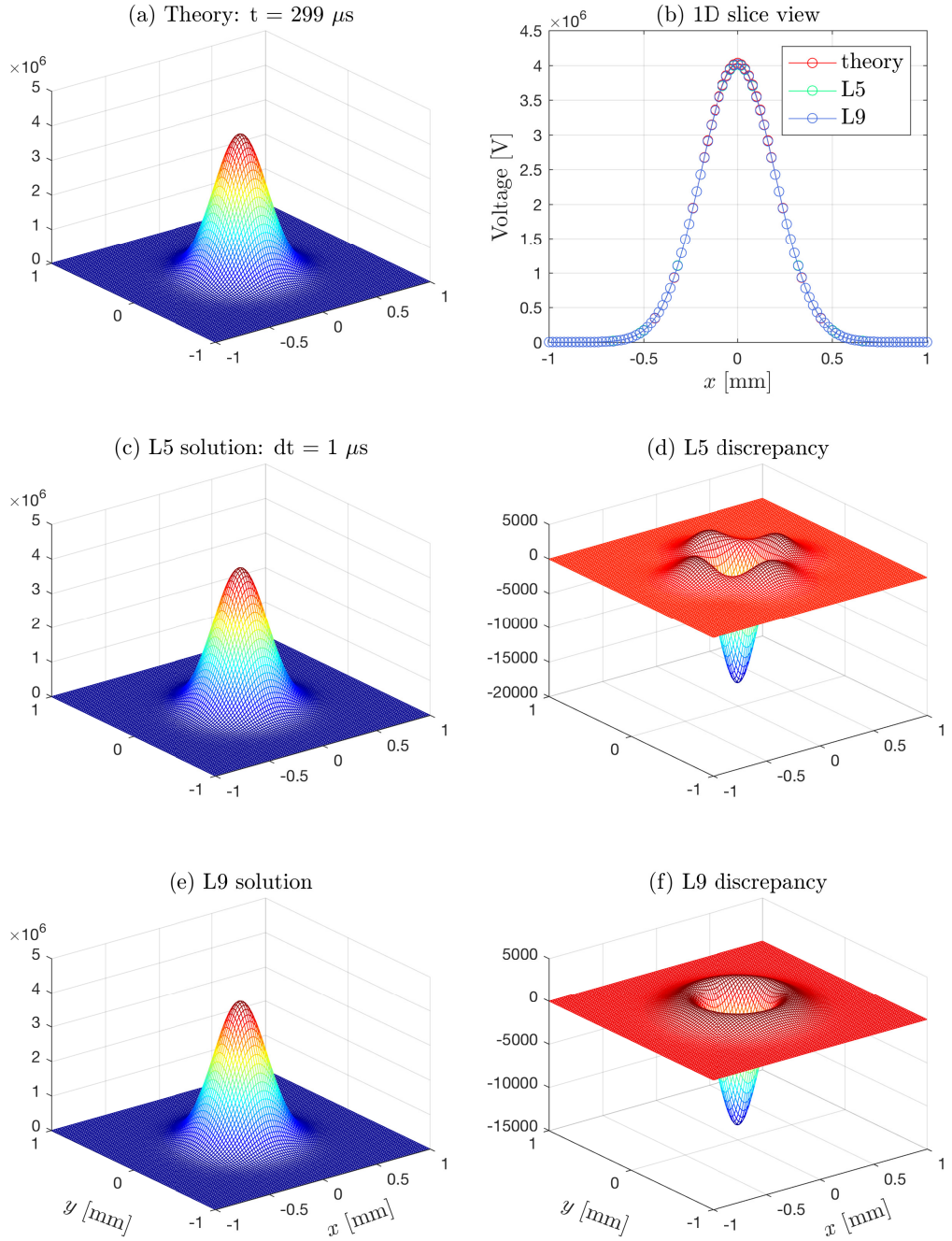

Figure 6.4: Performance of standard five-point (L5) and nine-point (L9) stencils against theory. Pure diffusion equation (6.11) is simulated for 299 μs on a 100×100 grid using L5 and L9. The system is driven by a delta-function impulse in space applied to the centre of the grid at time $t = 0$. Here, $D = 6.6 \times 10^{-5}$ $\mathrm{m^2 s^{-1}}$, $dx = 10\,\mu\mathrm{m}$, $B = 2$, and $\Delta t = 1\,\mu\mathrm{s}$ which is less than the maximum time-step (1.5 μs) predicted by CFL criterion. The voltage discrepancy plots in (d, f) are the grid differences between stencil numerics (c, e) and theoretical solution in (a): $\Delta V^{\mathrm{L}}(x, y) = V^{\mathrm{L}}(x, y) - V^{\mathrm{theory}}(x, y)$, with L = L5, L9.

where N_x and N_y are the number of rows and columns of the grid. Simulation results are

compared with the known analytical solution, a 2D Gaussian distribution which decays and diffuses outwards over time,

$$P(r,t) \;=\; \frac{1}{4\pi Dt} e^{\left(\frac{-r^2}{4Dt}\right)} \tag{6.12}$$

where r is the radial distance from the centre, which is mapped into Cartesian coordinates as $r^2 = x^2 + y^2$.

By comparing the discrepancy between theory and simulation for L5 and L9 in Fig. 6.4, it is obvious that L9 outperforms L5. This is because L9 uses nine grid points whereas L5 considers only five when calculating finite differences. Figure 6.5 shows that the growth of percentage rms discrepancy with time-step for both stencils has a power-law gradient of two. Interestingly, the figure also indicates that L9 remains accurate and stable for time-steps that exceed the CFL maximum by as much as one-third. This ability to use a larger time-step implies that L9 can produce reliable results with less computational cost than L5. For this reason, I choose to work with L9 for all grid simulations discussed in this thesis.

Thus, ∇^2 Laplacian differencing in Eqs. (6.1) and (6.4) are coded as a 2D periodic convolution of L9 across the grid using the `convolve2()` function in MATLAB [96]. For example, the

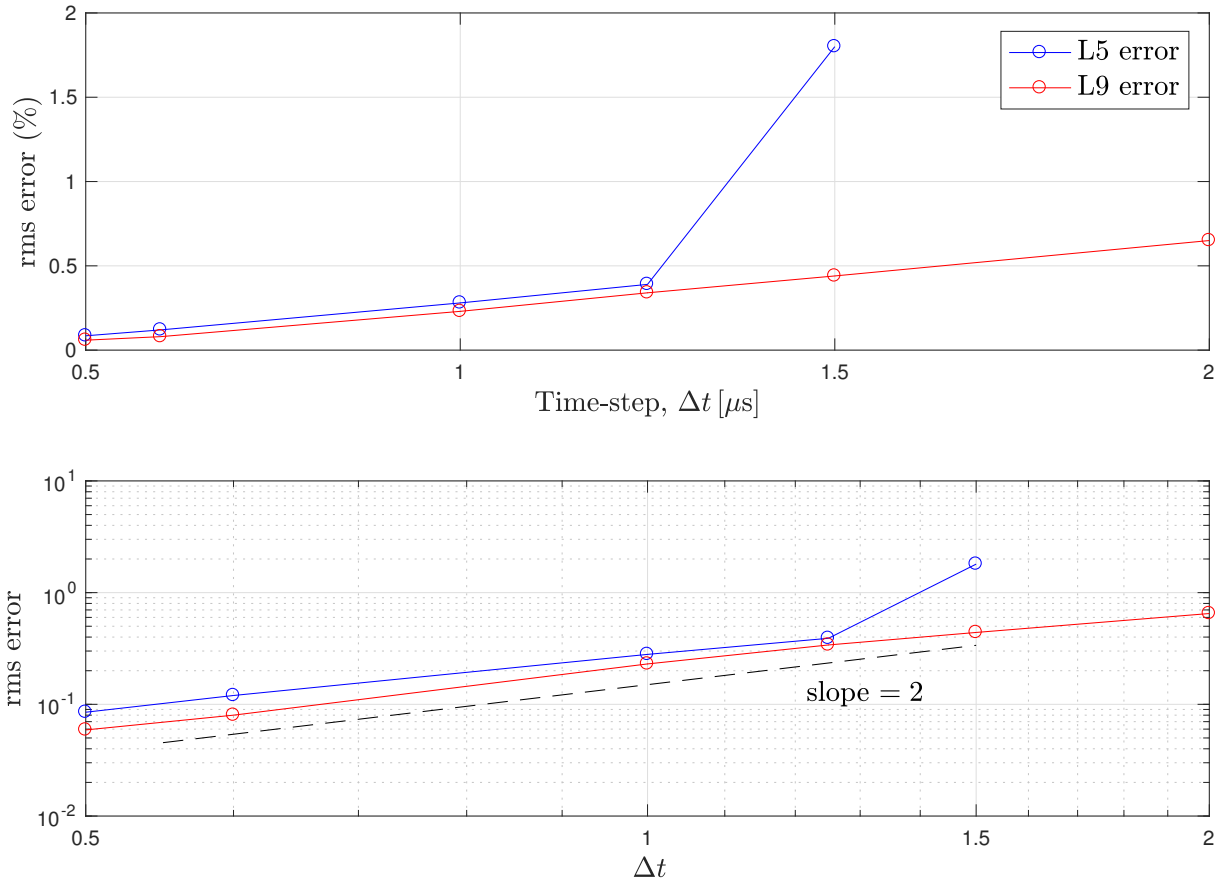

Figure 6.5: Relative discrepancy of L5 (blue) and L9 (red) with time-step plotted on linear (top) and log-log (bottom) axes. L9 consistently outperforms L5 and, surprisingly, remains stable for time-steps slightly in excess of the CFL-predicted maximum (1.5 μs). Dashed-black curve in lower panel confirms that error curves for both stencils follow a quadratic power law: error $\propto \Delta t^2$. The error divergence for L5 grows exponentially (not shown) beyond the CFL limit, while the L9 error is an acceptable ~0.7% at $\frac{4}{3}\Delta t^{\mathrm{CFL}} = 2.0$ μs.

$\nabla^2 V$ Laplacian terms in Eq. (6.1) can be coded as,

```
lap_V =  convolve2(V_grid, L9, 'wrap');
```

where `wrap` is used to indicate wraparound at the edges of the grid.

The ∇^4 biharmonic in Eqs (6.2) represents the squared Laplacian operator $(\nabla^2)^2$, so can be implemented as a pair of nested convolutions,

```
lap_V =  convolve2(V_grid, L9, 'wrap');
bih_V =  convolve2(lap_V, L9, 'wrap');
```

which is equivalent to a single convolution with a 25-element kernel,

```
bih_V =  convolve2(V_grid, L25, 'wrap');
```

where

$$\mathbf{L25} = \frac{1}{(36h^4)} \begin{bmatrix} 1 & 8 & 18 & 8 & 1 \\ 8 & -8 & -144 & -8 & 8 \\ 18 & -144 & 468 & -144 & 18 \\ 8 & -8 & -144 & -8 & 8 \\ 1 & 8 & 18 & 8 & 1 \end{bmatrix} \tag{6.13}$$

6.4 Dynamics of Human Brain Across Multiple Levels

In this section, I demonstrate that the True-field model is capable of reproducing the electrical behaviour of human brain across multiple scales by using homogeneous cortex (two neuron) point simulations as discussed in Section 6.3.1. In Fig. 6.6, I show a set of point simulations for a range of blocking ratios B describing the behaviour of brain at different levels; model parameters are presented in Table 6.3. We see that the intracellular spikes at low blocking ratios ($B = 2, 5$), become increasingly agglomerated into long lasting population events as

Table 6.3: Initial parameter settings for True-field model used to investigate electrical behaviour of cortex across multiple scales

Symbol	Description	Value	Unit
ρ_{ee}	$e \to e$ synaptic gain	90×10^{-3}	V per spike
ρ_{ei}	$e \to i$ synaptic gain	200×10^{-3}	V per spike
ρ_{ie}	$i \to e$ synaptic gain	-10×10^{-3}	V per spike
ρ_{ii}	$i \to i$ synaptic gain	-0.1×10^{-3}	V per spike
D_i	inhibitory voltage-diffusion coefficients	$500 D_0$	$\mathrm{m^2 s^{-1}}$
D_e	excitatory voltage-diffusion coefficients	$D_i/100$	$\mathrm{m^2 s^{-1}}$
D_{Ri}	inhibitory recovery-diffusion coefficients	2.47×10^{-13}	$\mathrm{m^4 V^{-1}}$
D_{Re}	excitatory recovery-diffusion coefficients	5.27×10^{-17}	$\mathrm{m^4 V^{-1}}$
Γ_b	voltage noise intensity	1×10^{-10}	$\mathrm{m^2 V^2 s^{-1}}$
Γ_R	recovery noise intensity	1×10^{-10}	$\mathrm{m^2 s^{-1}}$

$D_0 = 6.6 \times 10^{-4}$ $\mathrm{m^2 s^{-1}}$ is the original value used for D_i, for previous analyses in Chapter 4 and 5. These parameter settings are used to produce Fig. 6.6.

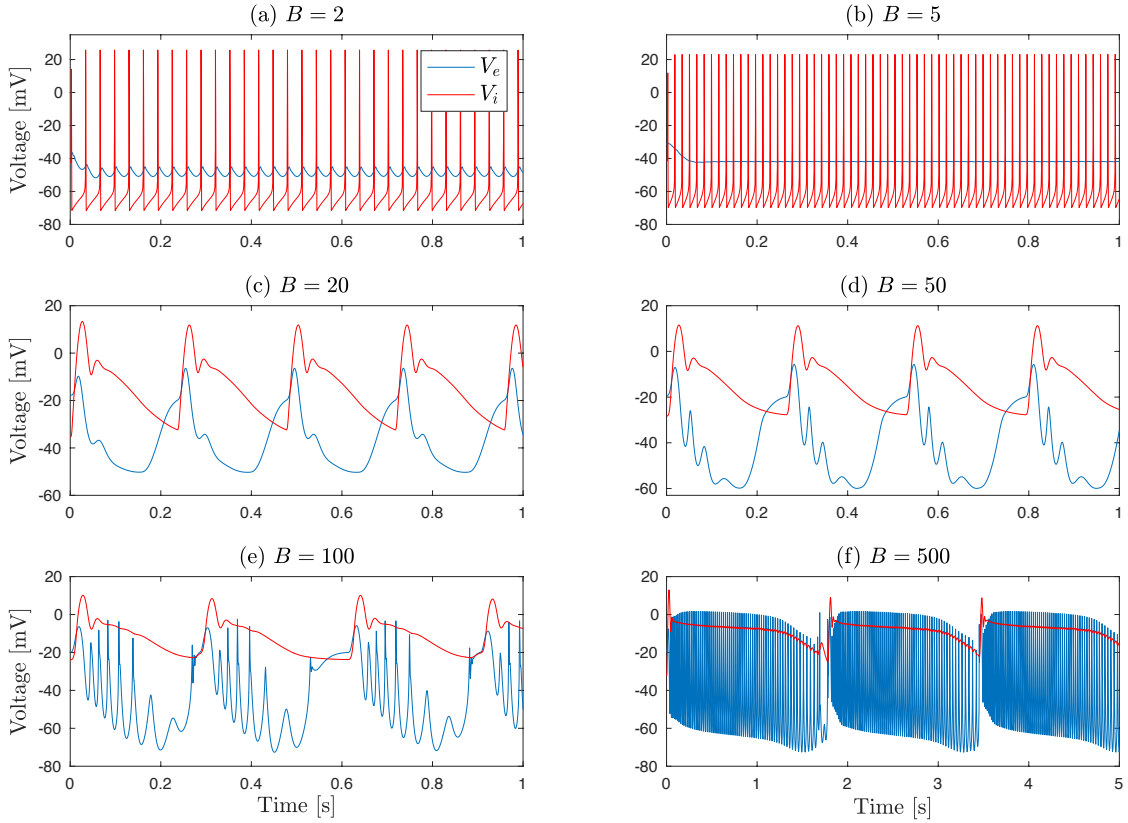

Figure 6.6: True-field simulations for a range of blocking B illustrating electrical behaviour of human brain across multiple levels: (a) and (b) illustrate spiking behaviour at microscopic level for low blocking; (c)–(f) reproduce agglomerated population events. Simulation time-step $\Delta t = 10\,\mu$s; I^{dc} stimulus currents are 0.01 and 5.89 Am^{-2} for (a, b) and (c)–(f) respectively. See Table 6.3 for parameter values.

blocking is increased. The modulated "fuzziness" seen in Fig. 6.6(e) and (f) suggests a mixture of low and high frequency components reflecting population activity and individual spike events respectively. Interestingly, $B = 500$ generates voltage patterns that resemble seizure-like events (SLE) seen in a slice of mouse brain sustained in a bath of artificial cerebro-spinal fluid (aCSF). SLEs are discussed in detail in Chapter 7.

However, to get biologically feasible electrical behaviour, I found that model parameters often needed to be tuned for each scale separately. This is because it is very challenging to have a single set of parameters that reproduces brain dynamics across multiple scales. For example, the Table 6.3 parameters can reproduce some of the expected micro- and macro-scale behaviours of cortex, but fail to evoke spiking in excitatory neurons (see Fig. 6.6(a), (b)). This need to retune is probably not biophysically unreasonable because the parameters of a brain are not always the same when different electrical measurements are considered. For example, synaptic connectivities are different for an EEG measurement of a normal brain and an intracellular or LFP recording of a crippled brain.

6.4.1 Spiking Behaviour at Microscale

A series of homogeneous-cortex point simulations were conducted looking for realistic electrical behaviour of human brain at microscopic level. In Fig. 6.7 (top three panels), I present simulation results that describe the intracellular spiking behaviour of individual neurons for low blocking

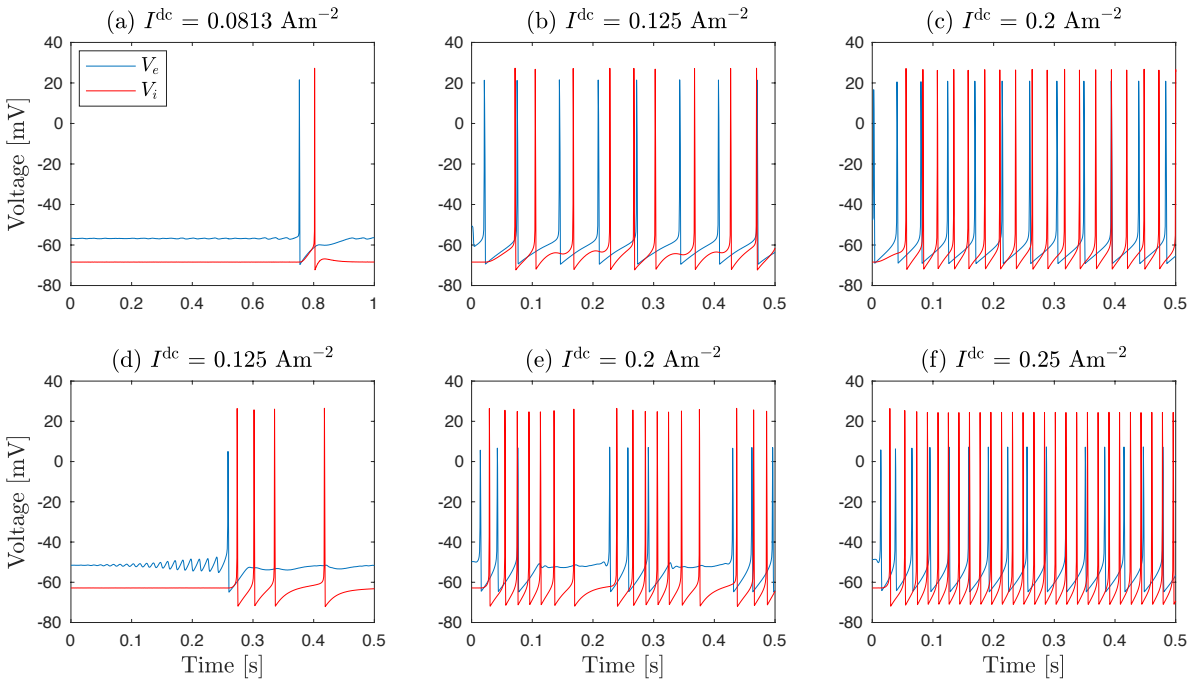

Figure 6.7: True-field simulations at low blocking to demonstrate intracellular spiking behaviour of individual neurons. Simulations are conducted at two blocking ratios: $B = 2$ (top row) and $B = 5$ (bottom row). Blue and red traces show excitatory and inhibitory membrane potentials respectively. Simulation time-step $\Delta t = 10\,\mu$s. I^{dc} stimulus currents are stated in each subplot title.

($B = 2$). Some Table 6.3 parameters have been retuned to reproduce the intracellular spiking behaviour of individual neurons: ρ_{ee} and ρ_{ei} are decreased to reduce excitation of excitatory and inhibitory neurons; ρ_{ie} is decreased to lessen inhibitory feedback on the excitatory neuron; the diffusivities are set back to default values; and voltage and recovery noise intensities are adjusted as required. The revised parameter values are listed in Table 6.4. Note that each time parameter settings are changed, the full set of reblocking corrections (as listed in Section 3.3.4) are recomputed; these recalculations take ∼10 s of MATLAB computing time.

Table 6.4: Adjusted parameter values of the True-field model required to reproduce spiking behaviour at microscale as illustrated in Fig. 6.7

Symbol	Description	Value	Unit
ρ_{ee}	$e \to e$ synaptic gain	0.1×10^{-3}	V per spike
ρ_{ei}	$e \to i$ synaptic gain	1.3×10^{-3}	V per spike
ρ_{ie}	$i \to e$ synaptic gain	-0.6×10^{-3}	V per spike
ρ_{ii}	$i \to i$ synaptic gain	-0.1×10^{-3}	V per spike
D_i	inhibitory voltage-diffusion coefficients	D_0	m^{2}s^{-1}
D_e	excitatory voltage-diffusion coefficients	$D_i/100$	m^{2}s^{-1}
D_{Ri}	inhibitory recovery-diffusion coefficients	2.47×10^{-13}	m^{4}V^{-1}
D_{Re}	excitatory recovery-diffusion coefficients	5.27×10^{-17}	m^{4}V^{-1}
Γ_b	voltage noise intensity	1×10^{-8}	m^{2}V^{2}s^{-1}
Γ_R	recovery noise intensity	1×10^{-8}	m^{2}s^{-1}
B	blocking ratio	$2, 5$	

$D_0 = 6.6 \times 10^{-4}$ m^{2}s^{-1}

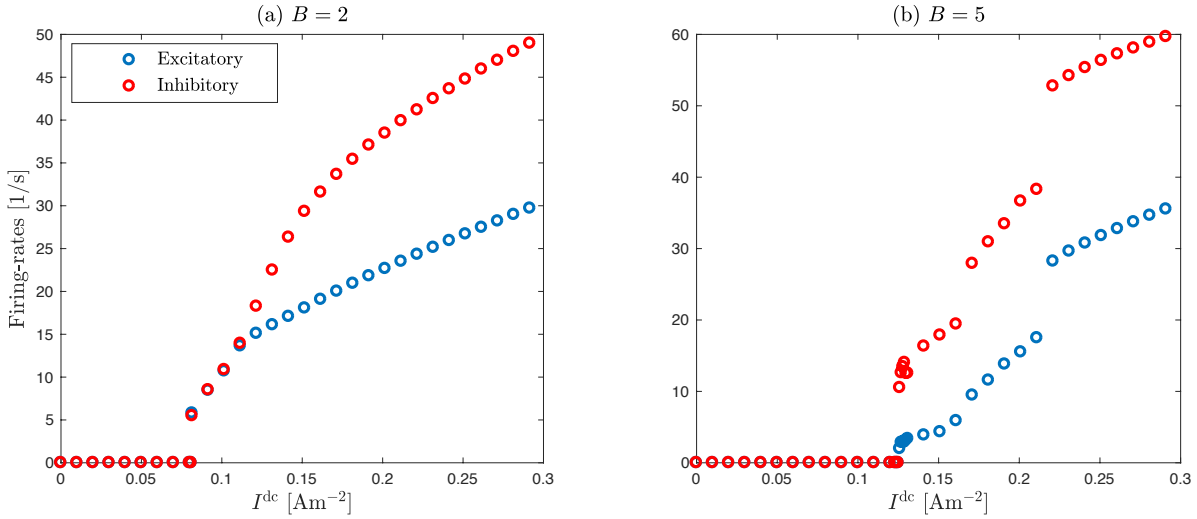

Figure 6.8: Firing-rate curves for excitatory and inhibitory neurons for Table 6.4 parameter settings with (a) $B = 2$, and (b) $B = 5$. Discontinuities seen in (b) mark the onset of distinct bursting patterns as seen in Fig. 6.7.

The firing-rate curves of Fig. 6.8(a) show that there is no firing activity until the drive current exceeds a threshold value I^{dc}_{min} ~0.0813 Am^{-2}: this marks the birth of spiking. As expected, the firing rate of excitatory and inhibitory neurons increases with stimulus current. With these settings, inhibitory firing tends to increase at a faster rate. If blocking ratio is increased to $B = 5$ without changing any other parameter, the threshold for firing (birth of spikes) moves to the left, indicating that the neurons become less sensitive to stimulus current (see Fig. 6.7, bottom panel). Interestingly, in Fig. 6.7(e) we see emergence of bursting patterns in both excitatory and inhibitory neurons which manifest as discontinuities in the firing-rate curves of Fig. 6.8(b).

These figures show that True-field can reproduce the discrete spiking events seen in any other point-neuron model (e.g., unmodified Wilson neuron). However, the set of parameter values listed in Table 6.4, are not unique: there are several ways that True-field can be tuned to generate spiking behaviour at microscopic level. For example, one can balance synaptic gain terms differently to alter the ratio of excitatory to inhibitory firing rates.

6.4.2 Agglomerated Population Level

Using a sequence of homogeneous-cortex point simulations, I demonstrate here that True-field at higher blocking can generate slow nonlinear oscillations that resemble delta-band electrical signals detected on the surface of scalp. I apply two different noise settings:

$$\text{Low:} \quad \Gamma_b = 10^{-8}\,\text{m}^2\text{V}^2\text{s}^{-1} \quad \text{and} \quad \Gamma_R = 10^{-8}\,\text{m}^2\text{s}^{-1}$$

$$\text{High:} \quad \Gamma_b = 10^{-6}\,\text{m}^2\text{V}^2\text{s}^{-1} \quad \text{and} \quad \Gamma_R = 10^{-6}\,\text{m}^2\text{s}^{-1}$$

In addition, to produce longer events, I had to decrease γ_{ib}, the inhibitory synaptic rate constant, from its original mean-field value of $100\,\text{s}^{-1}$ (Table 6.1) to $50\,\text{s}^{-1}$. All other parameter values are as listed in Table 6.3.

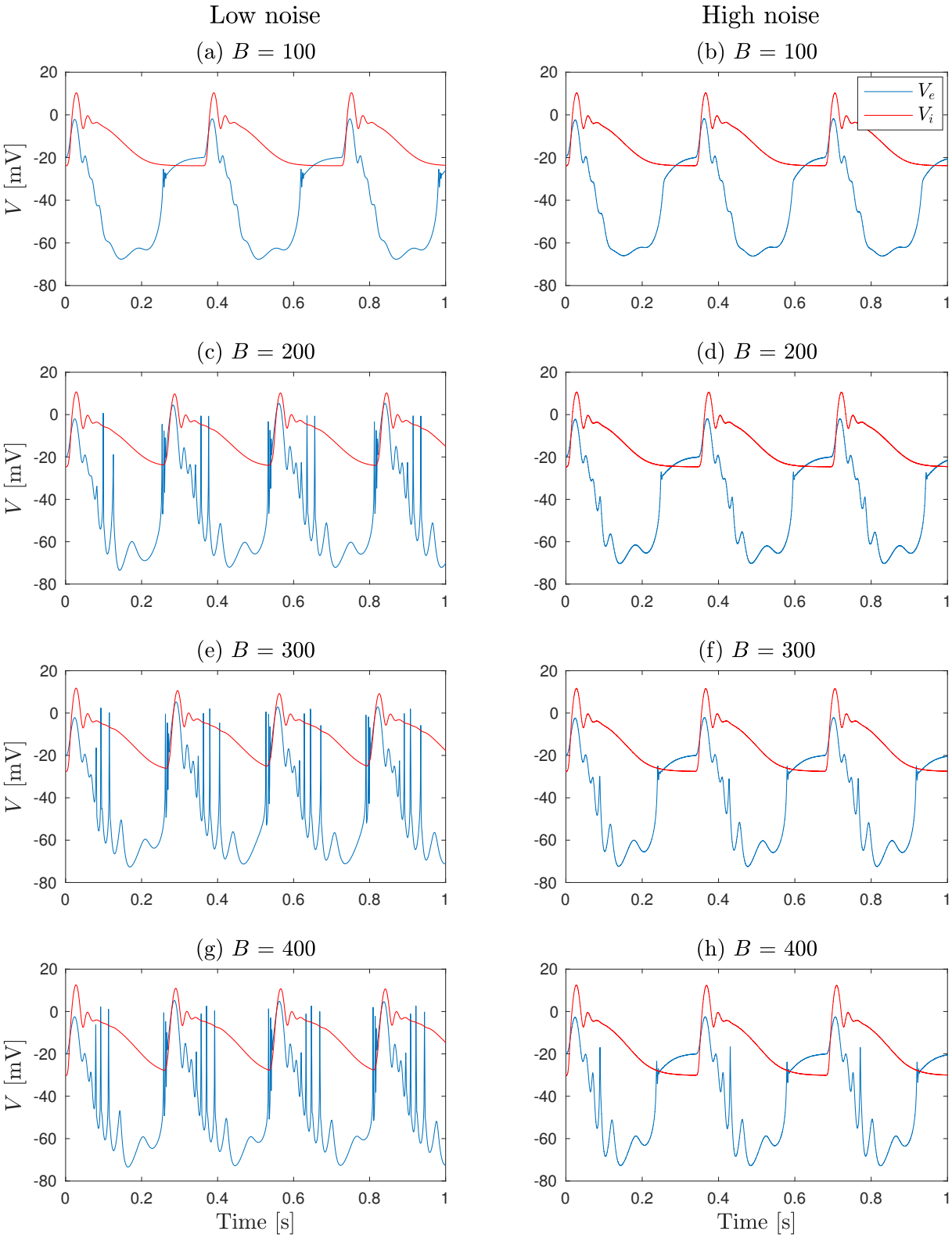

Figure 6.9: True-field simulations at higher blocking ($B = 100$ to 400) to demonstrate agglomerated population events. Simulations are conducted using two noise intensity settings: low (left column) and high (right column). Blue and red traces represents excitatory and inhibitory populations respectively. I^{dc} stimulus currents for left and right columns are 5.89 and 3 Am^{-2} respectively. Here, $\Delta t = 10\,\mu$s.

Figure 6.9 demonstrates emergence of ∼3 Hz delta-oscillations for the blocking range $B = 100$ to $B = 400$ using the two different noise intensity settings. A higher stimulus current is needed

when the simulations are run at lower noise (left column), indicating that increasing noise levels tend to make the neuronal populations more responsive. We see an increase in high frequency content as blocking is increased, particularly for the low-noise case, but the finest temporal structures tend to wash out at large noise (right column). We also observe an increase in delta frequency with blocking (from ∼3 to 4 Hz) in the low noise case.

To see the dominating frequencies of the time series in Fig. 6.9, I plot corresponding power spectral density graphs of the excitatory time series. For each case, I considered a 100 s simulation. The data set is split into 10 s segments and the mean of each segment is subtracted to remove the dc component of the signal. MATLAB `spectrogram` is then used to compute the power spectral density of each segment and finally the average across all the segments is considered.

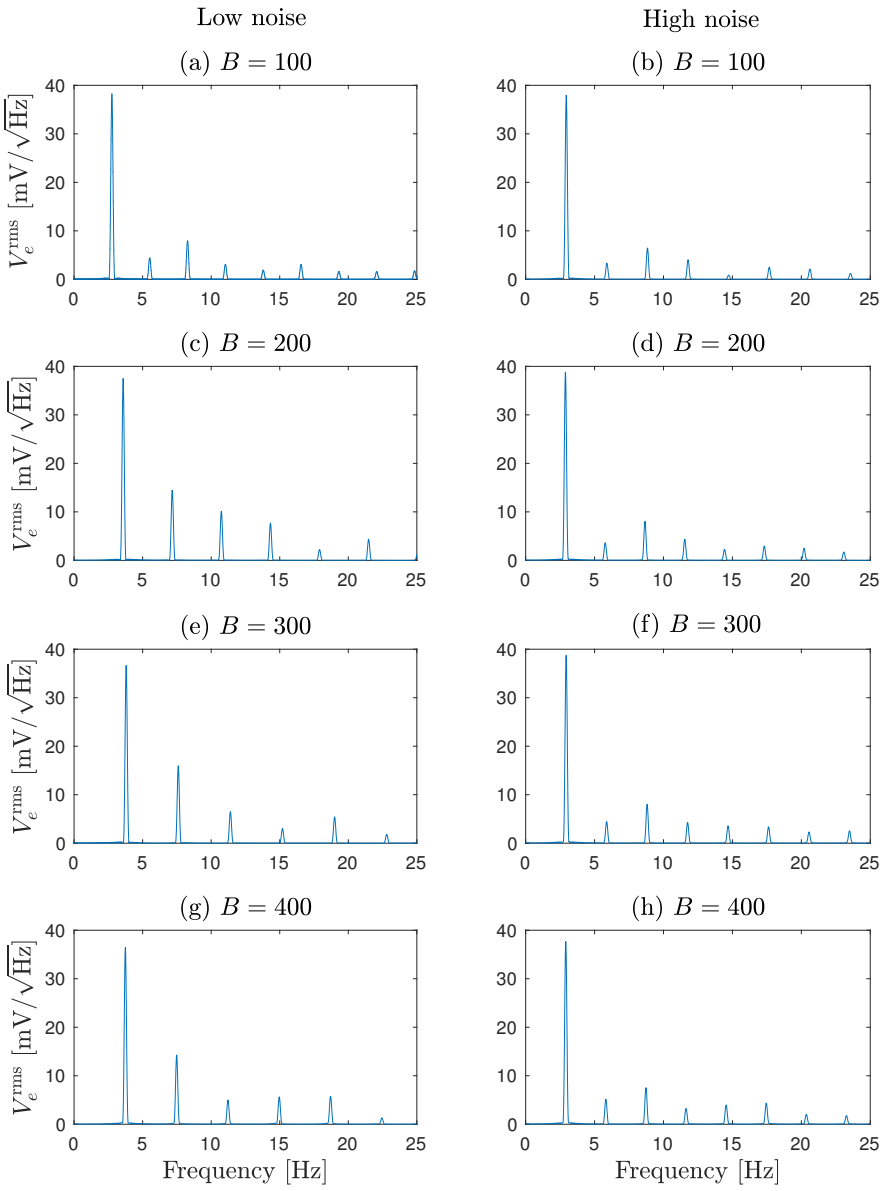

Figure 6.10: Power spectral density of excitatory time series in Fig. 6.10. The delta-frequency is dominating in each case.

We see that in low noise case, fundamental frequency tends to increase slightly with blocking but, in high noise case, there is no significant impact of blocking on the spectrum.

6.5 Grid Simulation Results

In this section, I use 2D grid simulations to show the variation of agglomerated population activity with blocking. Note that when blocking is less than 100 the CFL stability condition mandates a tiny time-step (see Table 6.2), thus it is not feasible to run grid simulations for low blocking values.

A series of 2D grid simulations of duration 1-s are run on a 101×101 square grid; spatial resolution, time-step, and approximate runtimes for each simulation are listed in Table 6.5. The centre of the grid is activated by applying a stimulus current just above threshold, while all other cells are driven with subthreshold current. Parameter settings are similar to the ones used to generate Fig. 6.9 (right column with high noise intensity) in the previous section.

Table 6.5: Spatial resolution and time-step used for grid simulations

Blocking ratio (B)	Spatial resolution ($\Delta x = B\ell$) in mm	Side length of 101×101 cortex in mm	Time-step in μs	Time taken in min (in NeSI)
100	1	101	0.7	90
150	1.5	151.5	1.5	42
170	1.7	171.7	2	35
200	2	202	3	21
300	3	303	5	13

Figure 6.11 presents $V_{e,i}(t, y)$ strip charts of excitatory and inhibitory voltage activity along the $x = 51$ central vertical axis for full 1-s simulation. $B = 100$ strip shows an initial hint of $\sim$0.6 ms^{-1} wavelet forming a momentary "<"-shape. When $B = 300$, a travelling wave is clearly evident with a propagation speed $\sim$0.32 ms^{-1}. It implies that for larger blocking, homogeneous slow-wave oscillations become destabilised promptly. $B = 170$ strip chart captures the transition between the two dynamical regimes, from whole-of-cortex synchronous delta oscillations to travelling waves of slow-delta activity. Travelling waves of slow cortical activity have been observed in scalp EEG recordings [55], but entire-cortex synchrony seems biologically implausible. It seems that long simulations are required to observe a well-formed travelling wave at low blocking ratios.

Figure 6.12 shows $V_e(t, y)$ strip charts of excitatory voltage activity along the $x = 51$ central vertical axis after 19 s. In $B = 170$ strip, we see that a well-defined travelling wave completely replaces homogeneous slow-wave oscillations after 19 s. It implies that the initial wavelets seen in Fig. 6.11 gradually stabilise into fully formed wavefronts after sufficient time has elapsed.

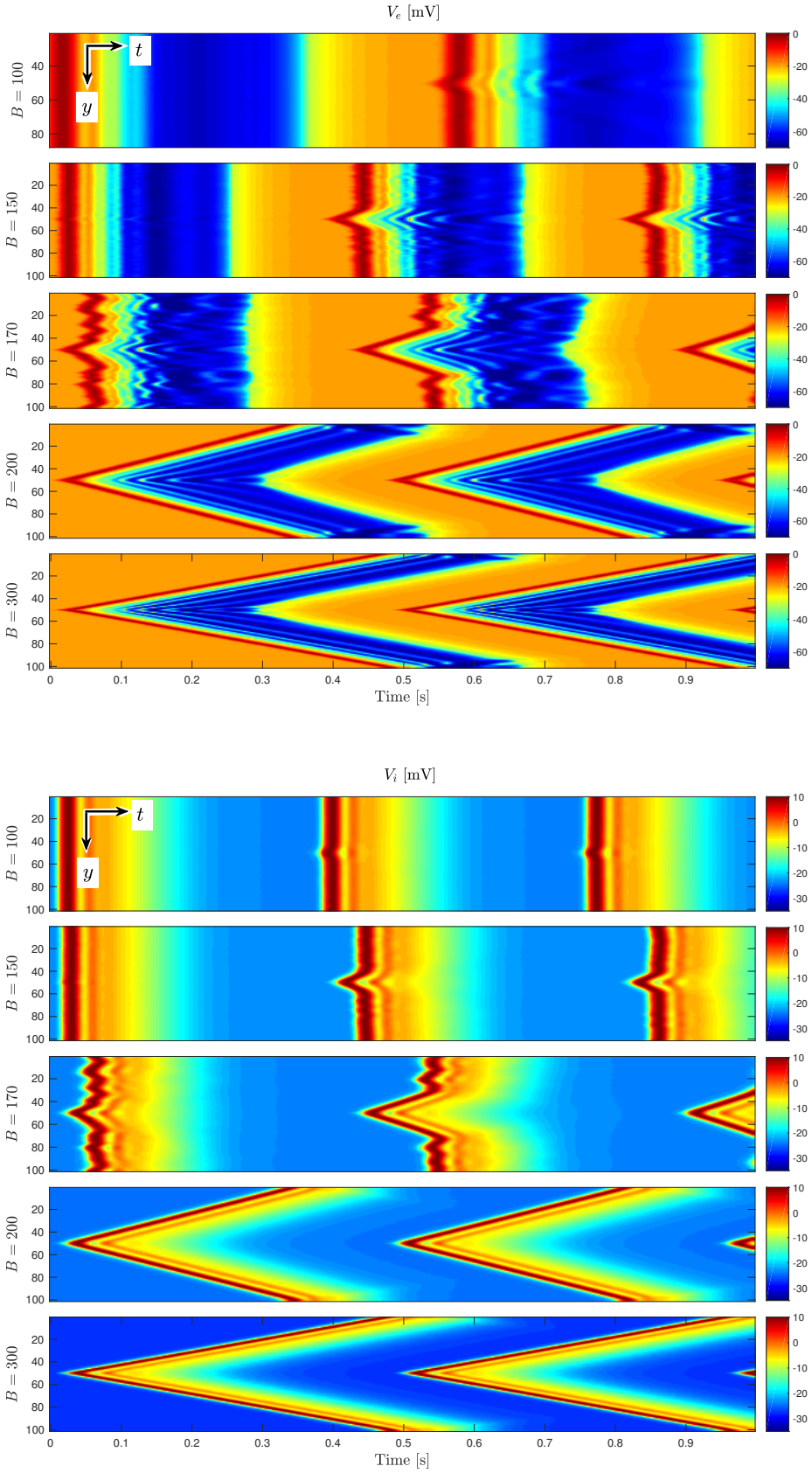

Figure 6.11: $V(t, y)$ space-time strips chart showing y-axis activity down the $x = 51$ centre line. Five blocking values are considered. As blocking is increased, homogeneous slow-wave oscillations tend to destabilise in favour of travelling waves of delta oscillations.

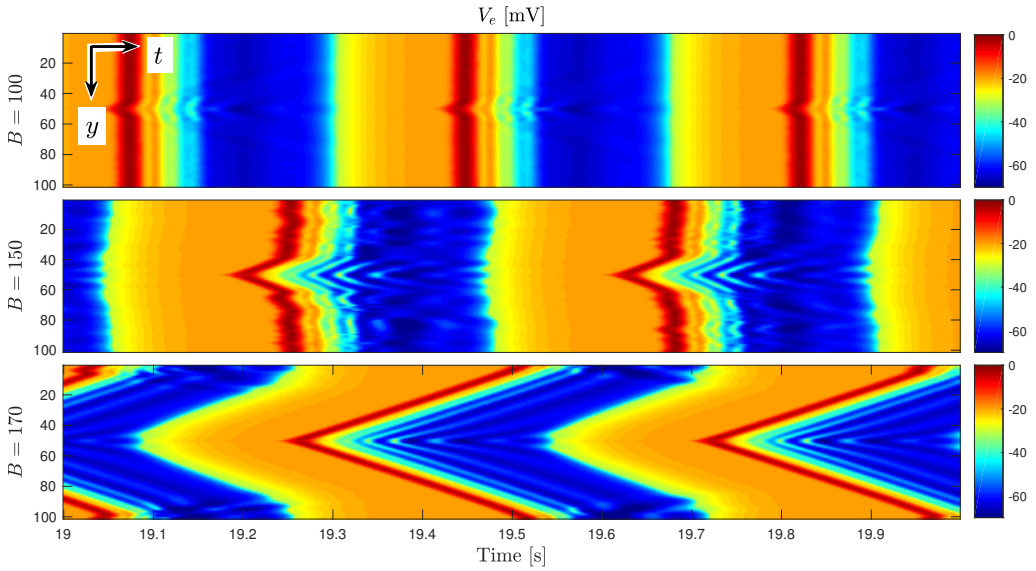

Figure 6.12: Extended $V_e(t, y)$ space-time strip charts showing the behaviour after 19 s for $B = 100$, $B = 150$, and $B = 170$. In Boyle, it take ∼16, 20, and 29 h to complete $B = 100$, 150, and 170 simulations respectively.

In Fig. 6.13, I show how wave propagation speed and delta oscillation frequency change with blocking, B.

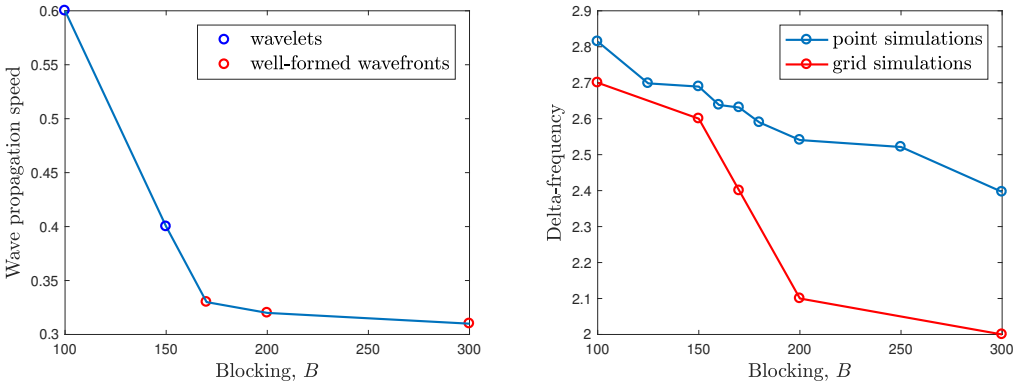

Figure 6.13: Variation of wave propagation speed and delta oscillation frequency with blocking, B.

Figure 6.14 shows time series for V_e, V_i at the (51, 51) grid position of each simulation. It is encouraging to see that the 2D grid simulations produce time series that are very similar to the homogeneous point simulations presented in Fig. 6.9 (right column).

Figure 6.15, presents time series of slow-delta oscillation at five grid points aligned parallel to the x-axis in $B = 300$ grid simulation. Events generated at the centre propagate outwards toward the edges of the grid with a speed of 0.32 ms^{-1}. This compares with 0.25 ms^{-1} for the SLE investigations in Section 7.5. Interestingly, we see that high frequency components (quill structure) seen at the end of each excitatory event tend to wash out as the wave travels.

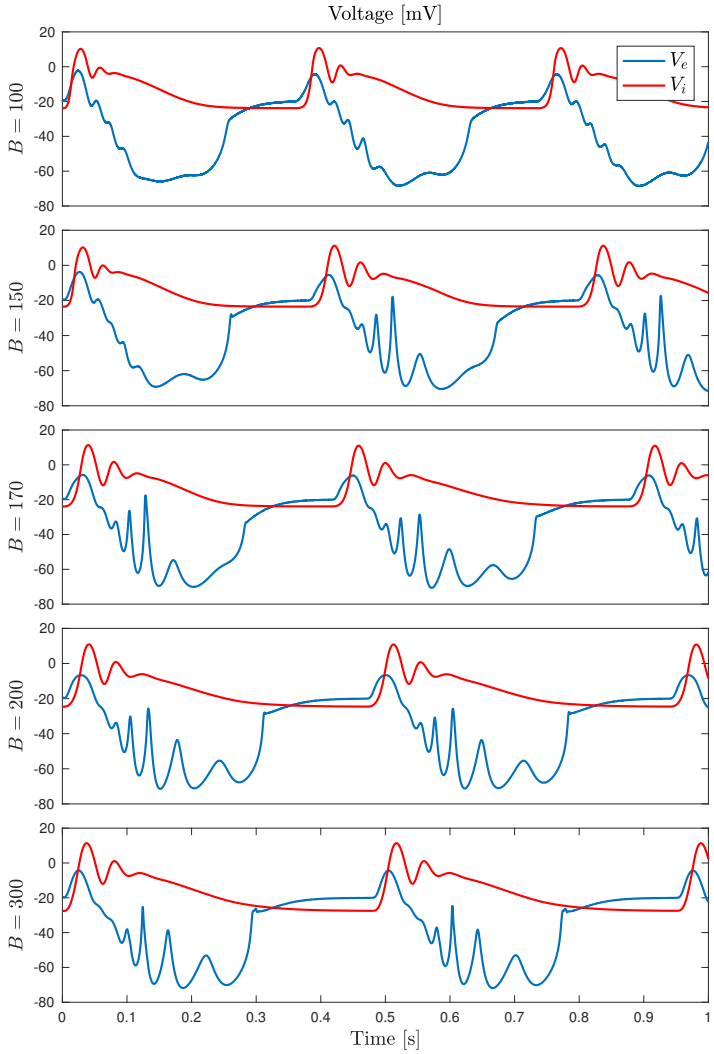

Figure 6.14: Time series of slow-delta oscillation at (51, 51), the centre of the grid. Grid simulations generate events that are qualitatively similar to those generated in point simulations of Fig. 6.9 (right column).

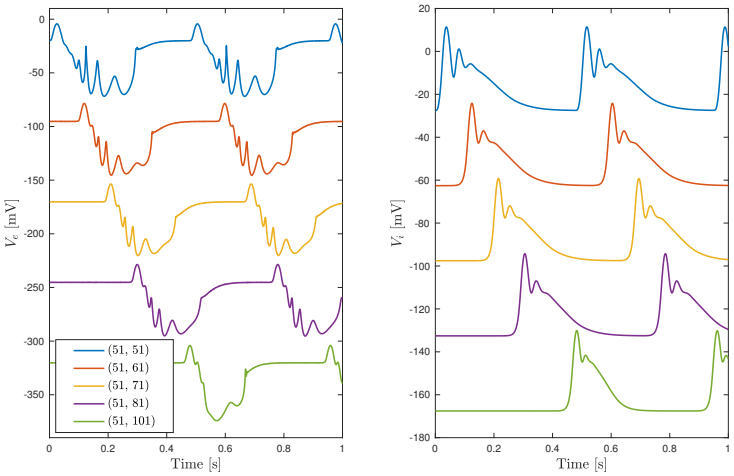

Figure 6.15: Time series of slow-delta wave oscillations for a subset of five grid points aligned parallel to the x-axis in $B = 300$ simulation. To improve visibility, V_e and V_i traces have been displaced vertically by $(-75h)$ and $(-35h)$ mV, where $h = 0, ..., 4$ is the curve number. Wavefronts propagate from centre to the edge of the grid with a speed of $\sim$0.32 ms^{-1}; high-frequency components (quills) tend to decay as the wavefront propagates.

Figure 6.16 shows four frames of $B = 300$ grid simulation illustrating the evolution and propagation of slow-delta oscillation through the grid.

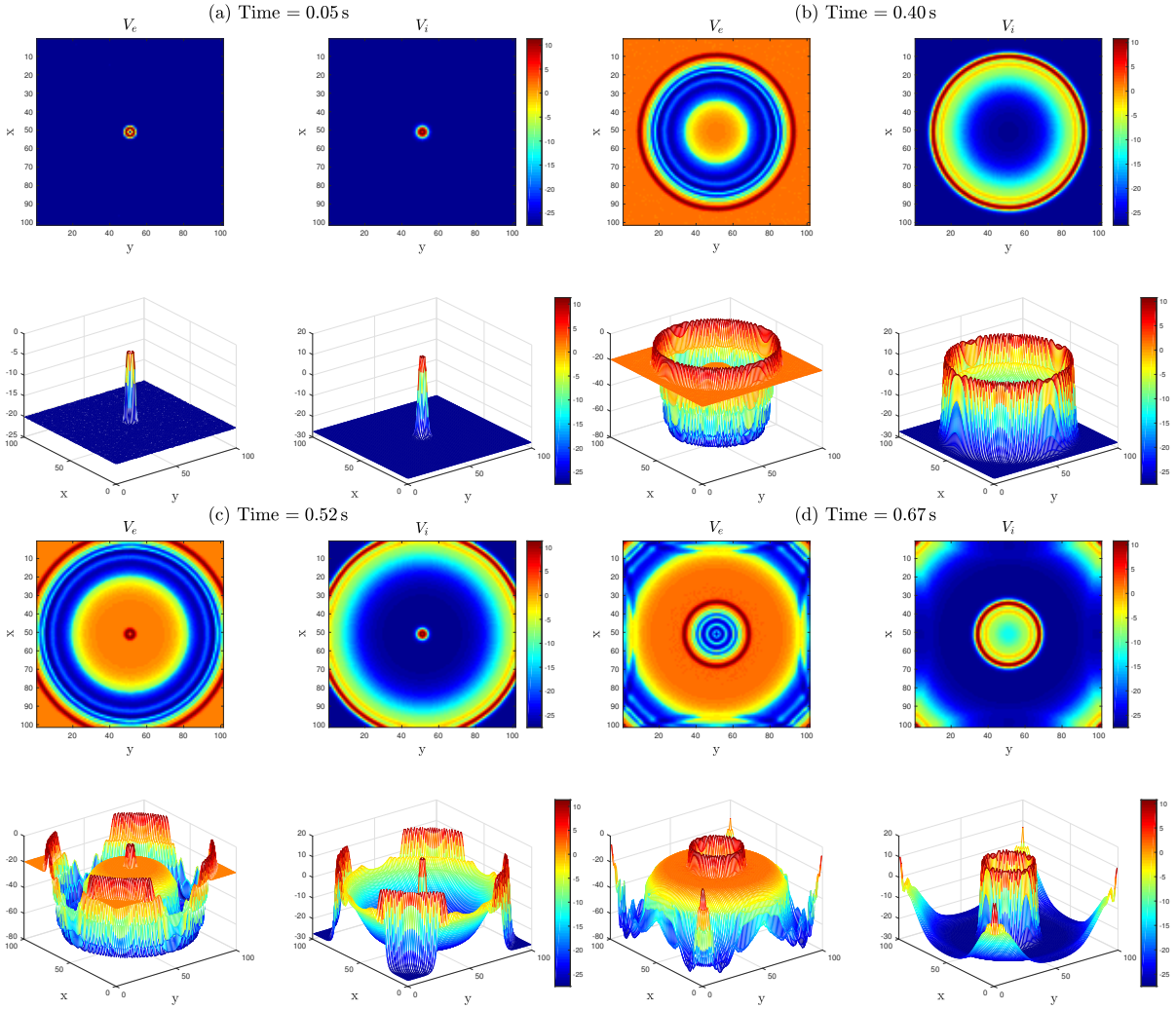

Figure 6.16: Propagation of True-field simulated slow-delta oscillation through grid. 101×101 square grid with spatial resolution 3 mm ($B = 300$) is simulated for 1 s: stimulus currents of 2.8 and 2.7 Am^{-2} are applied to the middle cell and rest of the grid respectively. Four frames are presented to show (a) the evolution of the first event at middle cell; (b) propagation of the first event through grid; (c) evolution of second event at middle cell; (d) propagation of the second event through grid. Here, $\Delta t = 5\,\mu$s; $\Gamma_b = 1 \times 10^{-6}$ $\mathrm{m^2V^2s^{-1}}$, $\Gamma_R = 1 \times 10^{-6}$ $\mathrm{m^2s^{-1}}$; and $\gamma_{ib} = 50\,\mathrm{s}^{-1}$.

6.6 Chapter Summary

In this chapter, I attempted to demonstrate that True-field model is able to generate plausible cortical dynamics across multiple scales. Two approaches were used: homogeneous-cortex point simulations, and full 2D grid simulations for a patch of cortical tissue. Initially, point simulations were used to tune True-field parameters to get the desired behaviour at microscale and macroscale. A series of grid simulations demonstrated changes in slow-delta cortical activity as blocking was increased from medium to large values. Both propagation speed and delta frequency were found to decrease monotonically with blocking.

Using a single set of parameters True-field can produce both intracellular spiking behaviour for low blocking, and agglomerated population events for higher blocking. However, I found

that at low blocking, activity of excitatory population was suppressed and action potentials were generated in the inhibitory population without synaptic stimuli from the excitatory population. This unexpected behaviour is a limitation of the model that needs further investigation.

In the next chapter, I demonstrate that True-field can also reproduce a pathological pattern of activity known as a seizure-like event (SLE).

Chapter 7

Simulating Seizure-like Events in Mouse Brain Slice using True-field

In the previous chapter I demonstrated that True-field can generate plausible spiking behaviour at microscale, and slow delta-like rhythms at macroscale. In this chapter, I show that True-field can also reproduce a pathological pattern known as a seizure-like event (SLE). Dr Logan Voss's mouse brain slice recordings are used to enable comparison with True-field outputs. I begin by describing how electrophysiological experiments are set up to record SLEs from mouse brain slice. I explain how the raw signals are processed to compensate for the shape distortions caused by the 1-Hz high-pass filter used during recording to eliminate slow dc drifts. I then present SLEs simulated by True-field and discuss how the parameters can be adjusted to alter event structure and duration. Finally, I assess how well the simulated seizure events match the mouse SLEs observed in slice experiments.

7.1 Seizures in brain tissue

Epilepsy is a neurological disorder characterised by repetitive and unpredictable interruptions of normal brain function, known as epileptic seizures. It is not completely understood how seizures occur, but is thought to be due to failure of normal inhibitory regulation mechanisms caused by damage to inhibitory neurons or suppression of GABA receptors [43].

7.2 Mouse Brain Slice Experiments

The electrophysiological experiments described here were performed by Dr Logan Voss at the Waikato Electrophysiology Lab.

SLEs generated in mouse brain slices are frequently used to model human seizure [5]. This is because *in vitro* slice technique offers more stable, convenient and affordable study than is achievable *in vivo* [17]. In addition, *in vitro* models provide control over parameters such as temperature and elements of the extracellular environment [56]. A standard method for inducing seizure activity is to remove the Mg^{2+} from the aCSF solution which bathes the slice of brain tissue; this is the technique used to induce SLEs in the experiments discussed in this chapter. Removing Mg^{2+} unblocks excitatory NMDA channels, increasing the level of tissue excitation and partially compensating for loss of long-range white-matter cortical connections caused by slicing.

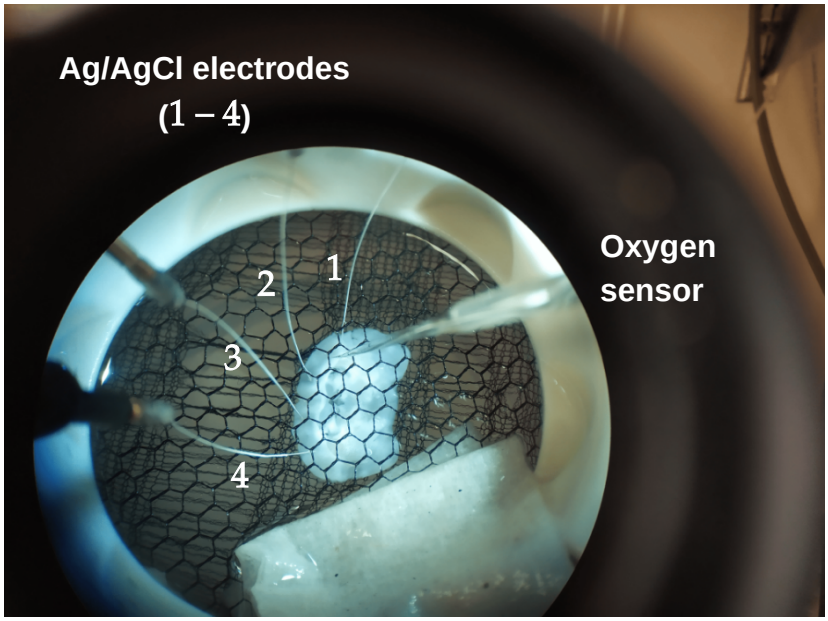

Figure 7.1: A close-up view of the LFP recording set-up. The 400 μm brain slice lies in the middle of the holding chamber resting on a mesh (spacing ∼1 mm), just submerged in the aCSF. Recording electrodes are numbered 1 to 4. The large white rectangular structure at the bottom centre is a saturated tissue paper that allows smooth egress of fluid from the bath via continuous capillary action (wicking). The reference electrode is located just out of shot and sits on the tissue paper. Photo by Dr Logan Voss.

Slice preparation and electrical recording procedures were detailed in Section 1.2.4. A close-up view of the experimental set-up is presented in Fig. 7.1. The LFP signal was detected with silver/silver-chloride electrodes, and sampled at 1 kHz. The level of tissue oxygen was also recorded (5 Hz sampling; see glass electrode in Fig. 7.1).

The LFP signal is captured by A-M Systems differential amplifiers and bandpass filtered via a high-pass filter set at 1 Hz, and low-pass filter set at 300 Hz. The 1-Hz high-pass filter eliminates dc drifts, but inevitably causes shape distortions in the low frequency content of the SLE waveforms. Because we know the mathematical form of the filter (Butterworth of second-order), these distortions can be eliminated by a Fourier deconvolution of the filter impulse response with the recorded time-series. The theory underpinning Butterworth deconvolution is summarised in Appendix B.

The top panel of Fig. 7.2 shows a sequence of six seizure-like structures extracted from a long (∼1 hour) LFP recording; the lower panel reports the time-varying levels of tissue oxygenation as an in-tissue partial pressure. The oxygen depletion observed during each SLE provides evidence of metabolic modulation of slice activity. In the absence of events, diffusion of oxygen from aCSF allows tissue-oxygen levels to rise. But SLE onset abruptly reverses this trend, with metabolic demand exceeding diffusive supply, eventually leading to SLE termination.

Figure 7.3 focuses on the first event of the LFP recording shown in Fig. 7.2. The raw (1-Hz highpass-filtered) signal is shown in blue, and the corrected (highpass-deconvolved) trace in red. Removal of the impulse distortion caused by the filter reveals an underlying slow (∼5-s) pulse-like voltage envelope with fast onset, slow offset. A sequence of much faster pulses (each lasting about 50 ms) rides atop the envelope, resembling the quills of a porcupine. Each "quill" also has a fast onset, slow offset, but on a much faster time-scale than the underlying envelope.

There are 48 quills in the event and the quill repetition rate slows from ∼5 to 2 s^{-1} towards the end of event.

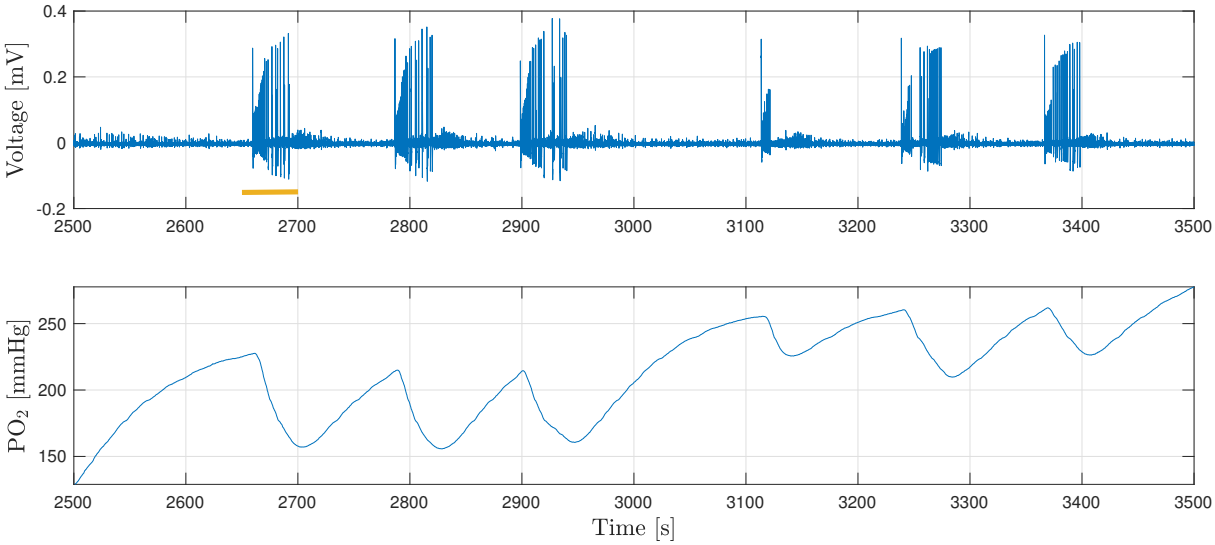

Figure 7.2: LFP recording showing SLEs and measured oxygen concentration in slice tissue. Oxygen depletion is observed during each event, followed by gradual recovery once the event has terminated. LFP activity was detected using 75 μm Ag/AgCl electrodes; amplified and bandpass filtered (1 and 300 Hz); and sampled at 1 kHz. Zoomed views of the first event (yellow highlight) are presented in Fig. 7.3. Data supplied courtesy of Dr Logan Voss.

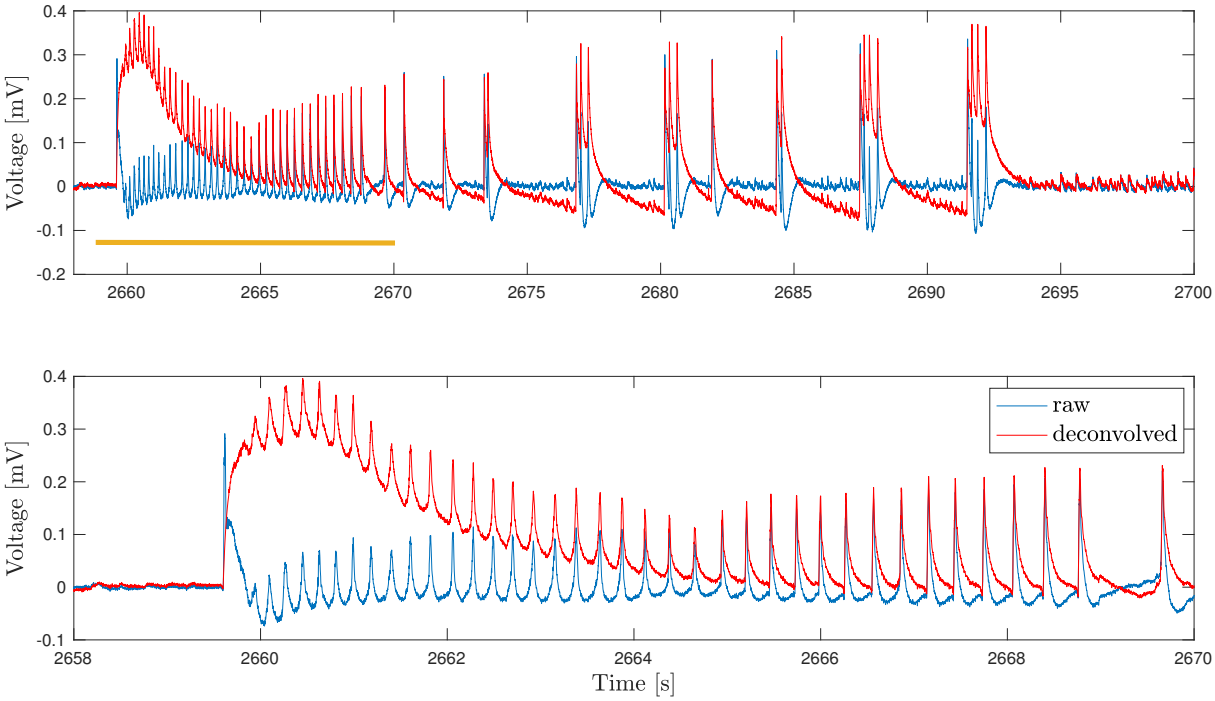

Figure 7.3: Fine structure within a single seizure-like event in a mouse brain slice extracted from the LFP trace of Fig. 7.2. Bottom panel shows an enlarged view of the upper highlighted section. Deconvolution reveals the underlying structure of the SLE: slow voltage pulse with fast onset, slow offset, containing a sequence of high frequency pulses ("quills") that are similar in shape to individual action potentials. Quill frequency slows from ∼5 to 2 s^{-1} and amplitude increases from 0.1 to 0.3 mV towards the end of event.

7.3 Simulated Seizure-like events

A series of homogeneous-cortex point simulations were conducted to demonstrate that, at high blocking ratios, True-field is capable of producing pathological voltage patterns that resemble seizure events in slice. In Fig. 7.4, I present simulated seizure-like events (sSLEs) generated by True-field using Table 6.3 parameters.

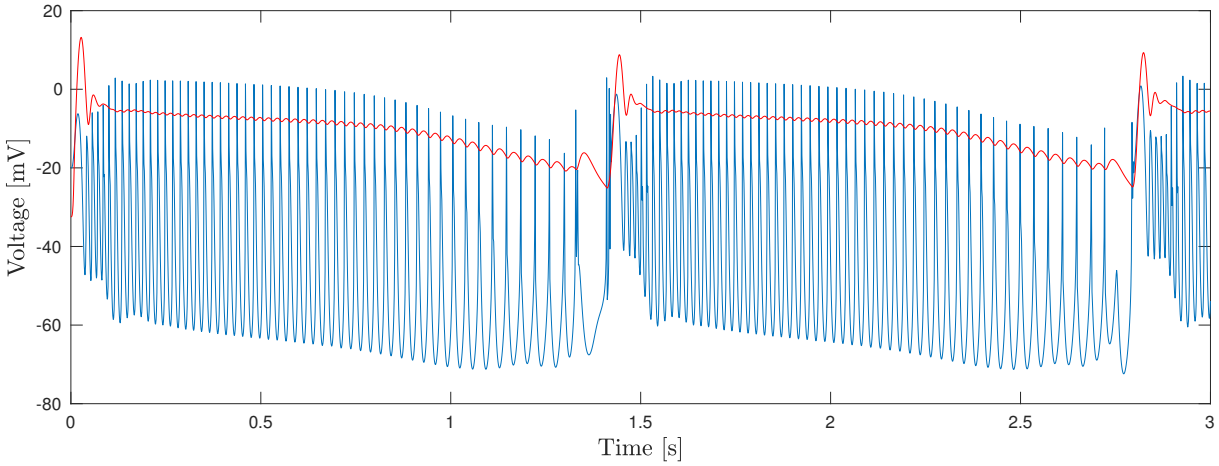

Figure 7.4: True-field simulation showing emergence of seizure-like patterns at higher blocking ($B = 500$). Blue and red traces represent excitatory and inhibitory populations respectively. The shape of sSLEs is similar to the structure of SLEs seen in mouse brain slice: fast onset, slow offset, containing a series of high frequency quills. Quill frequency slows from ∼56 to 26s^{-1} toward the end of each slow cycle. Stimulus current $I^{\mathrm{dc}} = 5.89\,\mathrm{Am}^{-2}$; time-step $\Delta t = 10\,\mu$s. See Table 6.3 for parameter values.

It is possible to change the structure and the duration of sSLEs by tuning some of the True-field parameters. For example, the behaviour in Fig. 7.5 results from raising ρ_{ee} (self-excitation of excitatory population), and lowering ρ_{ei} (excitation of inhibitory population). See Table 7.1 for parameter settings.

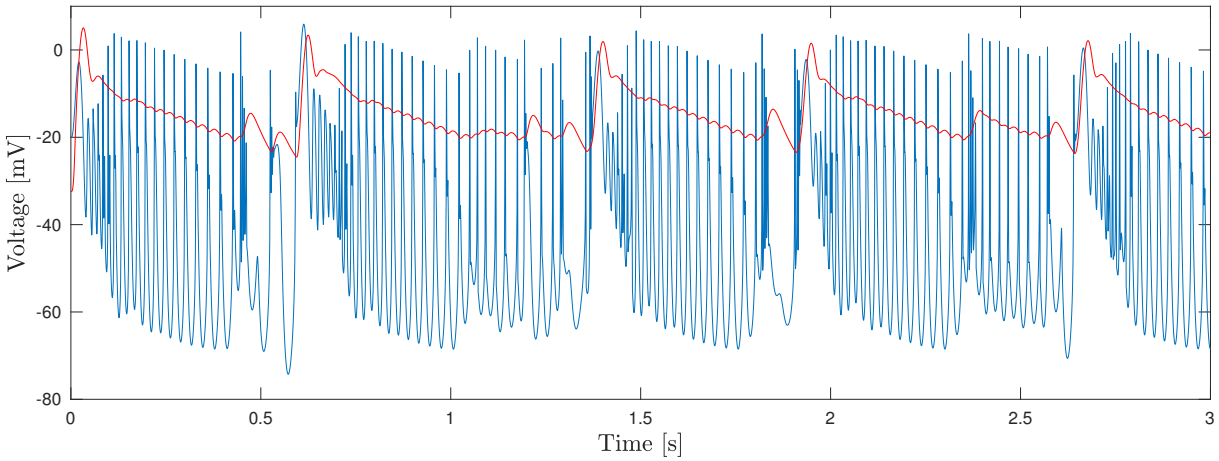

Figure 7.5: True-field simulated SLEs showing different structure and duration. Blue and red traces represent excitatory and inhibitory populations respectively. ρ_{ee} and ρ_{ei} are altered relative to Fig. 7.4: Simultaneous increase in excitation of excitatory population (ρ_{ee}) and decrease in excitation of inhibitory population (ρ_{ei}) generates more slow-envelope events per second. Here, $I^{\mathrm{dc}} = 5.89\,\mathrm{Am}^{-2}$; and $\Delta t = 10\,\mu$s. See Table 7.1 for parameter values.

Table 7.1: True-field settings for generation of simulated SLE patterns. Fig. 7.4 uses Table 6.3 default values; for Fig. 7.5, two synaptic gains are altered.

Symbol	Description	Fig. 7.4	Fig. 7.5	Unit
ρ_{ee}	$e \to e$ synaptic gain	90×10^{-3}	100×10^{-3}	V per spike
ρ_{ei}	$e \to i$ synaptic gain	200×10^{-3}	90×10^{-3}	V per spike
ρ_{ie}	$i \to e$ synaptic gain	-10×10^{-3}		V per spike
ρ_{ii}	$i \to i$ synaptic gain	-0.1×10^{-3}		V per spike
D_i	inhibitory voltage-diffusion coefficients	$500 D_0$		$\mathrm{m^2 s^{-1}}$
D_e	excitatory voltage-diffusion coefficients	$D_i/100$		$\mathrm{m^2 s^{-1}}$
D_{Ri}	inhibitory recovery-diffusion coefficients	2.47×10^{-13}		$\mathrm{m^4 V^{-1}}$
D_{Re}	excitatory recovery-diffusion coefficients	5.27×10^{-17}		$\mathrm{m^4 V^{-1}}$
Γ_b	voltage noise intensity	1×10^{-10}		$\mathrm{m^2 V^2 s^{-1}}$
Γ_R	recovery noise intensity	1×10^{-10}		$\mathrm{m^2 s^{-1}}$
B	blocking ratio	500		

$D_0 = 6.6 \times 10^{-4}\ \mathrm{m^2 s^{-1}}$

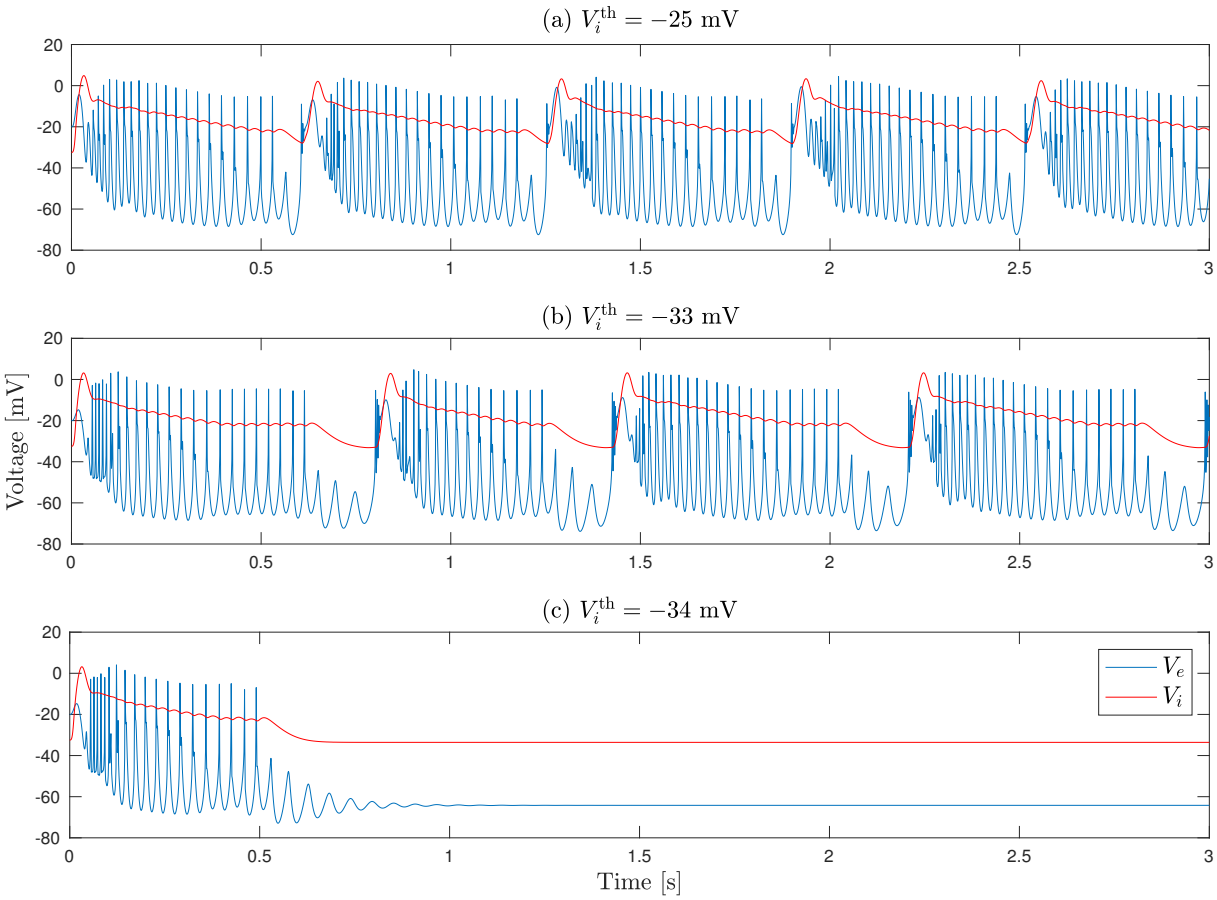

Figure 7.6: Simulated SLEs generated by homogeneous True-field cortex for varying V_i^{th}, the firing threshold for inhibitory neurons. Lowering V_i^{th} tends to slow and eventually suppress sSLE activity. Here, $I^{\mathrm{dc}} = 5.89\,\mathrm{Am^{-2}}$; and $\Delta t = 10\,\mu\mathrm{s}$.

In Fig. 7.6, I show that it is possible to quench sSLE activity by lowering V_i^{th}, the firing threshold for inhibitory neurons in the wave equation (see Eq. (6.4)). Lowering the threshold increases the synaptic flux of inhibitory spike events. When $V_i^{\mathrm{th}} < -34\,\mathrm{mV}$, sSLE activity ceases, implying a cutoff value lying between -33 and -34 mV that marks the death of sSLEs.

However, we see an initial event in (c) because, at simulation startup, system variables are not necessarily set to their steady-state values. Interestingly, in all plots the red trace (inhibitory) has two slopes (clearly visible in (b) and (c)): initially a shallow slope followed by a steeper one. We see that when the blue trace (excitatory) is generating spikes, the red trace has a shallow negative slope, which abruptly becomes steeper when the excitatory effect is no longer being felt by the inhibitory population.

7.4 Analysis of Simulated Seizure-like Event Properties

Comparing the slice SLE patterns of Fig. 7.2 with the True-field simulations of Figs. 7.4, 7.5, it is evident that they share similarities: slow pulse-like voltage envelope; fast onset and slow offset; a sequence of much faster pulses (quills) following the slow pulse. However, there are some differences such as noise characteristics, intermittency, duration of events, and quill structure. My aim in this section is to identify which True-field parameters can be tuned to resolve some of these differences.

7.4.1 Modulate Noisy Behaviour in sSLEs

An obvious difference between the biological SLE and its True-field simulation is the noisy background seen in SLEs (see Fig. 7.3). This can be easily modulated in simulated events by adding extra white noise in the V_e and V_i voltage equations. This noise addition is an artificial representation of the background noise sources present in the cortical tissue that are not modelled in the True-field equations. In Fig. 7.7, I present a simulation that corresponds to that of Fig. 7.5, after introducing additional external noise to the V_e and V_i voltage equations (6.1).

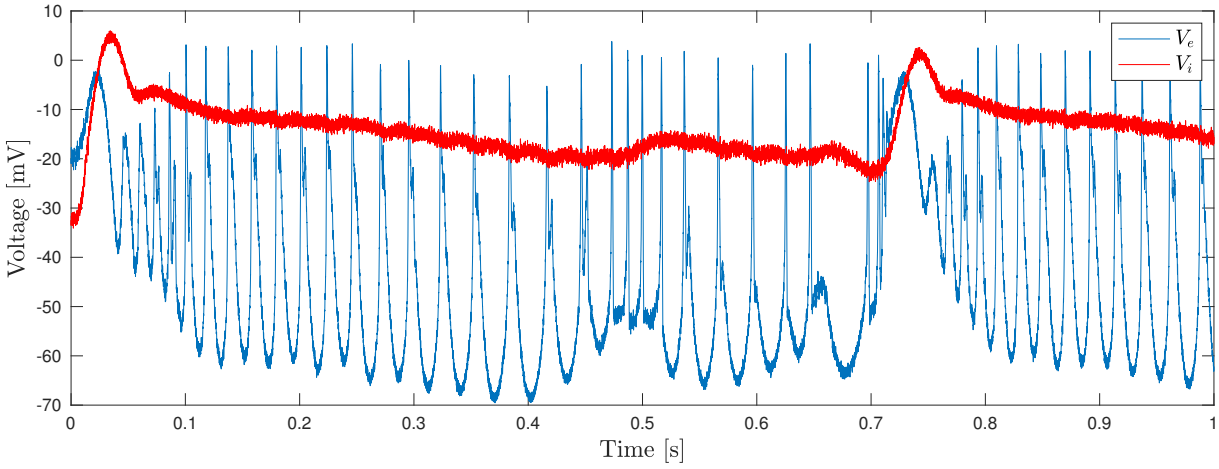

Figure 7.7: True-field simulation of noisy seizure-like events. Noisy behaviour is induced by adding external noise of intensity 0.01 $\mathrm{m^2V^2s^{-1}}$ in voltage equations. Here, $I^{\mathrm{dc}} = 5.89\,\mathrm{Am^{-2}}$; and $\Delta t = 10\,\mu\mathrm{s}$. See Table 7.1 for parameter values.

7.4.2 Developing Intermittent Behaviour in sSLEs

One non-biological feature of simulated seizure-like events is that they tend to be periodic in nature, rather than intermittent and isolated. This might be because there is no mechanism in

the equations to model metabolic fatigue effects seen in living tissue e.g., oxygen depletion of Fig. 7.2.

I investigate two different approaches to evoke sSLE intermittency. The first uses a threshold-and-reset mechanism on Brownian noise (integral of Gaussian noise) to produce artificial I^{dc} (stimulus) trigger events. A trigger event occurs whenever the Brownian-distributed random drift crosses a threshold (see Fig. 7.8). The artificially triggered sSLEs are shown in Fig. 7.9 (bottom panel). Here, I^{dc} stimulus is kept at subthreshold resting value, and pulsed high for 0.1 s at each trigger event. MATLAB code to generate trigger events is given below.

```
% Trigger-event generator: Use Brownian noise with threshold detection

dt = 1e-5;     % in s
time_end = 5;  % in s

time = [0 : dt : time_end];     % timebase

gnoise = randn(size(time));     % normally distributed fluctuations
bnoise = zeros(size(gnoise));   % Brownian noise = integral of gnoise
trig   = zeros(size(gnoise));   % trigger points

BMAX = 300;      % Brownian threshold ==> trigger and reset

bnoise(1) = gnoise(1);
for i = 2 : length(time)
    bnoise(i) = gnoise(i) + bnoise(i-1);
    if abs(bnoise(i)) > BMAX
        bnoise(i) = 0;
        trig(i) = 1;
    end
end

% find indices for trigger events
index = find(trig==1);

% Idc values
Idc_set = -0.9 + 0.1*trig;

% pulse Idc high (at critical value for firing) for 0.1 s
for i = 1:length(index)
    in = index(i);
    Idc_set(in:in + 10000) = 0.8;
end
```

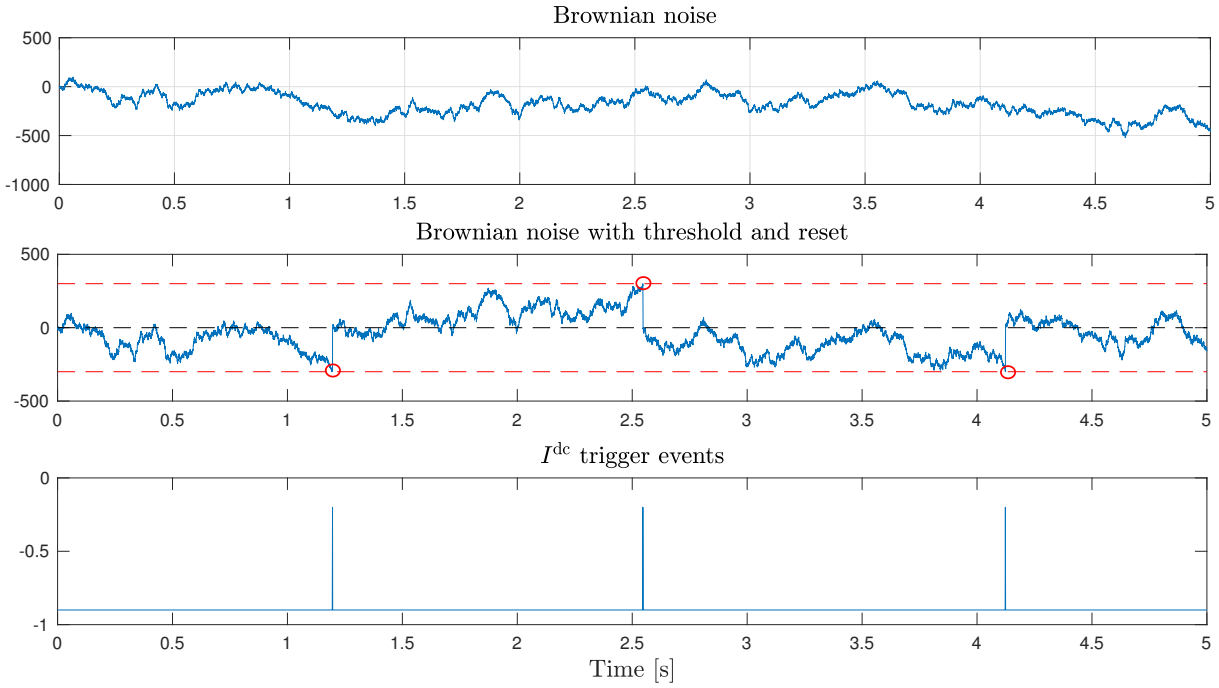

Figure 7.8: Trigger events generated by a threshold-and-reset mechanism on Brownian noise

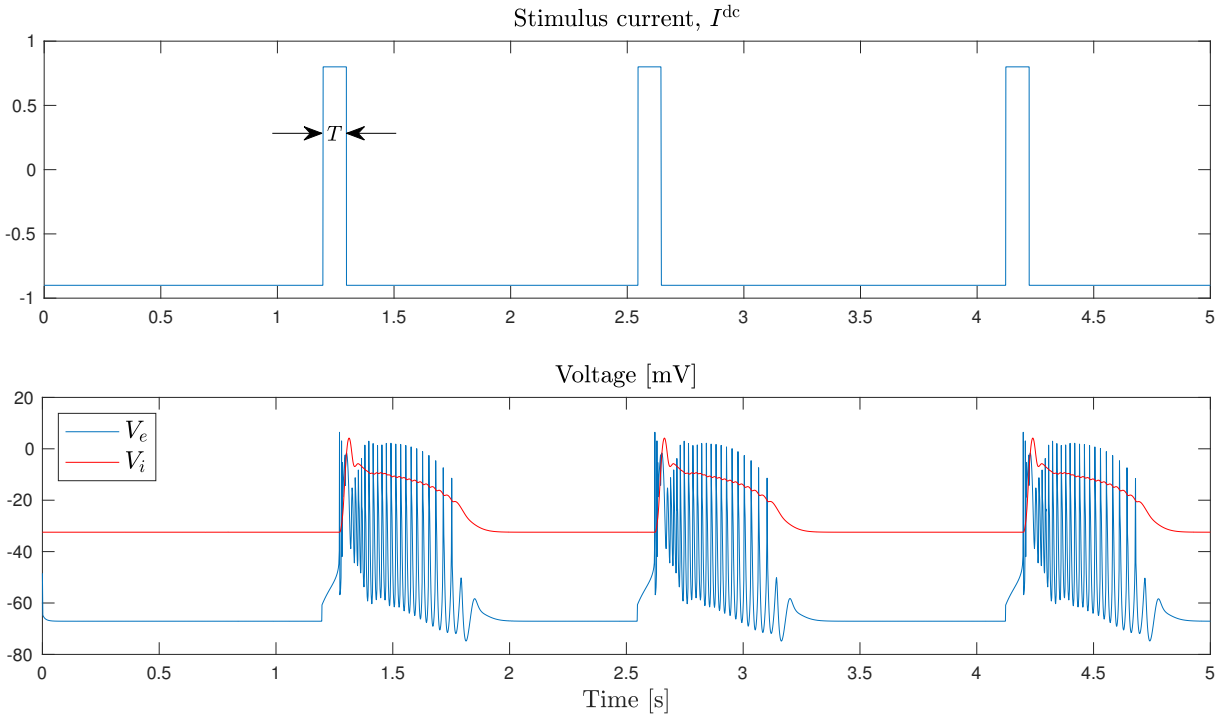

Figure 7.9: Artificially triggered sSLEs. I^{dc} is set at subthreshold resting value ($I^{dc} = -0.9\,\mathrm{Am}^{-2}$) and pulsed high ($I^{dc} = 0.8\,\mathrm{Am}^{-2}$) for $T = 0.1\,\mathrm{s}$ at each trigger event. Here, $\Delta t = 10\,\mu\mathrm{s}$. See Table 7.1 for parameter values.

The second approach is to allow trigger events to occur "naturally" by running the simulation at a stimulus current that is slightly below the critical value (threshold for generating an event), but with increased external noise in the voltage equations. This is demonstrated in the 20-s simulation shown in Fig. 7.10. See Table 7.2 for parameter settings.

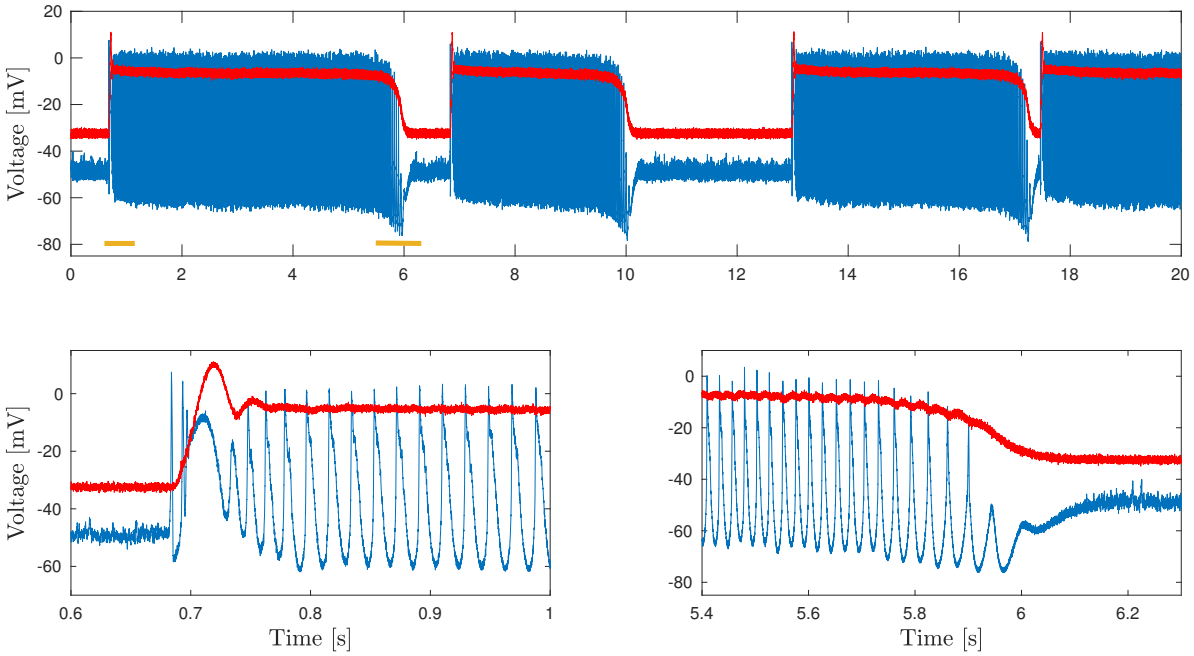

Figure 7.10: True-field simulations of noise-triggered intermittent seizure-like events. External noise of intensities 0.012, 0.01 $\mathrm{m^2V^2s^{-1}}$ are added to excitatory and inhibitory voltage equations respectively. Here, $I^{\mathrm{dc}} = 0.7\,\mathrm{Am^{-2}}$; and $\Delta t = 10\,\mu\mathrm{s}$. See Table 7.2 for parameter values.

Table 7.2: True-field settings used in Fig. 7.10 to explore intermittent sSLE behaviour

Symbol	Description	Value	Unit
τ_e	excitatory time constant	2×5.6	ms
τ_i	inhibitory time constant	6	ms
ρ_{ee}	$e \to e$ synaptic gain	100×10^{-3}	V per spike
ρ_{ei}	$e \to i$ synaptic gain	200×10^{-3}	V per spike
ρ_{ie}	$i \to e$ synaptic gain	-10×10^{-3}	V per spike
ρ_{ii}	$i \to i$ synaptic gain	-0.1×10^{-3}	V per spike
D_i	inhibitory voltage-diffusion coefficients	$500 D_0$	$\mathrm{m^2s^{-1}}$
D_e	excitatory voltage-diffusion coefficients	$D_i/100$	$\mathrm{m^2s^{-1}}$
D_{Ri}	inhibitory recovery-diffusion coefficients	2.47×10^{-13}	$\mathrm{m^4V^{-1}}$
D_{Re}	excitatory recovery-diffusion coefficients	5.27×10^{-17}	$\mathrm{m^4V^{-1}}$
Γ_b	voltage noise intensity	1×10^{-10}	$\mathrm{m^2V^2s^{-1}}$
Γ_R	recovery noise intensity	1×10^{-10}	$\mathrm{m^2s^{-1}}$
B	blocking ratio	500	
V_i^{th}	firing threshold for inhibitory neurons	-25	mV

$D_0 = 6.6 \times 10^{-4}\ \mathrm{m^2s^{-1}}$

7.4.3 Duration of sSLE

In Fig. 7.2, we see that a biological SLE lasts for about 5 s whereas the triggered SLEs in Fig. 7.9 only persist for about 0.5 s. I find that there are four True-field parameters that have a significant impact on the duration of sSLE:

- Voltage-diffusion coefficients, D_e and D_i
- Blocking ratio B
- Excitatory-to-inhibitory synaptic gain ρ_{ei}
- Excitatory recovery time constant τ_e

In Fig. 7.11, I examine the effect of voltage-diffusion coefficients (D_e and D_i) on the duration of sSLE. We see that the duration of the slow pulse-like voltage envelope can be lengthened by down-scaling either of the voltage-diffusion coefficients. In Fig. 7.11 (left panels), we also see that large inhibitory diffusivities tend to wash out the high-frequency quill structure.

Figure 7.12 shows that blocking tends to prolong sSLE duration and enhance quill production, while the converse is true for diffusion. Thus, we can increase the duration of sSLE either by reducing diffusion, or by increasing blocking.

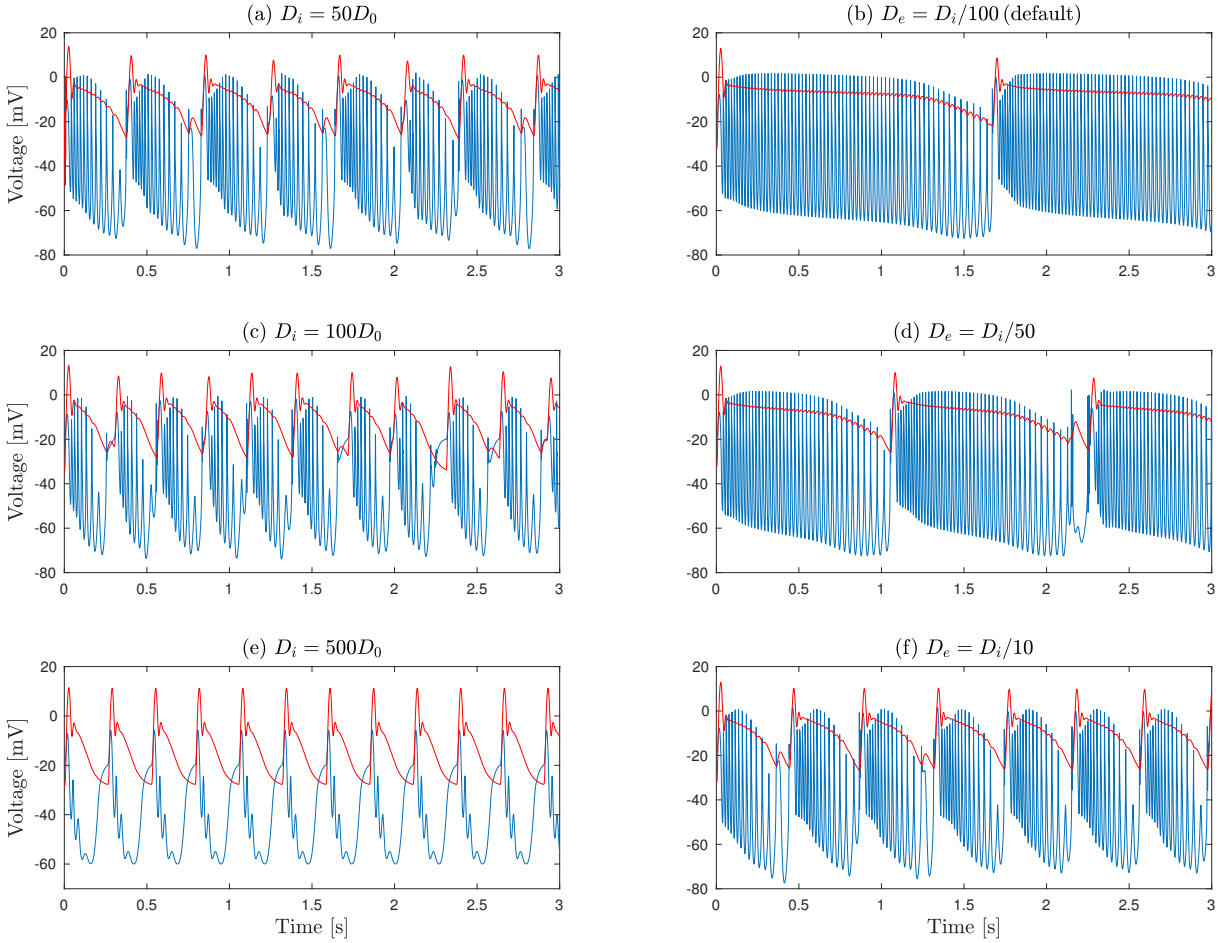

Figure 7.11: Effect of voltage-diffusion coefficients, D_i (left panels) and D_e (right panels) on the duration of simulated SLEs. Duration of sSLE increases with reduced D_e or D_i. For left panels $B = 50$ (length of macrocell $L = B\ell = 0.5$ mm), $D_e = D_i/100$; right panels $B = 500$ (length of macrocell $= L = 5$ mm), $D_i = 500D_o$. Here, $I^{\mathrm{dc}} = 5.89\,\mathrm{Am}^{-2}$; and $\Delta t = 10\,\mu$s. See Table 6.3 for parameter values.

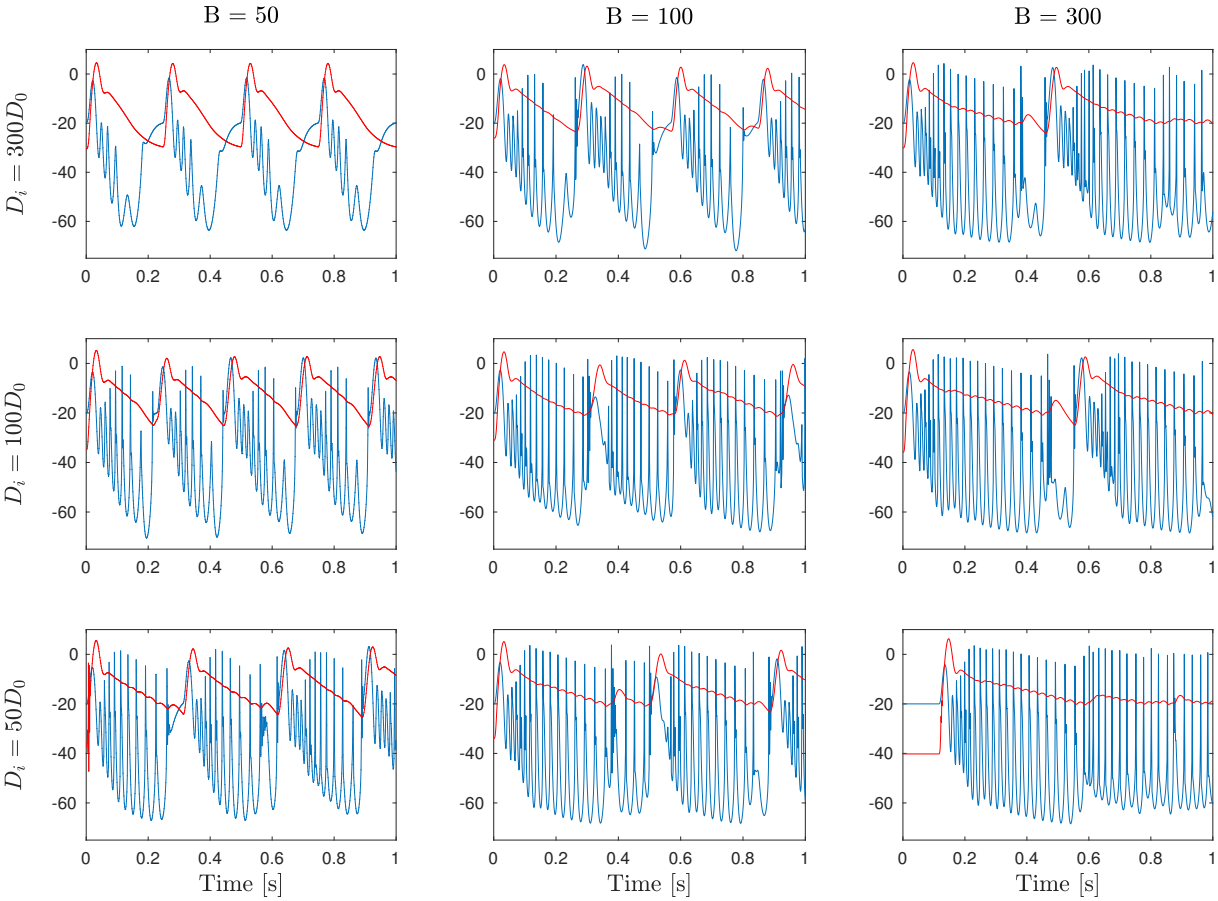

Figure 7.12: True-field simulated SLEs showing interaction between blocking and diffusion. Large diffusivity tends to wash out the quill structure; the duration of sSLE can be increased either by reducing diffusion (top to bottom), or by increasing blocking (left to right). Here, $I^{\mathrm{dc}} = 5.9\,\mathrm{Am}^{-2}$; and $\Delta t = 10\,\mu\mathrm{s}$. See Table 6.3 for parameter values.

Figures 7.13 and 7.14 show that sSLE duration can be prolonged by increasing ρ_{ei} synaptic gain, or by increasing the excitatory recovery time constant τ_e.

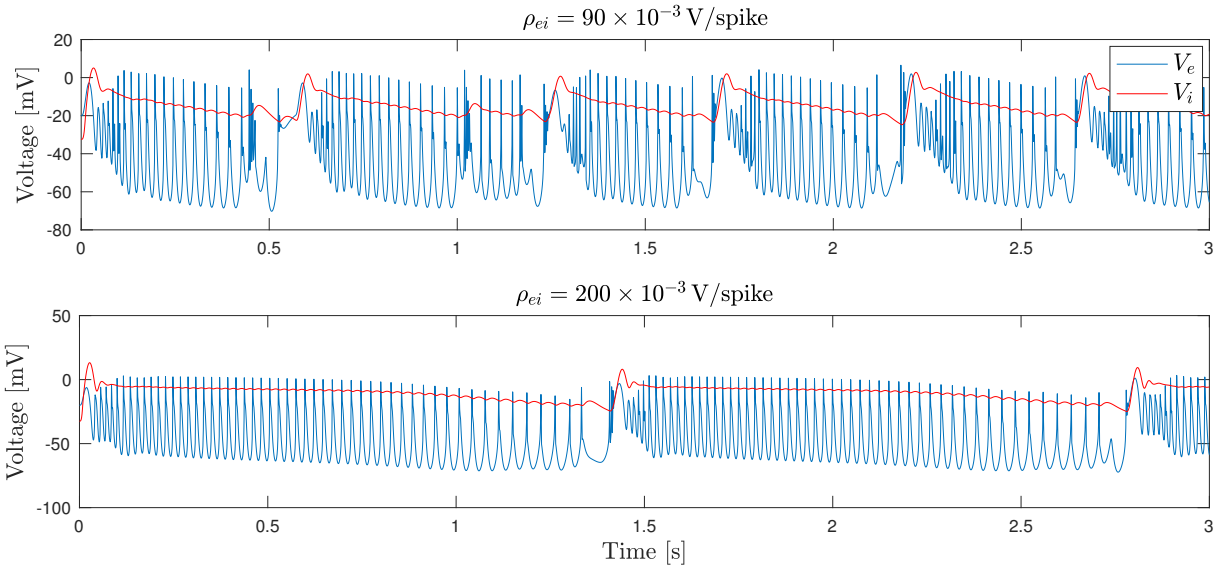

Figure 7.13: Effect of synaptic gain on structure of simulated SLE. Duration of sSLE increases with ρ_{ei}. Here, $I^{\mathrm{dc}} = 5.9\,\mathrm{Am}^{-2}$; and $\Delta t = 10\,\mu\mathrm{s}$. See Table 6.3 for parameter values.

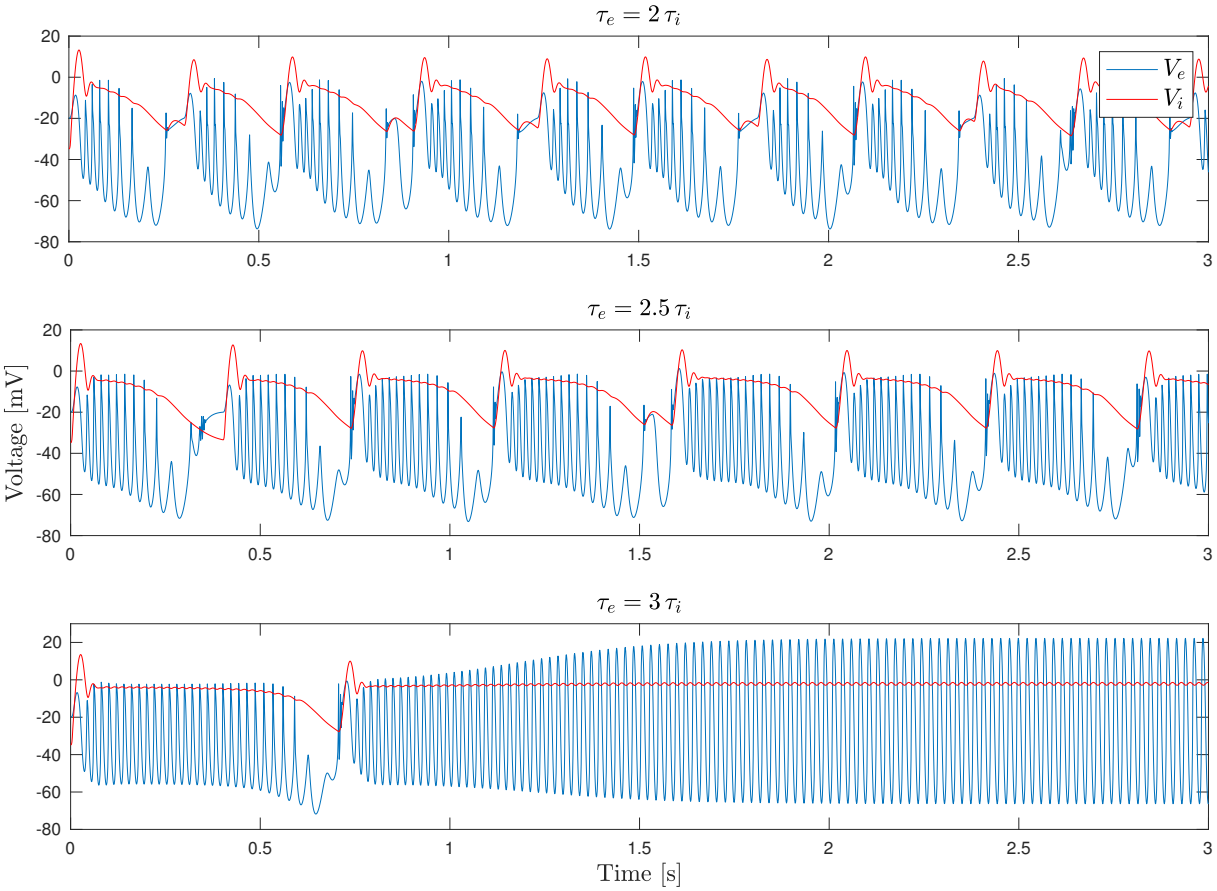

Figure 7.14: Effect of excitatory recovery time constant, τ_e on the duration of sSLE. Increase of τ_e tends to raise the duration of sSLE. Here, $B = 50$; $D_i = 100D_0$; $I^{\mathrm{dc}} = 5.89\,\mathrm{Am}^{-2}$; and $\Delta t = 10\,\mu\mathrm{s}$. See Table 6.3 for all other parameter values.

7.4.4 Quill Structure

In this section I investigate the formation and structure of high frequency components (quills) seen in True-field simulated SLEs.

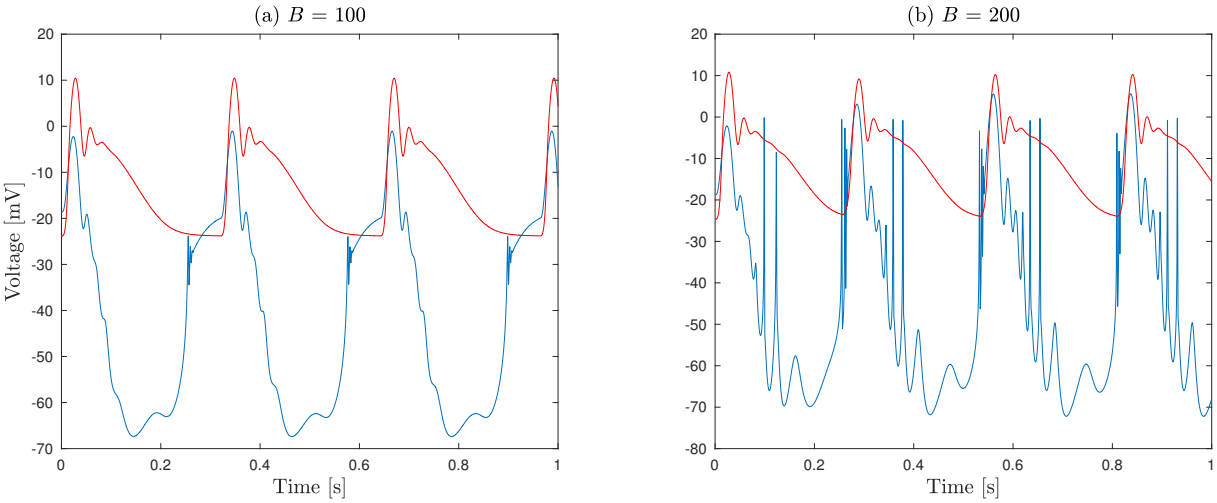

Figure 7.15: Emergence of high-frequency quill structures when blocking ratio is increased from $B = 100$ to 200. Here $\Gamma_b = 10^{-8}\,\mathrm{m^2V^2s^{-1}}$, $\Gamma_R = 10^{-8}\,\mathrm{m^2s^{-1}}$; $\gamma_{ib} = 50\,\mathrm{s^{-1}}$; $I^{\mathrm{dc}} = 6.5\,\mathrm{Am}^{-2}$; and $\Delta t = 10\,\mu\mathrm{s}$. See Table 6.3 for all other parameter values.

Fig. 7.15 shows that high-frequency quill structures can emerge as part of the underlying ∼3-Hz delta oscillation when blocking is raised from $B = 100$ to 200; these quill features appear in the leading and trailing edges of the nonlinear delta wave. This provides evidence that blocking has a significant impact on the formation and the structure of quills. There are 13 blocking-dependant correction terms,

$$G_1(V,R) = d_0 + d_1V + d_2V^2 + \boxed{d_3V^3} + \boxed{d_4V^4} + d_5VR + \boxed{d_6V^2R} + d_7R$$

$$G_2(V,R) = d_8 + d_9R + d_{10}V + d_{11}V^2 + \boxed{d_{12}V^3}$$

where $G_1(V,R)$ and $G_2(V,R)$ appear in voltage and recovery equations respectively. The equations for correction coefficients are listed in Section 3.3.4.

I find that of the 13 correction terms, only d_3V^3, d_4V^4, d_6V^2R, and $d_{12}V^3$ have significant impact on quill formation. These are the same dominant correction terms identified earlier in Section 5.4.

In Fig. 7.16, I quantify individual contributions of each term by turning on one at a time. Comparing Figs. 7.15 and 7.16, we see that d_4V^4 is responsible for forming the slow-wave delta oscillation. The other corrections set the dynamics of the high frequency components. Evidently, the fast quill structure seen in SLEs is formed by the interference of the d_3V^3, d_6V^2R, and $d_{12}V^3$ correction terms.

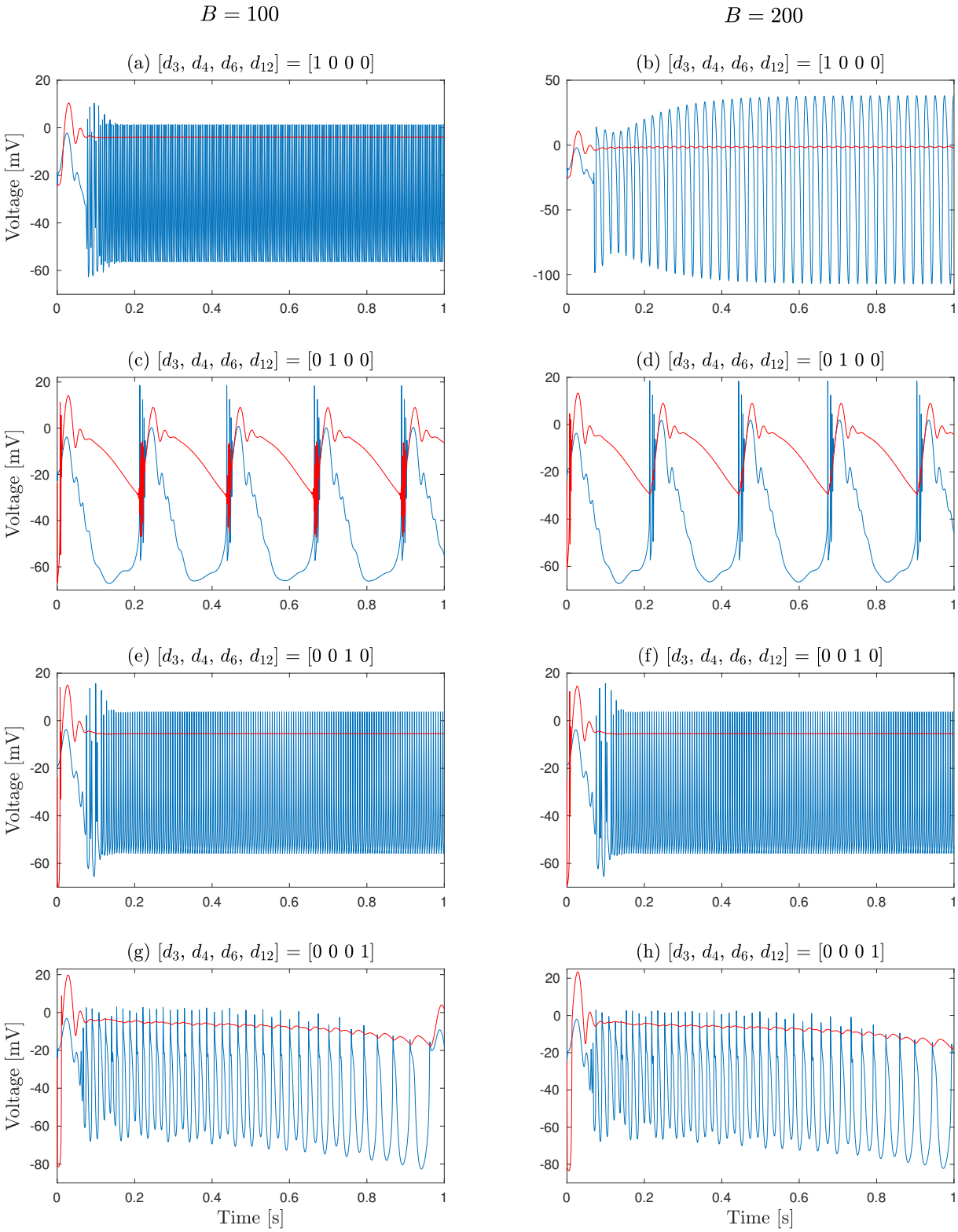

Figure 7.16: Impact of dominant correction terms on formation and structure of quills. Left and right columns represent $B = 100$ and 200 respectively. One dominant correction is turned on at a time (e.g., in (a) only d_3V^3 is turned on). Here $\Gamma_b = 10^{-8}\,\mathrm{m^2V^2s^{-1}}$, $\Gamma_R = 10^{-8}\,\mathrm{m^2s^{-1}}$; $\gamma_{ib} = 50\,\mathrm{s^{-1}}$; $I^{\mathrm{dc}} = 6.5\,\mathrm{Am^{-2}}$; and $\Delta t = 10\,\mu\mathrm{s}$. See Table 6.3 for all other parameter values.

In Fig. 7.2, we observe that the quill frequency of a biological SLE slows from ∼5 to 2 s^{-1} towards the end of event. However, simulated SLEs have a much faster quill structure, e.g., sSLEs in Fig. 7.4 slow from ∼56 to 26 s^{-1}.

Figure 7.12 provides evidence that higher blocking and lower diffusivities tend to boost emergence of quills. However, neither have a significant impact on quill frequency. Even though it is very challenging to reduce quill frequency by adjusting True-field parameters, I have been able to identify excitatory recovery time constant τ_e as parameter that has a direct impact on quill structure and frequency. Figure 7.17 shows that quills slow down with reduced τ_e.

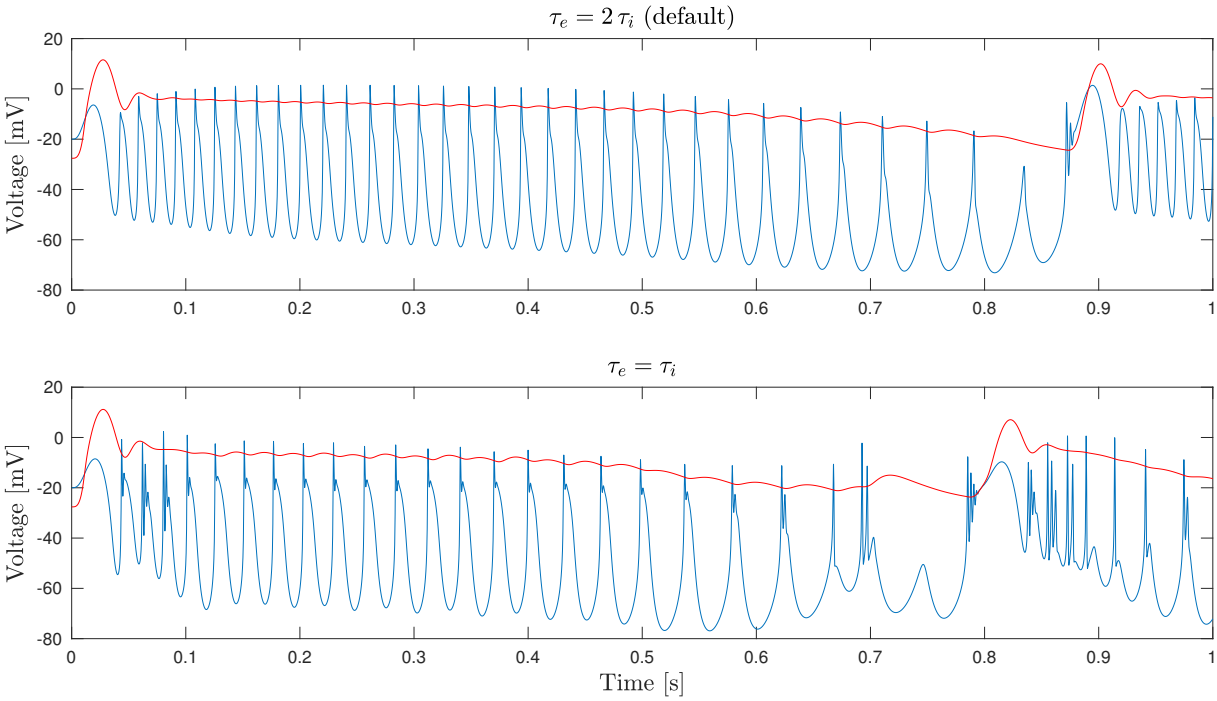

Figure 7.17: Effect of excitatory recovery time constant, τ_e on the quill structure of sSLE. Decrease of τ_e tends to slow down quills but generates higher-frequency sub-quill structures. Quill frequency slows down towards the end of event: ∼53 to 26 s^{-1} (top); ∼37 to 23 s^{-1} (bottom). Here, $B = 300$; $I^{\text{dc}} = 5.89\,\text{Am}^{-2}$; and $\Delta t = 10\,\mu$s. See Table 6.3 for parameter values.

7.5 Grid Simulations

In this section, I present a 2D grid simulation whose True-field parameter settings match those used in the homogeneous-cortex point simulation of Fig. 7.10. Simulation is run for 20 s on a 101×101 square grid with spatial resolution:

$$\Delta x = \Delta y = B\ell = 500 \times 10\,\mu\text{m}; \quad \text{length of grid} = 0.5\,\text{m}$$

The time-step is set at $\Delta t = 16\,\mu$s and at each time-step all grid points ($101 \times 101 = 10\,201$) are updated simultaneously using MATLAB array operators. A stimulus current just above threshold is provided to the middle cell, while all other cells are simulated with a subthreshold current. In Fig. 7.18, I present four frames of the grid simulation to show the evolution and propagation of simulated SLEs through the grid. See Table 7.2 for parameter settings.

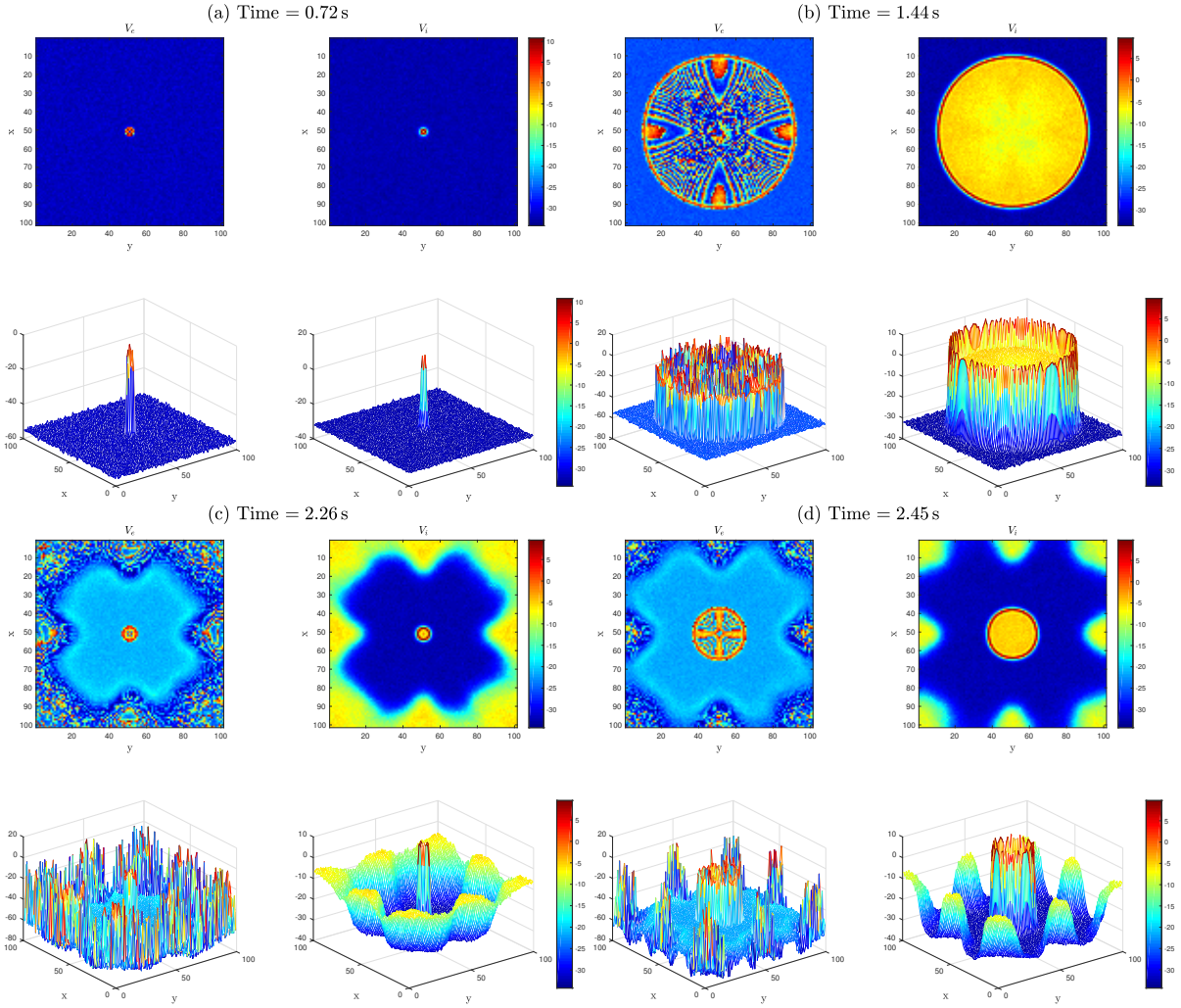

Figure 7.18: Propagation of True-field simulated SLEs through grid. 101×101 square grid with spatial resolution 5 mm ($B = 500$) is simulated for 20 s: stimulus currents of 0.74 and 0.6 Am^{-2} are applied to the middle cell and rest of the grid respectively. Four frames are presented: (a) evolution of first event at middle cell; (b) propagation of the first event through grid; (c) evolution of second event at middle cell; (d) propagation of the second event through grid. External noise of intensities 0.012, 0.01 $\mathrm{m}^2\mathrm{V}^2\mathrm{s}^{-1}$ are added to excitatory and inhibitory voltage equations respectively. Here, $\Delta t = 16\,\mu$s. See Table 7.2 for parameter values. In NeSI, it takes ∼3 h to complete simulation, and 17 h to create movie.

Figure 7.19 is a 2D strip chart of cortical activity along the $x = 51$ central vertical axis for the full 20-s simulation; Fig. 7.20 presents a close-up view of the first sSLE. The fine structure in the V_e strip trace are the excitatory quills observed in previous point simulations; the quill frequency slows down towards the end of each slow cycle. Unexpectedly, the wavefront patterns transform from semi-regular to chaotic after about 15 s. This is probably the result of interference effects caused by wrapping around of older wavefronts at the edges of the periodic grid. Using the $\Delta y/\Delta t$ slope of the first wavefront, wave speed is estimated to be 0.24 ms^{-1}.

In Fig. 7.21, I show time series of voltage at five grid points aligned parallel to the x-axis. It is clear that the events generated at the centre propagate outwards toward the edges of the grid. Propagation speed can be estimated from the time taken for the wave to transverse two grid cells ((51, 51) and (51, 55)) that are aligned perpendicular to the wave front,

$$\text{Wave speed} = \frac{(\text{difference between two grid positions}) \times (\text{spatial resolution})}{\text{time}}$$

$$= \frac{(55-51)\times(5\,\mathrm{mm})}{(2.27-2.19)\,\mathrm{s}} = 0.25\,\mathrm{ms}^{-1}$$

which is consistent with the value obtained from wavefront slope of the strip chart.

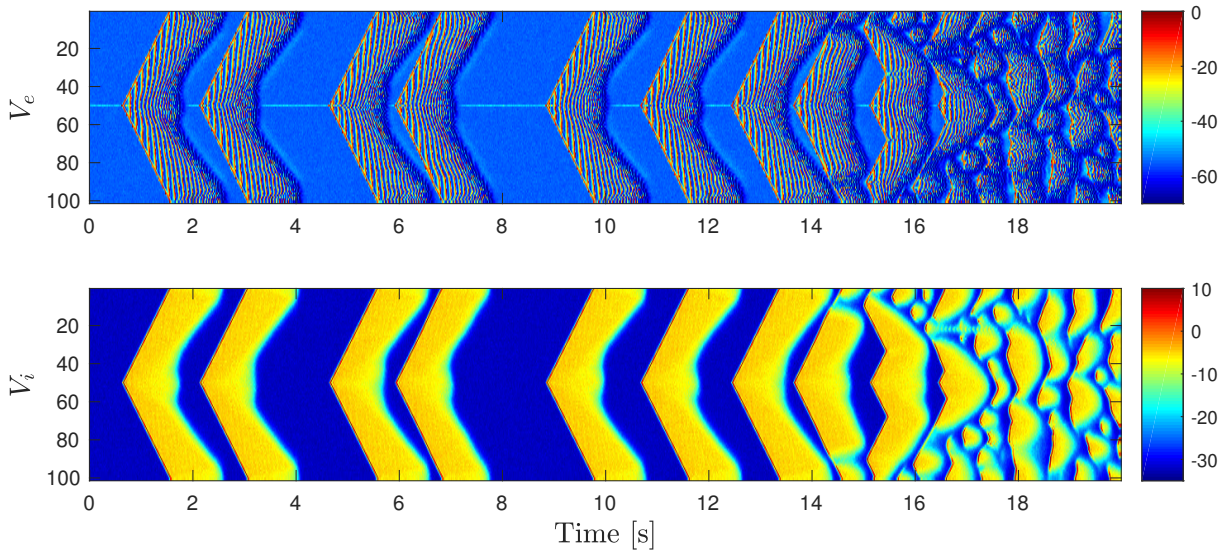

Figure 7.19: $V(t, y)$ space-time strip chart showing y-axis activity down the $x = 51$ centre line. Excitatory trace contains a fine substructure representing quill structure; inhibitory trace shows only slow-delta wavefronts. Around $t = 15\,\mathrm{s}$ wavefront patterns transform from semi-regular to chaotic when older waves wrap around the grid boundary to interfere with newer waves.

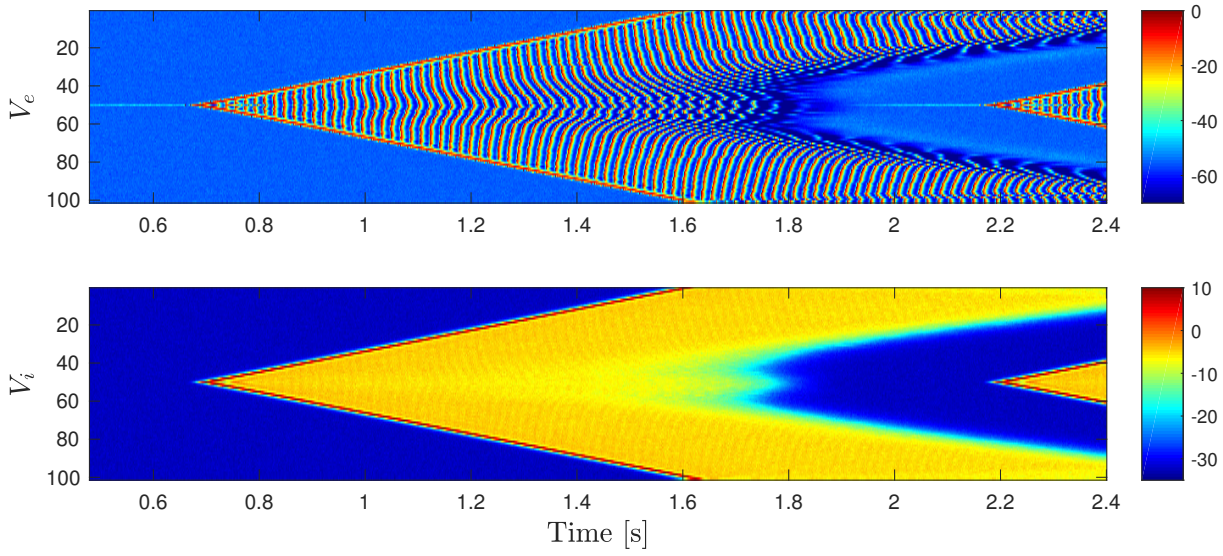

Figure 7.20: Zoomed view of the first event of $V(t, y)$ space-time strip chart of Fig. 7.19. Quill frequency slows down towards the end of event.

Figure 7.22 shows time series for V_e, V_i at the (51, 51) grid position. It is reassuring to see that the 2D grid simulations are similar to point simulation presented in Fig. 7.10. The excitatory delta-rhythm wavefronts contain quill-like substructures, whereas inhibitory activity shows only slow-delta travelling wavefronts.

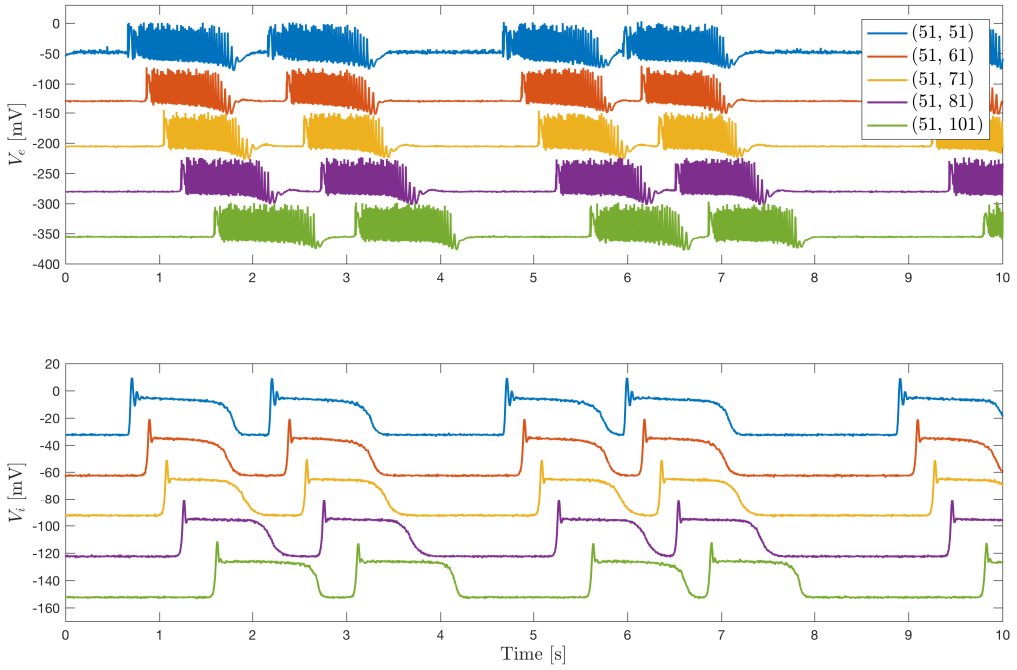

Figure 7.21: Time series of voltage for a subset of five grid points aligned parallel to the x-axis. To improve visibility, V_e and V_i traces have been displaced vertically by $(-75h)$ and $(-30h)$ mV, where $h = 0, ..., 4$ is the curve number. Wavefronts propagate from centre to the edge of the grid with a speed of ~ 0.25 ms^{-1}.

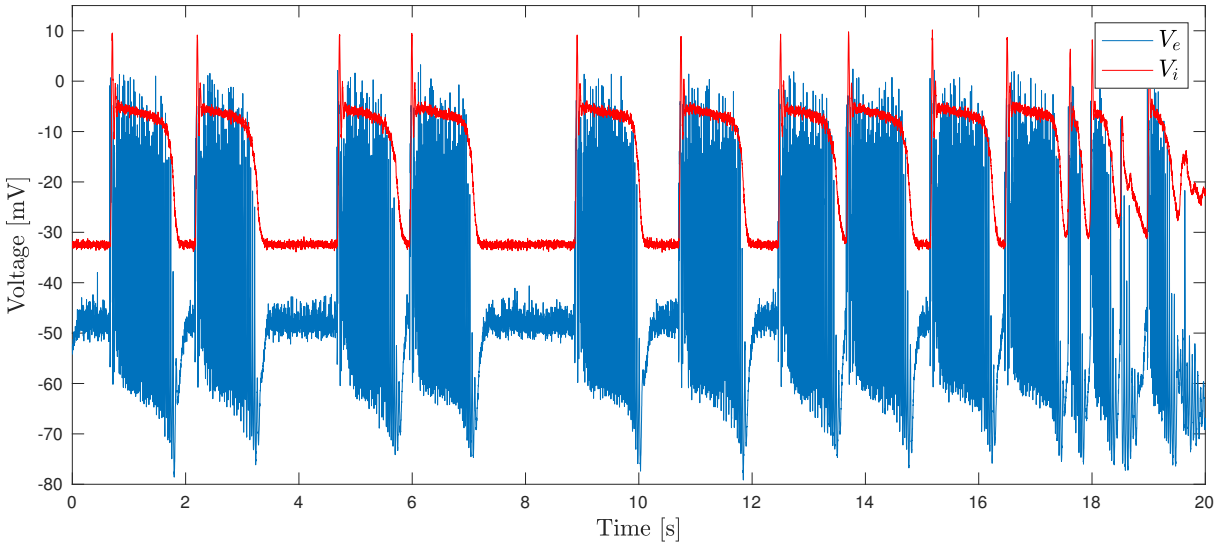

Figure 7.22: Time series of voltage at (51, 51), the centre of the grid. Grid simulations generate events that are qualitatively similar to those generated in point simulation of Fig. 7.10.

7.6 Chapter Summary

This chapter presented a comparison between True-field simulated SLEs and biological SLEs seen in slices of mouse brain tissue. After describing the electrophysiological experiments used to capture SLEs from mouse brain slice, I discussed how a deconvolution technique could be applied to eliminate shape distortions caused by the 1-Hz high-pass filter used during recording to remove

slow dc drifts. The properties of simulated SLEs were investigated using homogeneous-cortex point simulations and compared with the SLEs observed in slice experiments. I then showed how the characteristics of simulated SLEs can be altered by adjusting True-field parameters. Finally, a 2D grid simulation was presented to demonstrate propagation of simulated SLEs through the grid.

Chapter 8

Summary and Future Work

The true-field model describes the behaviour of interacting populations of excitatory and inhibitory neurons across multiple spatial scales. This thesis presents a preliminary analysis of the model. I focussed on four major surveys in this study: evaluation of blocking corrections; analysis of reblocked Wilson neuron; use of True-field to produce normal brain behaviours across multiple scales; tuning of True-field to induce a pathological pattern known as a seizure-like event (SLE).

8.1 Summary

Evaluation of reblocking corrections

The adiabatic elimination procedure used in the True-field model results in model equations defined at a larger spatial scale with reblocking corrections: 13 drift corrections, and eight diffusion corrections. My initial task was to evaluate the correction coefficients which depend on a set of wavenumber integrals and four other parameters: voltage and recovery noises, voltage and recovery diffusivities, side-length blocking ratio, and side-length of microcell. By choosing fixed values for blocking ratio ($B = 100$) and side-length of microcell ($\ell = 10\mu$m), I presented how I set the voltage and recovery diffusivities. The wavenumber integrals were then calculated numerically using Monte Carlo integration and were cross-checked using other numerical approaches. I evaluated correction coefficients using the calculated wavenumber integrals and pointed out that the squared-noise terms of correction coefficients can be safely ignored. I then investigated the variation of correction coefficients with blocking ratio and found that they all have initial growth or decay and tend to settle at higher blocking ($B > 300$).

Analysis of reblocked Wilson neuron

After calculating correction coefficients, my first task was to analyse a simplified version of the True-field model by suppressing chemical synapses: the reblocked Wilson neuron in the spatially homogeneous limit. I first investigated the reblocked neuron for negligible noise (small-noise limit) by re-doing the analysis of Steyn-Ross *et al* [72] and identified some corrections that caused a change in the mode of bifurcation to spiking from Hopf to saddle–node. The analysis was extended by turning on the noise-dependent correction terms, allowing the dynamical behaviour of the reblocked neuron to be compared with the original Wilson neuron. I analysed the effect of voltage and recovery noise intensities Γ_b and Γ_R on threshold for spiking and found that

increasing Γ_b at fixed Γ_R ($\Gamma_R = 0$) makes the neuron less sensitive (raises the threshold current), while increasing Γ_R at fixed Γ_b ($\Gamma_b = 10^{-10}$) makes the neuron more sensitive.

I also analysed the contribution of individual correction terms and identified d_3V^3, d_4V^4, and d_6V^2R as dominant voltage correction terms and $d_{12}V^3$ as the dominant recovery correction term.

True-field simulations to produce normal brain behaviours across multiple levels

My next goal was to demonstrate that True-field is capable of generating normal brain behaviours across multiple scales using a range of blocking ratios: spiking behaviour at microscale for low blocking, and agglomerated population events for higher blocking. I used a series of homogeneous-cortex point simulations to tune True-field parameters to enable transition from intracellular spiking to cortical-scale slow-delta waves. 2D grid simulations confirmed the generation and propagation of slow-delta oscillations across the reblocked cortical grid. I found that both wave propagation speed and delta frequency decrease with increased blocking.

True-field simulations to reproduce seizure-like events observed in mouse brain slice

In addition I was able to demonstrate that True-field can generate a pathological pattern of activity known as a seizure-like event (SLE). Homogeneous-cortex point simulations were used to tune parameters to get reasonable SLEs that are similar in shape to the bioelectrical events seen in mouse brain slice. I used Dr Logan Voss's mouse brain slice recordings to enable comparison with True-field simulated SLEs. I investigated how the properties of simulated SLEs can be altered by adjusting the underlying True-field parameters, and found that:

- the noisy background seen in biological SLEs can be reproduced by adding extra white noise in V_e and V_i voltage equations
- intermittency in simulated SLEs can be evoked by producing either artificial or natural I^{dc} (stimulus) trigger events
- four True-field parameters have a major impact on the duration of simulated SLEs: voltage-diffusion coefficients (D_e, D_i); blocking ratio (B); excitatory-to-inhibitory synaptic gain ρ_{ei}; excitatory recovery time constant τ_e
- blocking has a significant impact on the formation and the structure of quills: d_4V^4 controls formation of the slow-wave delta oscillation; interference of the d_3V^3, d_6V^2R, and $d_{12}V^3$ correction terms is responsible for the shape and frequency of the fast quill structures carried by the delta oscillations

A 2D grid simulation demonstrated propagation of simulated SLEs across the cortical grid. The wave propagation speed was calculated as 0.25 ms^{-1} which is slower than the normal slow-delta oscillation.

8.2 Limitations of True-field Model

- Inability to produce higher frequency brain rhythms due to lack of explicit connectivity between the cerebral cortex and the other regions of brain such as the thalamus.

- Need to continue re-tuning parameters for each mode of activity. In theory, only blocking parameters should change and the parameters associated with the dynamics should stay constant.

8.3 Future Work

In Chapter 6, I demonstrated that True-field can reproduce the electrical behaviour of human brain across multiple scales. However, in Fig. 6.6, we notice that, at low blocking, activity of the excitatory population is suppressed. This is unexpected because inhibitory neurons do not receive synaptic stimuli to generate action potentials until the excitatory neurons become active (see Fig. 6.1). I did some investigations using Table 6.4 parameter settings which generate the expected spiking behaviour at microscale. I turned off synaptic coupling between neurons,

$$\rho_{ee} = \rho_{ei} = \rho_{ie} = \rho_{ii} = 0$$

and conducted some homogeneous-cortex point simulations. In principle, when there is no coupling between the two populations, we expect to see spiking in the excitatory population only. Strangely, increasing the blocking tends to shut down the excitatory population and induce the activity of inhibitory neurons (see Fig. 8.1). Clearly, when blocking is raised, excitatory and

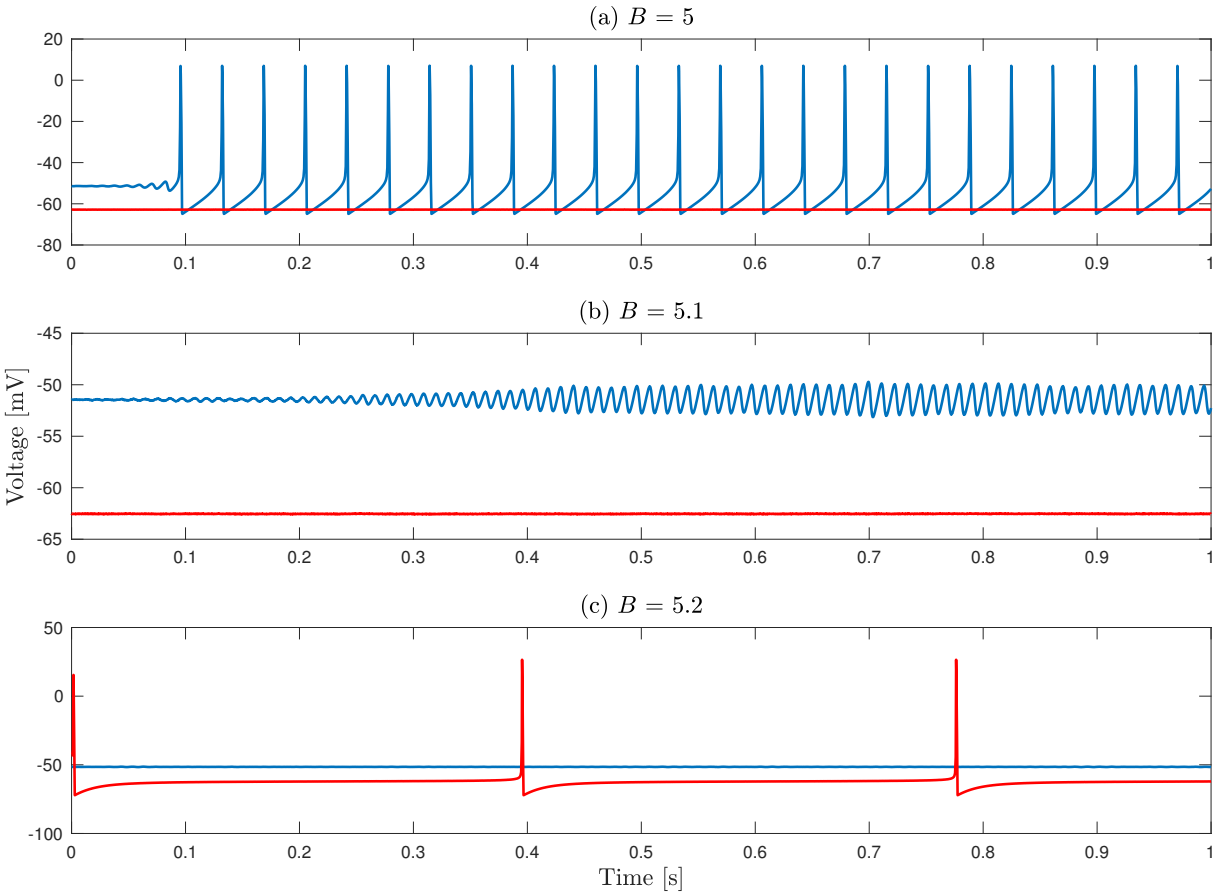

Figure 8.1: True-field simulations at low blocking when synaptic couplings are disabled. Increase in blocking tends to hyperpolarize excitatory neurons. Here, $I^{\mathrm{dc}} = 0.13\ \mathrm{Am}^{-2}$ and $\Delta t = 10\,\mu\mathrm{s}$. See Table 6.4 for all other parameter values.

inhibitory populations are behaving differently. Since synaptic couplings are disabled, it is clear that the blocking corrections are responsible for this difference. However, further investigations are required to identify the misbehaving blocking correction term.

Chapter 6 investigations could be extended to study cortical behaviour during natural sleep, anaesthetic-induced unconsciousness and epilepsy.

In Chapter 7, I showed that True-field is capable of generating pathological patterns that are similar in shape to seizure-like events observed in slice experiments. However, the quill frequency of a simulated event is much faster than that of a biological SLE. In Section 7.4.4, I showed that three correction terms (d_3V^3, d_6V^2R, and $d_{12}V^3$) are responsible for the formation of quill structure. One might attempt to slow the quill frequency by altering the interference of these three correction terms. This would require careful rebalancing of the underlying model parameters.

Appendix A

Matlab codes to evaluate wavenumber integrals $\overline{c}_{16}$ and $\overline{c}_3$

This appendix presents the MATLAB codes to calculate R2-restricted $\overline{c}_{16}$ and R0-restricted $\overline{c}_3$.

A.1 Matlab code to evaluate $\overline{c}_{16}$

```
% Evaluate c16 using Monte Carlo integration
clear; clc;

% parameter values

a0 = 17.81e3;       % per s
% Voltage diffusivity coefficients
Di = 6.60e-4;       % m^2/s
De = Di/100;
% Recovery diffusivity coefficients
DRi = 2.47e-13;     % m^4/V
DRe = 5.276e-17;
n_throws = 1e7;     % number of throws
l = 10e-6;          % side length of microcell in m
B = 100;            % blocking ratio
L = B*l;            % side length of macrocell in m

% define inner and outer bounds
vL = 2*pi/(L);

% define functions for integrand
lambda_b = @(qx, qy, Db) (4*Db/(l^2))*((sin(qx*l/2)).^2 + (sin(qy*l/2)).^2);
Lambda_b = @(qx, qy, Db) lambda_b(qx, qy, Db) + a0;

% generate random number matrix
R = (2*rand(6, n) - 1).*pi/L;

% define vectors in Q domain
Q1 = R(1,:) + 1i*R(2,:);
Q2 = R(3,:) + 1i*R(4,:);
Q3 = R(5,:) + 1i*R(6,:);
Q = Q1 + Q2 + Q3;

% find indices of points that fall inside annulus
index = find(abs(real(Q)) > pi/L | abs(imag(Q)) > pi/L);

% accepted q vector that satisfies the condition R1
q = Q(index);
```

```
N = length(q);
qx = real(q);
qy = imag(q);

% mean value of the integrand
fc16_e = Lambda_b(qx, qy, De).^-1;
fc16_e_mean = (1/n_throws)*sum(fc16_e);

fc16_i = Lambda_b(qx, qy, Di).^-1;
fc16_i_mean = (1/n_throws)*sum(fc16_i);

% volume of the domain
V2 = vL^6;

% Monte carlo integration approximation
c16_e = V2*fc16_e_mean;
c16_i = V2*fc16_i_mean;

% standard error
d_c16_e = V2*std(fc16_e)/sqrt(n);
d_c16_i = V2*std(fc16_i)/sqrt(n);
```

A.2 Matlab code to evaluate $\overline{c}_3$

This MATLAB code is similar to the code that evaluates the unrestricted wavenumber integrals in Section 4.2.1, but in addition we need to consider the R0 wavenumber restriction. Note that due to the additional computation of g and h complicated functions, the code is very long compared with the previous codes.

```
% Evaluate c3 using Monte Carlo integration
clear; clc;

% parameter values
a0 = 17.81e3;       % per s
b1 = 37.98;         % per V
E_K = -95e-3;       % V
gRb = 26e3;         % per s
g0R = gRb*abs(E_K);
% Voltage diffusivity coefficients
Di = 6.60e-4;       % m^2/s
De = Di/100;
% recovery time constants
tau_e = 2*5.6e-3;
tau_i = 5.6e-3;
% Recovery diffusivity coefficients
DRi = 2.47e-13;     % m^4/V
DRe = 5.276e-17;
n_throws = 1e7;     % number of throws
l = 10e-6;          % side length of microcell in m
B = 100;            % blocking ratio
L = B*l;            % side length of macrocell in m

% define inner and outer bounds
vL = 2*pi/(L);
vl = 2*pi/(l);
```

```
% define functions for integrand
lambda_b = @(qx, qy, Db) (4*Db/(l^2))*((sin(qx*l/2)).^2 + (sin(qy*l/2)).^2);
Lambda_b = @(qx, qy, Db) lambda_b(qx, qy, Db) + a0;
lambda_R = @(qx, qy, DR, taub) (16*DR/(l^4*taub))*((sin(qx*l/2)).^2 ...
                        + (sin(qy*l/2)).^2).^2;
Lambda_R = @(qx, qy, DR, taub) lambda_R(qx, qy, DR, taub) + (b1/taub);
w0_sqrd = @(Lambda_R) g0R* Lambda_R;
delta = @(Lambda_b, w0_sqrd) sqrt(Lambda_b.^2 - 4*w0_sqrd);
lambda_1 = @(Lambda_b, delta) (Lambda_b + delta)/2;
lambda_2 = @(Lambda_b, delta) (Lambda_b - delta)/2;

% generate random number matrix
R = 2*(rand(4, n) - 1).*pi/l;

% define vectors in q domain
q1 = R(1, :) + 1i*R(2, :);
q2 = R(3, :) + 1i*R(4, :);
q = q1 + q2;

% condition 1 for rejection
% any q lies outside the big box should also be rejected.
% q1 and q2 vectors causing that should also be rejected.
index_bad = find(abs(real(q))  > pi/l | abs(imag(q)) > pi/l);
q1(index_bad) = [];
q2(index_bad) = [];
q(index_bad) = [];

% condition 2 for rejection
% q1, q2 & q should lie outside the small square
% condition 1 for rejection
q1_rejected = find(abs(real(q1)) <= pi/L & abs(imag(q1)) <= pi/L);
q2_rejected = find(abs(real(q2)) <= pi/L & abs(imag(q2)) <= pi/L);
q_rejected = find(abs(real(q)) <= pi/L & abs(imag(q)) <= pi/L);
% select every index that should be rejected
rejected = unique([q1_rejected, q2_rejected, q_rejected]);

% delete rejected values
q1(rejected) = [];
q2(rejected) = [];
q(rejected) = [];

% accepted q vectors
N = length(q);

qx1 = real(q1); qy1 = imag(q1);
qx2 = real(q2); qy2 = imag(q2);
qx = real(q); qy = imag(q);

Lambda_b_q1_e = Lambda_b(qx1, qy1, De);
Lambda_b_q2_e = Lambda_b(qx2, qy2, De);
Lambda_b_q_e = Lambda_b(qx, qy, De);

Lambda_b_q1_i = Lambda_b(qx1, qy1, Di);
Lambda_b_q2_i = Lambda_b(qx2, qy2, Di);
Lambda_b_q_i = Lambda_b(qx, qy, Di);

Lambda_R_q1_e = Lambda_R(qx1, qy1, DRe, tau_e);
```

```
Lambda_R_q2_e = Lambda_R(qx2, qy2, DRe, tau_e);
Lambda_R_q_e = Lambda_R(qx, qy, DRe, tau_e);

Lambda_R_q1_i = Lambda_R(qx1, qy1, DRi, tau_i);
Lambda_R_q2_i = Lambda_R(qx2, qy2, DRi, tau_i);
Lambda_R_q_i = Lambda_R(qx, qy, DRi, tau_i);

% functions to evaluate g
w0_sqrd_q1_e = w0_sqrd(Lambda_R_q1_e);
w0_sqrd_q2_e = w0_sqrd(Lambda_R_q2_e);
w0_sqrd_q_e = w0_sqrd(Lambda_R_q_e);

w0_sqrd_q1_i = w0_sqrd(Lambda_R_q1_i);
w0_sqrd_q2_i = w0_sqrd(Lambda_R_q2_i);
w0_sqrd_q_i = w0_sqrd(Lambda_R_q_i);

delta_q1_e = delta(Lambda_b_q1_e, w0_sqrd_q1_e);
delta_q2_e = delta(Lambda_b_q2_e, w0_sqrd_q2_e);
delta_q_e = delta(Lambda_b_q_e, w0_sqrd_q_e);

delta_q1_i = delta(Lambda_b_q1_i, w0_sqrd_q1_i);
delta_q2_i = delta(Lambda_b_q2_i, w0_sqrd_q2_i);
delta_q_i = delta(Lambda_b_q_i, w0_sqrd_q_i);

L11_e = lambda_1(Lambda_b_q1_e, delta_q1_e);
L12_e = lambda_1(Lambda_b_q2_e, delta_q2_e);
L13_e = lambda_1(Lambda_b_q_e, delta_q_e);
L21_e = lambda_2(Lambda_b_q1_e, delta_q1_e);
L22_e = lambda_2(Lambda_b_q2_e, delta_q2_e);
L23_e = lambda_2(Lambda_b_q_e, delta_q_e);

L11_i = lambda_1(Lambda_b_q1_i, delta_q1_i);
L12_i = lambda_1(Lambda_b_q2_i, delta_q2_i);
L13_i = lambda_1(Lambda_b_q_i, delta_q_i);
L21_i = lambda_2(Lambda_b_q1_i, delta_q1_i);
L22_i = lambda_2(Lambda_b_q2_i, delta_q2_i);
L23_i = lambda_2(Lambda_b_q_i, delta_q_i);

Delta_e = (delta_q1_e.*delta_q2_e.*delta_q_e).^-1;
Delta_i = (delta_q1_i.*delta_q2_i.*delta_q_i).^-1;

% define g
g1_e = L11_e.*L12_e.*L13_e/(L11_e + L12_e + L13_e);
g2_e = L11_e.*L12_e.*L23_e/(L11_e + L12_e + L23_e);
g3_e = L11_e.*L22_e.*L13_e/(L11_e + L22_e + L13_e);
g4_e = L11_e.*L22_e.*L23_e/(L11_e + L22_e + L23_e);
g5_e = L21_e.*L12_e.*L13_e/(L21_e + L12_e + L13_e);
g6_e = L21_e.*L12_e.*L23_e/(L21_e + L12_e + L23_e);
g7_e = L21_e.*L22_e.*L13_e/(L21_e + L22_e + L13_e);
g8_e = L21_e.*L22_e.*L23_e/(L21_e + L22_e + L23_e);

g_e = Delta_e.*(-g1_e + g2_e + g3_e - g4_e + g5_e - g6_e - g7_e + g8_e);

g1_i = L11_i.*L12_i.*L13_i/(L11_i + L12_i + L13_i);
g2_i = L11_i.*L12_i.*L23_i/(L11_i + L12_i + L23_i);
g3_i = L11_i.*L22_i.*L13_i/(L11_i + L22_i + L13_i);
g4_i = L11_i.*L22_i.*L23_i/(L11_i + L22_i + L23_i);
g5_i = L21_i.*L12_i.*L13_i/(L21_i + L12_i + L13_i);
```

```
g6_i = L21_i.*L12_i.*L23_i/(L21_i + L12_i + L23_i);
g7_i = L21_i.*L22_i.*L13_i/(L21_i + L22_i + L13_i);
g8_i = L21_i.*L22_i.*L23_i/(L21_i + L22_i + L23_i);

g_i = Delta_i.*(-g1_i + g2_i + g3_i - g4_i + g5_i - g6_i - g7_i + g8_i);

% volume of the domain
V0 = vl^4 - vL^4;

% mean values of the integrands
fc3_e = g_e./(Lambda_b_q1_e.*Lambda_b_q2_e);
fc3_mean_e = (1/N)*sum(fc3_e);
fc3_i = g_i./(Lambda_b_q1_i.*Lambda_b_q2_i);
fc3_mean_i = (1/N)*sum(fc3_i);

% Monte Carlo approximation
c3_e = V0*fc3_mean_e; c3_i = V0*fc3_mean_i;

% standard error
d_c3_e = V0*std(fc3_e)/sqrt(n); d_c3_i = V0*std(fc3_i)/sqrt(n);
```

Appendix B

Butterworth Deconvolution Theory

The code for Butterworth deconvolution was written by my supervisor A/Prof D. A. Steyn-Ross. The following is a summary of the notes he provided.

To remove slow baseline voltage drifts, the slice recordings reported in Chapter 7 had been filtered with a 1-Hz Butterworth high-pass filter of second order. This 1-Hz filter causes shape distortions in the low frequency content of the waveform. Butterworth deconvolution theory is used to eliminate those distortions and recreate an idealized form of the original signal.

B.1 Butterworth Theory

An N^{th}-order Butterworth filter has N poles, equally spaced around a circle with radius equal to the filter cutoff frequency. A second-order Butterworth filter with 3-dB cutoff frequency $\omega_{3\,\text{dB}} = 1\,\text{rad/s}$ has two transfer function poles on the unit circle in the complex s-plane:

$$p_{1,2} \;=\; \frac{\omega_0}{\sqrt{2}}(-1 \pm j) \;=\; \frac{1}{\sqrt{2}}(-1 \pm j) \quad (\because \omega_0 = 1\,\text{rad/s})$$

Its high-pass transfer function is,

$$H(s) \;=\; \frac{s^2}{(s-p_1)(s-p_2)} \;=\; \frac{s^2}{s^2+\sqrt{2}s+1}$$

The corresponding impulse response $h(t)$ is given by the inverse Laplace transform of the transfer function,

$$\begin{aligned} h(t) \;&= \mathscr{L}^{-1}\big[H(s)\big] \\ &= \frac{1}{2\pi j}\int_{c-j\infty}^{c+j\infty} H(s)e^{st}ds \end{aligned}$$

Using Schaum Series Mathematical Handbook (1968, pp. 161–165), and validated against Symbolic Toolbox in MATLAB, we obtain impulse response,

$$\begin{aligned} h(t) \;&= \mathscr{L}^{-1}\Big[\frac{s^2}{(s-p_1)(s-p_2)}\Big] \\ &= \delta(t) - \sqrt{2}\,e^{-t/\sqrt{2}}\cos(t/\sqrt{2}) \end{aligned}$$

and for arbitrary corner frequency ω_0,

$$h(t) \;= \delta(t) - \sqrt{2}\,\omega_0\,e^{-\omega_0 t/\sqrt{2}}\cos(\omega_0\,t/\sqrt{2})$$

B.2 Butterworth Deconvolution

The shape distortions caused by the high-pass filter can be eliminated by deconvolving the 1-Hz high-pass impulse response against the recorded time series. The result is presumed to be equivalent to a "clean" drift-free recording at DC. Let $y(t)$ be the filter output, $x(t)$ the unfiltered signal input, and $h(t)$ the impulse response of the high-pass filter. From linear signal theory, the filter output is the temporal convolution of the input signal against the filter's impulse response,

$$y(t) \;=\; x(t) \otimes h(t) \;=\; \int_0^t x(\tau)\, h(t-\tau)\, d\tau$$

Taking Fourier transforms,

$$Y(\omega) \;=\; X(\omega)\, H(\omega) \;\Longrightarrow\; X(\omega) \;=\; \frac{Y(\omega)}{H(\omega)}$$

The inverse Fourier transform recovers $x(t)$:

$$x(t) \;=\; \mathscr{F}^{-1}\Big[\frac{Y(\omega)}{H(\omega)}\Big]$$

where

$$\begin{aligned} Y(\omega) &= \mathscr{F}(y(t)) \\ H(\omega) &= \mathscr{F}(h(t)) \\ &= \mathscr{F}\Big[\delta(t) - 2ce^{-ct}\cos(ct)\Big]; \quad c = \frac{\omega_0}{\sqrt{2}} \end{aligned}$$

For application to the 1-Hz high-pass filtered LFP recordings, we set $\omega_0 = 2\pi f_{\mathrm{HP}} = 2\pi$ rad/s. The following MATLAB code computes Butterworth deconvolution of time-series Y. The function is called using:

$$Y_{\mathrm{deconvolved}} \;=\; \mathrm{butterdeconv}(Y,\; dt,\; 2\pi,\; 2)$$

where dt is the time-step that scales proportionally with the sample rate of time-series Y.

```
function X = butterdeconv(Y, dt, w0, order)
% Butterworth deconvolution.
% Given Y, the output of a 1st- or 2nd-order high-pass Butterworth filter,
% attempt to reconstruct X, the original signal entering the filter,
% by 'deconvolving' the filter's impulse response H.
%
% Given,
%         y(t) = x(t) * h(t)
%
% Take Fourier transforms,
%         Y(w) = X(w) . H(w)
%         X(w) = Y(w) / H(w)
%
```

```
% Hence, deduce
%         x(t) = IFT[Y(w) / H(w)]
%
% ASR: 4-June-2008, 10-Mar-2016; 16-May-2016; 27-Jul-2020
%--------------------------------------------------------------------------

% record dimensions of input Y-vector
[m_Y, n_Y] = size(Y);
N = length(Y);

% map Y to row-vector for calculations
Y = Y(:).';

% construct timebase
t = [0: N-1]*dt;

% compute impulse response for high-pass filter
switch order
        case 1
        % impulse response of 1st-order (single-pole) high-pass filter at w0
                H_hp = -w0*exp(-w0*t);
                H_hp(1) = H_hp(1) + 1/dt;  % bring in Dirac delta function

        case 2
        % impulse response of 2nd-order high-pass Butterworth filter
                c = w0/sqrt(2);
                th = c*t;
                % hi-pass impulse response of filter
                H_hp = -2*c*exp(-th).*cos(th);
                % bring in Dirac delta function
                H_hp(1) = H_hp(1) + 1/dt;

        otherwise
                error('Unimplemented order!');
end

% compute the required Fourier transforms
Y_fft = fft(Y);                         % FT of filter output Y(t)
H_hp_fft = fft(H_hp);                   % FT of filter impulse response H(t)
X = real(ifft(Y_fft ./ H_hp_fft))/dt;  % IFT to retrieve X(t)

% remove DC offset in deconvolved result
X = X - X(1);

% ensure returned X-vector has same shape as input Y-vector
X = reshape(X, [m_Y, n_Y]);
end
```

References

[1] Abbott, L.F.: Lapicques introduction of the integrate-and-fire model neuron (1907). Brain research bulletin **50**(5-6), 303–304 (1999)

[2] Abbott, L., Kepler, T.B.: Model neurons: from Hodgkin-Huxley to Hopfield. In: Statistical mechanics of neural networks, pp. 5–18, Springer (1990)

[3] Amari, S.I.: Homogeneous nets of neuron-like elements. Biological cybernetics **17**(4), 211–220 (1975)

[4] Amari, S.i.: Dynamics of pattern formation in lateral-inhibition type neural fields. Biological cybernetics **27**(2), 77–87 (1977)

[5] Anderson, W.W., Lewis, D.V., Swartzwelder, H.S., Wilson, W.A.: Magnesium-free medium activates seizure-like events in the rat hippocampal slice. Brain research **398**(1), 215–219 (1986)

[6] Baladron, J., Fasoli, D., Faugeras, O., Touboul, J.: Mean-field description and propagation of chaos in networks of Hodgkin-Huxley and FitzHugh-Nagumo neurons. The Journal of Mathematical Neuroscience **2**(1), 10 (2012)

[7] Başar, E., Bullock, T.H.: Induced rhythms in the brain. Springer (1992)

[8] Beurle, R.L.: Properties of a mass of cells capable of regenerating pulses. Philosophical Transactions of the Royal Society of London. Series B, Biological Sciences pp. 55–94 (1956)

[9] Bressloff, P.C.: Stochastic neural field theory and the system-size expansion. SIAM Journal on Applied Mathematics **70**(5), 1488–1521 (2009)

[10] Buice, M.A., Chow, C.C.: Beyond mean field theory: statistical field theory for neural networks. Journal of Statistical Mechanics: Theory and Experiment **2013**(03), P03003 (2013)

[11] Buice, M.A., Cowan, J.D.: Field-theoretic approach to fluctuation effects in neural networks. Physical Review E **75**(5), 051919 (2007)

[12] Carlen, P.L., Skinner, F., Zhang, L., Naus, C., Kushnir, M., Velazquez, J.L.P.: The role of gap junctions in seizures. Brain research reviews **32**(1), 235–241 (2000)

[13] Cronin, J.: Mathematical aspects of Hodgkin-Huxley neural theory, vol. 7. Cambridge University Press (1987)

[14] De Ruiter, P.C., Wolters, V., Moore, J.C.: Dynamic food webs: multispecies assemblages, ecosystem development and environmental change, vol. 3. Academic Press (2005)

[15] Deco, G., Jirsa, V.K., Robinson, P.A., Breakspear, M., Friston, K.: The dynamic brain: from spiking neurons to neural masses and cortical fields. PLoS computational biology **4**(8), e1000092 (2008)

[16] Destexhe, A., Bedard, C.: Local field potential. Scholarpedia **8**(8), 10713 (2013)

[17] Dulla, C.G., Janigro, D., Jiruska, P., Raimondo, J.V., Ikeda, A., Lin, C.C.K., Goodkin, H.P., Galanopoulou, A.S., Bernard, C., de Curtis, M.: How do we use in vitro models to understand epileptiform and ictal activity? a report of the task 1-wg 4 group of the ilae/aes joint translational task force. Epilepsia Open **3**(4), 460–473 (2018)

[18] Einevoll, G.T., Kayser, C., Logothetis, N.K., Panzeri, S.: Modelling and analysis of local field potentials for studying the function of cortical circuits. Nature Reviews Neuroscience **14**(11), 770–785 (2013)

[19] El Boustani, S., Destexhe, A.: A master equation formalism for macroscopic modeling of asynchronous irregular activity states. Neural computation **21**(1), 46–100 (2009)

[20] Ermentrout, B.: Gap junctions destroy persistent states in excitatory networks. Physical Review E **74**(3), 031918 (2006)

[21] FitzHugh, R.: Mathematical models of threshold phenomena in the nerve membrane. The bulletin of mathematical biophysics **17**(4), 257–278 (1955)

[22] FitzHugh, R.: Impulses and physiological states in theoretical models of nerve membrane. Biophysical journal **1**(6), 445 (1961)

[23] Freeman, W.J.: Eeg analysis gives model of neuronal template-matching mechanism for sensory search with olfactory bulb. Biological cybernetics **35**(4), 221–234 (1979)

[24] Fukuda, T., Kosaka, T., Singer, W., Galuske, R.A.: Gap junctions among dendrites of cortical gabaergic neurons establish a dense and widespread intercolumnar network. Journal of Neuroscience **26**(13), 3434–3443 (2006)

[25] Galarreta, M., Hestrin, S.: A network of fast-spiking cells in the neocortex connected by electrical synapses. Nature **402**(6757), 72 (1999)

[26] Gardiner, C.: Stochastic methods, vol. 4. Springer Berlin (2009)

[27] Gardiner, C., Steyn-Ross, M.L.: Adiabatic elimination in stochastic systems. ii. application to reaction diffusion and hydrodynamic-like systems. Physical Review A **29**(5), 2823 (1984)

[28] Gerstner, W., Kistler, W.M.: Spiking neuron models: Single neurons, populations, plasticity. Cambridge university press (2002)

[29] Gibson, J.R., Beierlein, M., Connors, B.W.: Two networks of electrically coupled inhibitory neurons in neocortex. Nature **402**(6757), 75 (1999)

[30] Griffith, J.: A field theory of neural nets: I: Derivation of field equations. The bulletin of mathematical biophysics **25**(1), 111–120 (1963)

[31] Hamilton, B., Bilbao, S.: Fourth-order and optimised finite difference schemes for the 2-d wave equation. In: Proc. 16th Conference on Digital Audio Effects (DAFx-13) (2013)

[32] Herculano-Houzel, S.: The human brain in numbers: a linearly scaled-up primate brain. Frontiers in human neuroscience **3**, 31 (2009)

[33] Hines, M.L., Carnevale, N.T.: The neuron simulation environment. Neural Computation **9**(6), 1179–1209 (1997), doi:10.1162/neco.1997.9.6.1179, URL `https://doi.org/10.1162/neco.1997.9.6.1179`

[34] Hodgkin, A.L., Huxley, A.F.: Propagation of electrical signals along giant nerve fibres. Proceedings of the Royal Society of London. Series B, Biological Sciences pp. 177–183 (1952)

[35] Hodgkin, A.L., Huxley, A.F.: A quantitative description of membrane current and its application to conduction and excitation in nerve. The Journal of physiology **117**(4), 500–544 (1952)

[36] Hodgkin, A.L., Huxley, A.F., Katz, B.: Measurement of current-voltage relations in the membrane of the giant axon of loligo. The Journal of physiology **116**(4), 424–448 (1952)

[37] Hodgkin, A.L., Huxley, A.F.: The components of membrane conductance in the giant axon of loligo. The Journal of physiology **116**(4), 473–496 (1952)

[38] Hodgkin, A.L., Huxley, A.F.: Currents carried by sodium and potassium ions through the membrane of the giant axon of loligo. The Journal of physiology **116**(4), 449–472 (1952)

[39] Izhikevich, E.M.: Dynamical systems in neuroscience. MIT press (2007)

[40] Jirayucharoensak, S., Pan-Ngum, S., Israsena, P.: Eeg-based emotion recognition using deep learning network with principal component based covariate shift adaptation. The Scientific World Journal **2014** (2014)

[41] Johnston, D., Wu, S.M.S.: Foundations of cellular neurophysiology. MIT press (1994)

[42] Kandel, E.R., Markram, H., Matthews, P.M., Yuste, R., Koch, C.: Neuroscience thinks big (and collaboratively). Nature Reviews Neuroscience **14**(9), 659 (2013)

[43] Khalilov, I., Le Van Quyen, M., Gozlan, H., Ben-Ari, Y.: Epileptogenic actions of gaba and fast oscillations in the developing hippocampus. Neuron **48**(5), 787–796 (2005)

[44] Kloeden, P.E., Platen, E.: Numerical solution of stochastic differential equations, vol. 23. Springer Science & Business Media (2013)

[45] Koch, C.: Biophysics of computation: information processing in single neurons. Oxford university press (2004)

[46] Kowalski, T., Silny, J., Buchner, H.: Current density threshold for the stimulation of neurons in the motor cortex area. Bioelectromagnetics: Journal of the Bioelectromagnetics Society, The Society for Physical Regulation in Biology and Medicine, The European Bioelectromagnetics Association **23**(6), 421–428 (2002)

[47] Liang, P., Wu, S., Gu, F.: Single neuron models. In: An Introduction to Neural Information Processing, pp. 129–182, Springer (2016)

[48] Liley, D.T.: A continuum model of the mammalian alpha rhythm. Spatiotemporal models in biological and artificial systems. Amsterdam: IOS Press pp. 89–96 (1997)

[49] Liley, D.T., Cadusch, P.J., Dafilis, M.P.: A spatially continuous mean field theory of electrocortical activity. Network: Computation in Neural Systems **13**(1), 67–113 (2002)

[50] Liley, D.T., Cadusch, P.J., Wright, J.J.: A continuum theory of electro-cortical activity. Neurocomputing **26**, 795–800 (1999)

[51] Markram, H.: The blue brain project. Nature Reviews Neuroscience **7**(2), 153–160 (2006)

[52] Mathis, D.M., Furman, J.L., Norris, C.M.: Preparation of acute hippocampal slices from rats and transgenic mice for the study of synaptic alterations during aging and amyloid pathology. JoVE (Journal of Visualized Experiments) (49), e2330 (2011)

[53] Mihalaş, Ş., Niebur, E.: A generalized linear integrate-and-fire neural model produces diverse spiking behaviors. Neural computation **21**(3), 704–718 (2009)

[54] Minni, S., Ji-An, L., Moskovitz, T., Lindsay, G., Miller, K., Dipoppa, M., Yang, G.R.: Understanding the functional and structural differences across excitatory and inhibitory neurons

[55] Muller, L., Chavane, F., Reynolds, J., Sejnowski, T.J.: Cortical travelling waves: mechanisms and computational principles. Nature Reviews Neuroscience **19**(5), 255 (2018)

[56] Negahbani, E.: Dynamics and precursor signs for phase transitions in neural systems. Ph.D. thesis, University of Waikato (2014)

[57] Nunez, P.L.: The brain wave equation: a model for the eeg. Mathematical Biosciences **21**(3-4), 279–297 (1974)

[58] Nunez, P.L.: The neurophysics of eeg. In: IEEE TRANSACTIONS ON BIOMEDICAL ENGINEERING, vol. 30, pp. 549–550, IEEE-INST ELECTRICAL ELECTRONICS ENGINEERS INC 345 E 47TH ST, NEW YORK, NY (1983)

[59] O'Connor, W.T.: What can the brain science of learning teach us about cybernetics? In: 2012 IEEE 11th International Conference on Cybernetic Intelligent Systems (CIS), pp. 36–40, IEEE (2012)

[60] OReilly, R.C., Beck, J.M.: A family of large-stencil discrete laplacian approximations in three dimensions. Int. J. Numer. Methods Eng pp. 1–16 (2006)

[61] Pencheva, N., de Gooijer, M.C., Vis, D.J., Wessels, L.F., Würdinger, T., van Tellingen, O., Bernards, R.: Identification of a druggable pathway controlling glioblastoma invasiveness. Cell reports **20**(1), 48–60 (2017)

[62] Pharr, M., Jakob, W., Humphreys, G.: Physically based rendering: From theory to implementation. Morgan Kaufmann (2016)

[63] Press, W.H., Teukolsky, S.A., Flannery, B.P., Vetterling, W.T.: Numerical recipes in Fortran 77: volume 1, volume 1 of Fortran numerical recipes: the art of scientific computing. Cambridge university press (1992)

[64] Robinson, P., Rennie, C., Rowe, D.: Dynamics of large-scale brain activity in normal arousal states and epileptic seizures. Physical Review E **65**(4), 041924 (2002)

[65] Robinson, P., Wu, H., Kim, J.: Neural rate equations for bursting dynamics derived from conductance-based equations. Journal of theoretical biology **250**(4), 663–672 (2008)

[66] Robinson, P.A., Kim, J.: Spike, rate, field, and hybrid methods for treating neuronal dynamics and interactions. Journal of neuroscience methods **205**(2), 283–294 (2012)

[67] Robinson, P.A., Rennie, C.J., Wright, J.J.: Propagation and stability of waves of electrical activity in the cerebral cortex. Physical Review E **56**(1), 826 (1997)

[68] Schwalger, T., Deger, M., Gerstner, W.: Towards a theory of cortical columns: From spiking neurons to interacting neural populations of finite size. PLoS computational biology **13**(4), e1005507 (2017)

[69] Steyn-Ross, D.A., Steyn-Ross, M.: Modeling phase transitions in the brain. Springer (2010)

[70] Steyn-Ross, D.A., Steyn-Ross, M.L., Wilson, M.T., Sleigh, J.W.: White-noise susceptibility and critical slowing in neurons near spiking threshold. Physical Review E **74**(5), 051920 (2006)

[71] Steyn-Ross, M.L., Gardiner, C.: Adiabatic elimination in stochastic systems. iii. application to renormalization-group transformations of the time-dependent ginsburg-landau model. Physical Review A **29**(5), 2834 (1984)

[72] Steyn-Ross, M.L., Steyn-Ross, D.A.: From individual spiking neurons to population behavior: Systematic elimination of short-wavelength spatial modes. Physical Review E **93**(2)

[73] Steyn-Ross, M.L., Steyn-Ross, D.A., Sleigh, J.W.: Modelling general anaesthesia as a first-order phase transition in the cortex. Progress in biophysics and molecular biology **85**(2-3), 369–385 (2004)

[74] Steyn-Ross, M.L., Steyn-Ross, D.A., Sleigh, J.W., Liley, D.: Theoretical electroencephalogram stationary spectrum for a white-noise-driven cortex: evidence for a general anaesthetic-induced phase transition. Physical Review E **60**(6), 7299 (1999)

[75] Steyn-Ross, M.L., Steyn-Ross, D.A., Sleigh, J.W., Wilcocks, L.C.: Toward a theory of the general-anesthetic-induced phase transition of the cerebral cortex. i. a thermodynamics analogy. Physical Review E **64**(1), 011917 (2001)

[76] Steyn-Ross, M.L., Steyn-Ross, D.A., Sleigh, J.W.: Gap junctions modulate seizures in a mean-field model of general anesthesia for the cortex. Cognitive neurodynamics **6**(3), 215–225 (2012)

[77] Steyn-Ross, M.L., Steyn-Ross, D.A., Wilson, M.T., Sleigh, J.W.: Gap junctions mediate large-scale turing structures in a mean-field cortex driven by subcortical noise. Physical Review E **76**(1), 011916 (2007)

[78] Su, J., Fang, W., Yu, Q., Li, Y.: Numerical simulation of swift–hohenberg equation by the fourth-order compact scheme. Computational and Applied Mathematics **38**(2), 54 (2019)

[79] Teplan, M., et al.: Fundamentals of eeg measurement. Measurement science review **2**(2), 1–11 (2002)

[80] Velazquez, J.L.P., Carlen, P.L.: Gap junctions, synchrony and seizures. Trends in neurosciences **23**(2), 68–74 (2000)

[81] Voss, L.J., Jacobson, G., Sleigh, J.W., Steyn-Ross, A., Steyn-Ross, M.: Excitatory effects of gap junction blockers on cerebral cortex seizure-like activity in rats and mice. Epilepsia **50**(8), 1971–1978 (2009)

[82] Voss, L.J., Melin, S., Jacobson, G., Sleigh, J.W.: Role of cx36 gap junction modulation in general anaesthetic anticonvulsant action. European journal of pharmacology **643**(1), 58–62 (2010)

[83] Wikipedia contributors: Monte carlo integration — Wikipedia, the free encyclopedia (2004), URL `https://en.wikipedia.org/wiki/Monte_Carlo_integration`, [Online; accessed 02-March-2020]

[84] Wikipedia contributors: Neuron (software) — Wikipedia, the free encyclopedia (2019), URL `https://en.wikipedia.org/wiki/title=Neuron_(software)&oldid=899881763`, [Online; accessed 28-November-2019]

[85] Williams, R.W., Herrup, K.: The control of neuron number. Annual review of neuroscience **11**(1), 423–453 (1988)

[86] Wilson, H.R.: Simplified dynamics of human and mammalian neocortical neurons. Journal of theoretical biology **200**(4), 375–388 (1999)

[87] Wilson, H.R.: Spikes, decisions, and actions: the dynamical foundations of neurosciences (1999)

[88] Wilson, H.R., Cowan, J.D.: Excitatory and inhibitory interactions in localized populations of model neurons. Biophysical journal **12**(1), 1–24 (1972)

[89] Wilson, H.R., Cowan, J.D.: A mathematical theory of the functional dynamics of cortical and thalamic nervous tissue. Kybernetik **13**(2), 55–80 (1973)

[90] Wilson, K.G., Kogut, J.: The renormalization group and the expansion. Physics reports **12**(2), 75–199 (1974)

[91] Wilson, M.T., Robinson, P.A., O'Neill, B., Steyn-Ross, D.A.: Complementarity of spike- and rate-based dynamics of neural systems. PLoS computational biology **8**(6), e1002560 (2012)

[92] Wilson, M.T., Steyn-Ross, M.L., Steyn-Ross, D.A., Sleigh, J.W.: Going beyond a mean-field model for the learning cortex: second-order statistics. Journal of biological physics **33**(3), 213–246 (2007)

[93] Wright, J.J., Liley, D.T.: Simulation of electrocortical waves. Biological cybernetics **72**(4), 347–356 (1995)

[94] Wright, J., Liley, D.: A millimetric-scale simulation of electrocortical wave dynamics based on anatomical estimates of cortical synaptic density. Network: Computation in Neural Systems **5**(2), 191–202 (1994)

[95] Wright, J., Liley, D.: Dynamics of the brain at global and microscopic scales: Neural networks and the eeg. Behavioral and Brain Sciences **19**(2), 285–295 (1996)

[96] Young, D.: Convolve2 two dimensional convolution (2002), URL `https://tinyurl.com/y6ex4grd`